INJECTABLE INTERPENETRATING NETWORK HYDROGELS FOR BIOMEDICAL APPLICATIONS

INJECTABLE INTERPENETRATING NETWORK HYDROGELS FOR BIOMEDICAL APPLICATIONS

By TREVOR WILLIAM GILBERT, B.A.Sc., M.A.Sc

A Thesis Submitted to the School of Graduate Studies in Partial Fulfilment of the Requirements for the Degree Ph.D. of Chemical Engineering

McMaster University Ph.D. OF ENGINEERING (2016) Hamilton, Ontario (Chemical Engineering)

TITLE: Injectable Interpenetrating Network Hydrogels for Biomedical Applications

AUTHOR: Trevor William Gilbert, B.A.Sc., M.A.Sc. (University of Toronto)

SUPERVISOR: Professor Todd R. Hoare

NUMBER OF PAGES: xxiv, 212

Lay Abstract

This thesis describes the development of overlapping but unconnected polymer networks formed by mixing of completely injectable polymer precursors. The interlocking pair of networks is based on one component that shrinks upon heating and the other component that offers the potential for biological adhesion. Entanglement between the two components renders them mutually reinforcing and changes the shrinking and reswelling behaviour of the temperature-responsive component. The structure of the composite network is also distinctive from either individual component, forming alternating, unevenly mixed regions richer in one or the other component. The composite's properties are attractive for a potential bioadhesive drug delivery carrier and, in the future, a possible wound closure biomaterial.

Abstract

Interpenetrating polymer networks (IPN's) consist of two overlapping cross-linked networks that are not bonded to each other. Hydrogel IPN's are of application interest due to properties such as mechanical reinforcement, modulated drug release and biodegradation kinetics, dual polymer activities *in vivo*, and novel nanostructured morphologies. Prior IPN hydrogels reported in the literature either required surgical implantation (disadvantageous for several reasons) or were polymerized *in situ* (limited to a small subset of biologically safe chemistries). Alternatively, we formed IPN's using a mixing injector to deliver orthogonally reactive functionalized prepolymer solutions that gel upon contact. Specifically, we use hydrazone chemistry to gel a thermosensitive poly(N-isopropylacrylamide) (PNIPAM) network and kinetically orthogonal thiosuccinimide or disulfide chemistry to cross-link a second network of hydrophilic poly(vinylpyrrolidone) (PVP).

The resulting IPN's preserve the thermoresponsive properties of the PNIPAM constituent but exhibit slower, smaller, and more reversible transitions due to entanglement with the highly hydrophilic PVP network (potentially useful to reduce the problem of burst release in thermoresponsive drug delivery systems). Mechanical reinforcement was evidenced by the increased shear storage modulus of IPN composites relative to the sum of the individual component moduli, particularly so in IPN's employing the thiosuccinimide-cross-linked PVP.

The nanostructure of the IPN hydrogels was further studied using small angle neutron scattering with contrast matching, and was found to combine features characteristic to each single network component (PNIPAM-rich static domains embedded in PVP-rich

fractal clusters). However, our results suggest some slight changes to their scattering profiles, indicative of partial mixing or influence of each network structure upon the other. Corroborating investigations with single-molecule super-resolution fluorescence microscopy, operating at a slightly larger length scale, show the formation of separate populations of mixed and individual domains or clusters of each polymer type.

These properties suggest such injectable IPN's for further investigation as prospective biomaterials.

Acknowledgements:

First of all, I would like to thank Professor Hoare for supervising my research. Your guidance and patience through the many challenges encountered on this project have kept me on track through moments of doubt, and the example you set has helped me grow as a researcher and a technical writer. I would also like to thank Professors Filipe and Brook for their input on my supervisory committee – your perspective and suggestions during committee meetings have helped with several of the key technical issues, as well as valued advice on project flow planning, publishing, and presentation skills.

To my colleagues over the years in Professor Hoare's lab group (particularly Niels Smeets, Scott Campbell, Daryl Sivakumaran, Mathew Patenaude, Rabia Mateen, Danielle Maitland, Paniz Sheikholeslami, Emilia Bakaic, Madeline Simpson, Fei Xu, Katya D'Costa, Eva Mueller, Ian Gough and Angus Lam), your support and encouragement have been invaluable. You have made this place positive and productive to work, and many of you also became some of my first and closest friends in Hamilton.

I would also like to thank the rest of the Chemical Engineering faculty (particularly Professors Cranston and Adams) and staff (Paul, Dan, Lynn, Kristina, Michelle, Linda, and Mike) for the various forms of assistance (and the friendly environment!) they have provided over the years.

I would also like to gratefully acknowledge NSERC, the CREATE Integrated Design of Extracellular Matrices group, and the Ontario Ministry of Research and Innovation for funding this project. Under Professor Stover's direction, the CREATE organization has been a helpful place environment for those of us doing similar work to brainstorm shared

challenges and beta-test our research presentations in a low stress setting. Particular recognition to Allison (for commiserating over the difficulties of working with maleimide chemistry), Mike, Sheilan, Fei and Emilia.

Furthermore, I would like to gratefully acknowledge the technical assistance of:

-Our neutron scattering collaborators in the Department of Physics & Astronomy (Richard Alsop and Professor Maikel Rheinstadter), and the National Institute of Standards & Technology / National Center for Neutron Research staff scientists who have hosted / helped with our research visits (Dr. Yimin Mao, Dr. Boualem Hammouda, and Dr. Markus Blueul).

-Our single-molecule fluorescence imaging collaborators in the Department of Chemistry, Mouhanad Babi and Professor Jose Moran-Mirabal.

-Eric Quenneville of Biomomentum for collaboration on designing a new sample holder for testing adhesion mechanics on soft substrates, as well as the rest of the Biomomentum staff for their help during and after my visit to test out the prototype.

-Marcia West, for training on the Faculty of Health Sciences electron microscopy instruments.

-Nicholas Burke and Rachelle and Sam in Professor Stover's lab for training and access on the GPC instrument

-McMaster Department of Chemistry's NMR staff (Dr. Bob Berno, Dr. Hilary Jenkins, Dr. Dan Sorenson).

-Diane Sivakumaran, for her frequently used rendering figure of a double-barreled mixing injector.

I would also like to thank my many teammates and the organizers from the GSA & intramural sports (especially the Channel Six / Sax / Soul / etc. Panthers) for providing the social centre of my time at McMaster. Jake, Kyle, Pat, Kat, Kyla, Mark, Brian, Mike, Ryan, Scott Fitz, Kevin, Lexa, Brandon, Scott, Daryl, Maddie – thanks for the sports memories, one and all.

Finally, I wish to thank my family for their invaluable support over the years. Without you, I would not have made it this far.

Table of Contents

List of Figures

Chapter 1

Chapter 2

Chapter 2 Supporting Information

Chapter 3

Chapter 3 Supporting Information

Chapter 4

Chapter 4 Supporting Information

Chapter 5

List of Tables

List of Terminology, Symbols and Abbreviations

AA	Acrylic acid
ADH	Adipic acid dihydrazide
AEMA	N-(2-aminoethyl)maleimide (also, aminoethyl methacrylate)
AIBME	2,2-azobisisobutyric acid dimethyl ester
Ald	Aldehyde
Am /Aam	Acrylamide
Cht	Chitosan
Dex	Dextran
D_2O	Deuterium oxide
DIW	Deionized water
DMSO	Dimethyl sulfoxide
d_6DMSO	Deuterium-substituted dimethyl sulfoxide
DPT	3,3'-Dithiobis(propionic hydrazide)
DTT	D,L-dithiothreitol
EDC	N-3-dimethylaminopropyl-N-ethyl carbodiimide
FTIR	Fourier-transform infrared spectroscopy
G'	Storage modulus
G"	Loss modulus
GPC	Gel permeation chromatography
GSH	Glutathione
Hzd	Hydrazide
HCl	Hydrochloric acid

HPLC	High performance liquid chromatography
LCST	Lower critical solution temperature
MAA	Mercaptoacetic acid
Mal	Maleimide
M_n	Number average molecular weight
MPA	3-mercaptopropionic acid
M_w	Mass average molecular weight
NaCl	Sodium chloride
NaOH	Sodium hydroxide
NHS	N-hydroxysuccinimide
NIPAM	N-isopropylacrylamide
NMR	Nuclear magnetic resonance spectrometry
PBS	Phosphate buffered saline
PDMS	Poly(dimethylsiloxane)
PDI	Polydispersity index
PCL	Poly(ε-caprolactone)
PEG	Poly(ethylene glycol)
PLGA	Poly(lactic-co-glycolic acid)
PNIPAM	Poly(N-isopropylacrylamide)
PNIPAM-AA	Poly(N-isopropylacrylamide-co-acrylic acid)
PNIPAM-Ald	Aldehyde-functionalized poly(N-isopropylacrylamide)
PNIPAM-Hzd	Hydrazide-functionalized poly(N-isopropylacrylamide)
POEGMA	Poly(oligoethylene glycol methacrylate)

PVA	Polyvinyl alcohol
PVP	Poly(N-vinyl pyrrolidone)
PVP-Mal	Maleimide-functionalized poly(N-vinyl pyrrolidone)
PVP-SH	Thiol-functionalized poly(N-vinyl pyrrolidone)
PVP-VA	Poly(N-vinyl pyrrolidone co vinyl amine)
PVP-VF	Poly(N-vinyl pyrrolidone co vinyl formamide)
SANS	Small-angle neutron scattering
SEM	Scanning electron microscopy
SH	Thiol
T_g	Glass transition temperature
TGA	Thioglycolic acid
T_m	Melting temperature
UCST	Upper critical solution temperature
USANS	Ultra-small angle neutron scattering
UV	Ultraviolet
VA	Vinyl amine
VF	Vinyl formamide
VP	N-vinyl pyrrolidone
VPTT	Volume phase transition temperature

Declaration of Academic Achievement:

The majority of the written work herein recorded was conceived, carried out, analyzed and written by the author of this thesis, in consultation with Dr. Todd Hoare, except for the following:

Chapter 2: Dr. Niels Smeets (2nd author on the publication that serves as the basis for Chapter 2 and a post-doctoral researcher in Dr. Hoare's group at the time) suggested the method of thiol-conjugating the PVP polymers and directly aided in the synthesis of the required reagent 3,3'-dithiobis(propionic dihydrazide). Dr. Smeets also reviewed my interpretation of the mechanical testing data.

Chapters 3 and 4: Richard Alsop (2nd author on the pending publications on which these chapters are based, a Ph.D. student working in Dr. Maikel Rheinstadter's lab in the Department of Physics) collaborated on the neutron scattering section. We calculated the index matching solvent ratios jointly. Richard programmed the command sequence to run the various times of scattering exposures at each distance during our visit to the NCNR lab and ran the reduction macros to stitch the resulting spectra together to cover the entire angular range. He also evaluated my data fitting results, and wrote the hybrid Porod /squared Lorentzian function to use in the Igor software based on our joint conclusion that the IPN samples were not adequately modelled by either individual function.

Mouhanad Babi (3rd author on the pending publications involving super-resolution fluorescence, a 4th year undergraduate working in Dr. José Moran-Mirabal's lab in the

Department of Chemistry) collaborated on the dSTORM super-resolution microscopy section. We jointly developed the method to prepare thin-layer hydrogels by spin-coating them on the proprietary dishes that fit in the microscope's sample mount. Mouhanad then controlled the imaging parameters (excitation laser power, exposure times, etc.) and ran the resulting image stacks through his analysis macros to reconstruct fluorophore localizations with sub-wavelength resolution. He also wrote the methods paragraphs describing the microscopy apparatus, imaging conditions and analysis software employed for the dSTORM imaging section.

Chapter 5: Dr. Eric Quenneville (Biomomentum Inc.) collaborated on the design of a sample holder to mount the soft material adhesion substrates on Biomomentum's Mach-1 micromechanical tester for lap shear experiments. He converted my conceptual sketches to the SolidWorks plans reproduced herein, with attachment points matching the dimensions necessary to mount the finished product on their instrument, and supervised prototype testing during my visit to the Biomomentum head office. Paul Gatt (Chemical Engineering department machinist) cut the plastic prototypes on his CNC milling machine based on Dr. Quenneville's schematics, recommending and implementing a few slight adjustments.

Chapter 1: Introduction

1.1 Hydrogels and their biomedical applications

1.1.1 Overview

Hydrogels are networks of water-soluble polymers cross-linked to fill a three-dimensional space with a mesh of solvated polymers. The volume fraction of the hydrogel occupied by polymer is usually a significant minority compared to that of the solvent (frequently under 20%[1]), meaning the hydrogel has high porosity and high water content. These properties are generally favourable for loading / entrapping cargo of interest to biomedical applications (such as cells, therapeutic molecules, or both); furthermore, the high water content often confers low immunogenicity[2-3]. These advantages have been leveraged to design hydrogels for multiple biomedical applications, including tissue engineering, cell encapsulation and drug delivery.

1.1.2 Environmentally responsive hydrogels

Since the bulk volume of a hydrogel is the sum of its polymer and water volume fractions, the hydrogel's bulk dimensions depend upon the extent of the polymer network's hydration. For some polymers, the equilibrium hydration state is a function of certain physical, chemical, or biological factors in the hydrogel's environment, causing hydrogels made from these polymers to swell or shrink based on changes in the applicable variables. Such hydrogels are referred to as "smart" or stimuli-responsive hydrogels.

The broadest class of environmentally responsive polymers are those responsive to temperature (i.e. the thermoresponsive polymers). These exhibit a swelling change around their respective volume phase transition temperature (VPTT). Thermoresponsive polymers are further subdivided as lower critical solution temperature (LCST; well solvated below their VPTT and collapsed above it) or upper critical solution temperature (UCST; poorly solvated below their VPTT and swollen above it). LCST polymers used in thermosensitive hydrogels include poly(N-isopropylacrylamide) (PNIPAM)[4], poly(ethylene oxide) – poly(propylene oxide) – poly(ethylene oxide) triblock copolymers[5] (also known as Pluronics), poly(oligo ethylene glycol methacrylate) (POEGMA)[6], poly(ε-caprolactone)[7], and hydroxypropylcellulose[8]. Polymers used in hydrogels with UCST behaviour include gelatin[9], poly(N-acryloyl glycinamide)[10], and poly(allylurea-co-allylamine)[11].

Another common type of environmentally responsive hydrogels swell or de-swell dependent on local pH. Polymers with pH-responsive properties include poly(acrylic acid), poly(methacrylic acid), poly-(amino carbonate urethane)[12], and amine-functionalized poly(ethylene glycol)[13]. Hydrogels whose swelling state depends on the concentration of a solute in the aqueous phase can also be produced, including those responsive to glucose concentration[14] or ionic strength[15].

The osmotic pressure driving hydrogel swelling or deswelling is a combination of component effects from the mixing of polymer and solvent, the elastic behaviour of the network, and Donnan effects driven by the activity of counter-ions inside of gels with polyelectrolyte functionality[16] (Equations 1.1 & 1.2).

(Eq. 1.1) $$\pi_{total} = \pi_{mixing} + \pi_{elastic} + \pi_{Donnan}$$

(Eq. 1.2) $\pi_{total} = \frac{k_b T}{a^3}[-(\varphi + \ln(1-\varphi) + \chi\varphi^2) + \frac{\varphi_0}{N_x}[\left(\frac{\varphi}{2\varphi_0}\right) - \left(\frac{\varphi}{\varphi_0}\right)^{\frac{1}{3}}] + \frac{f\varphi_0}{N_x}\left(\frac{\varphi}{\varphi_0}\right)]$

k_b	Boltzmann constant
T	Temperature
a	Gel dimension
φ	Volume fraction polymer at equilibrium
φ_0	Volume fraction polymer at zero strain
χ	Solubility parameter
f	Mean number charges between cross-links
N_x	Mean number monomer repeats between cross-links

In conventional hydrogels, the mixing component of the osmotic pressure balance consistently drives swelling responses over the full range of accessible temperatures in water. However, for hydrogels based on temperature-responsive polymers that exhibit a lower critical solution temperature (e.g. poly(N-isopropylacrylamide) (PNIPAM)), the mixing contribution can change as a function of temperature based on the changing relative importance of the enthalpic contribution to swelling (driven by hydrogen bonding with surrounding water molecules) and the entropic component to swelling (driven by hydrophobic interactions between isopropyl groups), as per Equation 3. Since the entropic component increases in magnitude at higher temperatures, heating induces de-solvation of the polymers that is manifested as de-swelling of the hydrogel with the attendant expulsion of water (the volume phase transition).

(Eq. 1.3) $\Delta G_{mixing} = \Delta H_{mixing} - T\Delta S_{mixing}$

Environmentally responsive polymers that swell in response to a pH change, in contrast, deswell upon neutralization, at which point the Donnan component ceases to contribute

to the swelling pressure[17]. Although the specific pK_a values for polyacids and polybases differ from their constituent monoacids / monobases (due to electrostatic hindrance by charged groups on further dissociation of neighbouring sites), rational design of the swelling transition pH is generally possible by choosing an ionisable group with a pK_a in the targeted range. Fine-tuning the transition profile can be accomplished by copolymerizing with small amounts of hydrophobic residues that affect chain conformation near the transition[17].

1.1.3 Cell scaffolds for tissue engineering

Important factors in the design of extracellular matrices include porosity, mechanical strength, degradation profile, and materials chemistry (in particular, the capacity for dynamic or secondary functionalization[18]). Hydrogels offer significant latitude to tailor these properties to specific applications.

Porosity is among the most important concerns in tissue engineering due to the requirement for mass transport (nutrients and oxygen to and waste away from cells), the desirability of vascular infiltration into the scaffold material[18-21], and the potential for selectivity between cell types that will favour ingrowth into the scaffold[22]. Porosity can be introduced by adding additional components that can be selectively degraded (either *in vitro* or *in vivo*[23]), electrospinning[24], super-critical CO_2 foaming[25] or the use of porogens that can be selectively dissolved out after cross-linking[26-29].

The targeted rate of matrix degradation in tissue engineering (or whether the matrix is desired to degrade at all) is typically correlated to how quickly the cellular component in the targeted application can be predicted to remodel the construct by depositing new

natural extra-cellular matrix. The degradation rate can be tailored based on controlling hydrolysis (e.g. the differential backbone degradation rates in PLA/PLGA composites[30]), the degree of cross-linking in systems in which the cross-link itself is hydrolysable (e.g. hydrazones)[6, 31], or differences in backbone hydrophilicity that affect the microenvironment around the cross-links[32]. Alternatively, degradation may be controlled by using enzymatically cleavable peptide cross-linkers[33-34] or by reductively labile cross-links such as disulfide bonds[35-37].

The last several decades have seen an increasing understanding of the role of scaffold mechanical properties in influencing cell attachment, spreading, growth, viability and differentiation pathways in tissue engineering[38-42]. The scaffold must also closely enough match the native biological environment as to avoid bulk failures (internal if too weak, or interfacial if too strong) due to bodily movement when implanted[18]. The elasticity of a hydrogel formulation can readily be altered by adjusting the concentration and / or degree of cross-linking of its constituent polymers[43].

Furthermore, hydrogels whose constituent polymers bear functional groups in addition to any used for cross-linking can be modified at these sites with a variety of peptides that influence cell-scaffold interactions. The most common of such peptides is the RGD adhesive sequence[43] or more complicated sequences that contain RGD domains but are more selective by cell type and/or integrin interaction[44]. By mimicking the functionality of the natural ECM environment, such derivatized hydrogels can further improve cell spreading[45-47].

1.1.4 Drug delivery

The primary purpose of using hydrogels in therapeutic delivery is to create a depot that will release its cargo by diffusion to create a sustained higher concentration in the local vicinity of the hydrogel, generally (although not necessarily) while limiting systemic dosage. Thus, the predominant design considerations are facile delivery of the hydrogel to its site of action (see section 1.1.4), maximizing the loading of various types of pharmaceutical cargoes, and achieving prolonged and as linear as possible release kinetics[3].

One approach to addressing the latter two issues is to increase the affinity of the drug for the hydrogel, either non-covalently (such as by electrostatic interactions between a charged drug and an oppositely charged polyelectrolyte) or *via* degradable covalent bonds[3]. Charged hydrogels are typically produced by incorporating ionisable functional groups into the polymer backbone of the hydrogel; such systems have opposite trends for mesh size (and therefore diffusivity for any dissociated pharmaceutical cargo) as a function of pH changes depending whether they are designed to be cationic or anionic[48]. Polyvalent ionic groups such as phosphates are particularly efficacious for maximizing the loading of positively charged drugs[3, 49-50]. A variety of hydrolytically or enzymatically degradable drug-polymer covalent linkers such as lactides[51], esters[52], disulfides[53], hydrazones[54], or various peptide sequences[55] have also been explored, with their rate of decomposition (and drug release kinetics achieved) often being tunable based on the chemistry near the labile site[3]. Drug-polymer conjugates that release the drug from a hydrogel by degradation of the polymer backbone, rather than the link between drug and polymer, can also in some cases maintain significant pharmaceutical activity depending on the (formerly polymer-based) residues that remain attached to the release drug[56].

Alternately, release rates may be controlled by diffusive limitations alone. Increased cross-linking densities will result in a smaller mesh size and lower diffusivity in hydrogel drug carriers; however, this strategy can introduce undesirable consequences such as excessive material stiffness (potentially undesirable in certain applications where compliance matching with adjacent tissue is desired[57]) and / or unwanted constraints on environmentally responsive behaviour[3]. Alternately, a diffusion-limiting membrane barrier[58] may be used, although this approach is not feasible in injectable bulk hydrogels. When using environmentally responsive hydrogels, the collapsed state generally poses a greater barrier to diffusive release than the well solvated state; however, de-swelling transitions are typically associated with a potentially undesirable convective burst release of pharmaceutical cargo coupled with the expulsion of water during the phase transition[3].

Another approach to modulating drug release kinetics and / or increasing drug loading is to create composite systems in which the drug is loaded into smaller carriers (e.g. microemulsions[59-60], liposomes[61], polymeric micelles[62] or microgels[63] of a different formulation) dispersed in a hydrogel matrix. In these 'plum pudding' composites, loading is governed primarily by the solubility of the drug in the carrier phase while the hydrogel matrix immobilizes the carriers at the site of interest and masks them from the immune system. Release kinetics are governed by the two-step diffusion pathway from the carrier particle into the hydrogel matrix and then from the matrix to the surrounding tissues[3]. This two-step process allows more degrees of freedom to achieve an intended release profile, in most cases linear or first order but in other cases pulsatile (e.g. release from a thermoresponsive carrier phase externally actuated by infrared light[64] or magnetic fields[65]).

Network structure can also be manipulated by overlapping a second, chemically distinct network to form an interpenetrating polymer network (IPN) or dispersing free chains in a cross-linked network to create a semi-IPN. These architectures alter mechanical properties (stiffness and porosity), and may affect drug loading limits and release kinetics[3] (likely due to inhomogeneous mixing of the polymers to create domains enriched in one or the other phase). In this latter case, release may proceed similarly to the plum pudding hydrogels described above, in which two phases with distinct drug affinities and diffusivities collectively regulate release kinetics (see section 1.4 for details).

1.1.5 The case for injectable delivery

Broadly speaking, hydrogels for biomedical applications may be either pre-cast and surgically placed[66], or injected in a flowable state that sets by physical[67] and / or chemical[68] cross-linking *in vivo*. Most traditional methods of hydrogel synthesis involve co-polymerizing the constituent monomers with a bi- or multi-functional cross-linker; however, polymerization *in vivo* is rarely feasible given the toxicity of most monomers and initiators and/or the requirement for high temperatures or high intensities of UV irradiation for initiation. Thus, most of the early generation of hydrogels for biomedical applications required surgically implantation[56, 69].

Although injectable designs introduce additional design constraints, they are both simpler to administer for a doctor (generally avoiding the need for operating room resources) and less invasive for the patient (causing much less damage to surrounding tissue than surgical intervention, therefore healing more quickly)[70]. Thus, with the exception of hydrogel coatings for medical devices that already require surgical

implantation[66], injectable delivery is generally a preferred design strategy.

1.2 Cross-linking through reactive mixing

1.2.1 Design considerations

Ideally, reactive functional group pairs for cross-linking using a mixing injector should create a hydrogel network rapidly upon contact and without cross-reactivity with functional groups found in native tissue[16]. Exceptions to the latter guideline exist, however, for certain tissue adhesive applications in which covalently attaching the hydrogel to the tissue substrate[71-75] or mucosal membrane[76] via one of the same functional groups in cross-linking can be an elegant design solution. Even if tissue attachment is desired, a hydrogel for biomedical applications must elicit no more than a minimal inflammatory response *in vivo*, lest it provoke a foreign body response leading to fibrous encapsulation which would interfere with mass transport for tissue engineering or drug delivery applications[16, 77]. In general, most reactive mixing schemes involve either a nucleophile / electrophile pairing, addition of an oxidizing agent which triggers dimerization of an otherwise unreactive functional group, or the addition of a salt whose multivalent cations or anions act as centers for non-covalent complexation bonds.

1.2.2 Hydrazones

The hydrazone bond is formed in a nucleophilic addition of the nitrogen from a hydrazine (or, more commonly in biological applications, a less toxic analogue such as a hydrazide) to an aldehyde or ketone to form a Schiff base[16] (Figure 1.1). The rate of

gelation can be manipulated based on the ratio of more reactive aldehydes to less reactive ketones such that cross-linking can be manipulated from within seconds of mixing up to several hours[78-79]. An additional benefit of using hydrazides as the nucleophile in this Schiff pairing rather than hydrazines is enhanced hydrolytic stability, with cross-links degrading over weeks to months (depending on the degree of substitution of the functionalized cross-linking residues)[16, 80] without the need to reduce the bond to stabilize it in the aqueous environment.

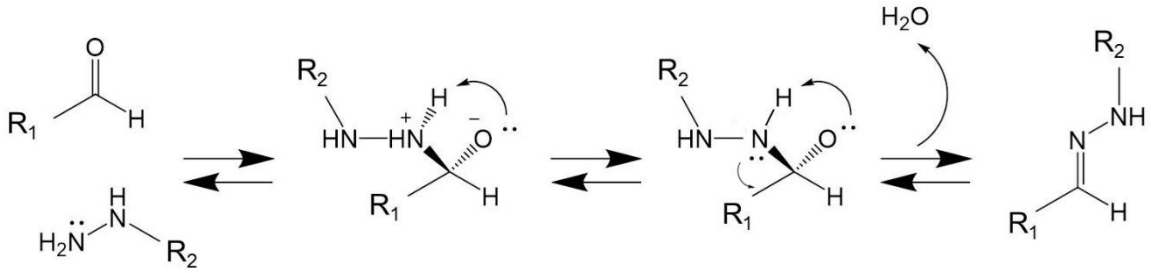

Figure 1.1: Mechanism of hydrazone bond formation.

Previous work within the Hoare lab has explored the use of gelation through reactive mixing of hydrazide and aldehyde-functionalized precursor polymers co-extruded from double-barreled mixing syringes[63, 81-82]. In particular, when short (approximately 20kDa) poly(NIPAM) chains are functionalized with the two types of reactive groups, the poly(NIPAM) single networks that result from reactive mixing display the expected volume phase transition temperature behaviour, along with minimal cytotoxicity *in vitro* and *in vivo*. Such single networks degrade by hydrolysis of the hydrazone cross-links, with the resulting short poly(NIPAM) chains falling within the applicable molecular weight range to be removed by the renal clearance mechanism.

1.2.3 Michael additions (maleimide, vinyl sulfone, etc)

In a 1,4-addition (or Michael-type) reaction, a nucleophile (Michael donor) adds to the β position of an α,β-unsaturated carbonyl structure (the Michael acceptor) (Figure 1.2). Physiologically compatible nucleophiles include thiols, alcohols and amines, with thiols generally being preferred because of their lower pK_a and greater nucleophilicity, (although they must be introduced by post-polymerization functionalization to avoid interference with radical polymerizations by chain transfer)[16, 83-84]. Common Michael acceptor electrophiles include acrylates[85-88], methacrylates[89], maleimides[90-92], quinones[73], and vinyl sulfones[93-94].

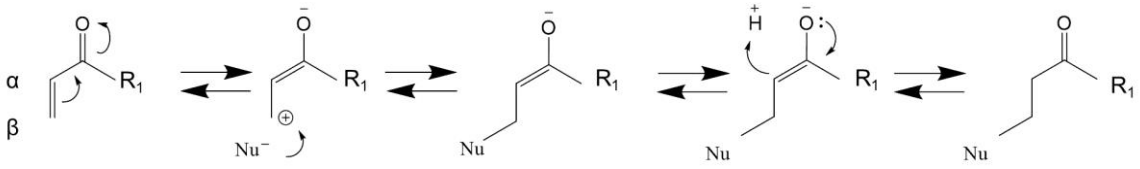

Figure 1.2: Mechanism of Michael-type addition reaction.

Gelation speeds can range from under a minute to several tens of minutes depending on the functional group pairing[16], with thiol-maleimide being among the fastest combinations at physiological conditions[95]. Degradation of Michael adducts produced using thiols as the donor via the retro-Michael pathway is slow but spontaneous for some possible acceptors at physiological conditions (such as vinyl sulfones[96]); however, for other acceptors such as maleimides containing amines in the N-substituent position (which undergo subsequent ring-opening to an irreversible structure[97]) or acrylates[16], the

Michael adduct is essentially non-degradable. In the latter case, if biological degradation and clearance are desired for the application, an enzymatically or hydrolytically labile site must be incorporated in the attachment between one of the polymer backbone types and its respective cross-linking moiety.

1.2.4 Disulfides

Disulfide bonding between thiol-bearing polymers will occur spontaneously in the physiological environment; thiols will be partially deprotonated at biological pH, and the oxidative environment is strong enough to permit disulfide formation[16] (Figure 1.3). However, the spontaneous reaction is too slow to be of practical use as a primary cross-linking mechanism in injectable hydrogels and must be either accelerated by reactive mixing with a biologically tolerable weak oxidant solution[98] or used as a secondary cross-link in systems in which physical gelation or a faster covalent gelation mechanism[99] provides the initial cross-linking to minimize polymer mobility and diffusion away from the injection site. In applications in which diffusion away from the injection site is already constrained, it is notable that disulfide cross-linking can yield hydrogels with excellent optical properties[100-101].

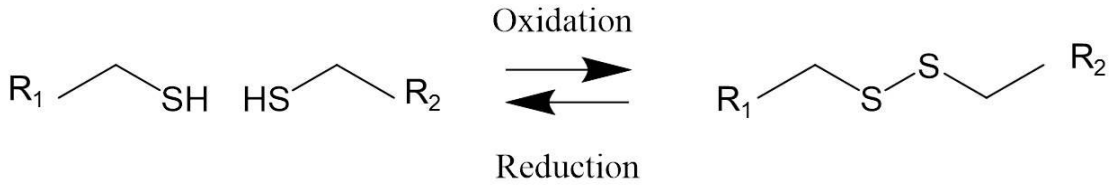

Figure 1.3: Mechanism of thiol-disulfide equilibrium.

In vivo, disulfide bonds are reductively cleaved by the tripeptide glutathione (GSH)[16], in addition to the normal equilibrium between the dissociation and reformation of disulfide cross-links. Disulfide cross-linking density can be used in both bulk and particulate gels[102-104] to adjust the degradation kinetics of networks. In block-based polymer micelles, a terminal thiol can be used to attach a sheddable corona to a separately cross-linked core via a disulfide bond[105]. The transient nature of disulfide cross-linking can be exploited to afford faster release kinetics than in more stably cross-linked hydrogels[106].

1.2.5 Catechol reactions (thiol, amines, phenylboronic acid, oxidation)

Catechols are a particularly widely investigated subset of polyphenols capable of a wide variety of covalent and non-covalent reactions that can provide a polymer network with both cohesive cross-linking and adhesive interaction to a range of surface chemistries. The most important of these are oxidative dimerization[107], covalent bonding of the oxidized quinone with thiols or amines[108] (a type of Michael addition), and non-covalent coordination with metal cations such as iron (primarily of interest for cohesion[109-110]) and titanium (among the strongest non-covalent adhesive bonds known[111]).

1.2.6 Other methods

The 1,3 cycloaddition between alkynes and azides (Figure 1.4) was one of the first identified ‘click’ chemistries but was not applied to hydrogel formation[112] until the development of a copper-catalyzed pathway that allowed the reaction to proceed at more practical temperatures[113]. The requirement for thorough dialysis with a chelating

agent such as EDTA to remove the copper catalysts before the introduction of these materials to a biological system has made this scheme impractical for most biomedical applications[16], particularly those requiring injectable materials. However, recent developments in the use of strained alkynes for cross-linking with azides have achieved rapid cross-linking without the requirement for copper catalysis[114].

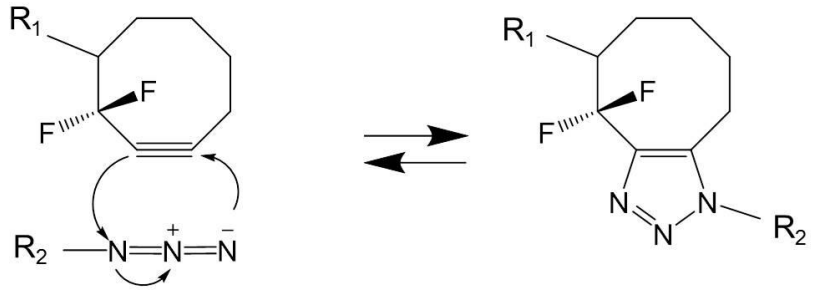

Figure 1.4: Mechanism of alkyne-azide cycloaddition.

By contrast, the Diels-Alder reaction, a [2+4] cycloaddition between maleimides and furans (Figure 1.5), is well suited for forming cross-links by reactive mixing *in vivo*. The reaction is spontaneous at physiological conditions and highly specific aside from cross-reactivity with any free cysteine on adjacent proteins. However, the reaction is relatively slow under physiological temperatures (on the timescale of hours), making this reaction best suited to use with thermosensitive polymers where initial immobilization can be provided by physical cross-links[16] or together with another rapidly gelling system.

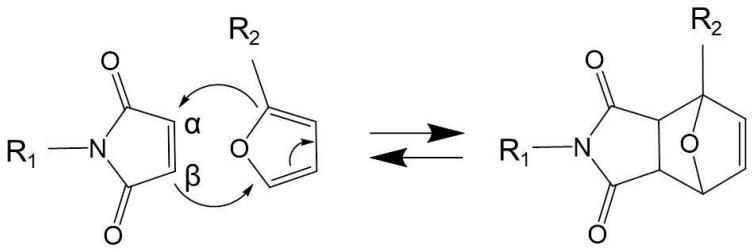

Figure 1.5: Mechanism of Diels-Alder reaction.

Some polyelectrolyte interactions also can drive rapid gelation upon mixing. For example, mixing alginate solutions with calcium chloride results in the formation of an electrostatic complex between guluronic acid residues of the polymer and Ca^{2+} ions, forming the so-called 'egg-box' structure[115]. This method is frequently used in microfluidic platforms to create cellular encapsulation scaffolds in the form of beads[116-117] or fibres[118-119], although it can also be used in bulk preparations[120]. This type of cross-link degrades according to dissociation of the complex and diffusion of calcium ions away from the polymer; exchange with Na^{+} ions to yield sodium alginate occurs at a rate dependent on sodium concentration and pH[121], while treatment with chelating agents such as EDTA or sodium citrate would accelerate the process if desired.

1.3 Interpenetrating Polymer Networks

Mixing different polymer backbones in composite formulations offers the capability to create intermediate properties or novel behaviours from the combination that are inaccessible using the pure materials alone[122-123]. IPN's are one such type of multi-component hydrogel formulation, distinguished from simple blends or block / graft copolymers as two (or more) entangled or juxtaposed cross-linked networks[124] that are

mechanically interlocked but not covalently cross-linked with each other. Full IPNs are formed from two cross-linked networks, while semi-IPN's in which uncross-linked chains of one polymer are entrapped within another cross-linked network[3] (Figure 1.6). In both configurations, chain entanglements confer a mechanical reinforcing effect on elasticity and toughness relative to each constituent phase in isolation. Other properties, such as thermosensitivity and drug loading capacity may often be tailored by varying the polymer concentrations used to produce each network.

In biomaterial applications, the chemical independence of the two backbones and the potential for surface modifications can be used to tune some aspects of the host-material interaction. For example, pore size can be designed to change over time based on differential degradation rates of the two components, affecting cellular responses to the foreign material and drug release kinetics[3, 125]. Although semi-IPN's offer somewhat less mechanical reinforcement and freedom to tailor degradation due to the lack of cross-links on the secondary polymer phase, they can be advantageous in applications where it is desirable to minimize the disruption of environmentally responsive swelling transitions since the free polymers exert less elastic resistance on the responsive networks than a cross-linked second network[3].

IPNs can be classified according to the mechanism by which the dual network structure is obtained as either sequential or simultaneous (Figure 1.7). Sequential IPNs, by far the most common type, are produced by first forming one network, diffusing the monomer / initiator / cross-linker for the second network inside the pre-formed first network, and triggering polymerization by the temperature / light conditions particular to the initiator used for the second network. This method is predominantly used when both networks are to be produced by radical polymerization, although a variant is possible where low

molecular weight prepolymers and a small-molecule cross-linker can be diffused into an existing network. In contrast, simultaneous IPNs in which both networks form independently at the same time are an option when the two networks are polymerized by different and non-competing mechanisms (usually a chain-growth and step-growth combination, such as radical and condensation mechanisms) [122, 126].

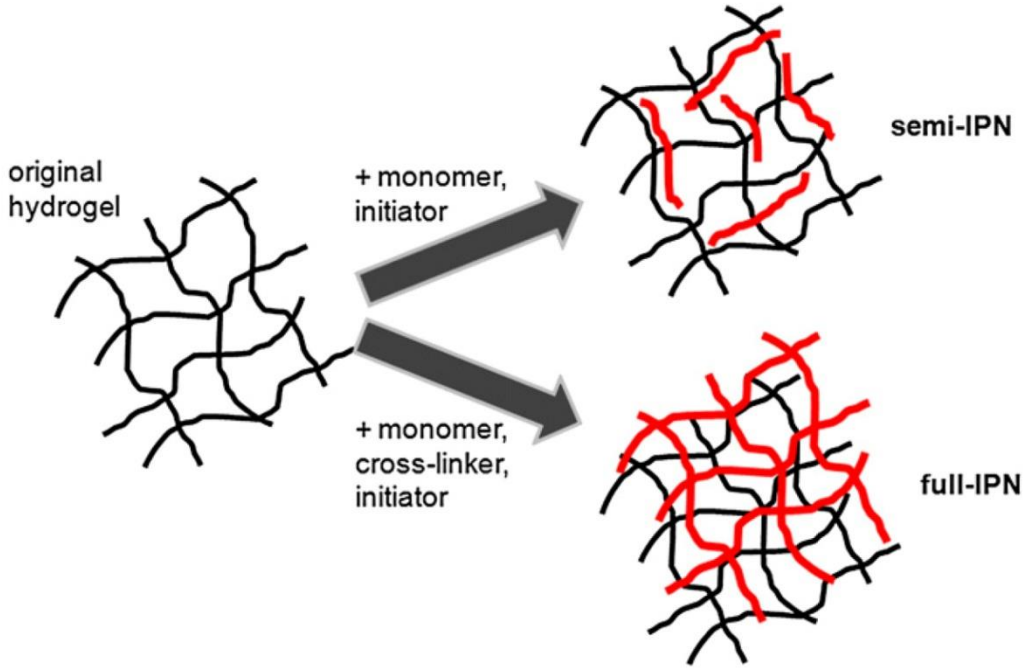

Figure 1.6: Schematic of fully and semi-interpenetrating networks, reproduced with permission from Hoare & Kohane 2008[3]. Depending on the mechanism of polymerization of the second network, monomer and initiator may be introduced by diffusion (as shown) to produce a sequential IPN or, if the two networks can be formed by orthogonal mechanisms, all components may be mixed and initiated at once to form a simultaneous IPN.

Simultaneous IPN's are therefore simpler to produce than sequential configurations, but with the drawback that they are impractical for some polymer combinations. Some other examples exist where network interpenetration is only found at the boundary between

two homogeneous polymer phases (e.g. core-shell latexes, or bulk systems with a mixed gradient interface between two mainly distinct networks[124]). However, none of these yield injectable bulk systems for biomedical hydrogels.

Generally, formation of an IPN is experimentally confirmed by using FTIR, NMR, or some other method of spectroscopy to show the absence of cross-reactions between the two networks[122]. In other words, spectroscopy of an IPN should reveal only a superposition of the two component networks. However, characterization methods based on varying temperature (such as dynamic thermomechanical and thermogravimetric analysis, or dynamic scanning calorimetry) also typically reveal a broadening of thermal phase transition phenomena in cases in which one or more of the interpenetrating phases is thermoresponsive. This can be useful for assessing how homogeneously the two networks are mixed within the IPN, which cannot always be predicted based on the polymer properties themselves. In some systems in which the precursors for the secondary network are miscible with those of the first network but the resulting polymers would not normally be miscible, polymerization can occur before or concurrent with phase separation. In this context, entanglement of the cross-linked networks can effectively freeze a thermodynamically unfavourable but kinetically stable mixing state[123-124]. One application of this mixing phenomenon is that such formulations tend to be effective broad-spectrum vibration damping materials[124].

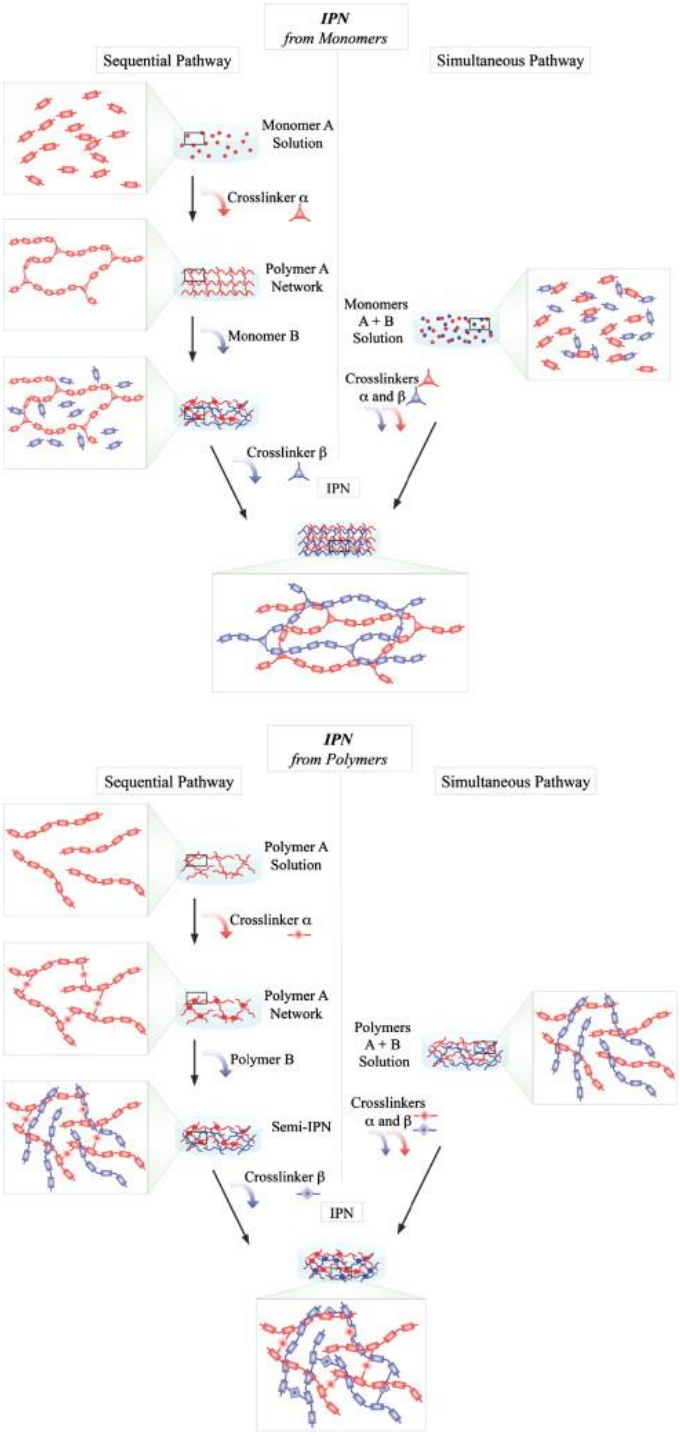

Figure 1.7: Schematic comparison of sequential and simultaneous pathways to IPN synthesis, reproduced with permission from Matricardi *et al.*, 2013[127].

Dynamic scanning calorimetry (DSC) is generally the favoured technique for at least semi-quantitative assessment of the extent of miscibility between networks, applicable to systems where all constituent polymers possess glass transition behaviour after dehydrating the networks. Transition curve features from the two constituent networks remaining distinguishable (with only slight broadening and shifting towards an intermediate transition temperature) is indicative of partial phase separation (i.e. formation of domains enriched in one or the other component); in contrast, a single broad transition curve at approximately the concentration-weighted average of the two components suggests homogeneous mixing[122, 124]. However, results must be interpreted with caution given the extent of signal processing required to draw conclusions about the extent of domain segregation. Indeed, little more can be stated conclusively aside from qualitatively comparing different IPN compositions in terms of their relative degrees of phase segregation. DSC is also unable to determine whether any observed increase in miscibility results from a change in the underlying thermodynamic favourability of mixing or kinetic effects due to network formation occurring faster than phase separation, thereby “locking-in” a thermodynamically unfavourable mixing state.

The majority of IPN systems feature some degree of uneven mixing, typically forming domains on the order of 100 nm or less with more densely cross-linked networks tending toward more extensive domain segregation[124]. The thermodynamic favourability of homogenous mixing can in some cases actually be lower for sequential IPN’s than blends of the corresponding linear polymers due to the elastic behaviour of the primary cross-linked network in response to the strain imposed by formation of the second network, although such phase separation can be reduced by cross-linking a mixture of

functionalized pre-polymers instead of the classic sequential approach starting from monomer units[124].

Although a wide range of polymers can be used in IPN systems, several polymer backbones are frequently used when certain properties are desired in the mixed formulation. Methacrylate backbones (predominantly poly(methyl methacrylate), or PMMA) are commonly employed in applications targeting mechanical strength[128-132]. Poly (hydroxyethyl methacrylate) (PHEMA) is an effective backbone to swell interpenetrating networks with high water content[133]. Hydrogel IPN's incorporating poly (N-isopropylacrylamide) (PNIPAM) will facilitate thermosensitive behaviour within the IPN[134].

For step-growth components in simultaneous IPNs, polyurethanes are widely used. The carbamate linkages between these units can be formed from polyols and isocyanates or diamines and bischlorofomates[135-136], typically formed following reactive mixing of long-chain prepolymers terminally functionalized with hydroxyls/amines with a small-molecule diisocyanate/bischloroformate. This approach allows wide latitude to design the internal chemistry of the long-chain components to the desired application, although the cross-reactivity of any unreacted residues of the small-molecule cross-linker must be considered in assessing the safety of any configuration meant for biological implantation[135-136]. The mechanism of the polyol/diisocyanate step growth polymerization is an ionic addition, although the kinetic and thermal parameters as well as cytocompatibility of such a mechanism are dependent on factors such as catalysis and the specific end-linkers employed[129, 137]. Depending which component is present in excess, residual functional groups can be left available to facilitate post-polymerization modifications. These are often focused on making the network adhesive to certain

common substrate chemistries such as amines or thiols[138-139] or tagging with tissue or site-specific bioadhesive moieties (potentially including internal degradation motifs)[140-141].

1.4 Hydrogel IPNs, related double networks, biological applications & design considerations

1.4.1 Designing for mechanical strength

Although some degree of mechanical enhancement is characteristic of most IPN systems, particularly significant results have been reported in a subset of IPNs termed double networks[142]. Such IPNs are formed by a sequential synthesis pathway, starting with a highly cross-linked polyelectrolyte network (classically poly(2-acrylamido-2-methylpropanesulfonic acid), PAMPS) followed by a loosely cross-linked neutral polymer (classically polyacrylamide, PAAM). By interlocking a ductile network into a brittle one, damage propagation under stress is greatly reduced (Figure 1.8). Such double networks can tolerate 90% compression, 1000% elongation, and show significantly elevated resistance to tearing[127]. Their elastic moduli can readily reach the 0.1-10 MPa rage of interest for load-bearing tissue engineering (such as artificial cartilage)[127, 143-144].

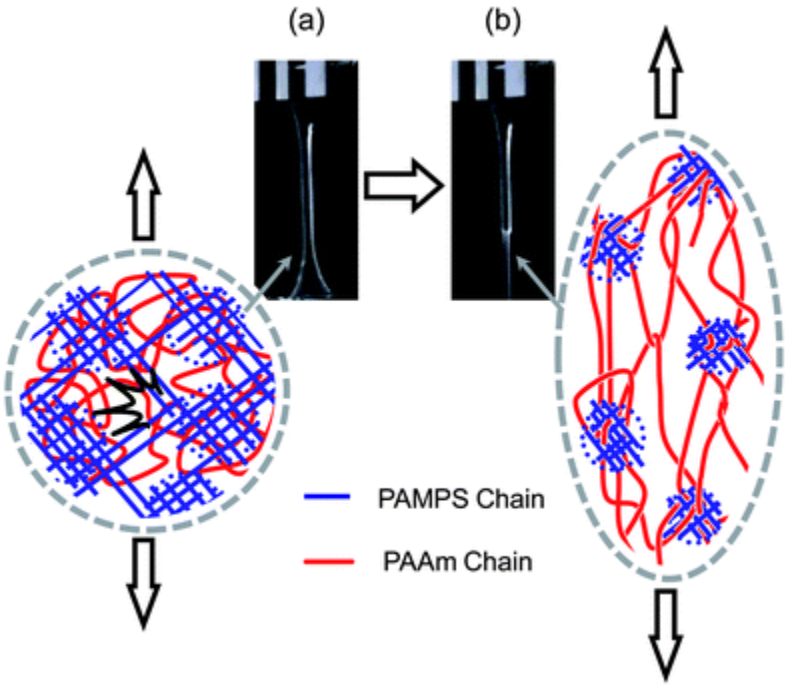

Figure 1.8: Mechanism of fracture blunting in double network hydrogels. Above the critical fracture stress for the brittle network, the ductile network continues elongating while the clusters of the brittle phase behaving as cross-linkers. Reproduced from Gong 2010[142] with permission from the Royal Society of Chemistry.

Another category of particularly high-strength IPN hydrogels can be created by sequential network formation using the same or structurally related backbone polymers for each step, with hydrogen bonding between networks contributing to the reinforcing effect. Using polyacrylate (PAC), polyacrylamide (PAAM) and polyvinyl alcohol (PVA), the Lin research group found that some combinations can achieve properties nearly as impressive as conventional brittle / ductile double networks (at least in some stress modes); PAam/PAam (1.2 MPa) and PAam/PVA (2.8 MPa) rival the tensile strengths seen in double networks. Although the enhancement in compressive strength for PAC/PAC (70 kPa) and PAC/PAam (160 kPa) is more modest than that reported in

double networks, these still represent major improvements over single network properties[145].

1.4.2 Designing for dual environmental responsiveness

Hydrogel IPN's or semi-IPN's with dual environmental responsiveness can be readily obtained by sequential polymerizations of pairs of environmentally responsive polymers. Systems combining thermoresponsive and pH-responsive swelling changes are among the most common. For example, PNIPAM / poly(acrylic acid) (PAA) IPNs have been used in a hollow nanoparticle to maximize isoniazid drug loading at low temperatures and then achieve pH-controlled release[146]. Similarly, a bulk PNIPAM / poly(methacrylic acid) (PMAA) IPN has been shown to preserve both the pH and temperature transition points[147] (albeit with moderated swelling ratios for both transitions). Films of this type were able change their permeability / size exclusion control by both stimuli. Triply responsive materials have also been reported, such as a poly(dimethylamine ethyl methacrylate -co- acrylamidephenylboronic acid) hydrogels in which swelling is influenced by pH, temperature, and glucose concentration[148].

Similar dual swelling responses have been demonstrated for semi-IPN's of PNIPAM in calcium-cross-linked alginate networks[149]. While drug release is typically fast in this system, slower and more practically useful release kinetics can be achieved by adding a chitosan-based membrane that functions as a diffusive barrier[150].

Alternately, dual control can be applied to degradation-controlled drug release by combining an upper critical solution temperature (UCST) polymer (i.e. physically cross-linked at low temperature) such as gelatin with a biopolymer such as dextran[151]. Since both polymers are enzymatically labile to degradation (by chymotrypsin and dextranase

respectively), degradation depends on both raising the temperature to drive the gelatin to a sol state and the presence of both enzymes to degrade the backbones. In the presence of either enzyme individually, degradation is very slow because the unaffected network functions as a steric barrier against the enzyme accessing the interior of the composite gels. UCST behaviour can also be imparted to IPNs by using PAA/PAAM copolymers or block copolymers of poly(ethylene oxide) and poly(propylene oxide)[152]. IPN systems with environmental responsive properties generally show less extreme (and frequently, slower) swelling changes than the component single networks[3, 153] due to the elastic resistance to swelling changes imposed by the non-transitioning network, although these trends are not universal. For example, interpenetrating networks that each have LCST behaviour, such as PNIPAM and hydroxypropyl cellulose, can result in a composite with a single LCST transition showing a transition temperature and deswelling kinetics intermediate between the two components and a transition amplitude equalling the larger of the two components[154]. Semi-IPNs are also likely to pose less inhibition of transition kinetics than full IPNs; for example, incorporating linear chitosan in PNIPAM networks showed no significant attenuation of thermal switching kinetics, although the transition amplitudes were reduced in the composite[155].

1.4.3 Designing for tissue engineering

Applications of IPNs in tissue engineering typically focus on exploiting the mechanical enhancement effect caused by the physical network entanglement. Strong scaffold materials are required, among other reasons, to sustain focal adhesions of cells[156] and/or more closely simulate the mechanics of native extracellular matrix in stiffer

tissues (e.g. cartilage or even bone), key in particular for directing the differentiation of stem cells toward their desired phenotype[157].

IPNs are particularly attractive for cartilage tissue engineering given that their inherent mechanical strength is a good fit for replacing load-bearing tissues. For example, a semi-IPN of poly(caprolactone) (PCL) in cross-linked polyvinyl alcohol showed approximately seven-fold increase in compressive failure loading, with the PVA component offsetting the hydrophobicity of PCL. Chondrocytes showed strong attachment to the IPN scaffolds, with normal spreading morphology and effective secretion of biological matrix components observed[158]. Similar results have been reported with interpenetrating systems of biologically-sourced polymers, such as a full IPN composed of collagen with methacrylated chondroitin sulfate and hyaluronan[159]. The degree of methacrylation can be tuned to adjust the swelling, degradation, and the extent of mechanical enhancement desired, while the chemical similarity of the backbone polymers to native cartilage is also helpful in directing mesenchymal stem cells towards a chondrocyte differentiation pathway. Agarose-PEG IPNs have also been reported as a favourable matrix for chondrocytes to survive and secrete native glycosaminoglycan[160].

In a dextran-gelatin IPN meant for vascular applications, the IPN formulation significantly outperformed conventional PEG gels used for smooth muscle cell constructs; one order of magnitude or greater improvement was observed in compressive and shear moduli, for corresponding polymer concentrations. Cell attachment, spreading, and ingrowth on the IPN formulations also increased significantly over their single network controls[156].

1.4.4 Designing for drug delivery

The majority of IPNs reported for drug release applications are based on dual-environmentally responsive IPNs (see sections 1.5.2 and 1.6) in which the choice of the interpenetrating phase and/or the microstructure of the IPN is applied to modulate some combination of drug loading, diffusive release, and/or IPN degradation as a function of a stimulus (most commonly, pH and temperature). However, IPNs and semi-IPNs may also be applied in single-variable responsive materials. For example, a semi-IPN of alginate in genipin-cross-linked N,O-carboxymethyl chitosan (NOCC) was found to offer improved swelling performance over NOCC alone, attributable to the higher concentration of carboxylic acid groups on alginate and hydrogen bonding between the two polymers[161]. Release dependent on pH alone was also demonstrated in full IPN beads of alginate and carrageenan (another ionically gelled seaweed-derived polysaccharide) for betamethasone acetate, a hydrophilic drug[162]. This system showed cooperative swelling at increasing pH values, with release rates achieved that were intermediate between the two single networks.

Solely thermosensitive IPNs can also be prepared. For example, PNIPAM-in-PNIPAM IPNs show cooperative thermal responses with great mechanical improvements[163]. The extent of mechanical enhancement (and, somewhat curiously, the glass transition temperature) varied depending on the weight ratio between first- and second-formed networks. However, all IPN combinations showed a distinctive morphology compared to the single network reference following dehydration (Figure 1.9). De-swelling of the composite at higher temperatures is also slower when the second-formed network is equal or greater in polymer weight fraction to the first, with corresponding decreases in both burst and maximal release of bovine serum antigen as a model drug observed.

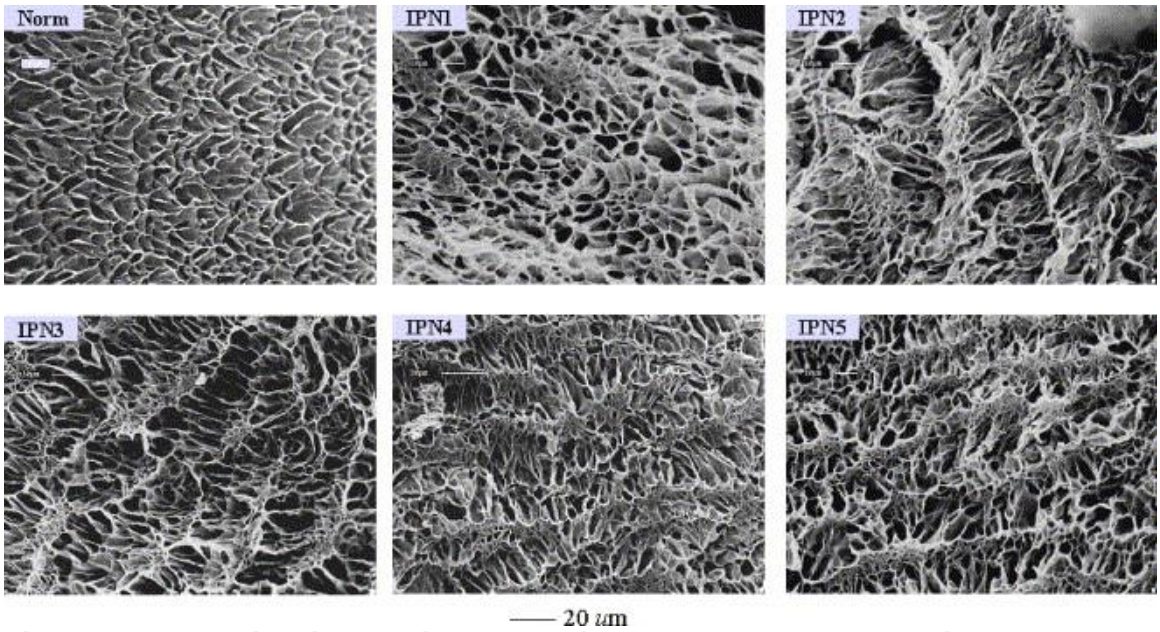

Figure 1.9: Porosity changes in PNIPAM-in-PNIPAM IPNs compared to a PNIPAM single network. Reproduced with permission from Zhang *et al*, 2004[163].

1.5 Dual drug delivery

Frequently, delivering multiple drugs simultaneously from one delivery device is a clinically desirable objective[164-169]. Since the hydrophilicity of the drug cargos may not be well matched, various micelle or particle-in-hydrogel composite configurations are common in these cases[167-169]. Dual release following different profiles can also be achieved from single-network hydrogels based on differential steric hindrance based on the molecular weight of the drugs in question[170], but typically requires drugs of similar hydrophilicity.

Dual environmental responsiveness (e.g. pH- and thermosensitive control) over single drug release profiles has also been achieved in IPN / semi-IPN hydrogels[126, 151, 171-172]. Although dual drug release from double-network hydrogels has yet to be reported in

literature, the same principles involved in dual release from single networks should apply together with the possibility of additional partitioning effects if the IPN is domain-segregated and the drugs involved have differential affinity for the two network types. Domain segregation and drug partitioning could reasonably be encouraged by manipulating the gelation rate and environmentally responsive transition thresholds for the two networks.

1.6 Mucoadhesion

1.6.1 Chemical basis of mucoadhesion

Mucoadhesion is a particular subset of bioadhesion and refers to an adhesive interface between a material and a mucosal membrane[173]. Mucosal membranes (including the oral and gastric environments, nose, eyes, vagina and rectum) are covered in a protective and lubricating layer of high molecular weight glycoproteins rich in O-linked oligosaccharides secreted by the epithelial layer[174]. Thus, it is the nature of the specific and/or non-specific interactions between those mucosal glycoproteins and the biomaterial that governs the strength of mucoadhesive interaction.

Four primary theories are used to explain the basis for adhesion of biomaterials to mucous membranes. Wetting theory is used to model low-viscosity bioadhesives that are applied as liquids, spread across the mucosal surface based on favourable surface tension, and set interlocked into surface irregularities. The wetting theory is modelled primarily using Dupre's equation for work of adhesion and Young's equation for contact angle, where γ represents the various surface tensions and θ is the contact angle[173, 175] (Equations 1.4 and 1.5).

(Eq. 1.4) $\omega_{adhesion} = \gamma_{polymer} + \gamma_{tissue} - \gamma_{interfacial}$

(Eq. 1.5) $\gamma_{tissue-air} = \gamma_{tissue-polymer} + \gamma_{polymer-air}\cos\theta$

Second, mucoadhesion can also be promoted by electrostatic interactions between the polymer and mucosal layers. The mucin glycoproteins are rich in sialic acid and sulfate groups, which are deprotonated and hence negatively charged at physiological pH [176]. Thus, use of positively charged polyelectrolytes in the adhesive formulation will result in attractive electrostatic forces between the mucosal membrane and the biomaterial[173].

Third, adhesion can be promoted by non-covalent (van der Waals, hydrogen bonding and hydrophobic) interactions between the adherent polymer and the mucin layer[173]. While the relative contribution of non-covalent bonding varies for different mucoadhesive polymers, carbopol, polycarbophil and acrylates have been noted as particularly helpful in promoting mucoadhesion by hydrogen bond formation due to their abundant carboxyl groups[177]. Van der Waals contributions are generally weaker, although they can be important in bringing particles into close contact with the mucosal surface in order for more persistent interactions to form[178].

Fourth, the diffusion theory attributes adhesion to interpenetration of the applied polymer into the mucin layer at the interface driven by concentration gradients. If the diffusion coefficient for the polymer with respect to the mucin layer is favourable for interdigitation to occur during the cross-linking of the applied mucoadhesive polymer, the adhesive strength is derived from the same chain entanglements that cause mechanical reinforcement in IPN systems[173].

After initial contact has been established between the mucin layer and the adherent

material, covalent bonding can also be important establish in establishing more permanent adhesion. For example, the high cysteine content (up to 10%[176]) in the protein portion of the mucin glycoprotein can be exploited for certain covalent interactions with functionalized polymers. These cysteine residues are responsible for disulfide bonding in the mucin layer, but thanks to the equilibrium nature of the disulfide bond, a percentage of them will be available to react with thiolated or Michael-acceptor-functionalized adhesive polymers. Hydrogels featuring thiolated hyaluronic acid have been reported as mucoadhesive films for insulin delivery devices[179]. However, this method can have drawbacks when used in nanoparticle formulations in which transport through the mucosal layer is desired; that is, if the adhesion is too strong, particles will lodge at the mucin surface rather than penetrate through the mucosa and into systemic circulation. For such applications, thiol-functionalized chitosan particles have been found to offer a good balance of adhesion and mobility/penetration[180] (within the studied range of functionalization densities).

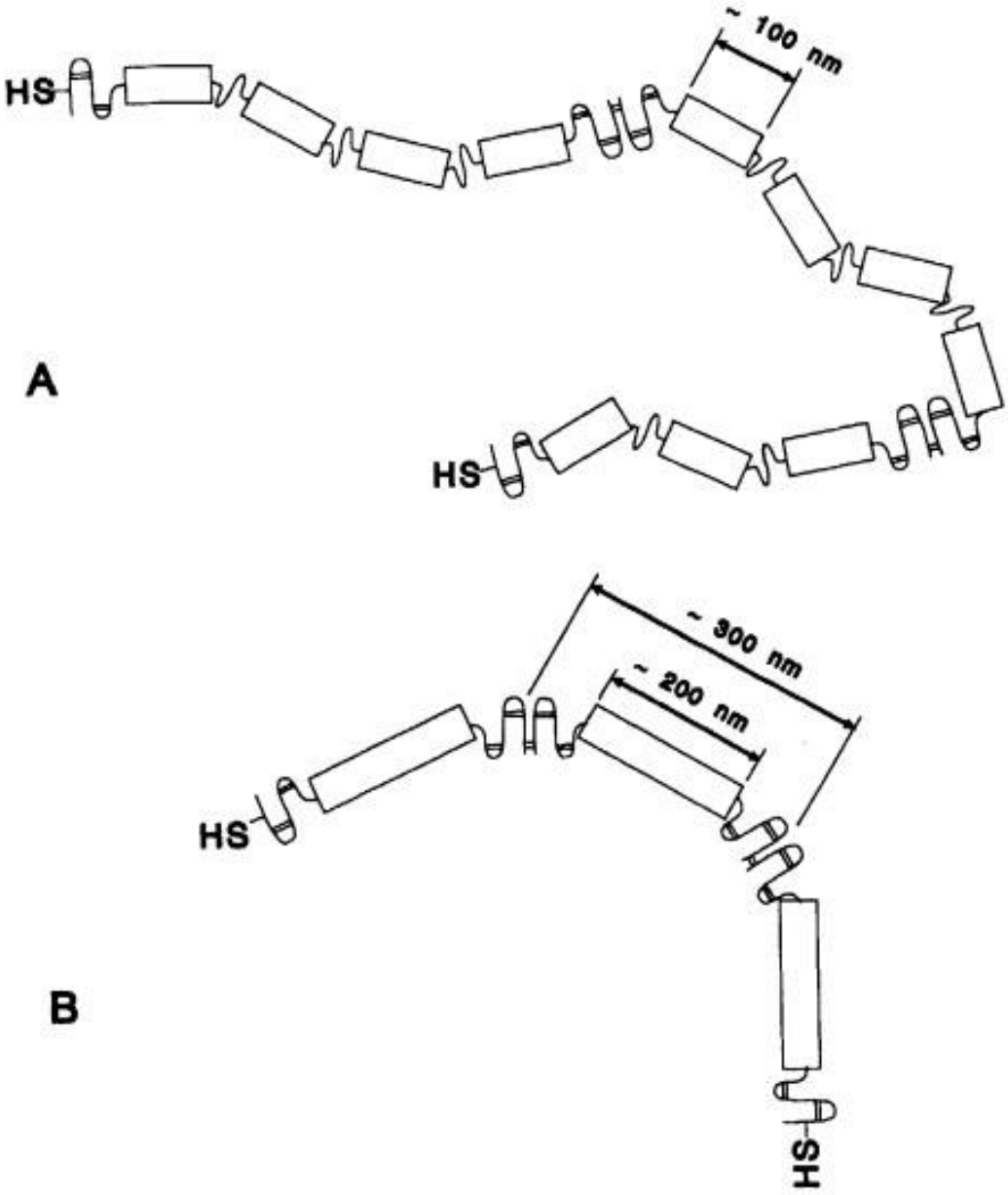

Figure 1.10: Oligomer structure of A) human cervical and B) rat gastric mucin, reproduced with permission from Strous & Dekker, 1992[174]. Blocks represent protease-insensitive glycopeptide domains, loops represent protease-sensitive regions, and double lines represent internal disulfide bonds.

1.6.2 Measurement of mucoadhesion and hydrogel-tissue interfacial mechanics

Methods of measuring adhesion of materials to mucosal membranes fall into two general categories: those using tissue samples (either in the form of *ex vivo* cadaver samples[181-182] or live animal models[175]), and those using artificial substrate-immobilized mucin films.

Animal tissue models are advantageous for experiments on mucoadhesion of bulk hydrogels, since they use the actual tissue substrates to which the biomaterials would adhere *in vivo*. They can also (at least theoretically) be easily arranged to perform both shear and perpendicular adhesion measurements on a universal mechanical tester, facilitating collection of standard adhesive properties such as the work of adhesion or the ultimate stress / strain to failure[178]. In practice, however, it can be difficult to prepare flat surfaces of larger tissue samples and to mount them in parallel / perpendicular (shear and tensile) testing configurations, particularly with softer mucoadhesive hydrogels. Use of *ex vivo* samples can also be problematic for researchers interested in longer-term studies of adhesive stability under repetitive cyclic loading, where it may be difficult to preserve sample freshness at ambient temperature.

Studies using artificial mucin films can address many of the shortcomings of tissue-based adhesion assays. For example, binding of putative mucoadhesive polymers and nanoparticles can be measured by flowing the analyte solution or suspension over mucin-coated QCM-D sensor chips[180, 183]. This is one of the more common *in vitro* methods because it has the advantage of simultaneously tracking the mass (and thus thickness) of the adhered layer (via changes in the resonant frequency of the system), the internal viscoelastic properties of the bound layer (via changes in the dissipation factor), and the penetration of thiolated polymer particles into the glycoprotein

membrane (assessed by spreading of the QCM-D overtones)[183-186]. Ellipsometry has also been reported as a method of tracking adsorbed mass vs. time in a similar configuration, but cannot provide direct information on the penetration/viscoelastic properties of the mucoadhesive available using QCM-D[187].

Several force-based measurements of mucoadhesion are also possible, but all currently have significant limitations that must be considered in interpreting the results. Atomic force microscopy, using tips modified with polymer beads functionalized with a mucoadhesive, can be used to record force-displacement information from contact and withdrawal from mucin substrates[178, 188]. This technique is most straightforward with hard polymer beads, since deformation of softer polymer beads can confound interpretation of adhesive forces; however, softer bead probes are typically more representative of the properties of some biomaterials. Relatively small areas are often probed, potentially problematic given the heterogeneity of many mucous-covered surfaces. Larger surface areas can be probed using a Wilhemy apparatus to track the resistive force on a polymer-functionalized glass slide being slowly pulled out of a dilute solution of mucin[178], or measuring the tensile-direction detachment force of a hydrogel from a pellet of highly concentrated hydrated mucin (30%)[189]. Work of adhesion for polymer solutions can also be inferred from wetting angle[190] (see also Figures 1.4 and 1.5). However, this method cannot be applied directly to hydrogels in which cross-linking prevents spreading onto the surface. Similarly, while the use of rheological synergism (i.e. the measurement of the excess modulus resulting from mixing mucin and a mucoadhesive polymer relative to the moduli of the two components measured individually) can be used to assess mucoadhesion using a relatively straight-forward test[187, 189], such measurements are also impractical for testing hydrogels since intimate mixing between the mucin and a

mucoadhesive polymer is required. Hydrogel mucoadhesion can be assessed more directly by placing a thin layer of mucin between polymer or gel-functionalized glass slides and measuring the shear or tensile separation force[178]. However, capillary effects between the two glass slides can confound interpreting specific versus non-specific adhesion. Thus, while there are several mechanical-based options for assessing mucoadhesion, there are associated drawbacks with using all currently available methods.

Generally speaking, *in vitro* mucoadhesion techniques are fairly effective at ranking formulations from most to least adhesive[189]. However, disagreements between techniques have been noted in some cases[187], and the use of mucin concentrations and/or geometries far removed from physiological makes it difficult to use these techniques for quantitative or semi-quantitative predictions of adhesive performance of bulk hydrogels in physiological conditions. Additionally, the *in vitro* methods that use mucin films on surfaces generally employ hard substrates, useful for isolating all of the viscoelastic response to the mucin-polymer interaction but also ignoring possible effects arising from interaction between the mucin layer and underlying elastic tissue in biological systems. It is therefore desirable to develop an *in vitro* adhesion measurement protocol that more closely recapitulates the physiological system, including the use of soft material substrates.

1.7 Objectives

Considering their ability to deliver novel structures, stronger mechanical properties and modulated environmental responsiveness, IPN hydrogels pose a significant potential as prospective biomaterials. However, compared to other classes of hydrogel composites, they have been relatively lightly represented in applications-focused literature. One contributing factor to this situation has likely been awareness within the biomaterials research community that lack of injectability posed a drawback to practical applications. The research described in this thesis is thus focused on exploiting the *de facto* orthogonality of several schemes for inducing network formation by reactive mixing to generate novel injectable, thermosensitive IPN hydrogels and comparing the properties of the resulting composites to the single network constituents, with a particular emphasis on understanding the underlying network structures of each material.

Chapter 2 covers our development of the first formulation of an injectable IPN hydrogel based on two fast, click-like mechanisms (hydrazone cross-linking PNIPAM, and thiosuccinimide-type Michael addition cross-linking PVP). Although the two mechanisms are not truly thermodynamically orthogonal, each combination is selective enough that NMR results for both small molecule models and the full polymer systems show no detectable levels of cross-reactivity, validating the system as kinetically orthogonal. The resulting IPN composites are compared to single network and semi-IPN compositional analogues to evaluate differences in the PNIPAM-driven thermoresponsive kinetics, degradation behaviour and mechanical strength.

Chapter 3 represents a thorough investigation of the hydrated network structure of the IPNs developed in Chapter 2 through small-angle neutron scattering with contrast

matching and dual-channel dSTORM super-resolution microscopy with fluorescent labelling of the two constituent polymer phases. SANS results suggest nano-scale domain formation is driven by PNIPAM, but with the extent of domain formation reduced in the IPN. The PVP phase assumes a clustered conformation (which microscopy results reveal to have discrete structures on larger length scales), with extremely minimal incorporation into the PNIPAM-rich domains where they occur. Microscopy results reveal that a distinct sub-population of PNIPAM domains occur embedded within larger PVP clusters, but incorporation of smaller PVP clusters into PNIPAM is not observed.

Chapter 4 deals with another SANS study of an alternate reactive pairing, introducing disulfide cross-linking in place of thiosuccinimide, to determine whether slower formation of the PVP network (prepared using a range of molecular weights and functionalization densities of thiolated PVP) leads to more extensive domain segregation. Similar to the original system in Chapter 3, PNIPAM domain formation seems to be partially disrupted by mixing into PVP-rich clusters. However, the thermal response of the PNIPAM domains that do form is altered in IPN's with extremely weak PVP networks (i.e. PVP gels prepared with low precursor polymer degrees of functionalization and molecular weights), with no evidence for PVP incorporation into PNIPAM domains observed.

Chapter 5 describes the development of a new testing method to assess the mucoadhesion (or more general adhesion) of hydrogels such as the thiol-rich IPNs developed in Chapters 2-4. Specifically, an artificial model of a mucin membrane on a soft material substrate is developed and validated as an *in vitro* analog for direct mechanical testing of hydrogel mucoadhesion. Design and proof of concept trials on the substrate attachment system are described using a disulfide cross-linked hydrogel

adhered directly to the functionalized PDMS, and physical tack measurements are performed after rupturing the adhesive interface. In combination, the two validate the prototype for measuring adhesive forces between the upper and lower bounds expected for adhesion to a mucin-coated surface.

Chapter 2: Injectable Interpenetrating Network Hydrogels via Kinetically Orthogonal Reactive Mixing of Functionalized Polymeric Precursors

Preface

This chapter and its appendix are reproduced from the initial publication describing the development of an injectable IPN formulation based on two click-like functional group pairings between four precursor polymers, with demonstration of no detectable cross-reactivity when all components are mixed together. The resulting composites are characterized for mechanical strength, microstructure (after freeze-drying), thermoresponsive transition properties, and hydrolytic degradation kinetics. (Due to the format of ACS Macro Letters, most methodological details are found in the supporting information, included here as Chapter 2S).

Trevor Gilbert, Niels M.B. Smeets, and Todd Hoare*

Department of Chemical Engineering, McMaster University, 1280 Main St. W, Hamilton, Ontario, Canada L8S 4L7

In ACS Macro Letters, **2015**, 4 (10), 1104-1109

Abstract

A fully injectable and thermoresponsive interpenetrating polymer network (IPN) formed by simultaneous reactive mixing of hydrazone cross-linked poly(N-isopropylacrylamide) (PNIPAM) and thiosuccinimide cross-linked poly(N-vinylpyrrolidone) (PVP) is reported. The resulting IPN gels rapidly (<1 minute) after injection without the need for heat, UV irradiation or small-molecule cross-linkers. The IPNs cross-linked by kinetically orthogonal mechanisms showed a significant synergistic enhancement in shear storage modulus compared to the individual component networks as well as distinctive pore morphology, degradation kinetics and thermal swelling; in particular, significantly lower hysteresis was observed over the thermal phase transition relative to single-network PNIPAM hydrogels.

2.1 Introduction

In biomedical applications of hydrogels such as tissue engineering and drug delivery, *in situ* gelation from injectable precursors is often desirable to avoid both the local trauma to the patient and the high costs associated with surgical implantation[70]. A variety of *in situ* reactive cross-linking chemistries active under physiological conditions has been reported for this purpose, including hydrazone bonding, the family of Michael-type additions, disulfide self-cross-linking of thiolated polymers, oxime formation, alkyne-azide 'click' reactions, and Diels-Alder cycloadditions[16]. Hydrazone cross-links can be formed following reactive mixing of aldehyde-functionalized polymers and small molecule dihydrazides[191-192] or hydrazide-functionalized polymers[3, 6, 31-32, 79, 81-82, 193-195], with gelation occurring rapidly after mixing (seconds to minutes) and degradation

occurring slowly (over months) at physiological pH[32, 82, 191]. Michael addition between thiolated polymers and maleimides[92, 196] (to form thiosuccinimides), acrylates[197-199] (to form thioesters), or vinyl sulfones[200-202] (to form thioethers) is typically slower (ranging from minutes to tens of minutes)[203] and (when the N-substituent of the maleimide contains an amine) creates a linkage that is essentially non-degradable[97]. Of interest, the thiosuccinimide bond has been noted to form with high specificity and orthogonality to hydrazone bond formation at physiological pH[78], with the thiosuccinimide and hydrazone linkages shown to be highly favoured over any potential cross-reactive bonding.

Interpenetrating polymer networks (IPNs) are formed when the polymer volume fraction of two networks co-exist within each other's free volume without the two networks being chemically bonded. The resulting interlocked network structure typically gives IPNs stiffer mechanical properties than corresponding single networks[204]. Network interpenetration also modulates the geometry and dimensions of the pore structure of the hydrogel, enabling regulation of diffusion into or through the gel phase[3, 163]. Furthermore, overlapping but unconnected networks can be designed such that the constituent networks degrade according to different kinetic profiles[3], allowing deliberate variation of properties over time[3, 163, 205-206] potentially useful in tissue engineering applications. In the context of drug delivery, the composition, pore structure, and degradation properties of the two interpenetrating networks can be used to tune drug loading and release, including mitigation of the extent of the initial burst release which is typically problematic in hydrogel release vehicles[163, 207].

Traditional sequential or simultaneous methods of producing interpenetrating networks generally involve *in situ* polymerization from monomeric precursors[122, 124]. However, gelation of functionalized prepolymers is generally more attractive in this context since it avoids the use of cytotoxic monomers and/or small molecule initiators, heat, or UV treatment that may induce local or systemic toxicity[32, 82, 92]. While nominally injectable thermosensitive IPN systems have been reported that include monomeric precursors[208], monomer toxicity is a particular concern in the polymerization of "smart" polymer precursors like N-isopropylacrylamide. UV-induced photo-gelation[18] may also be logistically difficult in some *in vivo* environments and may induce local tissue damage at doses required for cross-linking[209].

Recent work by Zhang *et al.,* in which oxidized dextran and thiolated chitosan were orthogonally cross-linked via two independent chemistries, demonstrated the potential to modulate gel degradation based on the differing labilities of two independent bonds[99]. However, since one polymer pair was used to host both reactive cross-linking chemistries, the resulting product was a doubly cross-linked single network rather than a truly independent IPN gel. Similarly, semi-interpenetrating networks in which free polymer chains are entrapped in a cross-linked network (achievable via a variety of pathways of varying biological compatibility and ease of implantation[210-212]) lack the interlocked networks of a full IPN, which can significantly affect both the mechanical properties of the overall network and the environmental responses of IPNs based on pH- or thermosensitive polymers[3]. Thus, a true injectable IPN that cross-links via substantially orthogonal chemistries hosted on different precursor polymers would represent a new hydrogel architecture with potentially useful mechanical and environmentally responsive properties.

Herein, we describe the first fully injectable, full interpenetrating network hydrogel comprised of a hydrazone cross-linked poly(N-isopropylacrylamide) (PNIPAM) network (previously demonstrated in our lab to form rapidly, degrade slowly, and elicit no significant cytotoxic, inflammatory, or capsule formation response through both in vitro and in vivo assays[82]) interpenetrated with a thiosuccinimide cross-linked poly(N-vinylpyrrolidone) (PVP) network (Figure 2.1). The orthogonal gelation of the two constituent networks from a single double-barrel syringe administration results in an IPN with significantly enhanced mechanical properties and tunable thermal, degradation, and morphological properties according to the type of interpenetration achieved.

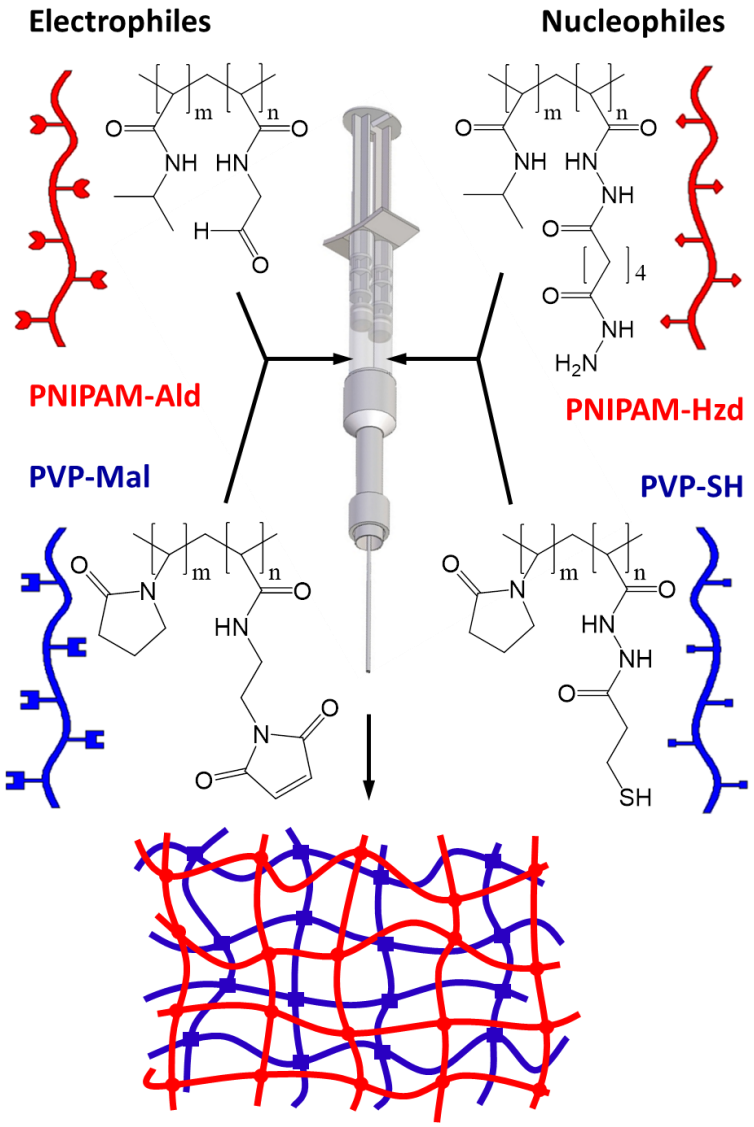

Figure 2.1: Schematic of chemistry and gelation strategy used for injectable IPN formation

2.2 Experimental Section

2.2.1 Synthesis of polymer precursors: Hydrazide-functionalized PNIPAM (PNIPAM-Hzd) was prepared by conjugating adipic dihydrazide to PNIPAM-co-acrylic acid precursor polymers. Aldehyde-functionalized PNIPAM (PNIPAM-Ald) was synthesized by copolymerizing NIPAM with N-(2,2-dimethoxyethyl)methacrylamide and subsequently hydrolyzing the acetal moieties to aldehydes. Thiol- and maleimide-functionalized PVP (PVP-SH and PVP-Mal) were obtained from a common PVP-co-acrylic acid copolymer. PVP-SH was synthesized by conjugating 3,3'-dithiobis(propanoic dihydazide) and cleaving the central disulfide bond with dithiothreitol. PVP-Mal was produced by conjugating N-(2-aminoethyl) maleimide via carbodiimide chemistry. See the Supporting Information for relevant NMR (Figures 2S.1 and 2S.2), FTIR (Figures 2S.3 2S.4), and degree of functionalization/molecular weight (Table 2S.2) characterization of these precursor polymers.

2.2.2 IPN preparation: Precursor polymers were loaded into a double barrel syringe (MedMix L system, 2.5 mL volume, 1:1 volume ratio between barrels) and separated by electrophilic/nucleophilic properties). Hydrogels were formed via co-extrusion of these precursor polymers, dissolved in 10mM phosphate buffered saline at pH 7.4, into cylindrical silicone molds, covered on the top and bottom with glass microscope slides. Samples were stored overnight at room temperature in a sealed vessel saturated at 100% relative humidity to ensure equilibrium cross-linking prior to testing. Rheology samples were prepared using silicone molds of 12.7 mm diameter and 1.6 mm thickness; samples for all other tests were prepared using silicone molds of 3mm diameter and 4.8 mm thickness.

2.2.3 Rheological testing: Measurement of the storage modulus G' was carried out using the Mach-1 micromechanical testing system (Biomomentum). All samples (*n*=4 per composition) were subjected to 20% precompression in the vertical axis. Stress sweeps were carried out to determine the linear viscoelastic regime of rotational amplitudes for each sample, followed by frequency sweeps within the linear viscoelastic region to determine G' and G".

2.2.4 Freeze-fracture scanning electron microscopy (SEM): Hydrogel samples were rapidly frozen in liquid nitrogen and cut with a razor blade under a dissection microscope. Fractured hydrogel samples were then lyophilized, mounted on SEM sample holders using double-sided carbon tape and colloidal silver conductive paint, and sputter-coated with gold. SEM images were collected using a Vega LSU instrument (Tescan).

2.2.5 Swelling and degradation measurements: The thermoresponsive behavior of each of the four samples prepared (*n*=4 per composition) was evaluated by tracking the overall mass change of the hydrogel (polymer + water) over multiple temperature cycles between 22°C and 37°C in 10 mM PBS at pH 7.4. Masses were normalized against the (hydrated) gel weights immediately after preparation (prior to incubation). As an accelerated simulation of degradation (for the purpose of comparison), mass changes were similarly tracked following incubation of the hydrogels in 0.1M HCl at 22°C. Samples were allowed to swell for 2 hours in PBS, weighed as the basis for subsequent normalization, transferred to 0.1M HCl, and weighed at pre-defined time points to track the kinetics of mass change in each hydrogel.

2.3 Results and Discussion

Small molecule analogue NMR experiments confirmed that the hydrazide-aldehyde (Hzd-Ald) and thiol-maleimide (SH-Mal) dual cross-linking configuration meets the required kinetic orthogonality constraints for forming an IPN. Co-storage of the SH/Hzd analogues and the Mal/Ald analogues (Figure 2S.6) for 40 days led to no significant peak changes over time, indicating the lack of reactivity between pre-polymers co-loaded into each barrel of the syringe. Furthermore, when equimolar amounts of the Hzd and Ald analogues were rapidly mixed with either the SH or Mal (Figure 2S.7) analogues, the expected hydrazone bond forms to the exclusion of side products. Indeed, when the potential cross-reactive Hzd/Mal pair was tested in a binary mixture, trivial (<1%) reaction was observed over three days (Figure 2S.9), suggesting that these gelling pairs are not just kinetically orthogonal but also largely chemically orthogonal. Thus, the intended hydrazone bond is highly favoured over any potential cross-reactions with thiol or maleimide, suggesting the potential utility of this pair of chemistries for the formation of an injectable interpenetrating network hydrogel. This is corroborated by solution-state NMR of IPN and single network control hydrogels formed by injecting precursor solutions in D_2O into NMR sample tubes (Bruker AV600; Figure 2S.10).

IPN hydrogels based on hydrazide and aldehyde-functionalized PNIPAM precursor polymers (PNIPAM-Hzd and PNIPAM-Ald respectively) and thiol and maleimide-functionalized PVP precursor polymers (PVP-SH and PVP-Mal respectively) were then formed by loading the electrophilic and nucleophilic components of each gelling mixture in separate barrels of a double barrel syringe and co-extruding the precursor reactive polymers through a static mixer into cylindrical silicone molds. Single network hydrogel controls, a full IPN of both networks, and a semi-IPN of unfunctionalized PVP (of

comparable molecular weight as PVP-Mal and PVP-SH, Table 2S.2) in a hydrazone cross-linked PNIPAM matrix (Table 2.1); this semi-IPN network enables clear distinguishing of the synergistic effects of dual cross-linking in the full IPN relative to the effects of incorporating additional polymer mass in an interpenetrating phase. All compositions gelled in < 1 minute, such that both interpenetrating networks are forming essentially simultaneously but rapidly following co-extrusion of the precursor polymers.

Table 2.1: Composition of hydrogel test samples

Hydrogel Composition	**Barrel 1**	**Barrel 2**
PNIPAM	*6 wt% PNIPAM-Hzd*	*6 wt% PNIPAM-Ald*
PVP	9 wt% PVP-SH	9 wt% PVP-Mal
Semi-IPN	*6 wt% PNIPAM-Hzd* *9 wt% unfunctionalized PVP*	*6 wt% PNIPAM-Ald* *9 wt% unfunctionalized PVP*
IPN	*6 wt% PNIPAM-Hzd* 9 wt% PVP-SH	*6 wt% PNIPAM-Ald* 9 wt% PVP-Mal

Morphological examination of the hydrogels by freeze-fracture SEM (Figure 2.2) shows considerable differences between the IPN and semi-IPN compared to the single network controls. The IPN systems cleaved along a more consistent cutting plane, consistent with their higher polymer concentration and stiffness. Both IPN hydrogels show pore sizes intermediate between the larger pores formed in the PNIPAM network and the smaller pores formed in the PVP network. In addition, the semi-IPN morphology is characterized by segments of flattened pores exhibiting a more lamellar geometry, similar to the PNIPAM control while the full IPN sample tends toward more regularly

rounded pore morphology consistent with the formation of a secondary network forming component being present.

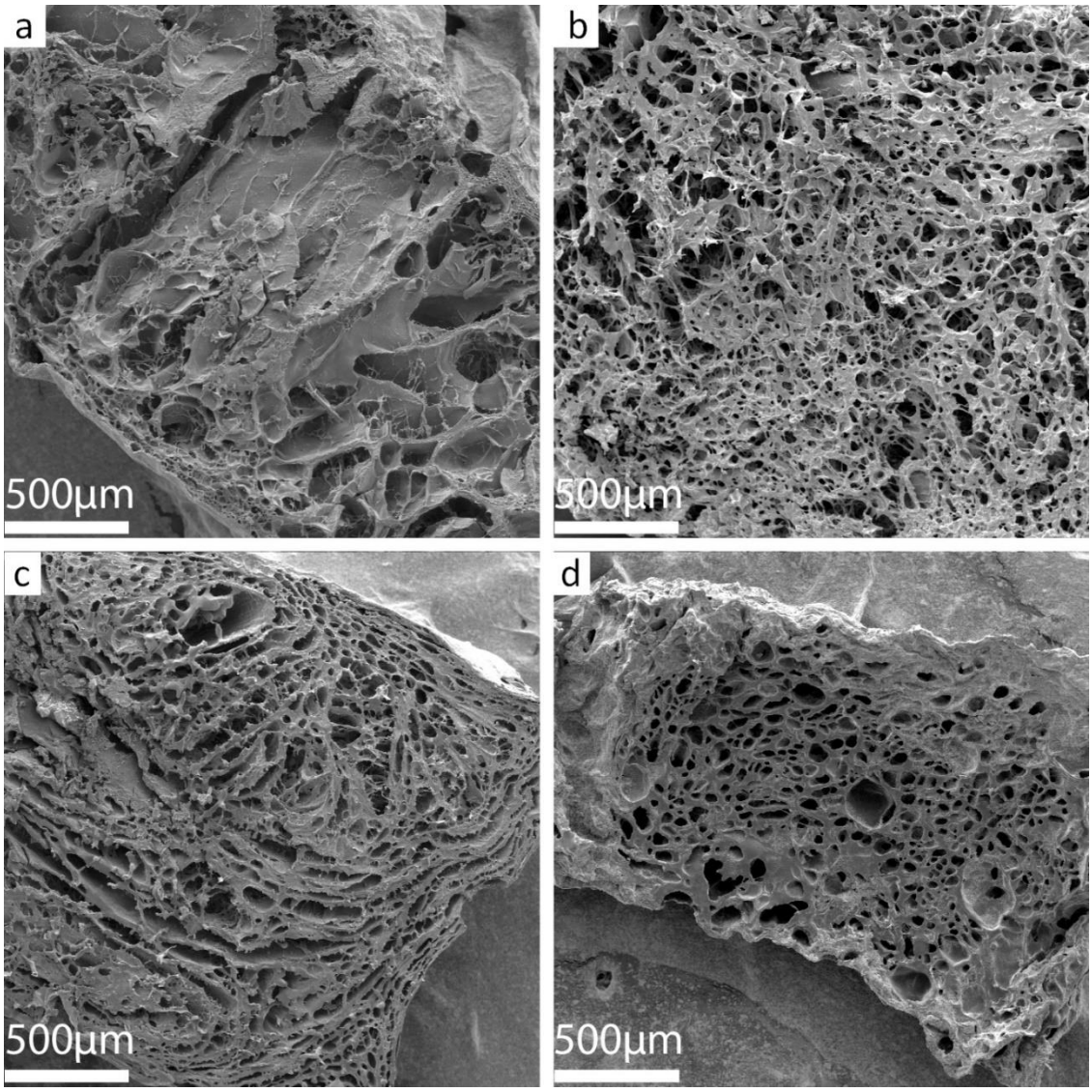

Figure 2.2: Scanning electron microscopy images of (a) PNIPAM single network hydrogel, (b) PVP single network hydrogel; (c) PNIPAM + unfunctionalized PVP semi-IPN hydrogel; (d) PNIPAM + PVP full IPN hydrogel

Comparison of the shear storage moduli of the individual hydrogel phases alone relative to the semi-IPN and full-IPN combinations of those hydrogels also indicates clear differences between the mechanics and thus morphologies of the different hydrogel networks (Figure 2.3). Note that a semi-IPN of unfunctionalized PNIPAM (again of similar molecular weight as PNIPAM-Hzd and PNIPAM-Ald, Table S2) in a thiosuccinimide cross-linked PVP was also prepared to confirm that gelation of both independent phases induced a significant mechanical synergism effect.

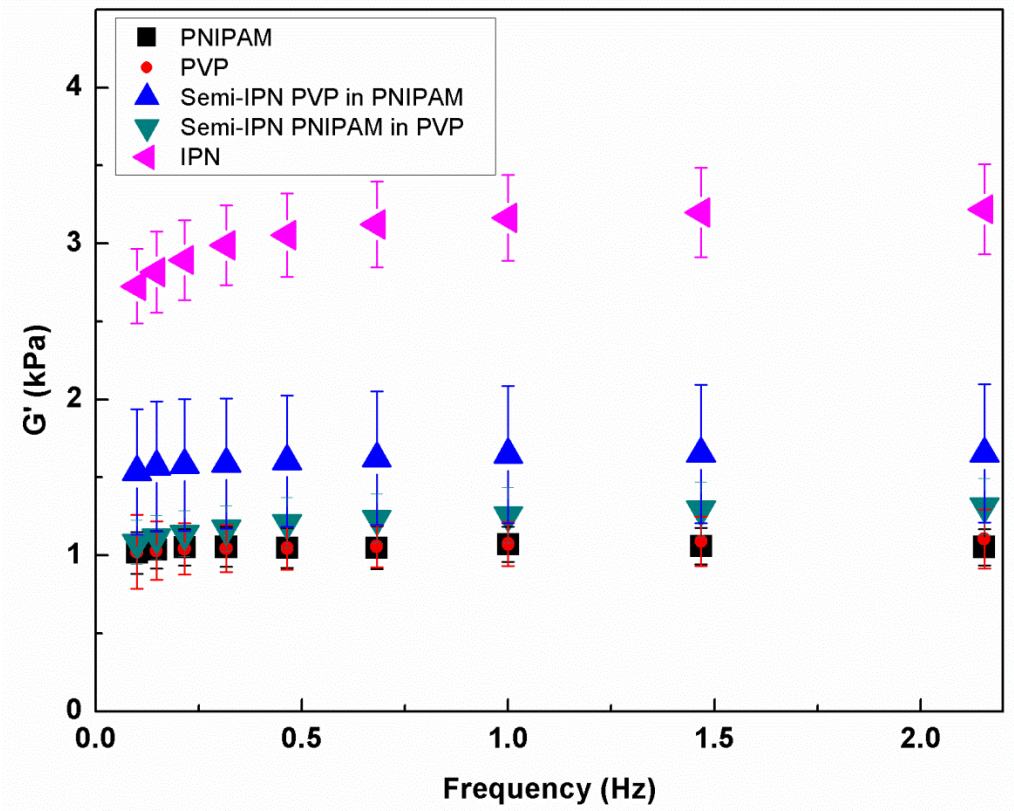

Figure 2.3: Shear storage modulus G' as a function of frequency for PNIPAM and PVP control hydrogels as well as the full IPN of those two networks and a semi-IPN analogue prepared by entrapping unfunctionalized PVP of the same molecular weight into the PNIPAM network

Approximately equal storage modulus (G') values were observed for the PNIPAM and PVP single network controls over the full frequency range tested. The semi-IPN containing free PVP showed a ~60% enhancement in storage modulus compared to the PNIPAM-Hzd/PNIPAM-Ald control alone (ANOVA: $p<10^{-65}$, $p<0.05$ at each frequency measured), while the inverse IPN (free PNIPAM in a PVP matrix) displayed minimal enhancement in modulus relative to the single network hydrogels. In comparison, the full IPN hydrogel samples prepared with PVP-Mal/PVP-SH showed a ~200% increase in storage modulus versus the PNIPAM or PVP control samples, with a modulus significantly (~2-fold) higher than that of the semi-IPN control (ANOVA: $p<10^{-48}$; t-test: $p<0.05$ for each frequency measured). In addition, the full IPN hydrogel shows a 50% higher G' value than that predicted by simply adding the constituent G' values of the control PNIPAM and PVP networks. Thus, the formation of an independently cross-linked interpenetrating PVP network provides synergistic reinforcement of the bulk hydrogel relative to that achieved by incorporating unfunctionalized PVP-based polymers, in which all potential intermolecular interactions aside from covalent cross-linking are still operable.

Cyclic swelling data between room temperature and 37°C (expressed relative to the initial gel mass, Figure 2.4a, and the equilibrium swelling degree following the previous thermal cycle, Table 2S.3) showed that both the semi-IPN and the IPN preserved the thermosensitive behaviour of the PNIPAM control. However, the full IPN maintained a significantly higher degree of swelling over multiple thermal cycles than either the single-component control gels or the semi-IPN. Furthermore, the hysteresis observed over the first thermal cycle in the single network PNIPAM hydrogel was significantly reduced in the semi-IPN and largely eliminated in the full IPN. We hypothesize these observations

are both attributable to the interpenetrated cross-linked hydrophilic PVP network that elastically resists thermal deswelling of the PNIPAM network while also maintaining a higher overall degree of hydration inside the hydrogel; the latter effect is particularly important for reducing the potential for hydrogen bond formation between adjacent NIPAM residues upon chain collapse and thus promoting more reversible swelling-deswelling transitions[213]. Figure 2.4b (graph) and Table 2S.4 (best-fit kinetics parameters) further indicate that the kinetic response of the IPN upon incubation at 37°C is significantly slower than in the PNIPAM control, with the full-IPN also significantly slower than the semi-IPN consistent with the presence of a more hydrophilic, cross-linked interpenetrating phase. Overall, the interpenetrating hydrophilic PVP phase damps the PNIPAM phase transition, suppresses bulk gel deswelling, and reduces hysteresis following the first heating cycle, with all effects enhanced in the fully cross-linked IPN relative to the semi-IPN consistent with the presence of a networked interpenetrating phase.

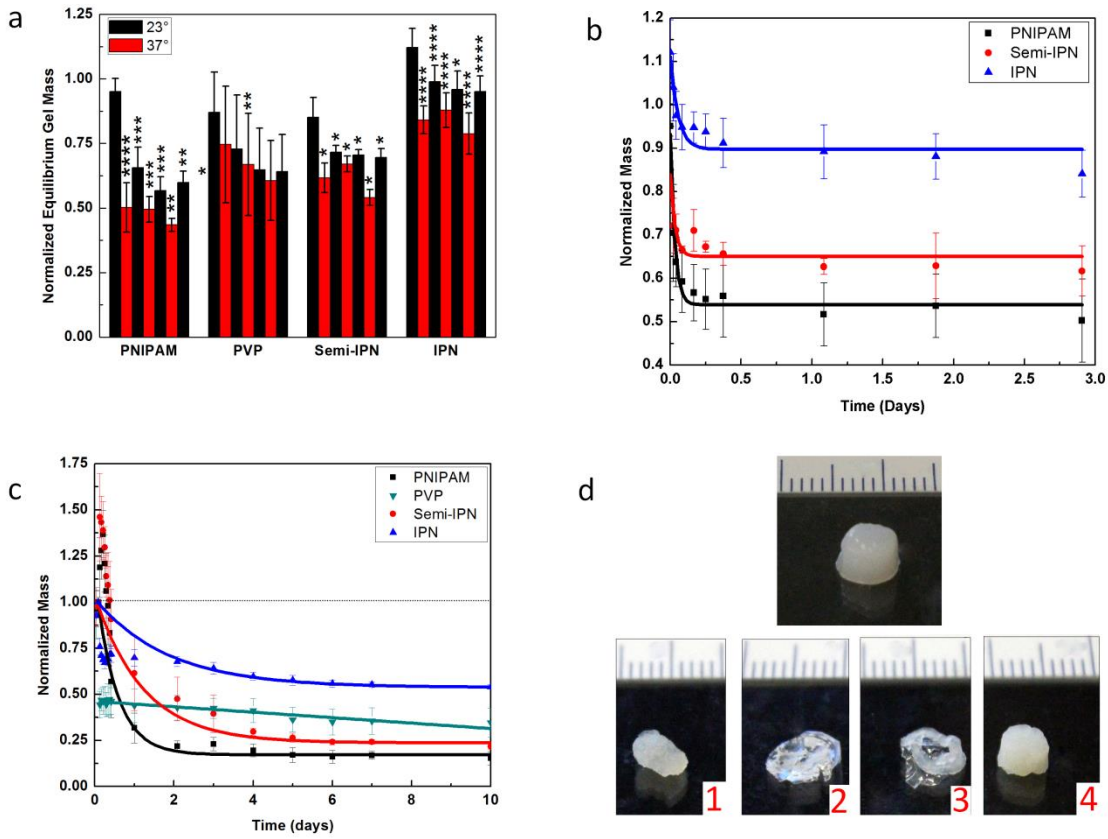

Figure 2.4: Swelling and degradation responses of injectable IPN hydrogels: (a) equilibrium swelling ratios (normalized to the hydrogel mass upon removal from mold) as a function of temperature for single-phase gels (PNIPAM, PVP) relative to semi-IPN and full-IPN gels over multiple heat-cool cycles (*p<0.05; ** p<0.01; *** p<0.005; **** p<0.001 for pair-wise comparisons relative to the previous cycle); (b) deswelling kinetics for thermosensitive hydrogels pre-equilibrated at 23°C transferred to a 37°C shaking incubator (lines represent exponential best-fit trend lines, see Table S4; note that PVP single network hydrogels showed no significant swelling changes over the course of the experiment and were thus omitted for clarity); (c) degradation of single network, semi-IPN, and full IPN hydrogels in 0.1M HCl (lines represent exponential best-fit trendlines, see Table S5); (d) Top: representative freshly molded hydrogel (PNIPAM shown; all compositions initially look substantively identical). Bottom: (d-1) PVP, (d-2) PNIPAM and (d-3) semi-IPN after 10 days in 0.1M HCl and (d-4) IPN incubated in 0.1M HCl for full 42 days with minimal deformation.

The hydrolytic degradation of the networks was assessed by immersion of gels in 0.1M HCl to investigate the role of the semi-IPN and full IPN network structures on controlling network degradability (see Figure 2.4c for graph and Table S5 for best-fit kinetic parameters). The hydrazone cross-linked PNIPAM network is hydrolytically labile (particularly in acidic conditions), while the thiosuccinimide cross-linked PVP network is hydrolytically stable; such differential degradation potential may be useful in ultimate applications of these hydrogels in terms of dynamically tuning the mechanics or pore size of the gels as a function of time. Single-phase PVP hydrogels rapidly de-swelled in 0.1M HCl (likely due to rapid hydrolysis of residual maleimides to maleamic acid that can hydrogen bond with other gel residues)[214] but then remained stable over time, consistent with the irreversible nature of the ring-opened thiosuccinimide cross-link (Fig. 2.4d-1). In contrast, an initial mass increase was observed in the first ~6-12 hours following acid incubation for the single-phase PNIPAM, semi-IPN and full IPN networks due to swelling as the hydrazone cross-links begin to hydrolyze. Subsequently, the PNIPAM single network quickly degraded, with the hydrogel decomposing to fragments at the bottom of the weighing insert within seven days of acid incubation (Figure 2.4d-2). The semi-IPNs gels degraded slower and retained their shape to day 10 (Figure 2.4d-3), attributable to the modest mechanical reinforcement effect of the entrapped PVP (Fig. 2.3) and/or the role of the interpenetrating PVP phase in immobilizing free water around the hydrazone cross-links. The IPN, in contrast, degrades much slower than the controls, retaining cylindrical sample geometry and 60% of its initial mass over 42 days of monitoring (Figure 4d-4). We anticipate that the thiosuccinimide cross-links of the PVP network preserve the macroscopic sample shape (analogous to the PVP control), with any degradation products from the hydrazone PNIPAM network captured inside the PVP

network to form a semi-IPN of PNIPAM linear polymers in a PVP network over time. This demonstrated modulation of the stability of the hydrazone cross-linked network using an interpenetrating network strategy is potentially useful for tuning the degradation time of a thermoresponsive hydrogel for targeted applications.

2.4 Conclusions

In summary, a novel method for creating a fully injectable, *in situ* gelling interpenetrating polymer network by orthogonal reactive mixing of functionalized polymer precursors has been demonstrated. Synergistic effects of the independently cross-linked networks were apparent in the mechanical properties, morphology, thermoresponsive swelling behaviour, and degradation kinetics of the resulting IPN hydrogels. Given the capacity of IPNs to facilitate decoupled control over drug loading/release and degradation/mechanical properties of the network as a function of time, we anticipate such a chemistry and morphology may have particular utility for the prolonged release of small molecule hydrophilic or protein drugs with minimal convective burst and wound healing materials with both tissue adhesive and wound closing properties.

Acknowledgments:
The Natural Sciences and Engineering Research Council (NSERC), the Ontario Ministry of Research and Innovation Early Researcher Award program (to TH) and the NSERC CREATE-IDEM (Integrated Design of Extracellular Matrices) program are gratefully acknowledged for funding. Nick Burke, Marcia West, and Katya D'Costa are thanked for their help with instrument training, consultation and sample preparation.

Appendix 2S: Supporting information to Chapter 2

Detailed Experimental Protocols

Materials: N-isopropylamide (NIPAM; 99%) was purchased from J&K Scientific and purified by recrystallization at 0°C from toluene, followed by washing with hexanes. N-vinylpyrrolidone (NVP; 99%), acrylic acid (AA; 99%) and thioglycolic acid (TGA; 98%) were purchased from Sigma Aldrich (Oakville, Canada) and used as received. 2,2-azobisisobutyric acid (AIBME, 98%) was purchased from Waterstone and stored under nitrogen. 1-ethyl-3-(3-dimethylaminopropyl) carbodiimide hydrochloride (EDC, 98%) was purchased from Carbosynth. N-2 aminoethyl maleimide (AEMA, 98%) was purchased from Toronto Research Chemicals. D,L-dithiothreitol (DTT; 99%) was purchased from Gold Biotechnology. 3,3'-dithiobis(propanoic dihydrazide) (DTP) was prepared according to the methods of Vercruysse *et al.*[98] (using 3,3'-dithiodipropionic acid - Sigma 99%, concentrated sulfuric acid – Caledon 95%, and hydrazine hydrate - Sigma 50%) and stored at -20°C until use. Hydroxybenzotriazole (HOBT, 98%) was purchased from ApexBio. Adipic acid dihydrazide (ADH; 97%) was purchased from Alfa Aesar. All water used was of Milli-Q grade.

Synthesis of hydrazide-functionalized PNIPAM (PNIPAM-Hzd): Hydrazide-functionalized PNIPAM oligomers were prepared as previously described[32] by dissolving 4 g NIPAM, 1 g AA, (corresponding to 28 mol% acrylic acid), 56 mg AIBME (initiator), and 80 µL TGA (chain transfer agent) in 40 mL anhydrous ethanol and heating the solution overnight at 56°C under a nitrogen purge. The polymer product was purified by exhaustive dialysis against DI water using 12-14kDa MWCO membranes. AA

incorporation was quantified by base-into-acid conductometric titration (ManTech Associates model 4510) of 50 mg polymer in 50 mL of 3 mM NaCl solution using 0.1 M NaOH as the titrant. Hydrazide functionalization was then carried out by conjugation of an eight-fold molar excess of ADH to the AA residues using a three-fold molar excess of EDC. Functionalized product was purified by dialysis and lyophilized for storage. NMR was conducted in d-DMSO (Figure 2S.1); δ (ppm) 1.05 (CH_3), 1.50 (broad - backbone CH), 2.01 & 2.12 (ADH & backboneCH_2 groups), 3.83 (NIPAM CH).

Synthesis of aldehyde-functionalized PNIPAM (PNIPAM-Ald): Aldehyde-functionalized PNIPAM was synthesized as previously described[79]. Briefly, N-(2,2-dimethoxyethyl)methacrylamide was copolymerized with NIPAM using the same 5 g total monomer / 56 mg initiator / 80 uL chain transfer agent. To ensure hydrazide is present in excess during gel formation, an 85:15 molar ratio of NIPAM to acetal monomer was used. Following polymerization, the ethanol solvent was removed under rotary evaporation, and the product was redissolved in 3M HCl for 24 h to hydrolyze the acetal groups to aldehydes. The copolymers were then purified by exhaustive dialysis against DI water, lyophilized, and stored at 4°C until use. NMR was conducted in d-DMSO (Figure 2S.2); δ (ppm) 1.04 (CH_3), 1.45 (backbone CH), 1.94 (backbone CH_2), 3.83 (NIPAM CH), 9.41 (aldehyde CH).

Synthesis of thiol-functionalized PVP (PVP-SH): Poly (vinyl pyrrolidone-co-acrylic acid) (PVP-co-AA) was prepared by dissolving 4 g NVP, 1 g AA, 56 mg AIBME (initiator) and 80 µL TGA (chain transfer agent) in 40 mL anhydrous ethanol and heating the solution overnight at 56°C under a nitrogen purge. Acid residues on PVP-co-AA were then functionalized with a 1.5 times molar excess of DTP conjugated to the polymer using a three-fold excess of EDC and subsequently dialyzed against DI water.

Following, the internal disulfide bond in the pendant DTP groups was cleaved using 4x excess DTT to yield a free thiol group, with a second round of reduction using 2x DTT after two cycles of dialysis. The product was dialyzed exhaustively against DI water adjusted to pH 4 (to prevent oxidation of thiol groups); following dialysis, the pH was adjusted to pH 7.4 and the sample was immediately frozen for lyophilization. The degree of thiol functionalization was measured using the Ellman's colourimetric assay, following manufacturer specifications. NMR was conducted in d-DMSO (Figure 2S.3); δ (ppm) (1.32, 1.45, 1.63, 1.86, 2.06, 2.22 assigned to CH's and CH_2's of the backbone and the vinyl pyrrolidone ring), 2.67 (broad – DTP CH_2's) and 9.83 (SH).

Synthesis of maleimide-functionalized PVP (PVP-Mal): PVP-co-AA was also used as the starting material for maleimide functionalization. EDC coupling of N-2-aminoethyl maleimide to the free acrylic acid residues of PVP-co-AA was subsequently carried out at pH 6 using a 1:3:3:1 ratio of polymer-bound COOH: EDC: HOBT: maleimide, with the HOBT used to minimize side reactions[196]. After dialysis and freeze-drying, the purified powder was redissolved by low-power sonication for 20 minutes before use. NMR was conducted in d-DMSO (Figure 2S.4); δ (ppm) (1.31, 1.53, 1.62, 1.85, 2.06, 2.13 & 2.21 (CH/CH_2 of the backbone and the vinyl pyrrolidone ring), 3.20, 3.54 (aminoethyl maleimide CH_2) and 7.10 (maleimide double bond CH). Note that approximately 50% of the maleimide residues are hydrolyzed to form maleamic acid (7.44 & 7.63 ppm) during synthesis and purification, a widely-recognized side-product of maleimides in aqueous solutions[97].

Synthesis of maleimide-functionalized PNIPAM and PVP: PNIPAM and PVP for the semi-IPN controls were synthesized using 5 g monomer : 56 mg AIBME : 80 uL TGA.

Polymer characterization: Polymer samples dissolved at approximately 10 mg/mL in d-DMSO were analyzed via ^{1}H NMR using a 700MHz Bruker instrument. Comparative peak integration for the functional group peaks versus the characteristic peaks from the main backbone units was performed in TopSpin 2.1 software to estimate the degree of functionalization of PNIPAM-Ald and PVP-Mal. Conductometric titration (performed both before and after the functionalization reactions, probing for the reduction in carboxylic acid groups of acrylic acid residues as a result of the functionalization) was used to quantify the degree of functionalization on PNIPAM-Hzd. The Ellman's assay was performed using the Ellman's buffer (0.1M sodium phosphate, 1mM EDTA, pH 8.0), with test samples prepared from 2.5mL buffer, 50µL of 4 mg/mL Ellman's reagent, and 250 µL analyte. The absorbance of the colorimetric probe was measured at 412nm and compared against a standard curve built using 0.1-1.5mM mercaptopropanol concentrations. FTIR was performed on a Thermo Scientific Nicolet 6700 operating in absorbance mode with 4 cm^{-1} resolution and 64 scans per sample. Samples were prepared as pressed pellets with potassium bromide. Gel permeation chromatography (GPC) was conducted using three different instruments according to polymer solubility and functionalization (Table S1). Polymers were dissolved at 10 mg/mL. To minimize potential interactions with the column, PVP-maleimide was capped by aqueous reaction with excess cysteamine at pH 7.4 prior to testing. The acidic column was used for capped PVP-Mal, the basic column for PNIPAM-Hzd, PVP-SH and unfunctionalized PVP, and the DMF column for PNIPAM-Ald.

Table 2S.1: GPC hardware, solvents and protocols for acidic, basic and DMF instruments.

	Solvent	Temp.	Pump & Flow rate (ml/min)	Detector	Auto-sampler	Columns
Acidic	1M acetate buffer, pH 4.7	30°C	Waters 515, 0.8mL/min	Waters 2414	Waters 717 Plus	Waters Ultrahydrogel -120, -250, -500; 7.8x300mm; 6µm particles
Basic	0.5M sodium nitrate, 25mM CHES, pH 10.0	30°C	Waters 515, 0.8mL/min	Waters 2414	Waters 717 Plus	Waters Ultrahydrogel-120, -250, -500; 7.8x300mm; 6µm particles
DMF	50mM LiBr in DMF	35°C	Waters 590, 0.5 mL/min	Waters 410	Manual	Waters HR-2, -3, -4; 7.8x300mm; 5µm particles

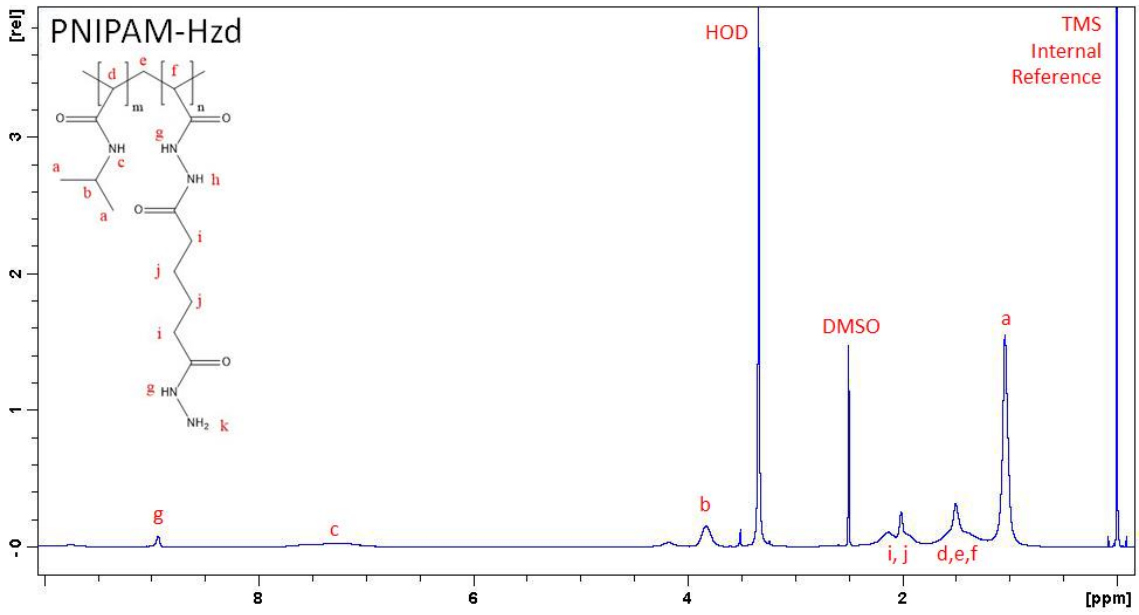

Figure 2S.1: ^{1}H NMR of PNIPAM-Hzd

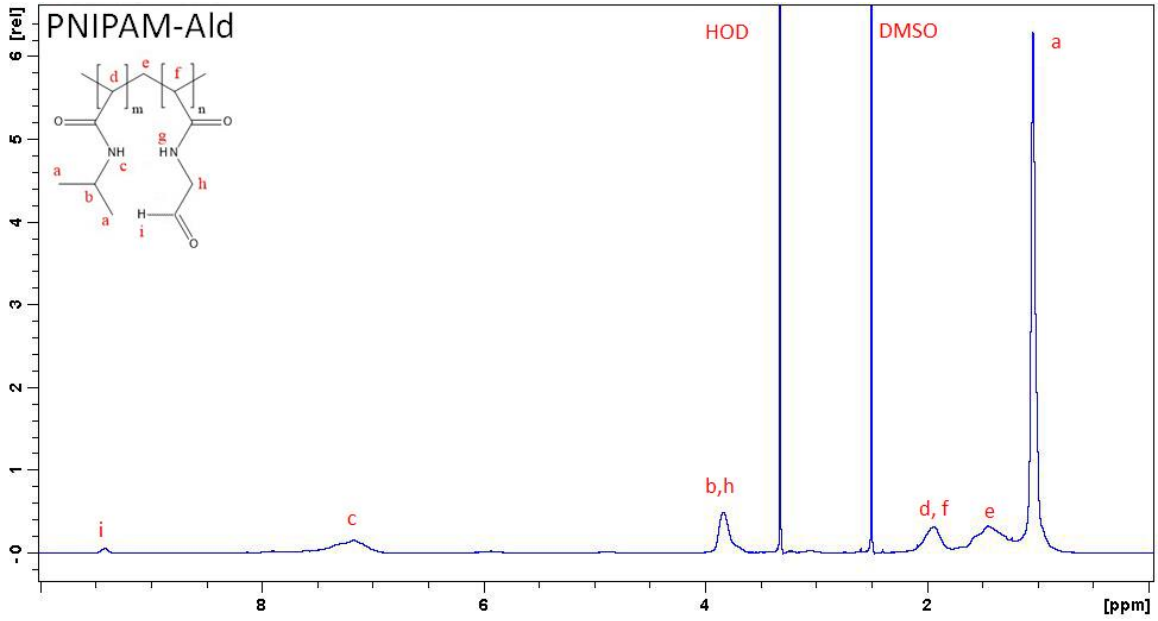

Figure 2S.2: 1H NMR of PNIPAM-Ald

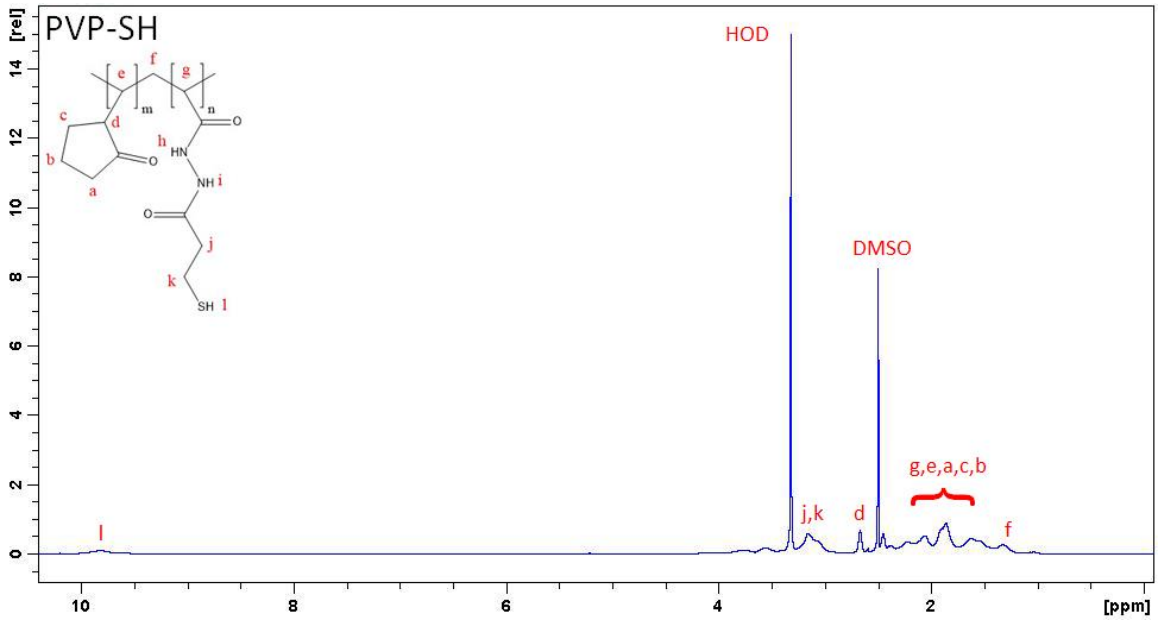

Figure 2S.3: ^{1}H NMR of PVP-SH

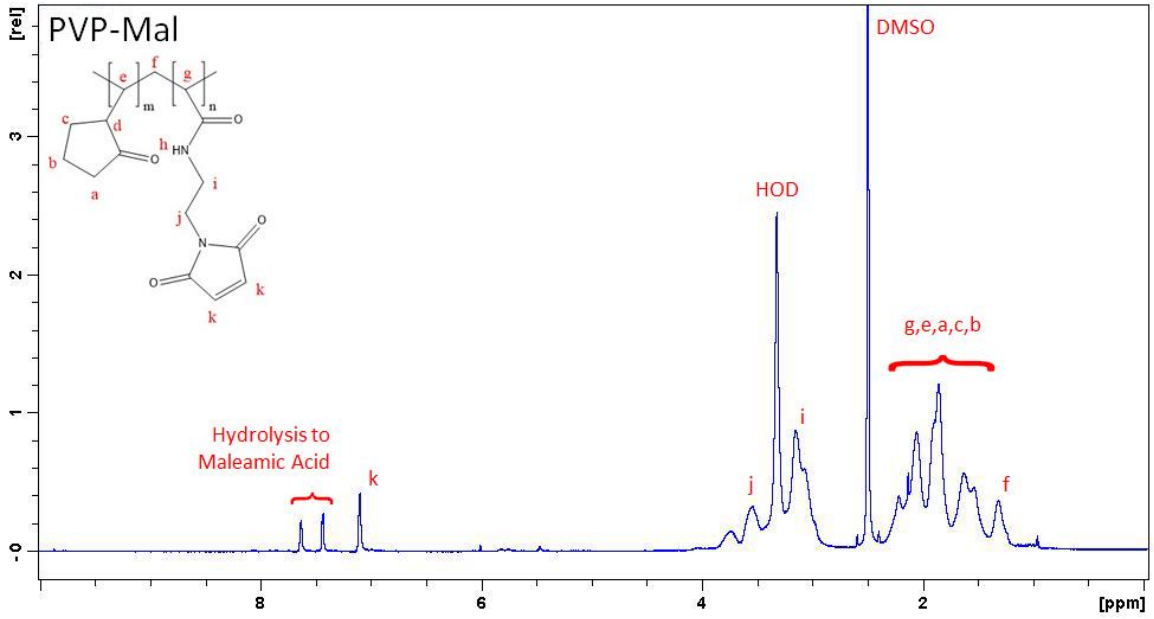

Figure 2S.4: ^{1}H NMR of PVP-Mal

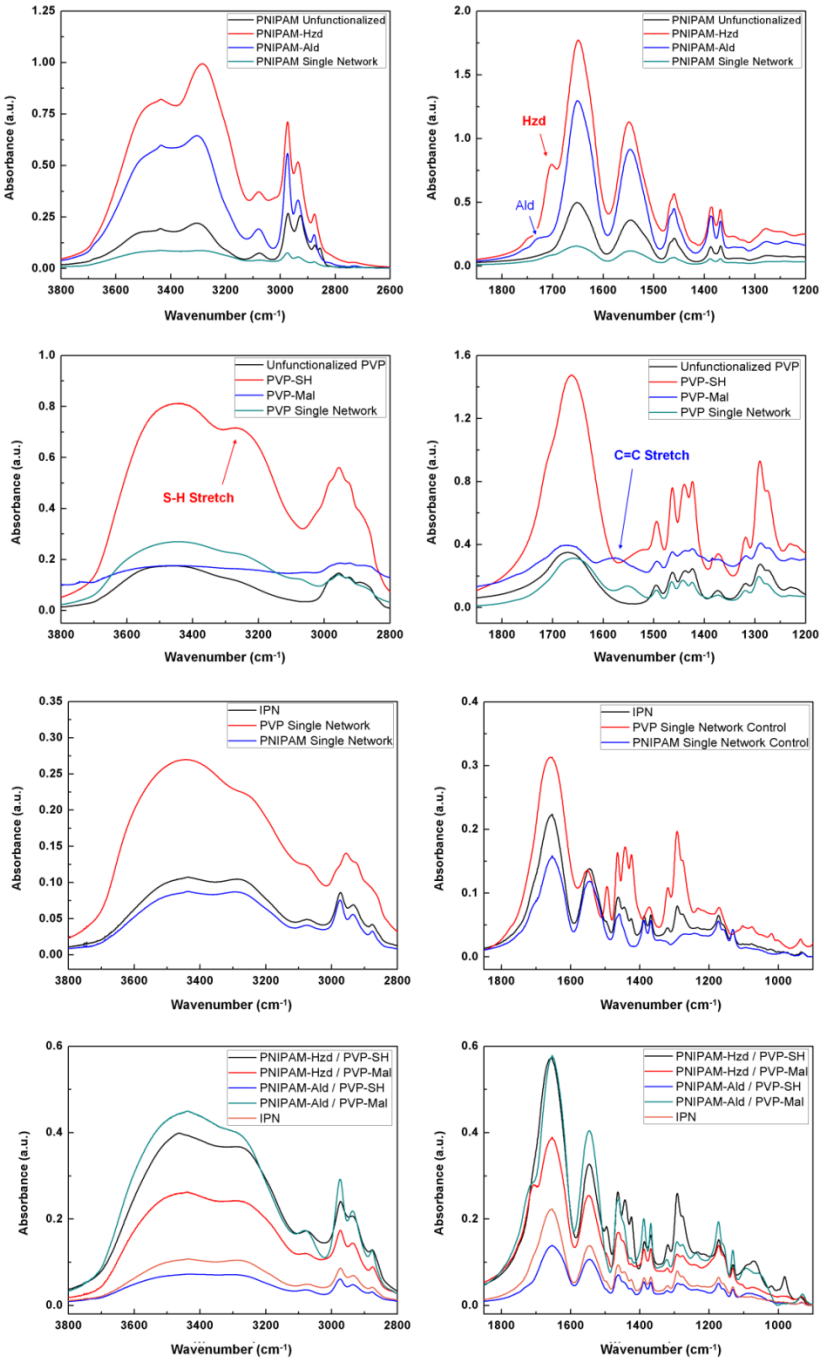

Figure 2S.5: FTIR spectra of individual polymers, lyophilized hydrogels and potential cross-reactive pairings. Results indicate IPN absorbances are a superposition of the two single network controls.

Table 2S.2 Molecular weight (from GPC), polydispersity (from GPC), and degree of functionalization (as a mole percentage of the total monomer units in the polymer backbone) as measured from conductometric titration (PNIPAM-Hzd), NMR (PNIPAM-Ald and PVP-Mal), or Ellman's assay.

Polymer	M_w (kDa)	PDI	GPC	Degree of Functionalization (mol% functional monomer)
PNIPAM-Hzd	*19*	3.2	Basic	20% (Titration before and after Hzd
PNIPAM-Ald	23	6.1*	DMF	conjugation)
PVP-SH	30	4.0	Basic	7% (NMR)
PVP-Mal	18	2.7	Acidic	15% (Ellman's assay)
PVP non-functionalized (for semi-IPN control)	26	3.1	Basic	10% (NMR) N/A
PNIPAM non-functionalized	*9*	3.2	DMF	N/A

* Note that the high PDI of the PNIPAM-Ald polymer is likely indicative of interactions with the packing material, as supported by the relatively flat elution profile observed. Aqueous GPC was not viable due to the proximity of the LCST of PNIPAM-Ald to the operating temperature of the aqueous GPC columns.

Verification of orthogonality: Small-molecule assessment of the cross-reactivity between the hydrazide, aldehyde, thiol and maleimide functional groups used as cross-linking chemistries for the IPN was carried out using N-methyl maleimide (Mal), 3-mercapto-1-propanol (SH), formic hydrazide (Hzd) and propanal (Ald) as model compounds. The orthogonality of the pairs of cross-linking reactions was tested by rapidly mixing equimolar amounts of the hydrazide and aldehyde with (separately) the thiol and the maleimide and comparing the ^{1}H NMR spectra (Bruker AV200; D_2O) to verify that the resulting mixture is a superposition of the expected hydrazone cross-linked product and the unreacted thiol or maleimide. Similarly, non-reactivity of the components intended to be co-loaded into different sides of the double-barreled syringe was tested by ^{1}H NMR analysis of mixtures of hydrazide/thiol and maleimide/aldehyde

over forty days to verify the absence of new peaks or peak shifts. Figures 2S.7 and 2S.8 show the raw NMR spectra of each mixing case described, while Figure 2S.9 shows the same data in overlay mode to confirm the lack of cross-reactivity of co-stored components as well as the single-path reactivity of each bonded network to the exclusion of potential cross-products (at least on a kinetic basis).

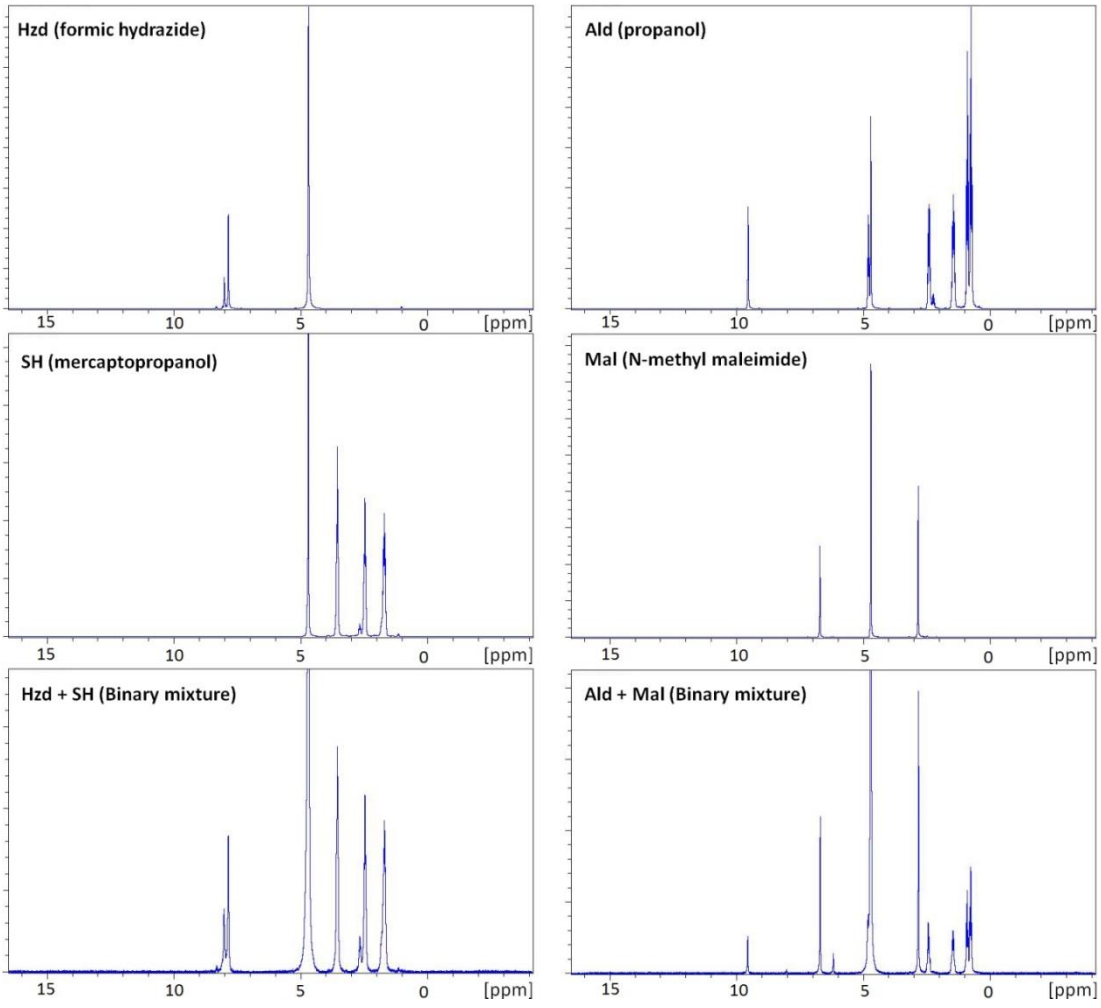

Figure 2S.6: NMR small molecule studies demonstrating non-reactivity of functional group storage pairings (hydrazide + thiol; aldehyde + maleimide) in D_2O.

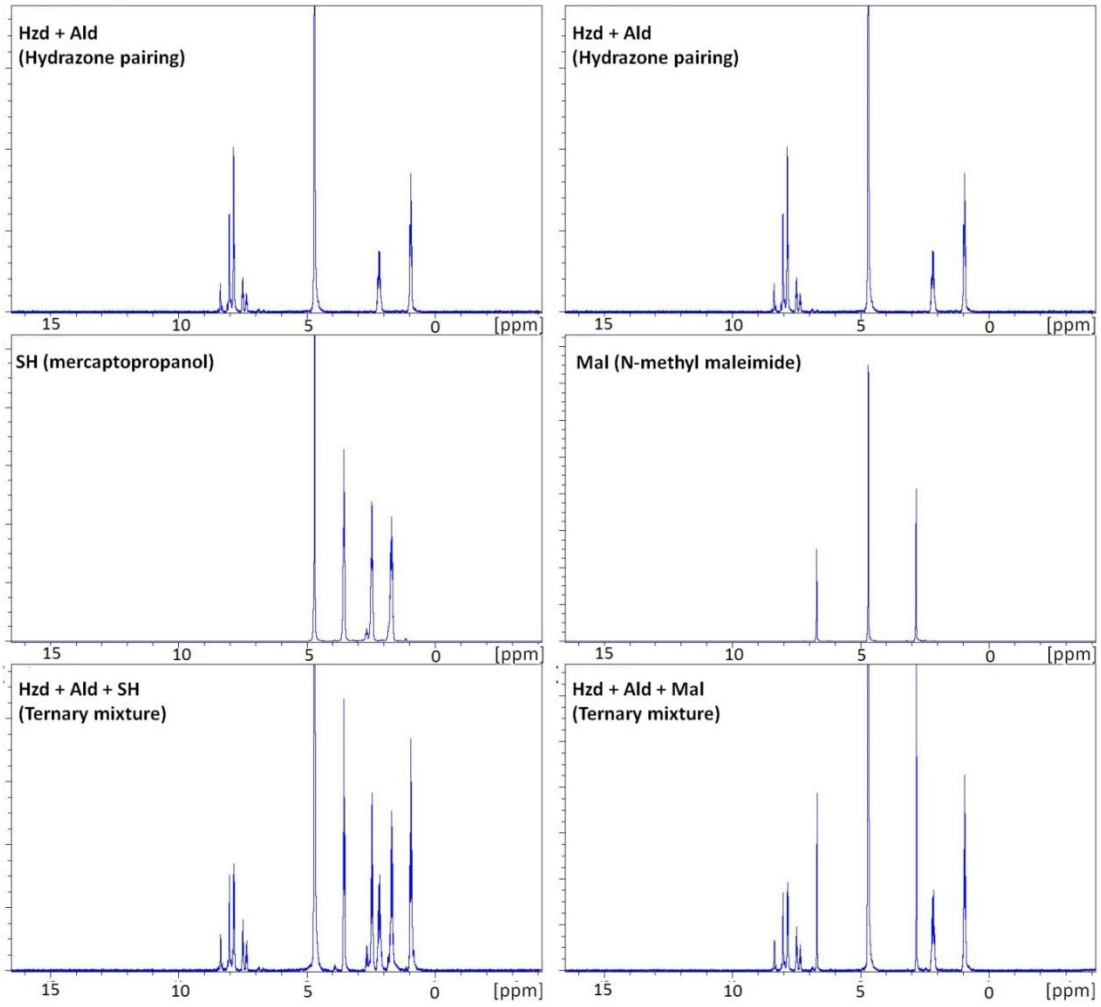

Figure 2S.7: Vertical stack of small molecule analogue NMR studies demonstrating kinetic orthogonality of hydrazone bond formation from presence of thiol or maleimide in D_2O.

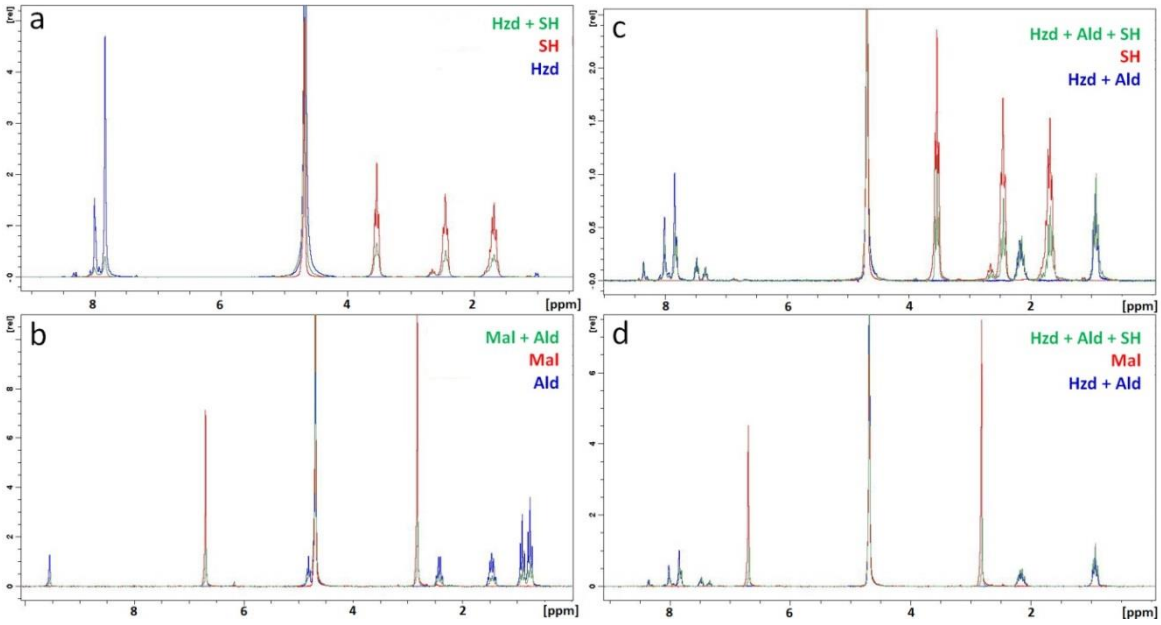

Figure 2S.8. Overlay figure of NMR data presented in Figs. S6 and S7 demonstrating orthogonality of hydrazone and thiosuccinimide bond formation using small molecule analogues (Hzd = formic hydrazide; Ald = propanal; SH = 3-mercapto-1-propanol; Mal = N-methyl maleimide). (a, b) non-reactivity of co-stored nucleophiles and electrophiles confirming storage stability of Hzd and SH together (a) and Ald and Mal together (b); note that the small new peak at 6.1 ppm in the Mal-Ald mixture, Fig. S9b, can be attributed to maleimide hydrolysis over the 40 day storage period[97] (see reference 10 in main paper); (c, d) formation of hydrazone bond without detectable side products from an equimolar mixture of Hzd, Ald, and SH (c) or Mal (d) small molecule analogues, confirming hydrazone formation preferentially to alternate nucleophile/electrophile reactions

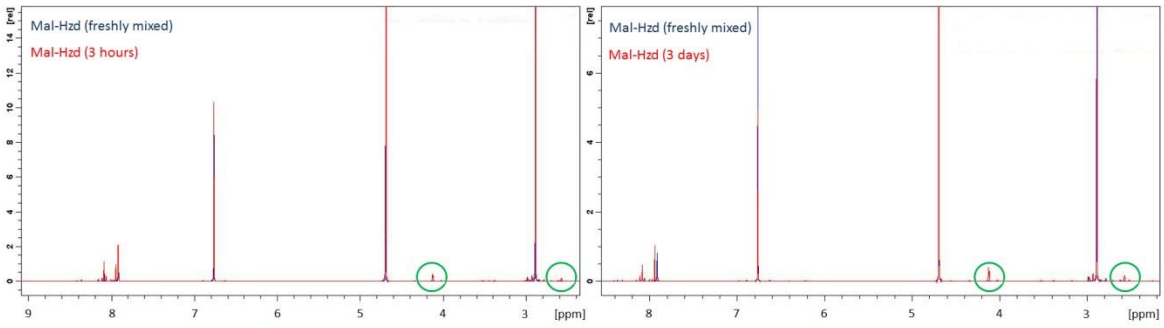

Figure 2S.9: Small molecule models demonstrating trivial cross-reactivity between maleimide and hydrazide functionalities, with new peaks three hours and three days after mixing circled.

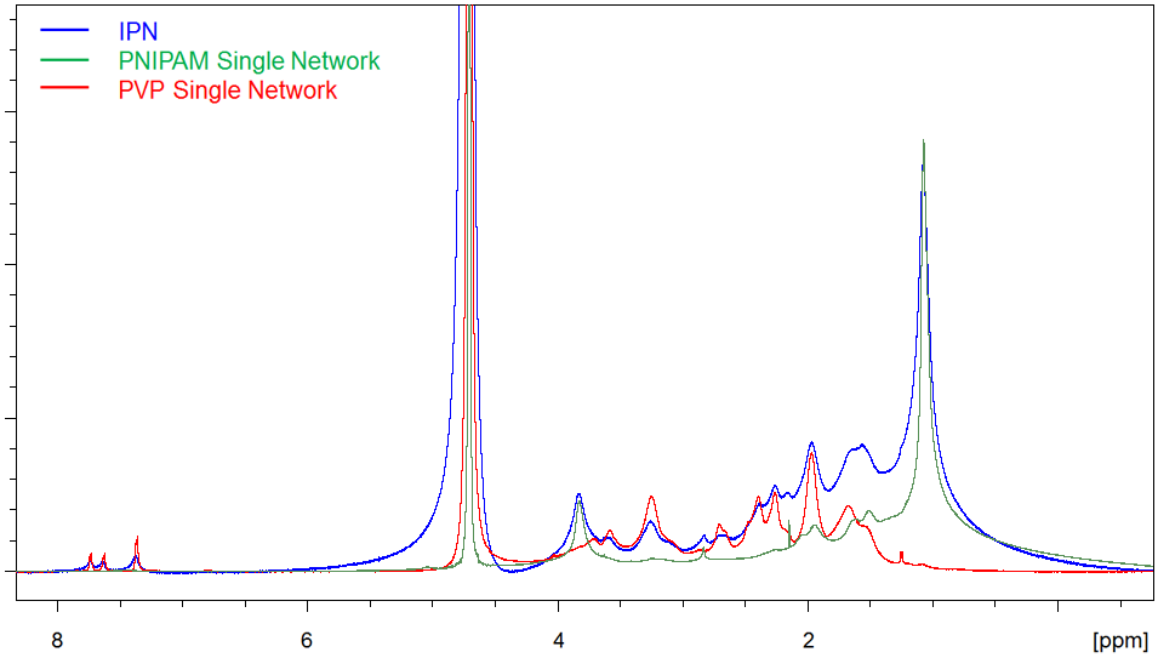

Figure 2S.10: Solution-state NMR of IPN and single-network control hydrogels in D_2O (Bruker AV600, 64 averages).

Swelling / Degradation Experiments: To minimize contact with the samples during weighing, hydrogels (n=4 for each composition and test type) were incubated in cell culture inserts within 24-well plates. The membrane at the bottom of each well was perforated to allow for drainage of the respective storage media (10 mM PBS for swelling experiments or 0.1M HCl for degradation experiments). Any residual solution on the top face of the hydrogel samples was gently wicked off using a Kimwipe and the insert itself was dried prior weighing the insert and sample, with the weight of each insert then subtracted to determine hydrogel mass. After returning the inserts to their wells, each well was refilled with PBS or HCl, as required for each experiment; this was repeated at each data point collected.

Table 2S.3: Percentage changes of gel mass over multiple thermal cycles relative to the equilibrium gel mass at the previous temperature (RT = room temperature).

	PNIPAM	PVP	Semi-IPN	IPN
RT->37	-47.2%	-14.4%	-27.6%	-25.0%
37->RT	30.8%	-2.4%	16.2%	17.7%
RT->37	-24.6%	-8.2%	-6.5%	-11.2%
37->RT	14.6%	-3.0%	5.3%	9.2%
RT->37	-23.3%	-6.5%	-23.4%	-17.9%
37->RT	37.7%	5.6%	28.6%	20.7%

Table 2S.4: Fitting parameters for the de-swelling kinetics in 10 mM PBS over the first thermal transition from room temperature to 37°C. Fit is made according to $y = Ae^{(-\frac{t}{\tau})} + y_0$ with time in hours.

	PNIPAM		Semi-IPN		IPN	
	Fit parameter	**St. Dev.**	**Fit parameter**	**St. Dev.**	**Fit parameter**	**St. Dev.**
y_0 (baseline)	0.54	0.01	0.65	0.01	0.88	0.02
A	0.40	0.02	0.19	0.03	0.17	0.03
t_1 (time constant)	0.68	0.09	0.63	0.20	4.14	1.63
R^2	0.98		0.58		0.75	

Table 2S.5: Fitting parameters of hydrogel degradation performed in 0.1M HCl. Fit is made according to $y = Ae^{(-\frac{t}{\tau})} + y_0$ with time in days.

	PNIPAM		Semi-IPN		IPN	
	Fit parameter	**St. Dev.**	**Fit parameter**	**St. Dev.**	**Fit parameter**	**St. Dev.**
y_0 (baseline)	0.17	0.01	0.24	0.01	0.54	0.01
A	0.97	0.05	0.80	0.02	0.48	0.01
t_1 (time constant)	0.52	0.05	1.22	0.08	1.84	0.11
R^2	0.94		0.97		0.97	

Chapter 3: Nanostructure of Hydrazone-Thiosuccinimide Injectable IPN's, Assessed by Small-Angle Neutron Scattering and dSTORM single-molecule Fluorescent Microscopy

Preface

This chapter describes an in-depth characterization of the meso- and nano-scale network structure of the IPNs described in Chapter 2, with structure being studied in the hydrated state to avoid inevitable structural distortions caused by the freeze-drying process required for TEM/SEM studies. These studies were based on small angle neutron scattering (SANS) and super-resolution dSTORM optical microscopy using fluorescent labelling. This chapter will be submitted for publication concurrently with the thesis.

Trevor Gilbert[1], Richard Alsop[2], Mouhanad Babi[3], José Moran-Mirabel[3], Maikel Rheinstadter[2] and Todd Hoare*[1]

1 Department of Chemical Engineering, McMaster University, 1280 Main St. W, Hamilton, Ontario, Canada L8S 4L7

2 Department of Physics, McMaster University, 1280 Main St. W, Hamilton, Ontario, Canada L8S 4L7

3 Department of Chemistry, Mc Master University, 1280 Main St. W, Hamilton, Ontario, Canada L8S 4L7

Abstract

The utility of interpenetrating network hydrogels in various applications is directly tied to the internal morphology of the network structure. Herein, we comprehensively investigate the internal morphology of fully injectable IPNs prepared via co-extrusion of functionalized precursor polymer solutions based on thermoresponsive poly(N-isopropylacrylamide) and non-thermoresponsive poly(vinyl pyrrolidone) by reactive mixing using kinetically orthogonal hydrazone and thiosuccinimide cross-linking mechanisms. Small angle neutron scattering (SANS), probing both the full IPN as well as the individual constituent networks of the IPN using index matching, suggests a partially mixed internal structure characterized by PNIPAM-rich domains entrapped in a clustered PVP-rich phase. This interpretation is supported by super-resolution fluorescence microscopy (dSTORM) measurements on the same gels at a different length scale which show both the overall phase segregation typical in an IPN as well as moderate mixing of PNIPAM into the PVP-rich phases. Such a morphology is consistent with the kinetics of both gelation and phase separation in this *in situ*-gelling system, in which gelation effectively traps a fraction of the PNIPAM in the PVP phase prior to full phase separation occurring (as is the case in semi-IPN control hydrogels). This knowledge has significant potential for the design of injectable hydrogel with internal morphologies optimized for particular biomedical applications.

3.1 Introduction

Interpenetrating network (IPN) hydrogels are distinguished by the interlocking of two independently cross-linked but chemically non-bonded networks that swell in water[3].

Much of the interest in hydrogel IPNs has stemmed from the proven degree of mechanical enhancement[204] that is achievable relative to the single networks as a result of the physical entanglements between the networks. While such enhancements are particularly demonstrated with double network IPNs consisting of one weakly cross-linked and one tightly cross-linked component[123, 142], such mechanical enhancements are more broadly used to increase the stiffness of hydrogels for potential use in more load-bearing applications (e.g. stiffer tissue scaffolds for cartilage[215] or bone[216]). However, the internal structure of IPNs can also be leveraged effectively in applications. The formation of distinctive micro- and nano-structures in IPNs and semi-IPNs can be used to regulate pore size/morphology (facilitating control over the diffusion properties for separations applications[217] and drug delivery[218]) as well as facilitate the creation of a network of segregated domains enriched with one or the other component polymer network (facilitating, for example, enhanced uptake and subsequent control over release of drugs with specific properties).

The nature of the morphologies formed in hydrogel IPNs is dependent on the kinetics of gel network formation in the two constituents[219], as well as propensity for phase separation between the two networks at the environmental conditions at which they are prepared[220]. The former is particularly important in regulating morphology development in simultaneous IPNs in which both networks are polymerized simultaneously through orthogonal chemistries – specifically, faster and more closely matched network formation rates between the two constituents generally favour more homogeneous IPN's[219]. Furthermore, for systems where phase separation is thermodynamically favoured but the rate of network formation exceeds that of mass transfer, gelation can 'lock in' otherwise

unfavourable morphologies[123] and significantly influence the ultimate morphology achieved in the IPN system.

Thorough characterization of these novel structural features is a necessity for rational design of network architecture for particular applications[3, 221]. In particular, the capacity for partial domain segregation is of particular interest for predicting the performance of IPNs as cell scaffold and / or drug delivery materials, as domain segregation is expected to significantly alter the capacity for drug uptake as well as both the partitioning and diffusion-based barriers to the subsequent release of that drug. Several methods have been applied to study the nature domain formation in IPN hydrogels, including differential scanning calorimetry[122, 124], electron microscopy[222], laser scanning confocal microscopy[223], and small angle neutron scattering[224] (SANS). However, among those methods, only SANS is capable of providing nanometer-level information about the nature of the network structure in the swollen state, the key piece of information required to effectively engineer hydrogel IPNs with specific morphological features. The technique of contrast matching in SANS is particularly useful for individually probing the nanostructures of each interpenetrating network in the presence of the other network and has been used previously to characterize the response of classical brittle-ductile double-network IPN hydrogels to tensile strain[225-226]. By preparing samples with one network made from the deuterated analogue mononer in aqueous solvents with different hydrogen/deuterium ratios that separately match the scattering length density of each of the component phases, scattering contributions from the network that is matched to the solvent are suppressed (i.e. that network is “invisible”) and the network structure of the other interpenetrating phase can be independently elucidated. This technique has also

previously been applied to investigate the morphology of PNIPAM-clay composites[227], magnetic nanoparticle-loaded hydrogels[228], and PEG/ poly(acrylic acid) IPNs[229].

The recent development of super-resolution fluorescence techniques such as direct stochastic optical reconstruction microscopy (dSTORM) has provided an additional possible avenue for the exploration of the nano and micro-structures of gel IPN systems. The technique is based on reversibly switching fluorophores between active and inactive states[230-231]; with a sparse subset of the entire fluorophores active at any given time, fitting of the two-dimensional point-spread function around single fluorophores can allow localization of the emitter to less than the diffraction limit associated with the resolution of conventional microscopy[232]. By collecting image stacks covering long acquisition times, the randomly sampled super-resolution localizations collected in each frame can be added to reconstruct the locations of the entire population of fluorophores. While this approach has been used extensively for biological applications such as live cell imaging[233-234], tracking assembly of the viral envelope in HIV[235] and tracking actin and myosin dynamics in skeletal muscle[236], multi-channel dSTORM imaging has not to our knowledge previously been applied to study phase segregation and internal morphology in IPNs or other multi-component hydrogels.

Recently, we reported a fully-injectable simultaneous IPN that forms by kinetically orthogonal mixing of two pairs of functionalized prepolymers (hydrazide-functionalized PNIPAM and thiol-functionalized PVP mixed through a double-barreled syringe with aldehyde-functionalized PNIPAM and maleimide-functionalized PVP)[237] (Figure 3.1). Such a protocol results in a hydrazone-cross-linked thermosensitive network interpenetrated with a thiosuccinimide-cross-linked hydrophilic network, with the two

networks showing no significant cross-reactivity on the detection threshold of NMR in the resulting composite hydrogel. Herein, we investigate the internal morphology of such simultaneous *in situ*-gelling IPNs using a combination of SANS (including scattering from both networks and using contrast matching to render each component network "invisible") and super-resolution fluorescence microscopy. In particular, given that one of the interpenetrating phases is thermosensitive and the other is not, the driving force for phase separation between the interpenetrating networks is a strong function of temperature; consequently, we expected to see significant domain formation in these IPNs. Both SANS and super-resolution fluorescence indicate phase separation on multiple length scales as well as the presence of a partially mixed internal structure consisting of PNIPAM-rich static inhomogeneities embedded in a clustered PVP-rich phase.

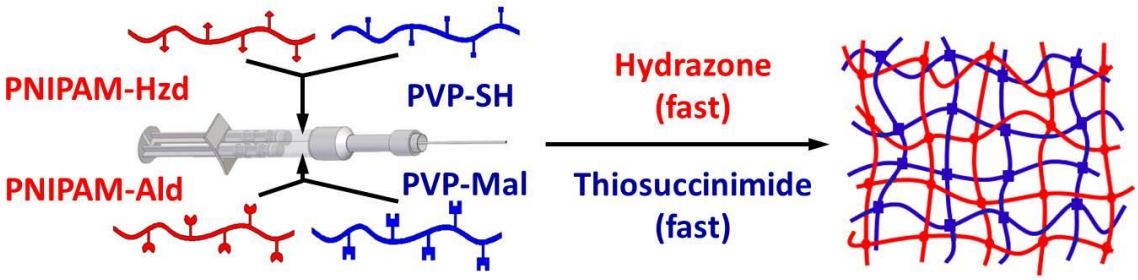

Figure 3.1: Schematic of chemistry and gelation strategy used for injectable IPN formation.

3.2 Materials and Methods

3.2.1 Materials:

N-isopropylamide (NIPAM; 99%) was purchased from J&K Scientific (Sunnyvale, USA) and purified by recrystallization at 0°C from toluene followed by washing with hexanes. Deuterated (d7) NIPAM (inhibitor-free) was purchased from Polymer Source (Montreal, Canada) and used as received. N-vinylpyrrolidone (NVP; 99%), acrylic acid (AA; 99%) thioglycolic acid (TGA; 98%), glucose oxidase, catalase and cysteamine were purchased from Sigma Aldrich (Oakville, Canada) and used as received. N-vinylformamide (NVF, >96%) was purchased from TCI (Portland, USA) and used as received. 2,2-azobisisobutyric acid (AIBME, 98%) was purchased from Waterstone and stored under nitrogen. 1-ethyl-3-(3-dimethylaminopropyl) carbodiimide hydrochloride (EDC, 98%) was purchased from Carbosynth (Berkshire, UK). N-2 aminoethyl maleimide (AEMA, 98%) was purchased from Toronto Research Chemicals (Toronto, Canada). Hydroxybenzotriazole (HOBT, 98%) was purchased from ApexBio (Houston, USA). Adipic acid dihydrazide (ADH; 97%) was purchased from Alfa Aesar (Tewksbury, USA). All water used was of Milli-Q grade.

Cy5-NHS was made by modifying Cy5 (Lumiprobe, Hallandale Beach, Florida) according to established protocols[238]. Cy3-maleimide was made by modifying Cy3-NHS (Lumiprobe) with N-(2-aminoethyl)maleimide in dimethylformamide. The solvent was evapourated and the residue was purified via liquid-liquid extraction of dichloromethane and saturated NaCl brine, after which the organic phase was evapourated again.

3.2.2 Precursor Polymer Synthesis and Characterization:

Hydrazide- and aldehyde-functionalized poly(N-isopropylacrylamide), both typical protonated polymers (PNIPAM-Hzd and PNIPAM-Ald) as well as deuterated analogues (d7-PNIPAM-Hzd and d7-PNIPAM-Ald), and maleimide-functionalized poly(vinyl pyrrolidone) (PVP-Mal) were prepared and characterized (via conductometric titration for Hzd derivatives and ^{1}H-NMR for Ald derivatives) as previously described[237]. Thiolated poly(vinyl pyrrolidone) (PVP-SH) was prepared by first copolymerizing N-vinyl pyrrolidone and N-vinyl formamide (10mL total monomer in a 4:1 molar ratio) in 55 mL of isopropanol, using 100mg AIBME initiator and 160µL TGA chain transfer agent. Polymerization was conducted overnight at 60°C, followed by removal of the solvent under reduced pressure. The product was subsequently redissolved in 1 M NaOH and heated at 70°C for 24 hours to hydrolyze vinyl formamide residues to vinyl amine residues, dialyzed exhaustively (6 x 6+ hour cycles), and lyophilized (as per established methods[239]). Amine content was determined by base-into-acid conductometric titration (0.1 M NaOH titrant, 50 mg polymer in 50 mL of 1 mM NaCl as the sample, Mantech Associates autotitrator). Following, functionalization of the amine residues to form thiols was carried out at room temperature using a 1:1.2:3 molar ratio of PVP-co-vinyl amine:3-mercaptopropionic acid:EDC, with the reaction run for 2 hours in water while manually controlling the pH at 4.75. The thiolated product was then dialyzed against dilute HCl (pH 4-5, 6 x 6+ hour cycles), after which the pH was adjusted to pH 7.4 and the solution was immediately lyophilized. The product was stored at -20°C and exhibited stable storage times of up to one month; although conversion is essentially quantitative for the EDC conjugation based on consumption of free amine groups, residual moisture on the lyophilized polymer can allow disulfide formation even at -20°C if the polymer is left for

an extended period under storage. Polymer molecular weight was measured using the gel permeation chromatography (GPC) configurations summarized in Supporting Information, Table 2S.1 according to the solubilities of each polymer tested.

Table 3.1: Properties of precursor polymers

Polymer	Mw (kDa)	PDI	GPC Method	Degree of Functionalization (mol % functional residues)
PNIPAM-Hzd	19	3.2	Basic	20% (Titration before and after functionalization)
PNIPAM-Ald	23	* 6.1	DMF	7% (NMR peak integration)
PVP-SH	26	2.7	DMF	22% (Titration & Ellman's assay)
PVP-Mal	18	2.7	Acidic	10% (NMR peak integration)
Unfunctionalized PVP	26	3.2	Basic	N/A
Unfunctionalized PNIPAM	9.2	3.2	DMF	N/A

* Likely indicating some association between the polymer and column packing material, rather than a true feature of the polymer

3.2.3 SANS Samples:

Neutron scattering experiments were carried out on the NG30 (30 m) SANS instrument at the NIST Center for Neutron Research (NCNR), Gaithersburg, MD, USA. Samples were prepared using 6 wt% PNIPAM precursor polymer and 9 wt% PVP precursor polymer in phosphate buffered D_2O (or mixed D_2O / H_2O for index matching); the concentrations were chosen such that the storage modulus (G') of the two constituent single networks was approximately equal[237]. Gelation times were fast for both systems,

particularly the PVP-thiosuccinimide network. Vial inversion tests show the PVP system ceased flowing within about five seconds, while the hydrazone-cross-linked PNIPAM took slightly longer to gel, at about 90 seconds. The precursor polymers were loaded into separate barrels of a double barrel syringe (MedMix L system, 2.5 mL volume, 1:1 volume ratio between barrels), adding the hydrazide/thiol polymers in one barrel and the aldehyde/maleimide polymers in the other barrel (as per Figure 3.1), and extruded directly into NCNR's custom titanium/quartz sample holders (diameter 19 mm and path length 1 mm). Each sample was allowed to gel for at least 12 hours before testing to ensure equilibrium cross-linking and network formation had occurred prior to analysis. Six groups of samples were assessed: (1) single network PNIPAM reference (6 wt%), (2) single network PVP reference (9 wt%), (3) semi-IPN reference consisting of 9 wt% unfunctionalized PVP in 6wt% PNIPAM (to discriminate the effects of additional polymer being incorporated into the network from the effects of the formation of the interpenetrating network), (4) the reverse composition of semi-IPN (unfunctionalized PNIPAM in PVP; for the same reason as group 3), (5) full IPN in D_2O (both interpenetrating networks visible via SANS) and (6) full IPNs at H_2O:D_2O scattering length density match points for each network to suppress scattering from one of the two constituent networks and independently probe the morphology of each individual network within the IPN phase. Data was collected at sample- to-detector distances of 1 m (high *q*; at anaverage acquisition time of 1 minute), 4 m (medium *q*, 3 minutes) and 13 m (low *q*; 15 minutes), using 6 Å wavelength neutrons. The *q* ranges were merged using the NCNR's customized data reduction package of Igor Pro macros[240-241].

To determine the H2O/D2O ratio required to contrast match a specific network, the theoretical scattering length density for the network was first calculated based on the

atomic composition. Calculations predicted a match point of 70:30 D_2O:H_2O to contrast-suppress scattering from the d7-PNIPAM network, and 23:77 D_2O:H_2O to match out PVP scattering. Next, experimental confirmation was determined based on preliminary scattering measurements at the calculated match point as well as D2O concentrations ±10% from the match point. Total scattering in each of the three conditions was determined and the D2O concentration producing zero scattering was determined by regression. The predicted D_2O:H_2O matching ratios were thus refined to 73:27 to hide d7-PNIPAM and 31:69 to hide PVP. Negative controls for each single network collected at the final D_2O:H_2O match points demonstrated greater than order-of-magnitude scattering suppression compared to the corresponding compositions in D_2O (see Supporting Information, Figure 3S.1).

3.2.4 SANS Data Fitting:

Three fitting models were used to assess the scattering curves acquired, with the choice dependent on the type of network analyzed. The classical Porod model[242] (Equation 3.1), which describes scattering from networks without any static inhomogeneities such as domains of varying polymer density (at least within the length scale accessible to the NG30 SANS), fit well to thiosuccinimide-cross-linked PVP networks and the room temperature data set for the semi-IPN of PNIPAM chains in a PVP network (although it fit poorly to a scattering spectrum collected at high temperature).

(Eq. 3.1) $$I(Q) = \frac{A}{Q^m} + \frac{B}{1+(\xi\,\mathrm{Q})^n} + C$$

Here, *m* is the low-*q* Porod exponent that describes the extent of swelling versus clustering in the network[242-243] (for our data, tending to the range characteristic of clustered mass fractals of polymer, as shown in Figure 3.2; such clusters represent long-range fluctuations of polymer density, which predominantly affect low-*q* scattering[242]), ξ is the correlation length/mesh size of the gel network (corresponding primarily to the pore size of the hydrogel), *n* is Lorentzian exponent for the fluid term characterizing polymer-solvent interactions at high *q* values (*n* <= 2 indicates favourable solvent interactions whereas *n* > 2 indicates unfavourable solvent interactions[244]) and C is the *q*-independent, incoherent background. See Supporting Information for raw scattering data and Porod fits using Equation 3.1 from both PVP single network controls (Table 3S.1 and Figure 3S.2) and the semi-IPN of free PNIPAM in a PVP matrix (Figure 3S.3).

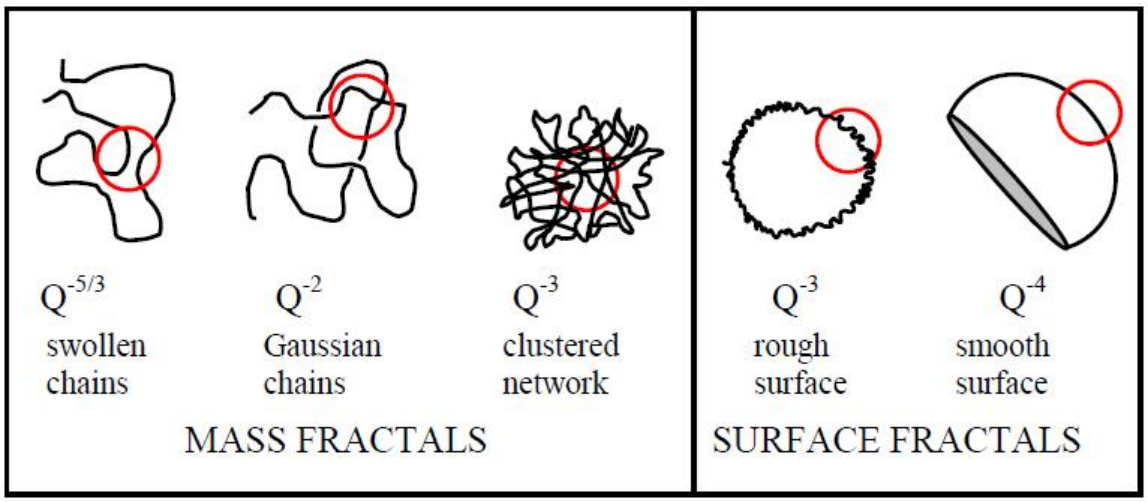

Figure 3.2: Interpretation of Porod exponents. Reproduced with permission[243].

Alternately, hydrazone cross-linked PNIPAM networks were best fit by a squared Lorentzian model (Equation 3.2). The first term describes scattering from static inhomogeneties occurring on the larger end of the range of length scales probed by SANS (such as domains of higher polymer concentration within a hydrogel), with *γ* representing the correlation length scale of these static inhomogeneities in the system[245] (proportional to the average distance between these static features). The second term, describing chain solvation and dynamic fluctuations, is conserved from the Porod model.

(Eq. 3.2) $$I(Q) = \frac{A}{(1+(\gamma Q)^2)^2} + \frac{B}{1+(\xi Q)^n} + C$$

(See Supporting Information for raw scattering data and squared Lorentzian fits using Equation 3.2 from PNIPAM single network controls (Table 3S.2 and Figure 3S.4) and semi-IPN controls of PVP (unfunctionalized) trapped inside a hydrazone-functionalized PNIPAM network (Table 3S.3 and Figure 3S.5)).

For non-contrast matched IPNs in which both the PNIPAM and PVP phase show significant scattering, neither the Porod nor the squared Lorentzian function adequately fit the curve shapes. As such, for those materials, a hybrid model (Equation 3.3) was used that sums the contributions from both Porod-type fractal scattering from the PVP phase (term 1) and squared Lorentzian scattering from the PNIPAM phase (term 2), with a common term used to fit the sum of the dynamic contributions from polymer-solvent interactions at the high *q* regime from both networks (term 3). Combining terms by summation is based on the assumption that scattering events from static domains and clustered regions are non-interfering with each other (i.e. cross-scattering is assumed

not to be a factor. Considering the hybrid model's empirical effectiveness at describing scattering from composite systems, this assumption seems to be supported (see Supporting Information for raw scattering data and hybrid fits using Equation 3.3 for IPN samples in Table 3S.6 and Figure 3S.6).

(Eq. 3.3) $$I(Q) = \frac{A}{Q^m} + \frac{B}{(1+(\gamma Q)^2)^2} + \frac{C}{1+(\xi Q)^n} + D$$

3.2.5 Super-Resolution Fluorescence Microscopy:

To corroborate the structural information inferred from neutron scattering fitting, direct stochastic optical reconstruction (dSTORM) microscopy was used to track the segregation of fluorescently labelled PNIPAM and PVP in IPNs prepared from the two kinetically orthogonal networks. PNIPAM-Hzd was labelled with Cy5-NHS, with ~0.005 mol% of total residues functionalized (a minimal amount to ensure insignificant disruption of the cross-linking chemistry by the fluorescent labeling). PVP-SH was labeled with a maleimide derivative of Cy3, with ~0.05 mol% of total residues being functionalized; the slightly higher labeling density used for PVP-SH is attributable to the differing brightness of the two fluorophores in the imaging buffer, but is still far below an amount that would alter the degree of cross-linking of the hydrogel. In both cases, the average labelling is less than one fluorophore per polymer chain.

Thin-layer hydrogels for imaging were obtained on microscope slides by spin-coating freshly mixed polymer solutions while gelation was in progress. PNIPAM networks produced thin hydrogel sheets at the same 6 wt% concentration used in SANS sample

preparation, but the greater viscosity of the PVP precursors required dilution to 3.5 wt% to sufficiently spread the precursor mixture. While the possible effect of this lower concentration on the phase structure of the IPN cannot be ruled out, it should be noted that the difference in gelation time between this concentration and the 9 wt% concentration used for the SANS studies is not particularly significant; indeed, even at the lower concentration, the PVP network still gels within <10 seconds. Also, solvent evaporation during the spin coating process will affect the precursor polymer concentration and inevitably accelerate the gelation time of both polymers during the spin coating process. As such, while it is recognized that these differences in sample preparation between the SANS and dSTORM measurements are not negligible and may have some impact in terms of the absolute comparisons between the two methods, both the relative gelation speeds of the two networks and the chemical nature of the two networks are similar in both cases.

Polymer precursor solutions were mixed for 5 seconds, spotted (at a 20 µL volume) on a plasma-cleaned MaTek glass-bottomed petri dish, and spun at 1500 rpm for PNIPAM single networks / 4000 rpm for more viscous PVP and IPN precursor mixtures, for 60 s in both cases. For the Cy5-PNIPAM single network, alignment of the image stack was facilitated by bonding fluorescent microsphere tracking beads (PS-Speck beads, excitation 540 nm, emission 560 nm; Molecular Probes, Eugene, Oregon, USA) to the slide. Fiducial markers were omitted in the Cy3-PVP single network samples and the IPN due to channel overlap with the Cy3 fluorophore with minimal degradation to imaging performance. An alternate PNIPAM single network control using 10 times higher labelling density and no fiducial markers was prepared to demonstrate lack of significant deviation in nanostructure from the PNIPAM control prepared with fiducial markers.

The gels were stored in (50mM Tris, 10mM NaCl, pH 8) until imaging. Samples were then transferred to Tris buffer also containing 10% glucose w/w, 100 mM cysteamine, 84 units/mL glucose oxidase, and 510 units/mL catalase five minutes before recording.

The samples were imaged using a Leica CTR6000 inverted fluorescence microscope with a Leica 100x, 1.47 numerical aperture oil-immersion objective. Illumination was achieved with solid-state lasers housed within a Spectral Integrated Light Engine (ILE) that controls light powers using a continuously variable neutral density filter and couples laser lines (405 nm, 488 nm, 561 nm and 647 nm) to a single output channel. The laser light was coupled to the objective using Spectral Borealis module and the samples were imaged in widefield, epifluorescence mode. Emission light was directed towards the cameras using a multi-line dichroic mirror and split into separate colour channels using a dichroic mirror with a cutoff of 640 nm. The emission light is filtered with the appropriate colour filters (40-60 nm bandwidth) and the images were simultaneously captured using two iXon Ultra DU-897U cameras in single-molecule mode (17 MHz readout mode, 3.30 µs vertical clock speed, electron-multiplying mode) with a frame size of 256×256 pixels (24.6 µm×24.6 µm field of view) and a binning mode of 1.

Selectively imaging the thin portions of the gel, a dSTORM acquisition was obtained by recording a 10,000 frame video (30 ms exposure) and illuminating the sample with 70% to 100% laser powers of the appropriate wavelength for the specific dye being probed (565 nm for Cy3 and 647 nm for Cy5). Short (2-3 second) bursts of 405 nm irradiation at 2% to 20% illumination power were used to reactivate the fluorophores (predominantly Cy5) as needed.

Image stacks were cropped to a time point of reasonable fluorophore densities. Localization-fitting analysis was accomplished using the ThunderSTORM ImageJ plugin[246] by applying a B-spline wavelet filter, approximating molecular positions through the local maximum method and calculating sub-pixel localizations by fitting a 2-dimesional integrated function using the weighted least squares method. Localizations with an unreasonable photon count, width, poor-fitting or high localization uncertainty were discarded. Sample drift was corrected using the cross-correlation method, and the super-resolution image was rendered with a magnification factor of 5 (19.2 nm pixel size) and slightly blurred with a lateral shift of 2 pixels.

3.3 Results and Discussion

Neutron Scattering:

We have previously shown that the thiosuccinimide-cross-linked PVP network and the hydrazone-cross-linked PNIPAM network form in a kinetically orthogonal manner, with no significant cross-reactivity occurring between the networks to produce an IPN structure[237]. Both the PNIPAM-hydrazone and PVP-thiosuccinimide networks gelled rapidly upon mixing, within 2-10 seconds for the PVP-thiosuccinimide network and 10-30 seconds for the PNIPAM-hydrazone network. Concurrent to gelation, the appearance of the gel converts from fully transparent in the precursor solutions to opaque on a time scale commensurate with the kinetics of gelation of the fastest component of the IPN system (PVP-thiosuccinimide at the polymer concentrations used), suggesting the formation of inhomogeneities on the length scale of visible light wavelengths. A similar switch in opacity was observed in semi-IPN hydrogels regardless of which polymer

constituted the entrapped polymer phase, again suggesting phase sequestration in these materials during gelation that could be probed using SANS techniques.

SANS analysis on the PVP and PNIPAM single network reference gels showed significant differences in nanostructure. In particular, the PNIPAM single network control exhibits a tendency toward a plateau at low *q* (Figure 3.3a), while the PVP single network control straight power law trend at low *q* (Figure 3.3b). Semi-IPNs prepared with both free PVP in a PNIPAM network (Figure 3.3c) and free PNIPAM in a PVP network (Figure 3.3d) show the same trends as their corresponding single network profiles, with an upward inflection observed in the PVP network semi-IPN and a decreasing slope observed in the PNIPAM network semi-IPN. This demonstrates that the cross-linked phase is the primary influence on the low-*q* scattering profile, as is expected given that the low-*q* scattering arises from larger network features. The Porod model (derived for networks characterized as mass fractals that lack the presence of static inhomogeneities[243]) fits the PVP scattering profile well, but fails to converge when tested against PNIPAM network scattering plots. In contrast, the squared Lorentzian model (designed to model such static inhomogeneities or domains[245, 247]) is able to accurately capture the trend towards a plateau seen at low *q* in PNIPAM networks, but cannot converge on the power law characteristic to PVP networks. Thus, the scattering profiles obtained suggest that PNIPAM networks form domains of static inhomogeneities, while PVP networks can be described as a mass fractal network (within the accessible length scale; it is possible static structures occur within the PVP network on larger length scales than the NG30 SANS can probe).

The correlation length (proportional to the inter-domain spacing) in the PNIPAM single network decreases slightly from 37 nm to 4.5 nm with heating from 25-45°C (Table 3.2). However, the semi-IPN consisting of free PVP inside a PNIPAM network exhibits a decrease in correlation length from 61 nm to 51 nm over the same temperature range (Table 3.2). Although a decrease in correlation length was expected for both these samples given the deswelling behaviour of PNIPAM above its LCST, the greater relative decrease of the correlation length observed in the semi-IPN was somewhat surprising, since our previous work showed bulk volume transitions in the semi-IPN formulation were smaller than those of the single network[237]. We hypothesize that the observed trend in correlation lengths may result from a combination of domain shrinkage and changes in the inter-domain spacing, with the semi-IPN more effectively sequestering water within the free PVP domains.

The Porod exponent (for which n=2 represents Gaussian chains and n=3 represents collapsed clusters[242]) was an intermediate 2.4 for the PVP single network and a more clustered 2.7 for the PNIPAM-in-PVP semi-IPN network (both assessed at 25°C, below the PNIPAM phase transition temperature; Table 3.2). This suggests the presence of PNIPAM polymers within the composite drives the structure toward additional clustering even when PNIPAM is not cross-linked, suggesting at least a moderate driving force for phase separation between the two polymers.

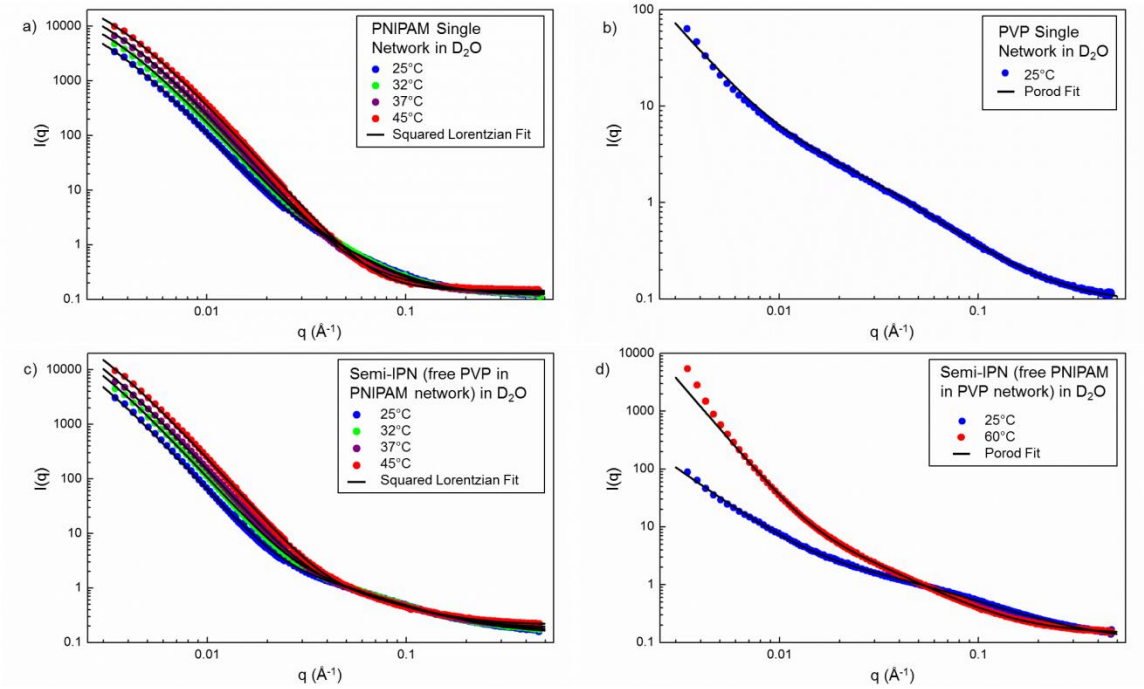

Figure 3.3: Scattering profiles for single networks and semi-IPNs in 10mM phosphate buffered saline prepared in D_2O: (a) Hydrazone-cross-linked poly(N-isopropylacrylamide) single network hydrogel as a function of temperature; (b) Thiosuccinimide-cross-linked poly(vinyl pyrrolidone) single network hydrogel (25°C); (c) Free PVP in a hydrazone cross-linked PNIPAM network semi-IPN network hydrogel (PVP-in-PNIPAM) as a function of temperature; (d) Free PNIPAM in a thiosuccinimide-cross-linked PVP semi-IPN network hydrogel (PNIPAM-in-PVP) as a function of temperature.

IPN hydrogels in which both PNIPAM and PVP are cross-linked showed neither of the inflection features at low *q* that correlated to the two previous fitting models. Instead, scattering from IPN's followed a smooth curve, with a broad and shallow peak overlapping at approximately q~0.015Å^{-1} developing at higher temperature (Figure 3.4a). Neither fitting model was able to capture both this small peak and the smooth trajectory of the low-*q* segment of the scattering plot. Reasoning that the scattering in the IPN would be a cumulative function of the contributions from the two constituent networks, a hybrid model (Equation 3.3) which combines scattering contributions from both a Porod function (for the PVP network) and a squared Lorentzian function (for the PNIPAM

network) was used to fit the full IPN data (Figure 3S.6 and Table 3S.7). In general, the Porod-component exponent was ~3.4 in the best set of fit values; while physically possible in systems that have experienced extreme clustering/collapse within certain scattering domains, this number is significantly higher than previously observed in hydrogels. Correspondingly, the squared Lorentzian correlation length decreases from 12 nm to 8 nm with increasing temperature (Table 3.2), suggesting significantly smaller average distances between the static inhomogeneities than in the PNIPAM single network.

Although the temperature-dependent peak at q~0.015 $Å^{-1}$ provides compelling evidence that PNIPAM is still driving static inhomogeneity formation and thermal collapse, the hybrid model is limited in its ability to quantitatively distinguish the scattering features attributable to the structure of each network. For example, the squared Lorentzian component of the hybrid model accounts for less than half of the total scattering intensity in the low-*q* portion of the scattering profile at all temperatures studied despite the fact that the single network controls indicated that PNIPAM scattered significantly more strongly than PVP at the low-*q* range (see Supporting Information Figure 3S.6 for comparisons of the contributions of the Porod and squared Lorentzian components to the hybrid fits for IPN's in D_2O). Thus, while the hybrid fits do give some insight into the structures formed in the IPN, further experimentation was deemed necessary to clarify the individual network structures inside the IPN.

To more clearly compare the structures formed by each polymer in the single network gels relative to the IPNs, SANS experiments with contrast matched samples were performed by preparing hydrogels with the deuterated analogue of PNIPAM to

selectively examine scattering contributions from each network. Figure 3.4 b and c show the index-matched SANS profiles for each network (with PNIPAM and PVP suppressed, respectively) over the full 25-45°C temperature range. Significant suppression of the matched-out component was effectively achieved in each case (see also Supporting Information, Figure 3S.1) using D_2O:H_2O ratios of 73:27 to hide the d7-PNIPAM network and 31:69 to hide the protonated PVP network. The temperature dependence of both index-matched samples further suggests success in isolating the scattering attributable to each network; no significant change in the scattering profile is noted as a function of temperature when the d7-PNIPAM phase was suppressed, while a clear temperature response was observed when the PVP phase was suppressed (Figure 3.4 b & c).

With d7-PNIPAM matched out (Figure 3.4b), the Porod model achieves reasonable fits with an exponent averaging 2.7 (see also Figure 3S.7 and Tables 3.2 & 3S.8). It should however be noted that the Porod model does not fully fit a small but distinct peak overlapped onto the Porod profile at q~0.007 $Å^{-1}$, an inflection that was not observed in the PVP single network control hydrogel (Fig. 3.3b). This feature could be interpreted either as interference arising from incomplete suppression of the PNIPAM scattering (as seen in the single network contrast matching control in Figure 3S.1, where the residual scattering from the matched-out PNIPAM phase still follows a squared Lorentzian type form, but lacks distinguishable temperature dependence), or as evidence for incorporation of a minority fraction of PVP into the PNIPAM-rich static domains that are themselves hidden at this contrast point.

With PVP matched out (“invisible”), the scattering profile for the remaining d7-PNIPAM network retains the temperature dependence normally associated with PNIPAM (Figure

3.4c). These data series also attained reasonable fits using the squared Lorentzian model previously found to effectively fit the PNIPAM single-network hydrogel, with the correlation length decreasing from 64 nm at 25°C to 40 nm at 45°C (see also Figure 3S.8 and Tables 3.2 & 3S.9). However, these values for the most part infer the plateau effect described in the squared Lorentzian model is occurring at q values below the experimental range, as no low-q plateau (like in the single network PNIPAM result) is observable in the accessible q range for the index-matched samples. Obtaining reasonable squared Lorentzian fits also depends on allowing the second Lorentzian term from Equation 3.2, representing fluid effects, to assume correlation lengths significantly larger than those seen in the PNIPAM single network control (Table 3S.8 vs. Table 3S.3). The correlation length in this term is meant to be proportional to network mesh size - while it is physically possible PVP interpenetration to increase the PNIPAM mesh size, the magnitude of the increase (see Table 3.2) suggests the squared Lorentzian model may not be realistically describing the behaviour of the IPN's with PVP matched out.

As such, both contrast supressed samples show some features inconsistent with the single network controls of those same networks; specifically, the small peak at q~0.007 $Å^{-1}$ in Figure 3.4b can be interpreted as some fraction of the PVP component entrapped in the (index-matched) PNIPAM-rich domains, while the suppression of the plateau feature seen in PNIPAM single networks within the studied q range in Figure 3.4d can be interpreted as mixing of some of the d7-PNIPAM into (index-matched) PVP clusters. To test this interpretation, the hybrid model was used to fit the contrast matched IPN data, looking for evidence of some of each network type being 'dragged' into the structural configuration expected for each index-matched IPN network.

Scattering curves for IPN networks in which the d7-PNIPAM phase was suppressed fit well to the hybrid model (Figure 3S.9 and Table 3S.10; fit traces also shown on Figure 3.4b), showing considerable improvement in the fitting error metrics compared with the unmodified Porod model. Specifically, inclusion of the squared Lorentzian term facilitates accurate fitting of the small feature at q~0.007. As expected, the Porod contribution (used to fit the PVP single network gel) dominated scattering fits in this system, with the exponent virtually unchanged (at 2.75) across all temperatures (Table 3.2). Across the temperature series, the contribution of the Porod component to the total hybrid fit grows from low to high temperature, while the importance of the squared Lorentzian term shrinks (see Supporting Information Figure 3S.9 for a specific breakdown of Porod and squared Lorentzian term contributions to hybrid fits). Furthermore, the squared Lorentzian component's correlation length shifted from 22 nm to 18 nm as the temperature was increased from 25-45°C (Table 3.2). The temperature dependence in this correlation length strongly indicates that the feature in question arises at least partly due to entrapment of some PVP into the PNIPAM-dominated static inhomogeneities that is physically compressed by the temperature-responsive collapse of the surrounding PNIPAM network.

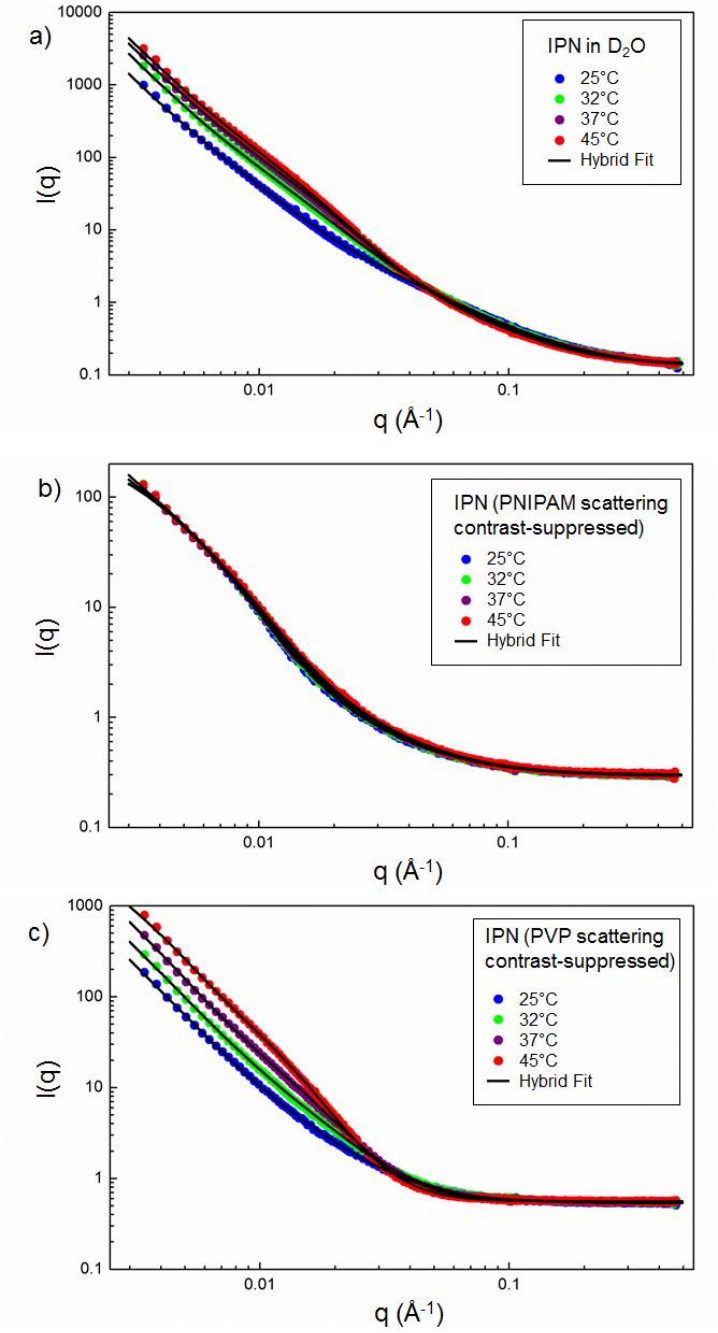

Figure 3.4: Scattering profiles for IPN hydrogels: (a) PVP/PNIPAM IPN hydrogels as a function of temperature in D_2O; (b) Temperature response of PVP/d7-PNIPAM IPN hydrogels in which the PNIPAM network is index matched out (at 31:69 D_2O:H_2O); (c) Temperature response of PVP/d7-PNIPAM IPN hydrogels in which the PVP network is index matched out (at 73:27 D_2O:H_2O).

The hybrid model is also successful at modelling the scattering profiles of IPNs in which the PVP network is matched out (Figure 3S.10 and Table 3S.11; fit traces also shown on Figure 3.4c); this is particularly true the low-*q* linear region of the scattering plot, for which the squared Lorentzian model alone assumed inflection points at *q* values below the experimental range. With increasing temperature, the correlation length parameter in the Lorentzian component of the hybrid model decreases from 53 nm to 39 nm, considerably closer to the values obtained in the PNIPAM single network fits (37 nm to 35 nm) than the parameter values extracted from using the squared Lorentzian model on the same index matched IPN data (64 nm to 40 nm) (Table 3.2). Interestingly, the Porod component (with exponents in the 2.6-2.8 range) contributes a surprising fraction of the overall scattering intensity observed at lower temperatures, although the growing Lorentzian contribution at higher temperatures (as the PNIPAM network collapses) reduces the importance of the Porod contribution to the fit (see Supporting Information Figure 3S.10 for component contribution breakdowns in IPN's with PVP contrast suppressed). Mechanistically, given the approximately 90 second gelation time for hydrazone cross-linking in the single network PNIPAM hydrogels, this result is physically consistent with the possibility of significant mixing of the PNIPAM-Hzd and PNIPAM-Ald prepolymers into the PVP-rich clustered fractal phase prior to full gelation of the PNIPAM network followed by physical entrapment of those precursor polymers in this mixed state. This interpretation is also consistent with the Porod component of the hybrid fits of total IPN scattering from D_2O (when both networks are visible) contributing a more significant fraction of the fit than expected from summation of the single network scattering intensities; that is, mixing with the PVP network appears to be partially disrupting static inhomogeneity formation by the PNIPAM network.

Table 3.2: Summary of key fitting parameters for SANS data

	T (°C)	Model Used	Porod exponent	Squared Lorentzian Correlation Length (nm)	Fluid Term Correlation Length (nm)	Fluid term exponent
PVP Single Network in D2O	25	Porod	2.4	-	3.7	1.7
Semi-IPN (PVP in PNIPAM Network) in D2O	25	Porod	2.4	-	2.1	1.6
	60		4.0	-	4.8	1.9
PNIPAM Single Network in D2O	25	Squared Lorentzian	-	37	3.0	2.3
	32		-	36	2.7	2.4
	37		-	36	1.1	3.0
	45		-	35	1.0	3.1
Semi-IPN (PVP in PNIPAM Network) in D2O	25	Squared Lorentzian	-	61	2.3	1.8
	32		-	58	2.3	1.9
	37		-	55	1.7	2.1
	45		-	51	1.2	2.3
IPN in D2O	25	Hybrid	3.5	12	4.4	1.9
	32		3.4	8.3	3.8	1.9
	37		3.5	8.2	2.1	2.0
	45		3.4	8.2	1.3	2.4
IPN (PNIPAM Scattering Suppressed, at 73 D_2O : 27 H_2O)	25	Porod	2.8	-	1.5	2.4
	32		2.8	-	1.6	2.3
	37		2.7	-	1.8	1.9
	45		2.7	-	2.0	1.7
IPN (PVP Scattering Suppressed, at 31 D_2O :69 H_2O)	25	Squared Lorentzian	-	21	4.5	3.0
	32		-	21	4.1	3.0
	37		-	22	4.0	3.0
	45		-	22	3.4	3.0
IPN (PNIPAM Scattering Suppressed, at 73 D_2O : 27 H_2O)	25	Hybrid	2.8	22	4.8	1.9
	32		2.8	21	4.5	1.9
	37		2.7	20	4.1	1.9
	45		2.7	18	3.5	2.0
IPN (PVP Scattering Suppressed, at 31 D_2O :69 H_2O)	25	Hybrid	2.7	53	6.9	2.2
	32		2.7	46	7.1	2.7
	37		2.8	45	7.2	3.7
	45		2.6	39	8.8	4.0

Of note, in the corresponding semi-IPN scattering profiles (Figure 3.3 c-d), the hybrid model is not necessary to fit the scattering curves. While mixing may occur similarly on the time scale of the gelation of the one network in the semi-IPN hydrogels, the entrapped free polymer maintains great mobility sufficient to allow phase separation in a way not possible in the full IPN samples, minimizing the effect of the second polymer phase on the types of structures formed within the gel.

To further validate our interpretation of the phase structure of these IPN hydrogels, super-resolution fluorescence microscopy was performed on PVP/PNIPAM IPN hydrogels. The dSTORM technique probes length scales slightly larger than those of SANS, with each reconstructed pixel in the images representing 19.6 nm in our configuration; however, the images show generally similar tendencies for each network type as suggested by the SANS experiments. The Cy5-PNIPAM network (Figure 3.5a) forms smaller and more distributed domains or clusters consistent with the formation of smaller static inhomogeneities in the network structure (largely insensitive to the labelling density and use of fiducial markers; see Figure 3S.11). In contrast, the Cy3-PVP network (Figure 3.5b) appears to organize in clusters with a significant distribution of sizes and shapes, as would be expected if the conclusion from the SANS data that the PVP network forms predominantly clustered mass fractals held true on larger length scales. Note that the necessity of using a higher labelling density of Cy3 (on PVP) than Cy5 (on PNIPAM) to achieve a good signal-to-noise ratio on each channel for each frame of the acquisition stack does have the potential to bias the result in terms of PVP only appearing to show larger clusters simply because it is more heavily labelled. However, the spaces between clusters with either no fluorophore signal or scattered, individual fluorophore signals are both also more pronounced in Figure 3.5a (Cy5

labeled) than Figure 3.5b (Cy3 labeled). As such, this strong cluster-to-background contrast in both reconstructed localization plots suggests the observed difference in cluster size and spatial frequency accurately reflects the underlying features of the two networks.

The IPN sample (Figure 3.5c) appears to preserve the characteristic features of both single network samples, with generally discrete smaller Cy5-PNIPAM domains in a field of larger, extended, and to some extent interconnected Cy3-PVP clusters. Interestingly, while the majority of the signals from each network are discrete (as would be expected in a conventional IPN in which the two interpenetrating phases are fully phase-separated), there is also clear evidence of PVP clusters also containing signal associated with PNIPAM. Such an observation is consistent with the SANS data that suggested the presence of PVP-rich mass fractal clusters containing a significant fraction of intermixed PNIPAM. However, relatively few of the discrete PNIPAM structures show evidence of any smaller clusters of PVP co-localized. Indeed, at high magnifications of the IPN image (Fig. 3.5d), a significant minority of the larger Cy3-PVP clusters contain smaller pockets of overlapping Cy5-PNIPAM, but the discrete Cy5-PNIPAM domains much less frequently contain overlapped Cy3-PVP signals (i.e. it is more common to see large Cy3-PVP clusters with smaller co-localizations of Cy5-PNIPAM than vice versa). Stacking in the vertical direction was deemed unlikely to account for the observed instances of overlapping structures, due to structures of both labelling types being found in the same focal plane.

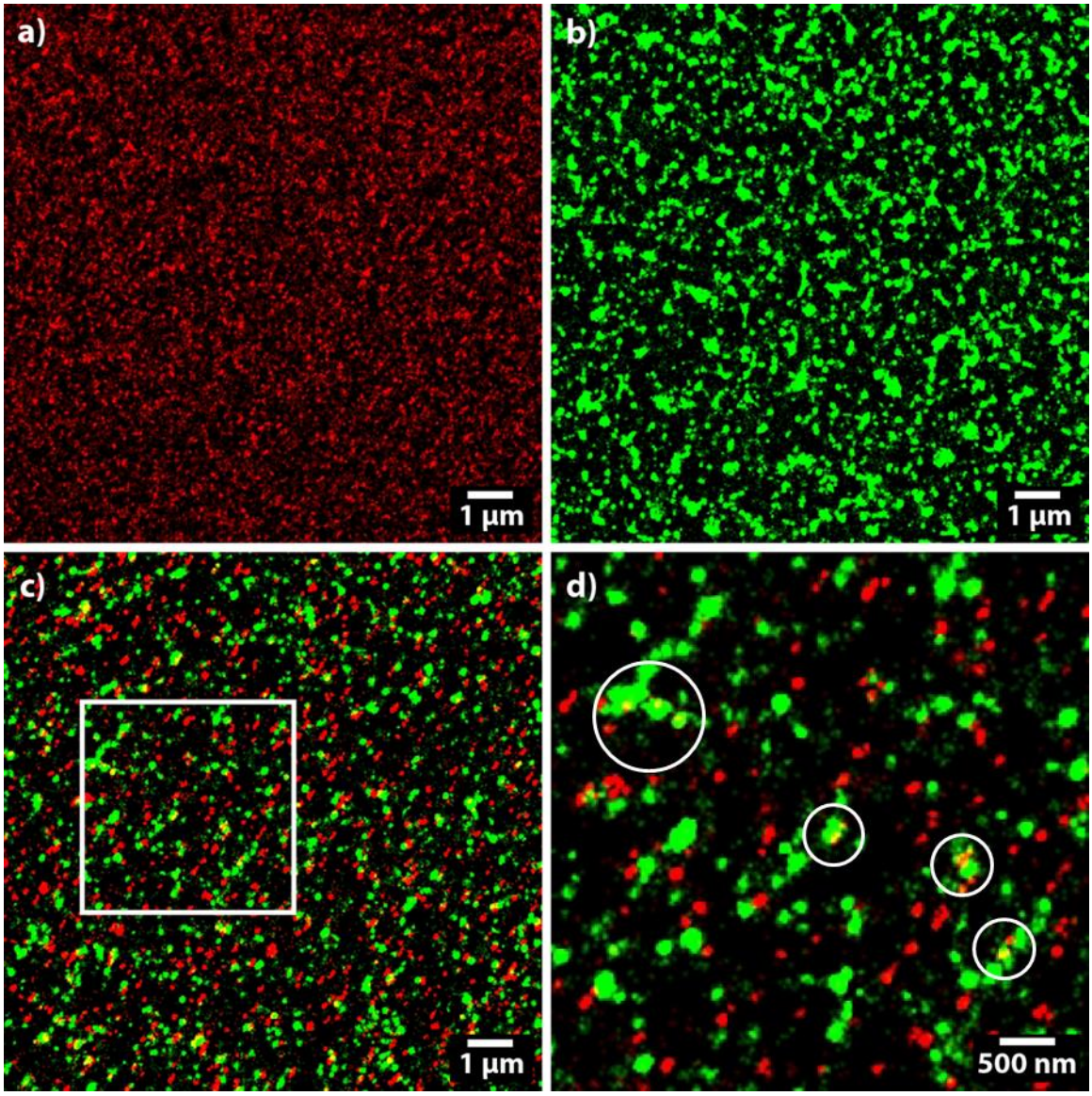

Figure 3.5: dSTORM reconstructed optical images of Cy3-PVP/Cy5-PNIPAM single network and IPN hydrogels (all false-colour representations of calculated fluorophore localizations): (a) PNIPAM single network (note that large dots surrounded by bleached areas are due to bleed-through of green-fluorescent fiducial beads used for image stack alignment onto the red detector channel); (b) PVP single network; (c) PVP/PNIPAM IPN; (d) magnification of inset region of IPN, highlighting several instances of PNIPAM domains within larger PVP features (circled).

This is consistent with the index-matched SANS fitting, in which the scattering plot of IPN's matched to hide PVP while showing d7-PNIPAM suggest a reduced scattering contribution from static domains as compared to PNIPAM single networks controls. If the pattern of PNIPAM incorporation into PVP clusters seen at the mesoscale with dSTORM imaging also extends to the length scale probed by SANS, this suggests that the effects seen in SANS might result not from a generally consistent extent of mixing throughout the network, but from the frequency of PNIPAM-rich domains occurring within larger PVP clusters vs. in isolation.

This work represents, to our knowledge, the first instance of contrast-matching SANS and super-resolution optical techniques being combined to probe the meso- and nano-scale structure of a hydrogel composite. By combining conventional SANS, index-matched SANS in which each network is individually visible (hiding the other network), and dSTORM super-resolution fluorescence microscopy, a coherent picture of the structure of these hydrazone cross-linked PNIPAM/thiosuccinimide cross-linked PVP interpenetrating network hydrogels emerges. Phase separation appears to occur faster than the timescale of gelation, leading to the creation of interlocking networks that form relatively (but not totally) independently to create nanoscale morphologies similar to those observed in a corresponding single network gel (i.e. analogous to a conventional IPN system). However, the relatively fast gelation kinetics appear to also lead to the entrapment of a fraction of one phase in another, primarily some PNIPAM (the slower gelling component of the gelling pair) entrapped inside the (faster-gelling) PVP-rich fractal-like domains. This domain structure may present significant interest in the context of controlled release from these networks given that drugs with a high affinity for the PNIPAM phase (particularly if loading is done at temperatures above the phase

transition of the PNIPAM phase) may be released at two independent rates: one corresponding to release from the phase-separated PNIPAM network and another corresponding to release from the PNIPAM phase entrapped inside the PVP clusters. The fully injectable nature of this particular IPN, in contrast to previously reported IPNs, also makes it more amenable to potential translation to biomedical applications if the anticipated dual-phase release kinetics were achieved, as surgical implantation would not be required. Understanding this morphology may also give insight into the mechanics of these IPNs, as the minority population of interlocked structures inside a largely phase-separated matrix suggests a significant possible role for these mixed clusters in the observed enhancement of mechanical strength of the IPN relative to the two single networks alone[237].

3.4 Conclusions

Small angle neutron scattering and super-resolution fluorescence microscopy have been applied to investigate the internal morphologies of fully injectable interpenetrating network hydrogels comprised of thiosuccinimide cross-linked poly(vinyl pyrrolidone) and thermoresponsive hydrazone cross-linked poly(N-isopropylacrylamide). Investigations at both the nanoscale (SANS) and the mesoscale (dSTORM) suggest phase segregation into discrete populations of predominantly PNIPAM, predominantly PVP, and mixed domains, with the trend of PVP-rich structures containing more PNIPAM than vice versa apparent across both scale ranges. Such a morphology is consistent with the relative kinetics of gelation and phase separation in these hydrogels, as (unlike the semi-IPN controls, in which no significant mixed domains were visible through SANS fitting)

gelation can effectively freeze the diffusion of a fraction of one polymer out of a phase rich in the other polymer before complete phase separation can occur. We anticipate that understanding this domain structure can be used to optimize the drug release kinetics and mechanical enhancements possible with such fully injectable IPN systems. Furthermore, this work suggests that the combination of dSTORM and (index matched) SANS has significant potential to better understand the internal morphologies of IPN hydrogels across multiple length scales and thus design more effective IPN structures targeted to applications.

Acknowledgements

This work utilized facilities supported in part by the National Science Foundation under Agreement No. DMR-0944772. We acknowledge the support of the National Institute of Standards and Technology, US Department of Commerce, in providing the neutron facilities used in this work.

We also thank Yimin Mao, NCNR instrument scientist for the NG30 SANS, for supervising our research visit as well as all the other NCNR staff who helped facilitate our experiments.

Appendix 3S: Supporting Information to Chapter 3
Fitting parameters and X^2 Values for Hydrazone-Thiosuccinimide IPN SANS models.

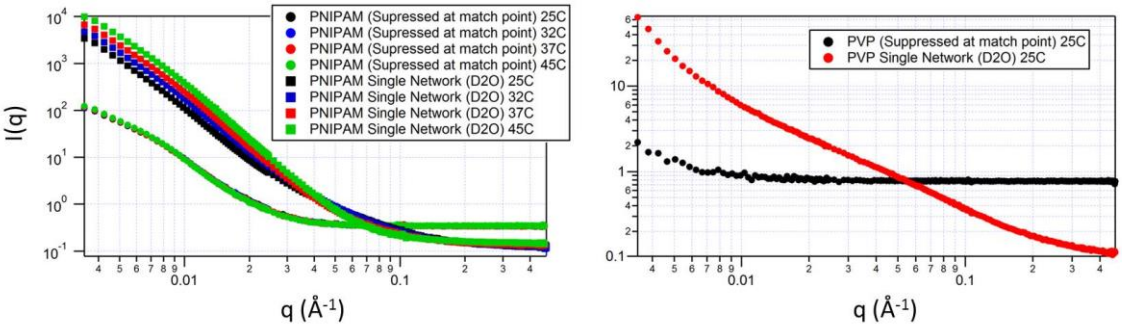

Figure 3S.1: Greater than order-of-magnitude suppression of low *q* scattering in contrast matched single network hydrogels.

Table 3S.1: PVP in D_2O Porod model fitting parameters

PVP D_2O	PVP SH-Mal 25°C
Porod Scale	6.54E-05
Porod Exponent	2.39
Lorentzian Scale	2.74
Lor Screening Length [Å]	37.2
Lorentzian Exponent	1.71
Bgd [1/cm]	8.83E-02
X^2	1580
Sqrt(X^2/N)	2.57

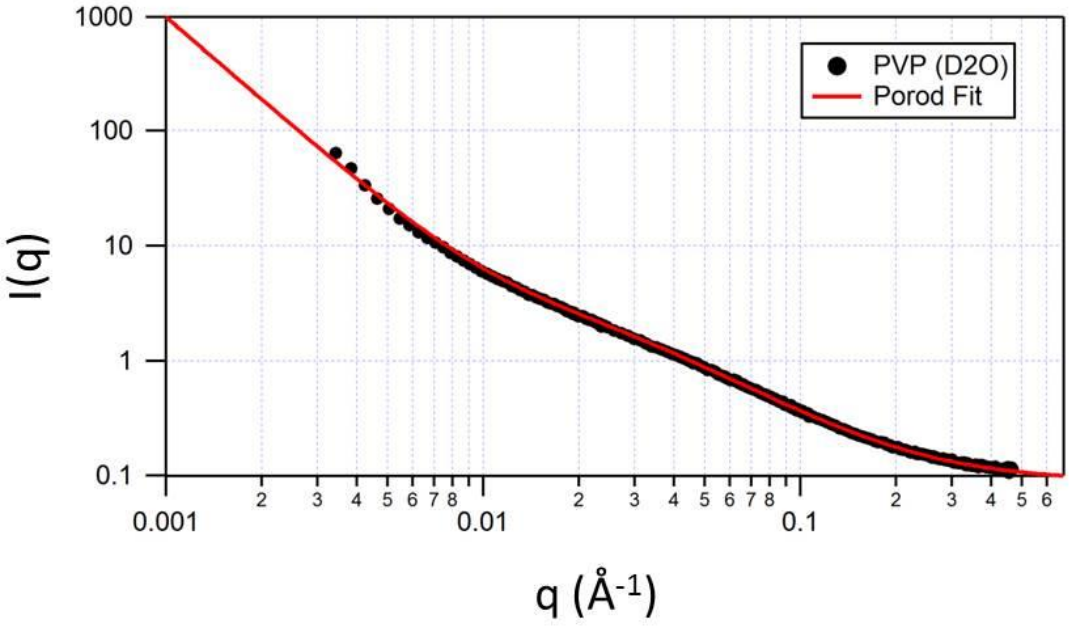

Figure 3S.2: Raw scattering curve and Porod model fit of thiosuccinimide-cross-linked PVP single network (9 wt%) in D_2O (25°C)

Table 3S.2: PVP in D_2O Porod model fitting parameters

PNIPAM-in-PVP semi-IPN	25°C	60°C
Porod Scale	8.25E-05	3.07E-07
Porod Exponent	2.42	4.00
Lorentzian Scale	1.68	5.73
Lor Screening Length [A]	21.0	48.1
Lorentzian Exponent	1.57	1.94
Bgd [1/cm]	9.83E-02	1.41E-01
X^2	762.5	1417.9
Sqrt(X^2/N)	1.79	2.44

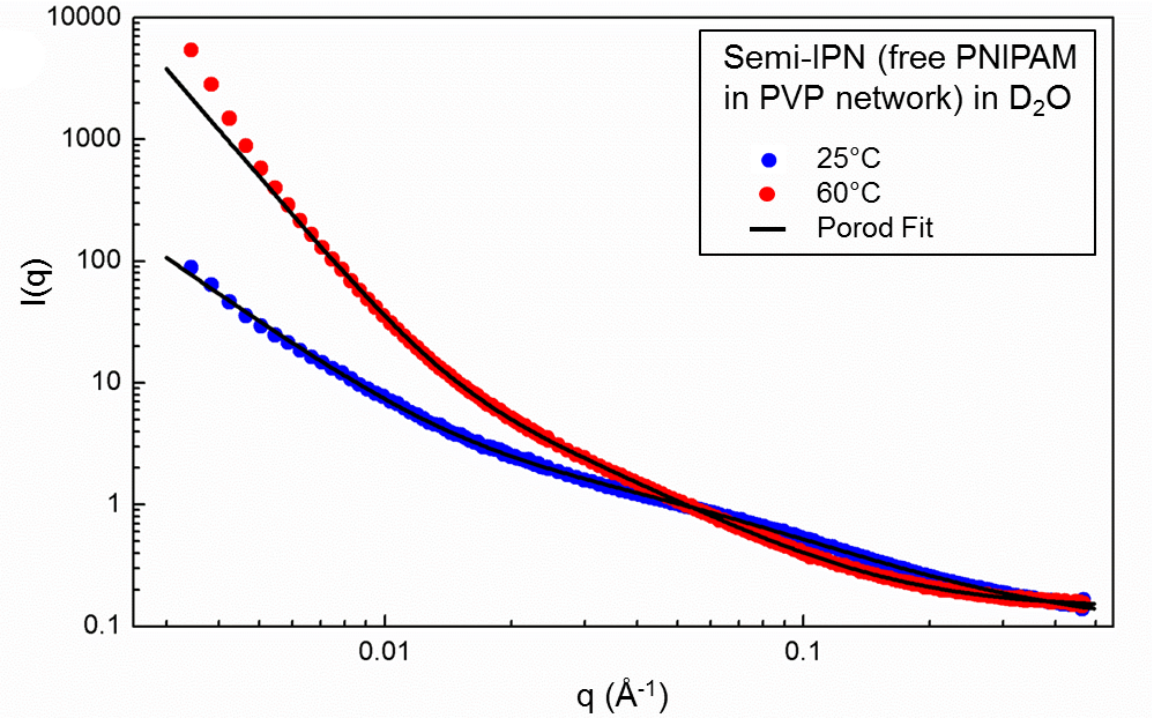

Figure 3S.3: Raw scattering curve and Porod model fit of semi-IPN of free PNIPAM in thiosuccinimide-cross-linked PVP network (9 wt%) in D_2O. Porod model fits reasonably at 25°C, but poorly at low *q* for high temperature.

Table 3S.3 PNIPAM single network in D_2O squared Lorentzian model fitting parameters

PNIPAM D_2O	25 °C	32 °C	37 °C	45 °C
Lorentzian #1 scale	2.43E+04	3.28E+04	4.58E+04	5.90E+04
Correlation length #1 [A]	374	357	357	345
Lorentzian #2 scale	1.95E+00	1.32E+00	1.60E-01	2.28E-02
Correlation length #2 [A]	29.8	26.6	11.2	10.0
Lorentzian #2 exponent	2.34	2.44	3.00	3.10
Bkg [1/cm]	0.121	0.126	0.136	0.145
X^2	1040	1170	1240	7670
Sqrt(X^2/N)	2.07	2.18	2.27	5.64

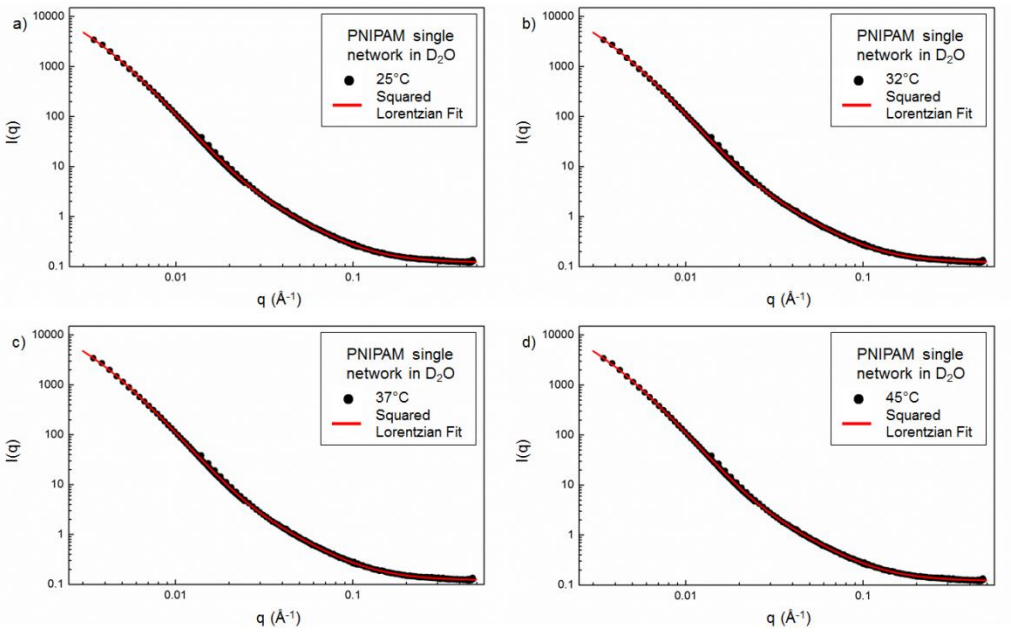

Figure 3S.4: Raw scattering curves and squared Lorentzian model fits of hydrazone-cross-linked PNIPAM single network hydrogels in D_2O as a function of temperature: (a) 25°C; (b) 32°C; (c) 37°C; (d) 45°C.

Table 3S.4: Semi-IPN in D_2O squared Lorentzian model fitting parameters

Semi-IPN D_2O	25 °C	32 °C	37 °C	45 °C
Lorentzian #1 scale	8.90E+04	1.25E+05	1.43E+05	1.64E+05
Correlation length #1 [A]	606	580	550	505
Lorentzian #2 scale	1.79	1.67	1.03	0.581
Correlation length #2 [A]	22.9	22.6	17.1	12.2
Lorentzian #2 exponent	1.79	1.85	2.05	2.35
Bkg [1/cm]	0.143	0.159	0.183	0.212
X^2	2210	1910	1360	3120
Sqrt(X^2/N)	3.00	2.80	2.37	3.60

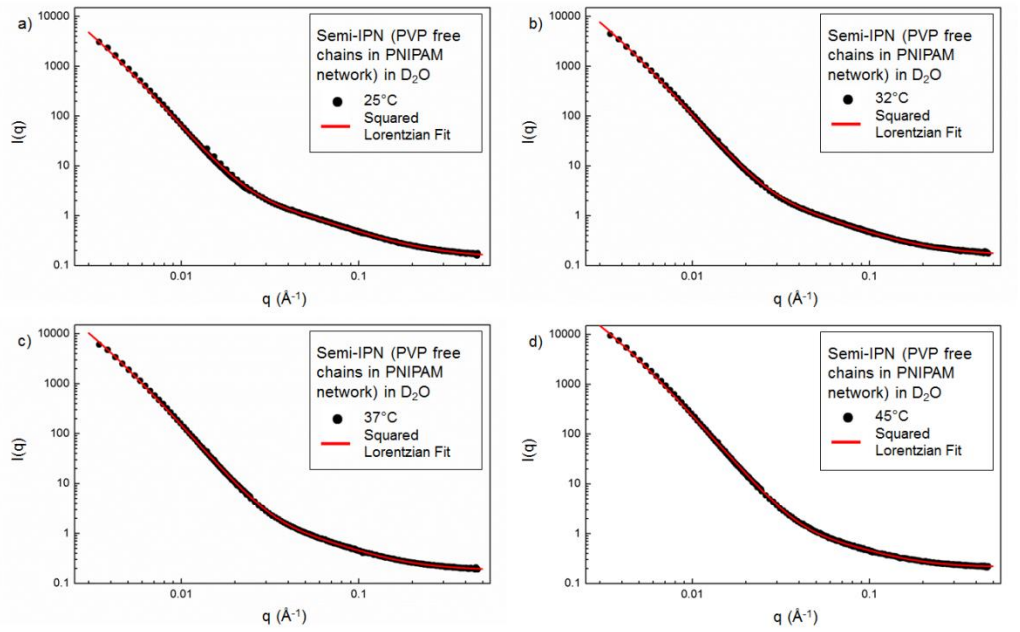

Figure 3S.5: Raw scattering curves and squared Lorentzian model fits of the semi-IPN control of unfunctionalized PVP trapped inside a cross-linked PNIPAM network hydrogels in D_2O as a function of temperature: (a) 25°C; (b) 32°C; (c) 37°C; (d) 45°C.

Table 3S.5: d7-PNIPAM single network at match point to suppress its scattering (confirmation of scattering suppression) squared Lorentzian model fitting parameters

PNIPAM (Index 2 - matched out)	25 °C	32 °C	37 °C	45 °C
Lorentzian #1 scale	257	268	280	281
Correlation length #1 [A]	212	213	217	215
Lorentzian #2 scale	0.192	0.139	0.129	0.0426
Correlation length #2 [A]	44.6	41.3	39.9	33.7
Lorentzian #2 exponent	3.00	3.00	3.00	3.00
Bkg [1/cm]	0.343	0.342	0.341	0.347
X^2	438.6	393.4	405.6	572.7
Sqrt(X^2/N)	1.36	1.29	1.31	1.55

Table 3S.6: PVP at match point to suppress its scattering (confirmation of scattering suppression) Porod model fitting parameters

Porod	PVP SH-Mal Index 1 (Matched out)
Porod Scale	2.78E-07
Porod Exponent	2.70
Lorentzian Scale	0.138
Lor Screening Length [A]	112
Lorentzian Exponent	1.92
Bgd [1/cm]	0.774
X^2	250
Sqrt(X^2/N)	1.02

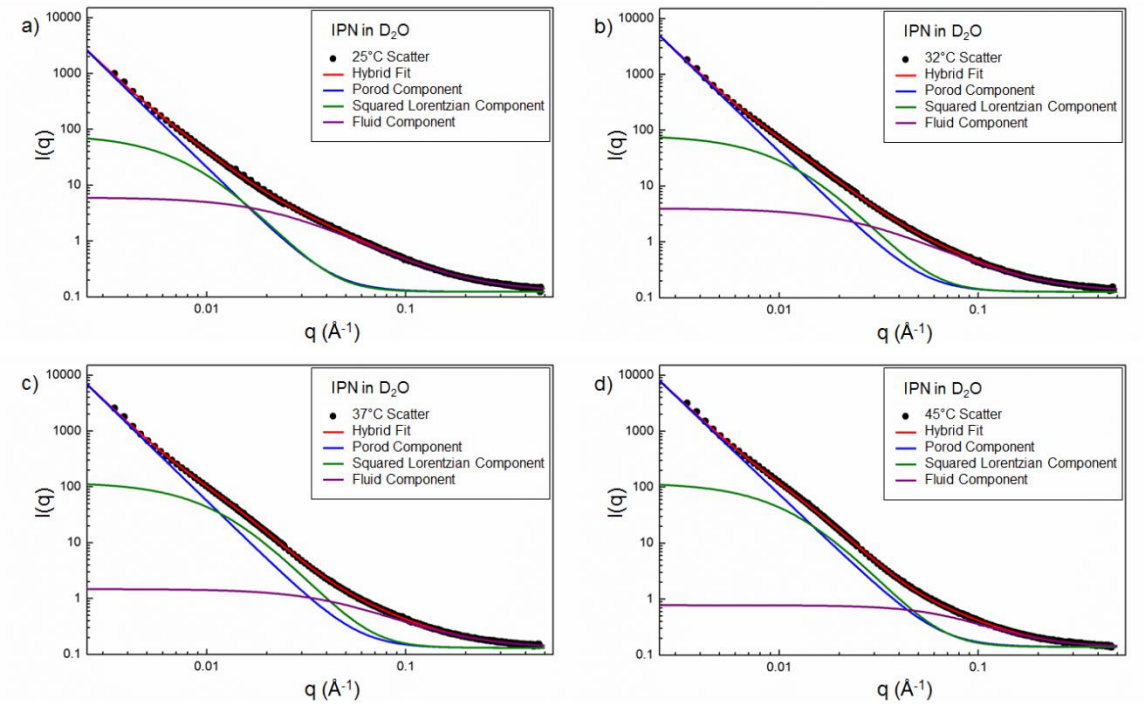

Figure 3S.6: Raw scattering curves and hybrid model fits (with component breakdowns) of PNIPAM-PVP IPN hydrogels in D_2O as a function of temperature: (a) 25°C; (b) 32°C; (c) 37°C; (d) 45°C.

Table 3S.7: IPN in D_2O hybrid model fitting parameters

Combined IPN D_2O	25°C	32°C	37°C	45°C
Porod Scale	2.39E-06	5.17E-06	6.74E-06	1.35E-05
Porod exponent	3.47	3.45	3.46	3.37
Static Domains scale	80.5	81.0	121	120
Domains Length 1	115	83.2	81.8	81.7
Fluid scale	5.93	3.87	1.35	0.639
Fluid Correlation Length	44.2	38.0	21.2	13.1
Fluid exponent expon	1.88	1.88	1.97	2.39
Incoherent Bgd (cm-1)	0.124	0.128	0.131	0.140
X^2	828	482	363	1430
Sqrt(X^2/N)	1.84	1.41	1.22	2.44

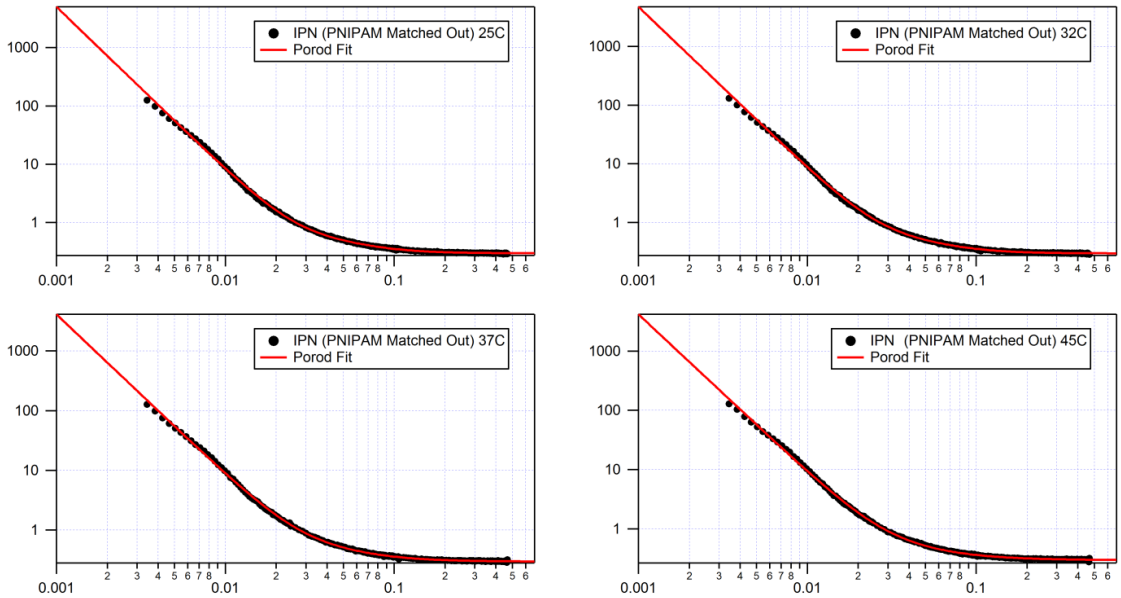

Figure 3S.7: Raw scattering curves and Porod model fits of IPN hydrogels with d7-PNIPAM scattering suppressed by contrast matching as a function of temperature: (a) 25°C; (b) 32°C; (c) 37°C; (d) 45°C. The Porod model does not describe the small but distinct feature seen below q=0.01 Å^{-1}.

Table 3S.8: IPN using d7-PNIPAM with PNIPAM scattering contrast-suppressed Porod model fitting parameters

IPN - PNIPAM Matched Out	25°C	32°C	37°C	45°C
Porod Scale	2.09E-05	2.61E-05	3.66E-05	4.23E-05
Porod Exponent	2.79	2.75	2.68	2.66
Lorentzian Scale	0.170	0.173	0.182	0.204
Lor Screening Length [A]	15.4	15.8	17.6	20.3
Lorentzian Exponent	2.41	2.33	1.95	1.67
Bgd [1/cm]	0.297	0.295	0.296	0.297
X^2	1350	1290	1370	1400
Sqrt(X^2/N)	2.39	2.34	2.41	2.42

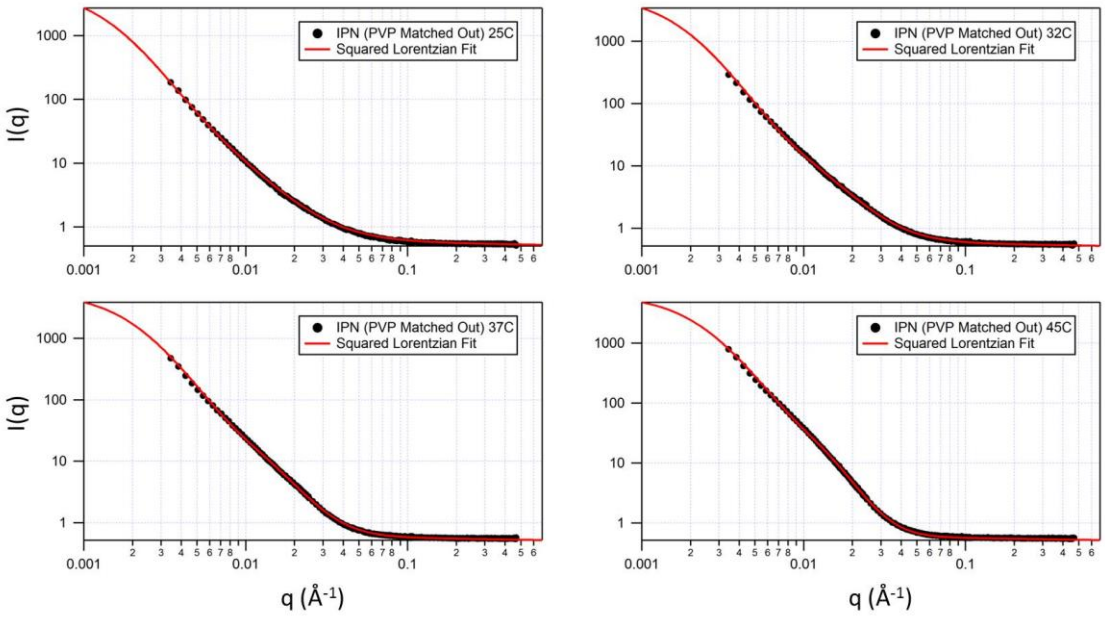

Figure 3S.8: Raw scattering curves and squared Lorentzian model fits of IPN hydrogels with PVP scattering suppressed by contrast matching as a function of temperature: (a) 25°C; (b) 32°C; (c) 37°C; (d) 45°C. This model on assuming a plateau feature below the *q* range of the NG30 SANS instrument to fit the data collected.

Table 3S.9: IPN using d7-PNIPAM with PVP scattering contrast-suppressed squared Lorentzian model fitting parameters

IPN- PVP Matched Out	25 °C	32 °C	37 °C	45 °C
Lorentzian #1 scale	5.30E+03	5.52E+03	5.59E+03	6.36E+03
Correlation length #1 [A]	636	522	450	396
Lorentzian #2 scale	36.2	13.0	14.2	17.6
Correlation length #2 [A]	193	88.5	77.3	75.6
Lorentzian #2 exponent	2.20	2.68	3.24	4.12
Bkg [1/cm]	0.534	0.552	0.559	0.564
X^2	355	712	1080	1590
Sqrt(X^2/N)	1.23	1.74	2.14	2.58

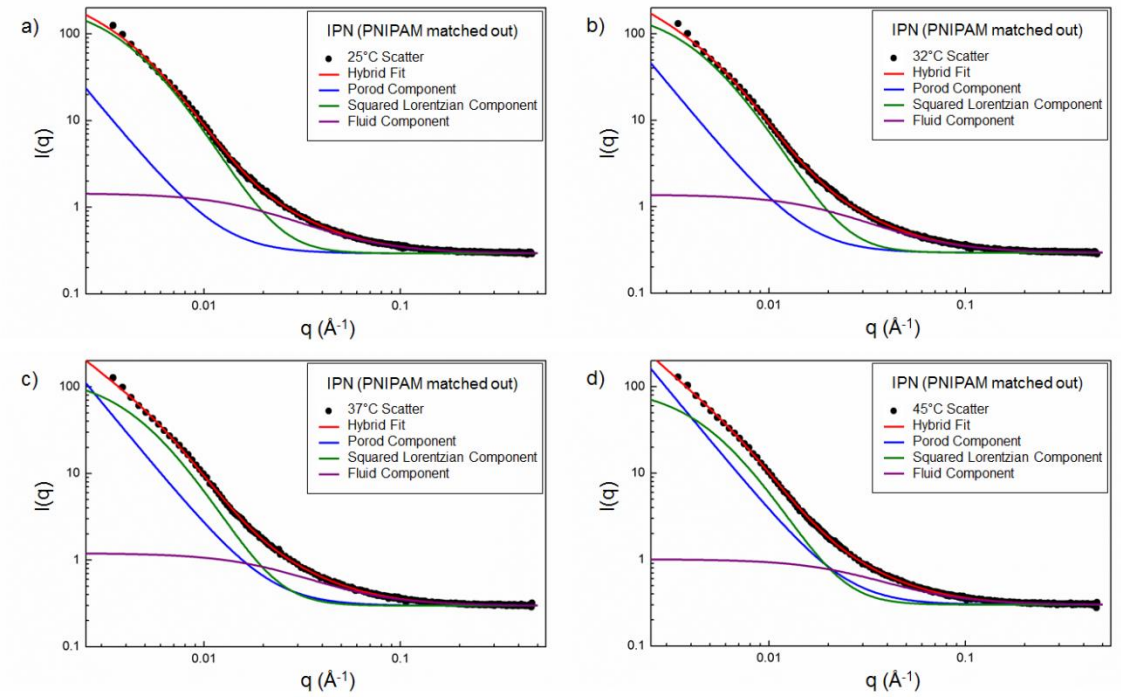

Figure 3S.9: Raw scattering curves and hybrid model fits (with component breakdowns) of IPN hydrogels with d7-PNIPAM scattering suppressed by contrast matching as a function of temperature: (a) 25°C; (b) 32°C; (c) 37°C; (d) 45°C.

Table 3S.10: IPN using d7-PNIPAM with PNIPAM scattering contrast-suppressed hybrid model fitting parameters

IPN - PNIPAM Matched Out	25°C	32°C	37°C	45°C
Porod Scale	1.62E-06	3.17E-06	7.65E-06	1.12E-05
Porod exponent	2.75	2.75	2.75	2.75
Static Domains scale	238	202	140	102
Domains Length 1	219	209	197	181
Fluid scale	1.16	1.09	0.906	0.708
Fluid Correlation Length	48.3	45.2	41.3	35.2
Fluid exponent expon	1.89	1.93	1.94	2.00
Incoherent Bgd (cm-1)	0.294	0.294	0.298	0.301
X^2	410	416	427	350
Sqrt(X^2/N)	1.31	1.33	1.35	1.21

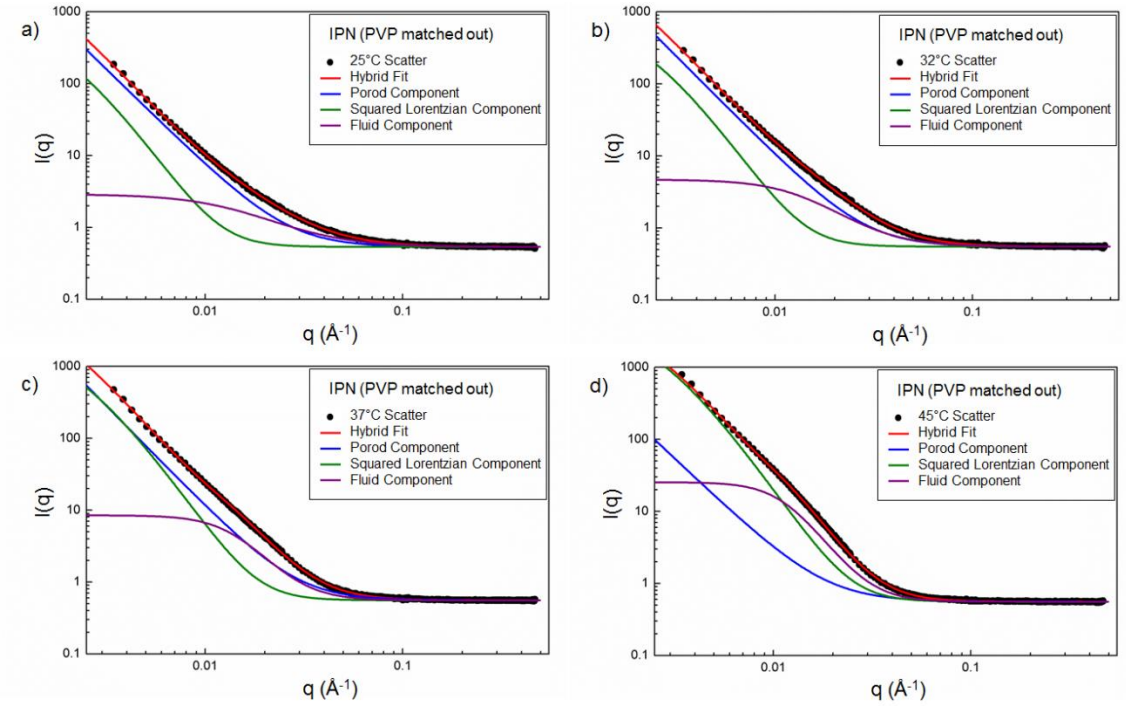

Figure 3S.10: Raw scattering curves and hybrid model fits (with component breakdowns) of IPN hydrogels with PVP scattering suppressed by contrast matching as a function of temperature: (a) 25°C; (b) 32°C; (c) 37°C; (d) 45°C.

Table 3S.11: IPN using d7-PNIPAM with PVP scattering contrast-suppressed hybrid model fitting parameters

IPN- PVP Matched Out	25°C	32°C	37°C	45°C
Porod Scale	3.14E-05	3.20E-05	2.81E-05	1.70E-05
Porod exponent	2.68	2.75	2.80	2.60
Static Domains scale	864	987	2560	4910
Domains Length 1	526	456	447	387
Fluid scale	2.36	4.14	7.92	24.9
Fluid Correlation Length	69.0	71.0	71.8	87.8
Fluid exponent expon	2.15	2.72	3.68	4.00
Incoherent Bgd (cm-1)	0.536	0.552	0.558	0.560
X^2	322	356	609	586
Sqrt(X^2/N)	1.17	1.23	1.61	1.57

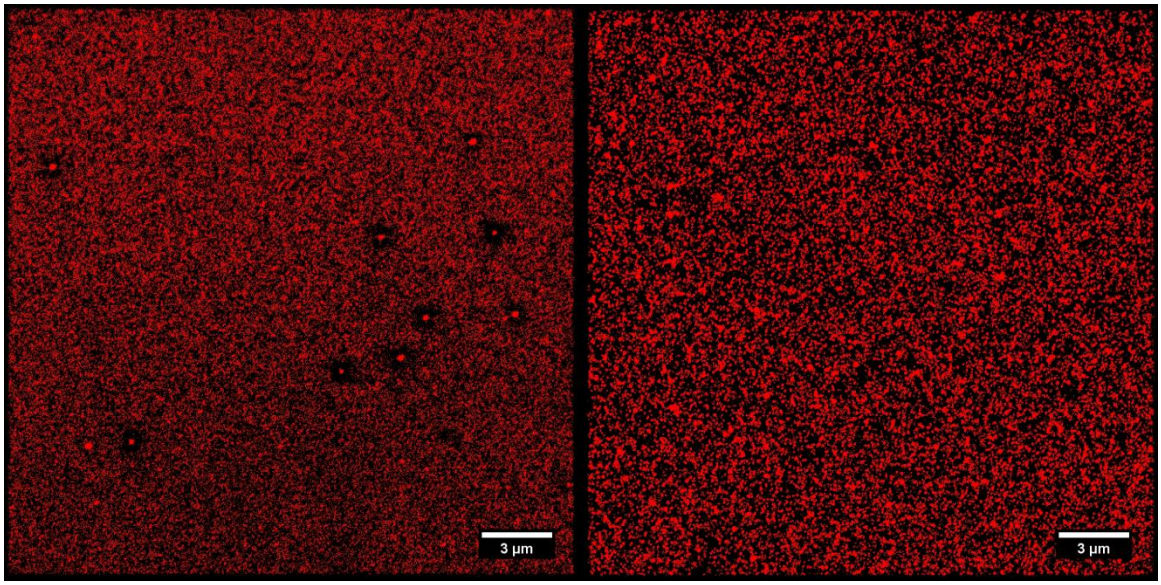

Figure 3S.11: Comparison of dSTORM reconstructed images of PNIPAM single networks using 1 Cy5 per 500 residues with fiducial markers (left) to 1:50 labelling without markers (right). Higher labelling leads to slightly larger cluster sizes (although still markedly smaller than Cy3-PVP, and lacking the extended structure), and use of the fiducial markers does not substantially affect localization accuracy.

Chapter 4: Nanostructure of Injectable Poly(N-Isopropylacrylamide) / Poly(vinyl pyrrolidone) Interpenetrating Network Hydrogels Formed via Hydrazone / Disulfide Cross-Linking: A Small-Angle Neutron Scattering Study

Preface

This chapter describes SANS experiments analogous to those of Chapter 3, but using slower disulfide cross-linking for the PVP network, and varying the molecular weight and functionalization density of the PVP-SH used as its precursor. The SANS investigation is complete, but several smaller experiments – described in the Conclusions and Future Work section – with hydrazone / disulfide IPN's are pending to improve the impact of a final submitted paper based on this chapter.

Trevor Gilbert[1], Richard Alsop[2], Mouhanad Babi[3], José Moran-Mirabal[3], Maikel Rheinstadter[2] and Todd Hoare*[1]

[1] Department of Chemical Engineering, McMaster University, 1280 Main St. W, Hamilton, Ontario, Canada L8S 4L7

[2] Department of Physics, McMaster University, 1280 Main St. W, Hamilton, Ontario, Canada L8S 4L7

[3] Department of Chemistry, Mc Master University, 1280 Main St. W, Hamilton, Ontario, Canada L8S 4L7

Abstract

A fully injectable interpenetrating network hydrogel comprised of hydrazone cross-linked poly-(N-isopropylacrylamide) (PNIPAM) combined with disulfide cross-linked poly(vinyl pyrrolidone) (PVP) is reported for the first time, and characterized using small angle neutron scattering with and without contrast matching to allow for individual analysis of the microstructure of each interpenetrating phase. The PVP network properties (primarily, gelation times) were varied systematically by changing the molecular weight and the thiol functionalization density of the PVP precursor polymers, with the resulting morphologies compared to those observed using much faster thiosuccinimide cross-linking for gelling the PVP network. Increasing the gelation time resulted in more complete phase separation between the PVP and PNIPAM domains and, for weaker PVP networks, more pronounced thermal responses that imply additional phase separation above the volume phase transition temperature of the PNIPAM network. Contrast matching results suggest the spacing between PNIPAM-rich static domains varies inversely with the molecular weight and degree of thiolation of the PVP-SH precursors, implying that faster-gelling and stronger PVP networks increase the separation between the PNIPAM-rich domains. However, even the weaker and orders-of-magnitude slower gelling PVP-disulfide network was still shown to perturb the structure of the interpenetrating PNIPAM-hydrazone network, with a particular role in preserving its hydration at higher temperatures. Overall, these results substantially inform how to design fully injectable IPNs with well-defined internal phase structures.

4.1 Introduction

Interpenetrating polymer network (IPN) hydrogels are distinguished from other forms of multi-component hydrogels by two volumetrically interlocking but covalently unconnected networks. This class of hydrogels is of interest as a potential biomaterial due to the mechanical advantages conferred by the interlocked network structure[142, 204], the potential for differential degradation of the two networks[3], novel structural properties related to the partitioning between the two phases[163, 237] (often arising from changes to porosity or from incomplete mixing into distinct phases enriched in one or the other component[122, 124]), and potentially improved drug release properties compared to single-network hydrogels[126, 146, 151, 171] due to the segregation between phases with high and low drug affinities.

As with single network hydrogel biomaterials, injectable delivery designs for IPNs are preferable to those requiring surgical implantation, resulting in both reduced invasiveness to the patient and reduced costs related to medical time and resources[70]. The preparation of fully injectable IPNs necessarily requires that the two constituent networks undergo non-interfering cross-linking[237], placing stringent requirements on the chemistry of the precursor polymers used for such applications. Furthermore, given that such systems are cross-linking simultaneous to phase separation of the pre-polymers (initiated immediately following mixing), the relative rates of gelation of the two interpenetrating phases are expected to significantly influence the ultimate morphology of the IPN hydrogel[219-220]. This effect is likely to be particularly significant when two orthogonal chemistries with substantially different gelation times are used; the fast-gelling network would achieve a defined morphology that is quickly locked into place, while the slow-gelling network would have ample time to phase separate[219] (closer to or

at a thermodynamic equilibrium for phase segregation) prior to kinetic freezing of the secondary network structure via cross-linking. Such a combination is also useful in the context of expanding the types of chemistries possible to be used in the context of injectable IPN hydrogels, since the fast-gelling network can effectively immobilize all the network components at the injection site by entrapping the slow-gelling components in a semi-IPN structure. In this context, slow-gelling chemistries that would be dissolved away prior to gelation if applied alone can be used *in vivo* when incorporated in an IPN structure, opening new possibilities for introducing injectable hydrogels with new and useful chemistries.

We have previously reported a method of fabricating injectable IPN hydrogels by co-extruding pre-polymers functionalized with two kinetically orthogonal reactive pairings (hydrazide-aldehyde and thiol-maleimide) through a double barrel syringe (Chapters 2 and 3). Hydrazone and thiosuccinimide cross-link formation can generate IPNs with no cross-reactivity within the detection sensitivity of NMR[237], representing the first reported fully injectable IPN hydrogel. Small angle neutron scattering and super-resolution fluorescence microscopy analysis of the resulting microstructures indicated the formation of two independent networks, albeit with a fraction of the slightly slower gelling hydrogel component (hydrazone cross-linked poly(N-isopropylacrylamide)) seemingly entrapped within the faster gelling hydrogel component (thiosuccinimide cross-linked poly(vinyl pyrrolidone)). However, both hydrazone and thiosuccinimide cross-linking are relatively fast-acting, with both individual networks gelling completely within two minutes. Thus, phase separation has minimal time to create segregated domains in the IPN hydrogel prior to kinetic freezing of the IPN structure via cross-linking. Given the potential advantages of IPNs with highly segregated domain structures, developing new

kinetically or thermodynamically orthogonal chemistries with highly differential gelation times (and thus higher potential for phase separation) may be desirable in several potential applications of *in situ* gelling hydrogels.

Herein, we report on the fabrication and microstructural characterization of IPN hydrogels consisting of hydrazone cross-linked poly(N-isopropylacrylamide) (PNIPAM) and disulfide cross-linked poly(vinyl pyrrolidone) (PVP). Disulfide formation occurs at a rate much slower than thiosuccinimide cross-linking, with gelation of single networks occurring over the time scale of days rather than seconds; in contrast, the hydrazone cross-linked PNIPAM phase gels in less than one minute. Consequently, we observe significantly different and more phase segregated morphologies in these hydrazone/disulfide cross-linked IPNs, with the phase structures achieved tunable according to the molecular weights and degrees of functionalization of the thiolated PVP used to prepare the IPN. We anticipate this insight will facilitate rational design of gelation times within injectable IPN hydrogels to achieve desired morphologies.

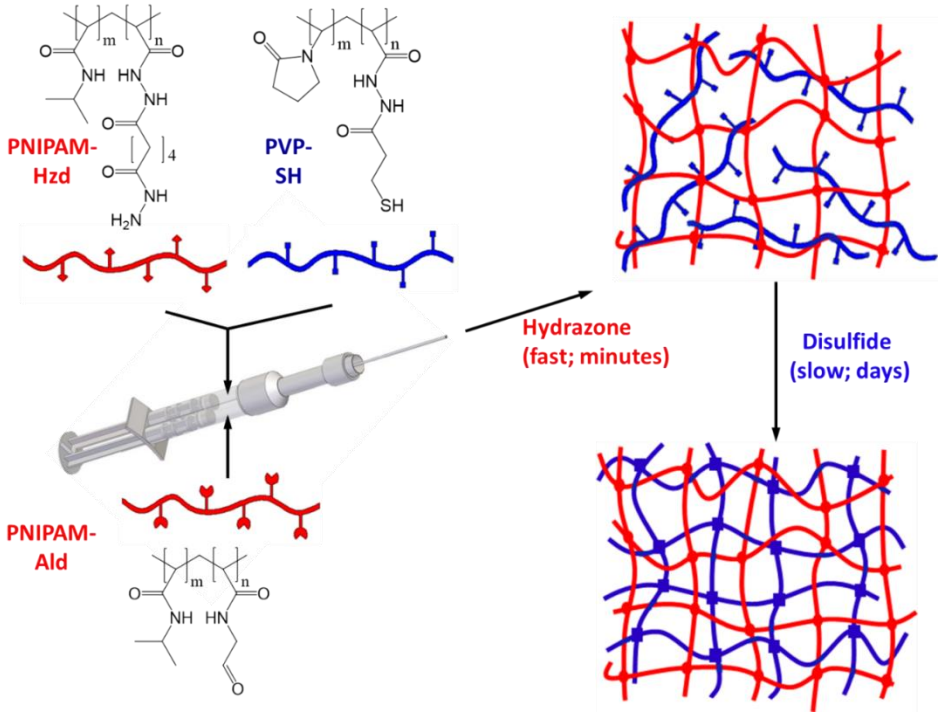

Figure 4.1: Schematic of dual hydrazone and disulfide cross-linking in injectable PNIPAM-hydrazone/PVP-disulfide IPN hydrogel.

4.2 Materials and Methods

4.2.1 Materials:

N-isopropylacrylamide (NIPAM; 99%) was purchased from J&K Scientific and purified by recrystallization at 0°C from toluene followed by washing with hexanes. Deuterated d7-NIPAM monomer (inhibitor-free) was purchased from Polymer Source and used as received. N-vinylpyrrolidone (NVP; 99%), acrylic acid (AA; 99%) and thioglycolic acid (TGA; 98%) were purchased from Sigma Aldrich (Oakville, Canada) and used as received. N-vinylformamide (NVF, >96%) was purchased from TCI (Portland, USA) and used as received. 2,2-azobisisobutyric acid (AIBME, 98%) was purchased from Waterstone and stored under nitrogen. 1-ethyl-3-(3-dimethylaminopropyl) carbodiimide

hydrochloride (EDC, 98%) was purchased from Carbosynth. N-2 aminoethyl maleimide (AEMA, 98%) was purchased from Toronto Research Chemicals. Adipic acid dihydrazide (ADH; 97%) was purchased from Alfa Aesar. All water used was of Milli-Q grade.

4.2.2 Precursor Polymer Synthesis:

Hydrazide- and aldehyde-functionalized poly(N-isopropylacrylamide) (PNIPAM-Hzd and PNIPAM-Ald) were prepared as previously described[237]. A series of thiolated poly(vinyl pyrrolidone) (PVP-SH) polymers with varying degree of thiolation and molecular weight was prepared using our previous method of copolymerizing N-vinyl pyrrolidone with N-vinyl formamide, hydrolyzing under basic to convert NVF residues to vinyl amine residues (70°C in 1M NaOH, 24 hour reaction time), and subsequent EDC-mediated conjugation of the vinyl amine residues with 3-mercaptopropionic acid to create free thiols (Chapter 3). Recipes for each functionalized PNIPAM and thiolated PVP polymer prepared are summarized in Table 4.1. Each sample is coded as $PVP_{x\text{-}y}$ where x is the targeted mol% of thiols in the polymer (per repeat unit of the polymer backbone) and y is the relative molecular weight of the polymer (where y = “high” corresponds to 130-180 kDa, y = “med” corresponds to 40-50 kDa, and y = “low” corresponds to 10-20 kDa).

Table 4.1: Polymer synthesis recipes

Polymer	Target M_w (kDa)	Target mol% functional groups	Mass AIBME (mg)	Volume TGA (µL)	Volume or mass backbone monomer (mL / g)	Volume or mass functional monomer (mL / g)	Volume solvent (mL)
PNIPAM-Hzd	10-20	20%	56	80	4 g	1 g	40
PNIPAM-Ald	10-20	10%	56	80	4.5 g	0.5 g	40
$PVP\text{-}SH_{30\text{-}high}$	130-180	30%	10	2	7.8 mL	2.2 mL	10
$PVP\text{-}SH_{30\text{-}med}$	40-50	30%	20	20	7.8 mL	2.2 mL	30
$PVP\text{-}SH_{30\text{-}low}$	10-20	30%	100	160	7.8 mL	2.2 mL	55
$PVP\text{-}SH_{20\text{-}high}$	130-180	20%	10	2	8.6 mL	1.4 mL	10
$PVP\text{-}SH_{20\text{-}med}$	40-50	20%	20	20	8.6 mL	1.4 mL	30
$PVP\text{-}SH_{15\text{-}high}$	130-180	15%	10	2	9 mL	1 mL	10
$PVP\text{-}SH_{15\text{-}med}$	40-50	15%	20	20	9 mL	1 mL	30

The initial PVP-VF copolymers were made to contain 15-30 mol% vinyl formamide. All polymerizations were performed in isopropanol overnight at 60°C, before drying under reduced pressure. High molecular weight polymers were prepared using 50 vol% monomer, 10 mg AIBME radical initiator, and 2 µL TGA as a chain transfer agent. Medium molecular weight polymers were prepared using 25 vol% monomer, 20 mg AIBME, and 20 µL TGA. Low molecular weight polymers were prepared using 15 vol% monomer, 100 mg AIBME, and 160 µL TGA.

Table 4.2: Polymer properties (GPC configurations as detailed in Table 2S.1). Titration results are considered accurate to ±5% at the 95% confidence interval, based on regression of linear conductance regions to plot intersections at the beginning and end of the neutralization regime.

Polymer	Actual M_w (kDa)	PDI	GPC Method	Actual mol% functional groups	Functional mol% method
PNIPAM-Hzd	19	3.2	Basic	20	Conductometric titration
PNIPAM-Ald	10	2.6	DMF	12	^{1}H NMR
PVP-$SH_{30\text{-high}}$	176	3	DMF	36	Titration (for amine content) Ellman's assay (for conversion)
PVP-$SH_{30\text{-med}}$	47	2.7	DMF	34	
PVP-$SH_{30\text{-low}}$	14	2.3	DMF	33	
PVP-$SH_{20\text{-high}}$	133	3.2	DMF	18	Titration (for amine content) Ellman's assay (for conversion)
PVP-$SH_{20\text{-med}}$	43	3.2	DMF	23	
PVP-$SH_{15\text{-high}}$	136	3.6	DMF	15	Titration (for amine content) Ellman's assay (for conversion)
PVP-$SH_{15\text{-med}}$	41	3.6	DMF	13	

Amine content in the hydrolyzed copolymers was determined by base-into-acid conductometric titration (1 mg/mL polymer in 1 mM NaCl, 0.1 M NaOH titrant, ManTech Associates). Subsequent thiol functionalization of these amine residues was performed using a 1:1.2:3 molar ratio of polymer-bound amines : 3-mercaptopropionic acid : EDC under manual pH control (pH = 4.75, 4 hours). The thiolated product was then dialyzed against dilute HCl (pH<5), adjusted to pH 7.4, immediately lyophilized, and subsequently stored at -20°C until use. Thiol conjugation is assessed by both conductometric titration (based on the difference in the number of free amine groups before and after conjugation) and Ellman's assay (using the manufacturer's protocol) to be essentially (at least 95%) quantitative with the number of initial amine groups present (specifically, the colourimetric assay reads a slightly higher quantity of free thiols per unit polymer weight

than that calculated from conductometric titration, which is considered the more reliable technique). However, the lyophilized product is susceptible to disulfide formation even in the dry state due to residual / adsorbed atmospheric moisture, with the polymer exhibiting a shelf life of ~1 month in terms of maintaining its ability to gel via disulfide formation. Resulting polymer properties are summarized in Table 4.2.

4.2.3 SANS Sample Preparation: Neutron scattering experiments were carried out on the NG30 (30 m) SANS instrument at the NIST Center for Neutron Research (NCNR), Gaithersburg, MD, USA. Samples were prepared using 6 wt% PNIPAM precursor polymers and 3.5 wt% PVP-thiol in phosphate buffered D_2O (or mixed D_2O / H_2O for index matching) and extruded directly into NCNR's custom sample holders (1 mm path length). IPNs were allowed to gel for 7 days before data collection to ensure full disulfide cross-linking. Scattering data was collected from (1) single network disulfide-cross-linked PVP networks prepared with PVP-thiol precursor polymers of different degrees of functionalization and molecular weights (in deuterated phosphate buffered saline), (2) IPNs prepared using PNIPAM and each PVP formulation studied (in D_2O-PBS, i.e. with scattering observed from both IPN components), and (3) IPNs prepared using a subset of the PVP-thiol polymers (representative of the full range of polymers generated), deuterated PNIPAM-Hzd precursor polymers, and protonated PNIPAM-Ald precursor polymers in a solvent containing H_2O:D_2O ratios that can effectively index match (i.e. suppress scattering from) one of each constituent network per solvent ratio studied. Solvent ratios for index matching were identified by first theoretically calculating solvent matching points based on the known polymer compositions (predicted at 44:56

D_2O:H_2O to match out deuterated PNIPAM networks, and 21:79 D_2O:H_2O to match out PVP networks). Empirical refinements were carried out by bracketing these values by 20% in both the H_2O- and D_2O-rich directions, testing all three samples for scattering intensity, and using linear regression to subsequently solve for the composition that minimizes the scattering intensity of that network. Match points were thus solved to 50:50 D_2O:H_2O to hide deuterated PNIPAM and 25:75 D_2O:H_2O to match out PVP networks.

Data was collected at sample- to-detector distances of 1 m (high q; 1 minute), 4 m (medium q, 3 minutes) and 13 m with lens (low q; 22 minutes), using 6 Å wavelength neutrons at high and medium *q* and 8.4 Å neutrons at low q. The *q* ranges were merged using NCNR's data reduction tools and customized Igor Pro macros[240-241].

4.2.4 SANS Data Fitting:

As in our prior work with injectable IPNs prepared using thiosuccinimide-cross-linked PVP (Chapter 3), we used three different equations to fit neutron scattering data. The Porod model (Equation 4.1) is derived for hydrogels that do not contain static inhomogeneities locked into the polymer network (e.g. domains with higher local polymer concentration that persist within the network).

(Eq. 4.1) $$I(Q) = \frac{A}{Q^m} + \frac{B}{1+(\xi\,Q)^n} + C$$

The first term describes the larger scale network geometry in which *m* is the low-*q* Porod exponent, describing the network's extended or collapsed state[243]. The second term describes polymer-solvent interactions and small-scale network features, where ξ is the

correlation length (proportional to the mesh size between cross-links) and *n* is the high-*q* exponent characterizing polymer-solvent interactions. *n* <= 2 indicates favourable solvent interactions, whereas n > 2 indicates unfavourable interactions. This model was previously found to effectively describe the morphology of thiosuccinimide-cross-linked PVP single networks across all tested temperatures (Chapter 3).

The squared Lorentzian model (Equation 4.2) can additionally account for the presence of static inhomogeneities in the network.

(Eq. 4.2) $$I(Q) = \frac{A}{(1+(\gamma Q)^2)^2} + \frac{B}{1+(\xi Q)^n} + C$$

The first term models the low-*q* scattering from these static features, with γ representing the characteristic length scale (i.e. average separation distance) of static inhomogeneities. The second term is conserved from Equation (1), representing the polymer-solvent interactions and any smaller-scale dynamic inhomogeneities. This model was previously found to account effectively for the scattering observed from hydrazone-cross-linked PNIPAM single networks (Chapter 3).

A hybrid model, developed in our previous work to describe composite systems with both Porod-type fractal scattering from PVP networks and squared Lorentzian scattering from PNIPAM networks, was used to describe the IPN data (Equation 4.3).

(Eq. 4.3) $$I(Q) = \frac{A}{Q^l} + \frac{B}{(1+(\gamma Q)^2)^m} + \frac{C}{1+(\xi Q)^n} + D$$

This hybrid model is derived by summing the individual network-scale terms from both models (term 1 from the Porod model, term 2 from the squared Lorentzian model) while adding a single fluid-scale (high-q) Lorentzian term to model the overall polymer-solvent

interactions throughout the IPN hydrogel. As previously discussed in Chapter 3, this additive model implicitly assumes cross-scattering (interference between neutrons scattered from each network phase) to be insignificant. It is, however, empirically successful at explaining the scattering profile of gel networks that combine power law regions with overlapped peaks indicative of static structuring, implying cross-scattering is indeed negligible in our systems.

4.3 Results and Discussion

Gelation time of network precursors: Gelation time tests were performed using the vial inversion test, in which a vial containing the disulfide-containing pre-polymer was rotated 180° at pre-determined intervals and allowed to flow for 5 seconds; the first timepoint at which no flow was observed over the sample observation time corresponded to the gelation time of that network. Gelation times for both the PNIPAM-hydrazide/aldehyde gelling pair (at the same 6 wt% concentration used within the IPN) and each (self cross-linking) PVP-thiol polymer (at the same 3.5 wt% concentration used within the IPN) are shown in Table 4.3.

Table 4.3: Gelation times for each network comprising an IPN

Network Type	Gelation time
PNIPAM	90 s
$PVP\text{-}SH_{30\text{-}high}$	1.5 d
$PVP\text{-}SH_{30\text{-}med}$	3.5 d
$PVP\text{-}SH_{30\text{-}low}$	6 d
$PVP\text{-}SH_{20\text{-}high}$	4 d
$PVP\text{-}SH_{20\text{-}med}$	5.5 d
$PVP\text{-}SH_{15\text{-}high}$	4.5 d
$PVP\text{-}SH_{15\text{-}med}$	6 d

Gelation time increases systematically as the molecular weight of the PVP precursor polymer decreases and/or the degree of thiol functionalization on the pre-polymer decreases. Both of these results conform to prediction (i.e. more cross-links must form and/or a higher percentage of available functional groups must cross-link to induce gelation). However, all PVP-thiol polymers gel at rates significantly slower than the PNIPAM-hydrazone network, resulting in all IPNs studied herein having highly differential gelation times (i.e. one fast gelling and one slow gelling network). Note that all PVP-SH pre-polymers self-gel no later than six days after dissolution at 3.5 wt%, ensuring that gelation of the PVP-SH network has occurred within each of the IPN samples examined via SANS (all of which were left to gel for seven days prior to analysis).

SANS on PVP single network hydrogels: In light of our previous work on hydrazone/ thiosuccinimide crosslinked IPNs, we first aimed to determine whether scattering from disulfide-cross-linked PVP single networks follows the previously established Porod model power-law dependence seen in PVP networks crosslinked using thiosuccinimides. As shown in Figure 4.2, the Porod model reasonably fits most of the PVP single network scattering data. However, some samples, particularly PVP samples with higher molecular weights and higher degrees of thiol functionalization (e.g. PVP-$SH_{30\text{-high}}$ and PVP-$SH_{30\text{-med}}$, Figs. 4.2a, b), have small but apparent peaks overlapped onto the power law trend from the Porod model at q~ 0.005 $Å^{-1}$. Similar but much less prominent features were also noticeable in the scattering profiles of PVP-$SH_{30\text{-low}}$ and PVP-$SH_{20\text{-high}}$ (Figure 4.2 c, d), both of which also lie on the upper end of the molecular weights and/or degrees of functionalization studied.

Generally, the Porod exponents for all samples fell in the 2.7-3 range (Table 4.4), suggesting a predominant microstructure of clustered PVP fractals similar to that observed with thiosuccinimide cross-linked PVP networks (Chapter 3). Exceptions to this range are found in the fits of PVP-$SH_{30\text{-low}}$ (m = 3.3) and PVP-$SH_{20\text{-high}}$ (m = 2.2), although the Porod model gives only imperfect fits to both these networks; the Porod model particularly under-fits the curvature in the PVP-$SH_{20\text{-high}}$ scattering plot at low q (Fig. 4.2 d). Furthermore, the PVP-$SH_{15\text{-med}}$ sample set appears to be affected by an artefact of the data reduction process used to stitch together the different detector distance data sets (q 0.01 Å and 0.1Å), although the correspondence between the data and the fit curve is only minimally affected over most of the q range.

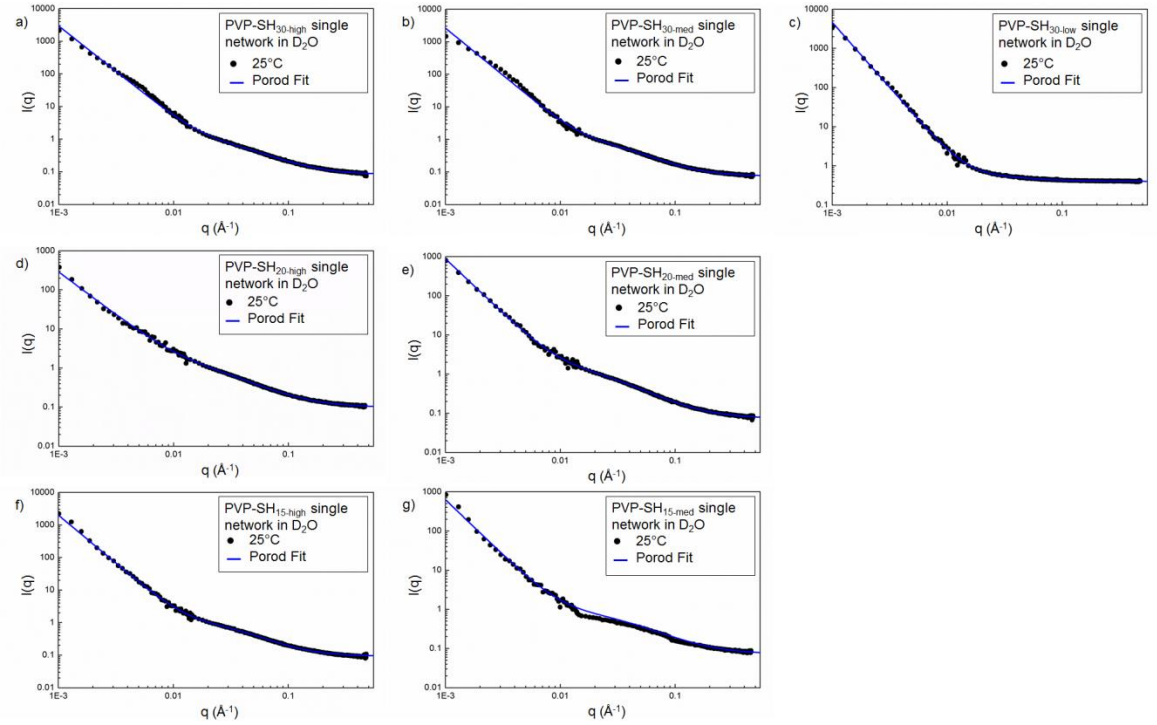

Figure 4.2: SANS scattering profiles and Porod model best-fits of PVP disulfide single networks measured in D_2O (3.5 wt% polymer). (a-c) 30% thiol functionalized high (PVP-$SH_{30\text{-high}}$, a), medium (PVP-$SH_{30\text{-med}}$, b) and low (PVP-$SH_{30\text{-low}}$, c) molecular weight PVP; (d,e) 20% thiol functionalized high (PVP-$SH_{20\text{-high}}$, d) and medium (PVP-$SH_{20\text{-med}}$, e) molecular weight PVP; (f,g) 15% thiol functionalized high (PVP-$SH_{15\text{-high}}$, f) and medium (PVP-$SH_{15\text{-med}}$, g) molecular weight PVP. Note that solutions of low molecular weight PVP-$SH_{20\text{-low}}$ and PVP-$SH_{15\text{-low}}$ do not gel at this concentration and are thus excluded from this analysis.

Applying the hybrid model to the PVP single network scattering data yielded improvements ranging from slight (for the lower molecular weight and lower degree of functionalization PVP-SH formulations, already well-fit by the Porod model itself) to significant (primarily for the higher molecular weight/higher degree of functionalization gels such as PVP-$SH_{30\text{-high}}$ and PVP-$SH_{30\text{-med}}$, Figs. 4.3a, b, that contained features not fit by the Porod model alone). Comparing the goodness of fits observed between Fig. 4.2 (Porod model, no static inhomogeneities considered) and Fig. 4.3 (hybrid model, static

inhomogeneities considered) suggests an increasing degree of static inhomogeneity formation within PVP-disulfide networks are formed from precursor polymers with higher molecular weights and degrees of functionalization. Such domain formation may be accounted for via two mechanisms: (1) the observed lower solubility of higher molecular weight/higher degree of thiolation polymers results in more heavily intramolecularly cross-linked single chains attached by fewer intermolecular cross-links or (2) the significantly lower hydrophilicity of the disulfide bond (particularly in comparison to the previously studied thiosuccinimide bond) relative to both free thiols and vinylpyrrolidone residues results in some degree of internal self-association between PVP sub-chains upon cross-linking.

Although the squared Lorentzian only contributes significantly to the total hybrid model fit intensity profile for the higher molecular weight and highly thiolated PVP-SH disulfide single networks, a generally inverse relationship was observed between the inter-domain correlation length and the PVP-SH molecular weight (Table 4.4; particularly for PVP-SH_{30} where three different M_w composition points yielded gels). This trend in correlation lengths is also consistent with the physical expectation that slower gelation allows for phase separation to progress further in disulfide systems that form more elastic gels.

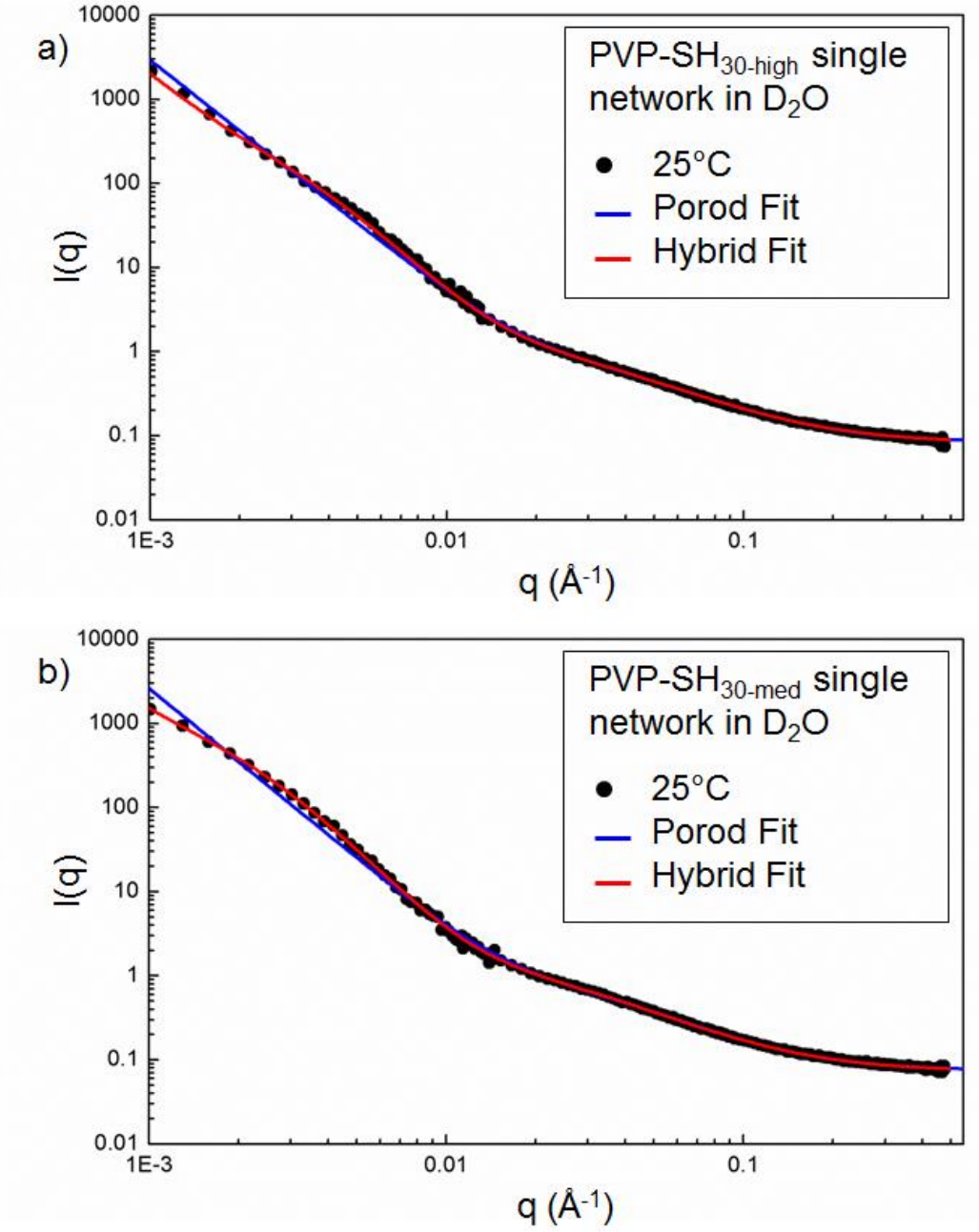

Figure 4.3: Comparison of the suitability of the Porod and hybrid model fits for PVP-$SH_{30\text{-high}}$ and PVP-$SH_{30\text{-med}}$ SANS scattering profiles. Corresponding comparisons for other PVP-disulfide single networks for which the hybrid model provided a lesser improvement in fitting can be found in Supporting Figure 4S.1, with the relative importance of the model components to overall fits shown in Figures 4S.2.

Table 4.4: Summary of key fitting parameters for single network SANS data

(* used to indicate particularly improved fits when using the hybrid model)

	T (°C)	Model Used	Porod exponent	Squared Lorentzian Correlation Length (nm)	Fluid Term Correlation Length (nm)	Fluid term exponent
PNIPAM Single Network in D_2O (reproduced from Chapter 3)	25	Squared Lorentzian	-	37	3.0	2.3
	32		-	36	3.0	2.4
	45		-	35	1.0	3.1
$PVP\text{-}SH_{30\text{-}high}$	25	Porod	2.8	-	2.2	1.9
$PVP\text{-}SH_{30\text{-}med}$	25		2.9	-	2.5	2.0
$PVP\text{-}SH_{30\text{-}low}$	25		3.3	-	2.1	2.0
$PVP\text{-}SH_{20\text{-}high}$	25		2.2	-	3.6	1.7
$PVP\text{-}SH_{20\text{-}med}$	25		2.8	-	3.7	1.8
$PVP\text{-}SH_{15\text{-}high}$	25		3.0	-	2.6	2.1
$PVP\text{-}SH_{15\text{-}med}$	25		2.8	-	2.8	1.7
$PVP\text{-}SH_{30\text{-}high}$ *	25	Hybrid	3.0	29	3.1	1.8
$PVP\text{-}SH_{30\text{-}med}$ *	25		3.1	46	3.7	1.8
$PVP\text{-}SH_{30\text{-}low}$	25		3.5	49	3.6	1.7
$PVP\text{-}SH_{20\text{-}high}$ *	25		2.7	13	4.1	1.7
$PVP\text{-}SH_{20\text{-}med}$	25		2.8	36	4.0	1.8
$PVP\text{-}SH_{15\text{-}high}$	25		3.2	14	2.7	2.1
$PVP\text{-}SH_{15\text{-}med}$	25		3.3	14	2.9	1.7

For comparison, a copy of the prior scattering data and squared Lorentzian fitting plots for the PNIPAM single network hydrogel (at 6 wt%, again matching the concentration used for the subsequent hydrazone/disulfide IPNs herein) is reproduced here from Chapter 3 (Figure 4.4). Compare to the PVP-SH disulfide single networks, characterized by a power law intensity curve at low *q* (i.e. linear behaviour on a log-log plot), the PNIPAM single network is characterized by a broad, shallow curve trending toward a low-*q* plateau.

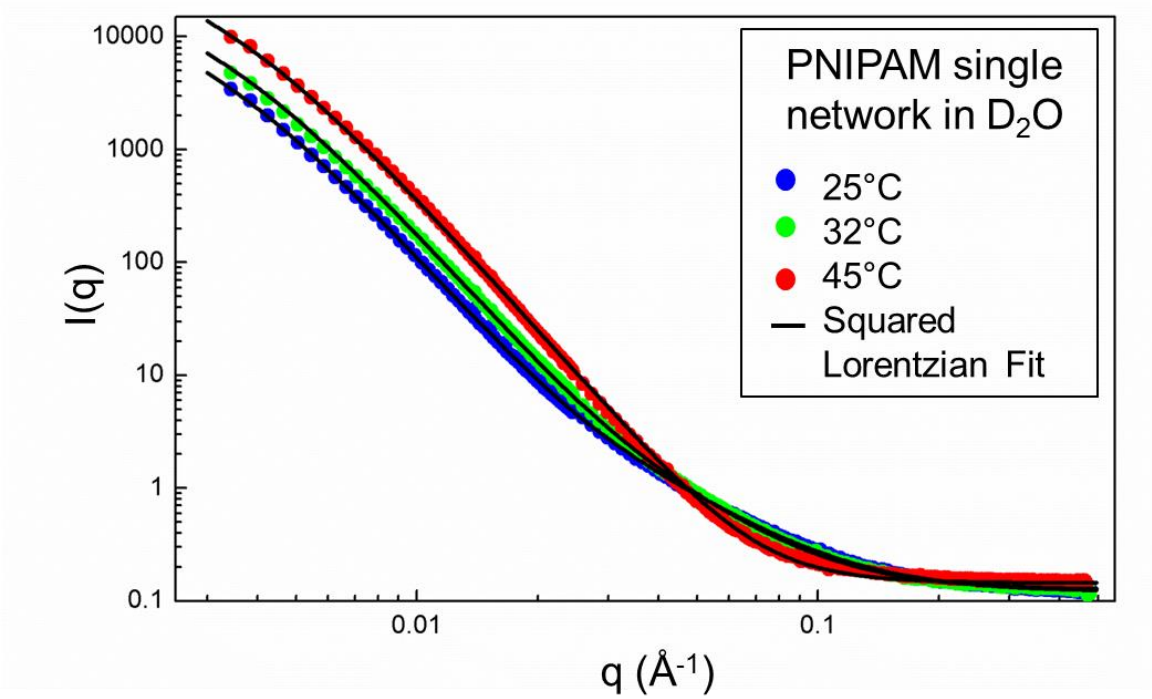

Figure 4.4: SANS scattering profiles for PNIPAM single networks at 25°C, 32°C, and 45°C, reproduced from Chapter 3 for comparison to PVP-disulfide networks.

SANS on IPN hydrogels: Scattering data for PNIPAM-hydrazone/PVP-disulfide IPNs in D_2O, a solvent in which both (protonated) constituent networks of the IPN contribute to the scattering signal, show general similarities to PNIPAM-hydrazone / PVP-

thiosuccinimide IPN SANS profiles previously presented in Chapter 3 (Figure 4.5). The scattering profiles show an underlying Porod-type power law dependence with overlapping peaks indicating static structures growing in scattering intensity with increasing temperature. Peak features seem to be distinct in that, with the exception of the anomalous set using PVP-$SH_{15\text{-med}}$, discussed later, all the temperature sets converge back to the underlying power law slope below the *q* range where the temperature-dependent peak is found. This general result is consistent with the collapse and further phase segregation induced by the thermoresponsive PNIPAM network.

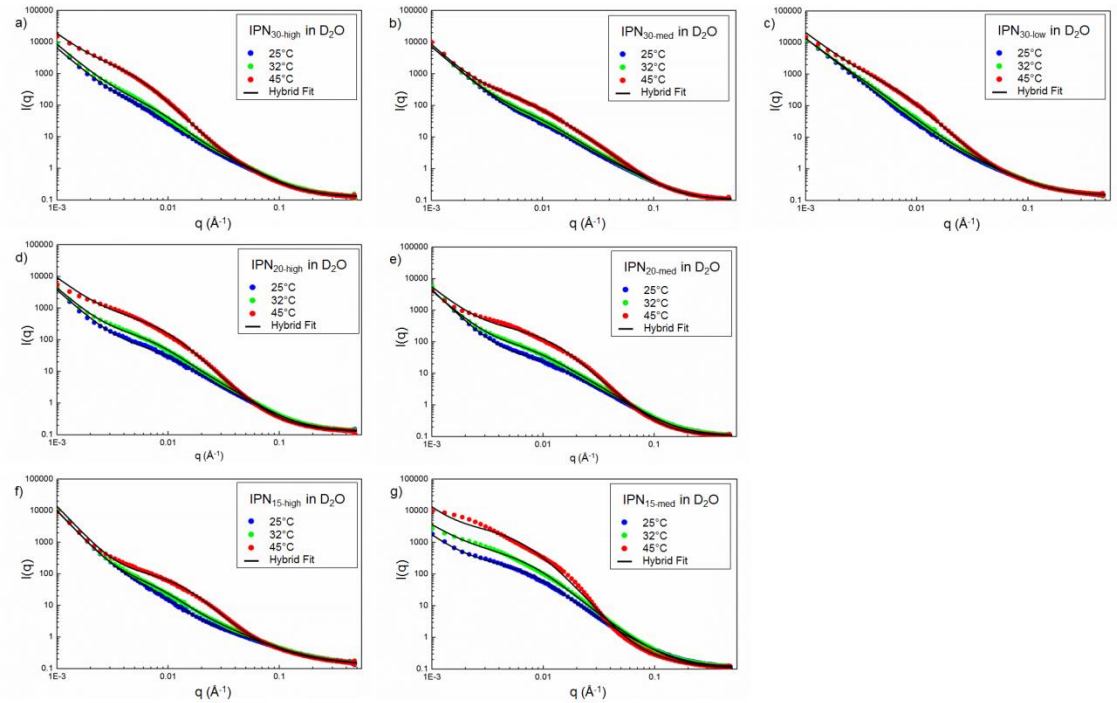

Figure 4.5: SANS scattering profiles and hybrid model best-fits of PVP-disulfide/PNIPAM-hydrazone IPNs in D_2O as a function of temperature. (a-c) 30% thiol functionalized high (PVP-$SH_{30\text{-high}}$, a), medium (PVP-$SH_{30\text{-med}}$, b) and low (PVP-$SH_{30\text{-low}}$, c) molecular weight PVP; (d,e) 20% thiol functionalized high (PVP-$SH_{20\text{-high}}$, d) and medium (PVP-$SH_{20\text{-med}}$, e) molecular weight PVP; (f,g) 15% thiol functionalized high (PVP-$SH_{15\text{-high}}$, f) and medium (PVP-$SH_{15\text{-med}}$, g) molecular weight PVP.

For IPNs made using each molecular weight of the 30% thiolated PVP (PVP-SH_{30} series), the hybrid model fit accurately at all studied temperatures (Figure 4.5 a-c; see also supporting Figure 4S.3-4S.5 for individual hybrid model fits and component breakdowns). However, as the degree of thiolation (and thus potential for cross-linking) was decreased, the scattering peak related to the static structures within the network was broadened at high temperatures, resulting in slight deviations from the hybrid model fits at 45°C (a temperature well above the volume phase transition temperature, VPTT, of the thermoresponsive PNIPAM network prepared alone) for the PVP-SH_{20} series (20% thiolation, Fig 4.5 d,e) and PVP-$SH_{15\text{-high}}$ (Fig. 4.5 f) and at both 32°C (at the VPTT of the PNIPAM network) and 45°C for PVP-$SH_{15\text{-med}}$ (Fig. 4.5 g). The 45°C scattering profile for PVP-$SH_{15\text{-med}}$ in particular exhibited serious deviations between the observed and fit traces, in which the static scattering feature widens to reach the low-*q* edge of the data set and takes on a flattened central profile. (See also Supporting Figures 4S.6-4S.9 for individual plots and hybrid model component breakdowns for the PVP-SH_{20} and PVP-SH_{15} IPNs.)

Thus, as the degree of thiolation (i.e. potential for disulfide cross-link formation) and molecular weight (i.e. the inherent network stiffness resulting from “pre-cross-linking” of the PVP relative to lower molecular weight pre-polymers) are decreased, more substantial conformational change is observed as the thermoresponsive IPN is heated. This result is consistent with the anticipated lower stiffness and higher mobility of the less cross-linked or less thiolated PVP pre-polymers tested. Indeed, PVP-$SH_{15\text{-med}}$ was specifically chosen as a limiting case given that it cross-links into a network only barely strong enough to resist flowing after 6 days; all other samples that significantly deviated from the hybrid model fits were also based on weakly networked PVP formulations.

We speculate that this result is linked to the role of the (more mechanically strong) deswelling PNIPAM domains effectively perturbing the weakly cross-linked PVP networks upon heating. Increasing the amount of PNIPAM-PNIPAM interactions upon collapse is thermodynamically favorable above the VPTT[248], and in weaker PVP networks such phase separation is less constrained by the interpenetrating PVP phase. Furthermore, given the equilibrium nature of disulfide cross-linking, the smaller and more lightly thiolated PVP systems are overall weaker, but may reasonably have a dispersity of mechanical properties on the nanoscale, compared to more heavily thiolated and longer PVP chains that form stronger and more consistent networks. Thus, as the PNIPAM domains contract in response to temperature changes, they are likely experiencing varying degrees of elastic resistance from the more sporadically cross-linked PVP phase, further resulting in this broadening effect in the thermosensitive scattering features.

Similar to the previous work with PNIPAM-hydrazone/PVP-thiosuccinimide IPNs (Chapter 3), it is difficult to extract specific details about nanostructural features from the numerical parameters of hybrid fitting (Table 4.5). Mixing may (and evidence suggests, at least to some extent does) alter the structures each network adopts in the IPN relative to in isolation; in addition, each phase exhibits different scattering cross-sections depending on the local composition of the IPN along the neutron beam path. However, the squared Lorentzian component (used to fit primarily the PNIPAM network) adopts markedly smaller inter-domain spacing correlation lengths in the IPN than the PNIPAM single network control, with most IPN compositions close to the same ~10nm values seen in the previous hydrazone / thiosuccinimide system (Chapter 3). This implies that the model may be describing not only the spacing between static inhomogeneities within

the PNIPAM network but also the length scale of interactions between the two networks. However, unlike with the thiosuccinimide-hydrazone IPNs, the interpretation of hydrazone / disulfide IPNs in D_2O is further complicated by the fact that the hybrid model is required to explain the behaviour of some of these PVP networks in isolation, while the thiosuccinimide cross-linked PVP fit well to a simple Porod model. The Porod exponents also tend slightly higher in the disulfide IPN's, implying more extensive collapse of the fractal network components that lack discrete domain features.

Table 4.5: Summary of key fitting parameters for PNIPAM-hydrazone/PVP-disulfide IPN's in D_2O using each PVP-SH pre-polymer tested

	T (°C)	Model Used	Porod Exponent	Squared Lorentzian Correlation Length (nm)	Fluid Term Correlation Length (nm)	Fluid Term Exponent
$IPN_{30\text{-}high}$	25	Hybrid	3.0	13	4.5	1.9
	32		3.0	12	3.4	2.2
	45		2.8	20	2.6	2.0
$IPN_{30\text{-}med}$	25	Hybrid	3.0	7.7	3.1	2.1
	32		3.0	8.6	3.5	2.2
	45		3.2	12	6.2	2.5
$IPN_{30\text{-}low}$	25	Hybrid	2.7	38	3.9	1.7
	32		2.6	22	3.5	1.8
	45		2.7	15	1.1	2.3
$IPN_{20\text{-}high}$	25	Hybrid	3.1	8.8	3.9	2.1
	32		3.1	11	4.0	2.3
	45		2.7	10	8.3	1.8
$IPN_{20\text{-}med}$	25	Hybrid	3.4	7.3	3.5	2.2
	32		3.1	9.0	4.2	2.3
	45		2.8	7.9	7.1	2.2
$IPN_{15\text{-}high}$	25	Hybrid	3.7	13	5.3	1.6
	32		3.8	11	4.8	1.8
	45		3.7	7.1	4.6	1.5
$IPN_{15\text{-}med}$	25	Hybrid	2.6	11	7.2	2.0
	32		2.3	12	6.7	2.4
	45		3.0	15	1.0	2.0

SANS on IPN hydrogels with contrast matching: To isolate the individual network structures inside the IPN phase without scattering interference from the corresponding interpenetrating phase, four PVP-SH pre-polymers selected to cover the full scope of gelation times and gel strengths among the measured samples (i.e. PVP-$SH_{30\text{-}high}$, PVP-$SH_{30\text{-}low}$, PVP-$SH_{15\text{-}high}$ and PVP-$SH_{15\text{-}med}$) were further investigated using contrast matching SANS experiments which allow the structure of the PVP-based networks to be independently measured in the presence of deuterated PNIPAM networks. Using solvent conditions that match out the PNIPAM network such that only the PVP network contributes significantly to scattering (50:50 H_2O:D_2O, Figure 4.6), no temperature dependency nor any peak features indicative of static inhomogeneities on SANS-accessible length scales were observed. This result strongly suggests that only the (non-thermoresponsive) PVP network is being probed in these experiments, as desired. These index-matched samples exhibited excellent fits to the Porod model (see also Supporting Figures 4S.10 & 4S.11), yielding exponents in the 3.2-3.3 range (Table 4.6) indicative of extensively collapsed networks. The fitted Porod component model parameters have no significant temperature dependence in the low to mid q region (such that only a single average fit line is presented in Figure 4.6).

This is a notable change from our previous work using thiosuccinimide cross-linking of the PVP network (Chapter 3), in which the IPN with PNIPAM matched out required use of the hybrid model to fit a slight but distinct static domain feature attributed to the incorporation of a small amount of PVP into PNIPAM-rich domains. In this case, we attribute the absence of such domain features to the starkly different gelation times of the PVP network between these two cross-linking functionalities. Thiosuccinimde cross-linked PVP networks form within seconds, too quickly to allow PVP to fully phase-

segregate out of nascent PNIPAM domains on the nanoscale length scale studied by SANS. In contrast, even the fastest gelling disulfide networks require gelation times on the length scale of days, slow enough that essentially complete diffusion of the PVP out of the (rapidly forming) PNIPAM-hydrazone network can occur prior to PVP gelation.

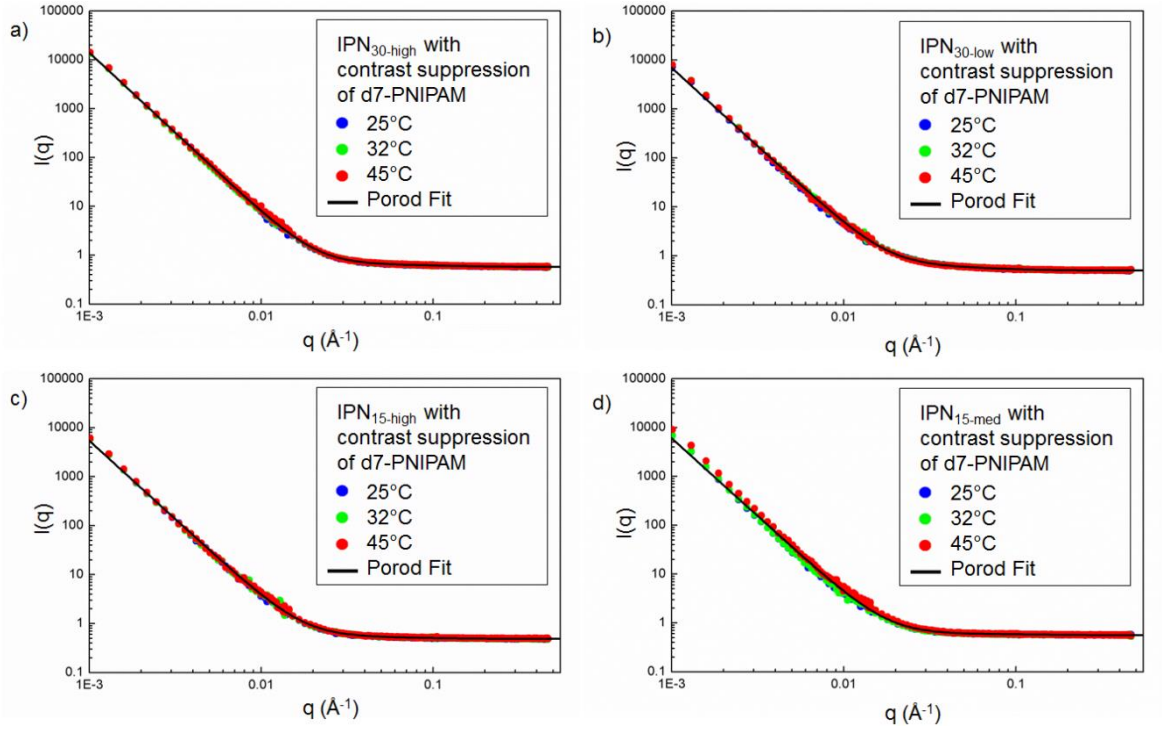

Figure 4.6: Contrast-matched SANS profiles for PNIPAM-hydrazone/PVP-disulfide IPNs with d7-PNIPAM scattering suppressed as a function of temperature. (a) $PVP_{30\text{-}high}$; (b) $PVP_{30\text{-}low}$; (c) $PVP_{15\text{-}high}$; (d) $PVP_{15\text{-}med}$. Thermosensitivity is suppressed, and the data follows a power law form without discernible domain-induced peak features. Single Porod fit lines (averaged over those fit for each of the four samples) are shown on each plot for simplicity due to the insignificant temperature variation observed with each sample.

It is also noteworthy that the small peaks observed in the SANS scattering profiles of the PVP-SH disulfide single networks composed of high molecular weight, highly thiolated polymer (Figure 4.2 a,b) are apparently absent in IPNs formed with those same PVP

networks. This result strongly suggests that the attribution of this feature to the decreasing solubility of PVP-SH polymers as the molecular weight and degree of thiolation is unlikely to be accurate, as any altered solubility at the nanoscale associated with the PVP chains should also be apparent in the contrast matched IPNs in which only PVP scattering is visible. Instead, we can attribute this result to the formation of any self-associated PVP domains suppressed via the creation of the IPN, perhaps attributable to the role of the stiffer and rapidly gelling PNIPAM network limiting any further phase segregation within the weaker and slowly gelling PVP network as it forms.

Subsequent contrast suppression of the PVP scattering signal from these same IPNs (such that only the PNIPAM phase contributes significantly to the scattering at 75:25 H_2O:D_2O ratio, Figure 4.7) shows the expected thermosensitivty and static domain scattering contributions consistent with the single network PNIPAM hydrogel. However, the overall profile also clearly includes a power law contribution to scattering based on the linear region observed at low q. Thus, the hybrid model was again applied to fitting these data sets (see also Supporting Figures 4S.12 - 4S.15 for individual plots and hybrid model component contributions) and accurately captured all scattering features observed. The squared Lorentzian component accounts for most of the scattering intensity at mid-*q* regions coinciding with the peak features, while the Porod component (with exponents in the 3.1-3.4 range again indicative of extensive collapse of the domains within the IPN, Table 4.6) becomes dominant in the low-*q* regime. The presence of significant Porod-type scattering contributions at low *q* (i.e. pertaining to larger-scale features) suggests that, despite the orders-of-magnitude slower cross-linking speed of the PVP network relative to the PNIPAM network, the PVP network still at least partially perturbs the structure of the interpenetrating PNIPAM network. We

attribute this result to the PVP phase partially disrupting the static domain organization otherwise observed in PNIPAM single networks; the highly water binding PVP phase may effectively suppress the total degree of dehydration possible within the directly adjacent PNIPAM phase inside the IPN.

Apart from a few exceptions, most of the fitting parameters (Table 4.6) in IPNs with PVP scattering suppressed (i.e. focusing on PNIPAM scattering) follow the expected temperature trends. The static component inter-domain correlation length typically decreases with increasing temperature, while the fluid term Lorentzian exponent typically increases (indicating poorer solvation) over the same temperature range. This consistency with theory increases our confidence in the use of the hybrid model to fit and interpret the SANS scattering profiles of the contrast-matched IPNs. Smaller increases in the fluid term exponents were also observed in contrast matched IPNs in which PNIPAM scattering is matched out, indicating a possible influence of the PNIPAM phase transition on network hydration in areas of thorough nano-scale mixing of the networks. Note that similar slight decreases in the fluid term exponent upon increasing temperature were also seen in the prior hydrazone / thiosuccinimide IPNs (Chapter 3).

Compared to the prior work with contrast matching on PNIPAM-hydrazone/PVP-thiosuccinimide IPNs (Chapter 3), the most notable observation is that the Porod model is able to adequately fit the PVP phase of the IPNs with PNIPAM matched out. This result suggests that phase separation within the injectable IPN may be more extensive when using the slower disulfide cross-linking chemistry for PVP. However, the Porod exponents for all disulfide-based IPNs are higher than those observed for the thiosuccinimide-based IPNs, suggesting more extreme clustering within that more phase

separated PVP phase. In addition, the correlation lengths in the disulfide IPNs with PVP matched out were consistently slightly smaller than those observed for the thiosuccinimide IPNs; however, it is difficult to assess the clear significance of this small difference in fitting parameters without additional replicates.

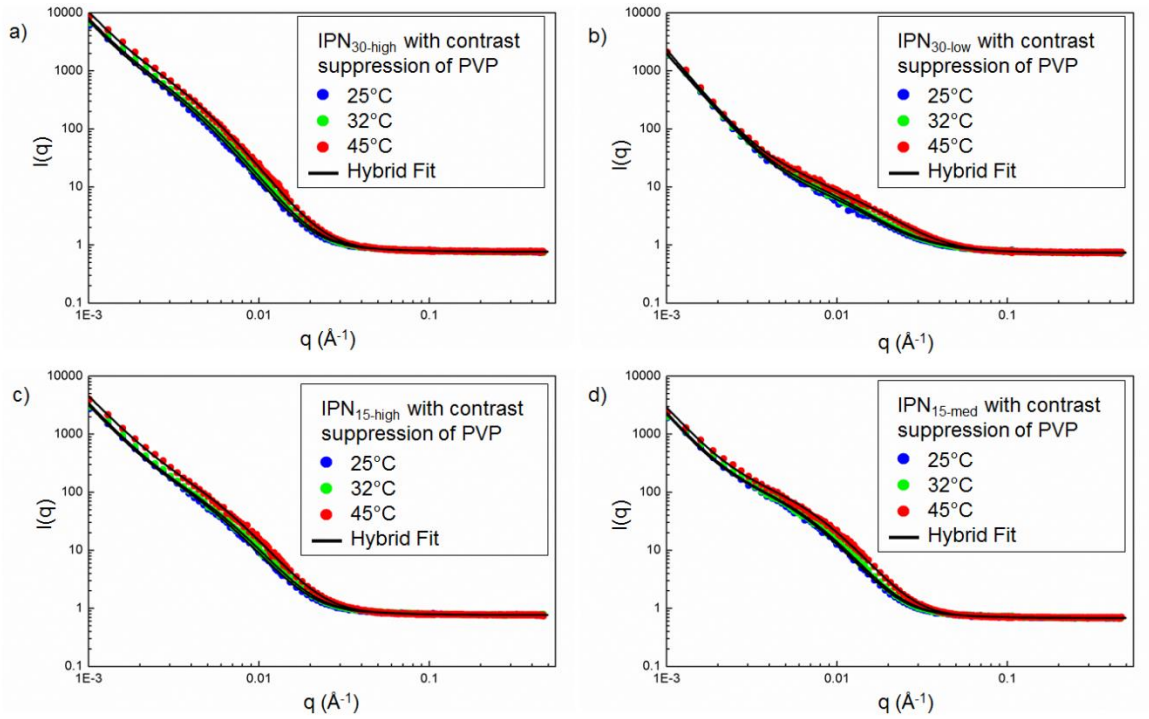

Figure 4.7: Contrast-matched SANS profiles for PNIPAM-hydrazone/PVP-disulfide IPNs with PNIPAM scattering suppressed as a function of temperature. (a) $PVP_{30\text{-}high}$; (b) $PVP_{30\text{-}low}$; (c) $PVP_{15\text{-}high}$; (d) $PVP_{15\text{-}med}$. Thermosensitivity is apparent, and the data follows a power law form with significant domain-induced peak features. Hybrid model fits are shown for each temperature.

Overall, the SANS analysis performed herein gives significant insight into the nature of simultaneous IPN formation for *in situ*-gelling hydrogels. First, the fabrication of an IPN can significantly impair phase segregation within *in situ*-gelling hydrogels, as evidenced by the disappearance of the static inhomogeneity term observed in the PVP-SH single

network hydrogel profiles in the PNIPAM contrast-matched IPN hydrogel profiles (i.e. IPN's showing only the PVP-related network features). Second, the relative gelation times of the two phases have a significant impact on the degree of interpenetration between the phases. By slowing the PVP gelation time from seconds (with thiosuccinimides, Chapter 3) to days, we do not observe the same entrapment of PVP within PNIPAM-rich domains observed in the thiosuccinimide cross-linked IPN, hypothesized to relate to the PVP having sufficient time to phase separate from the rapidly gelled PNIPAM phase prior to its own gelation. Third, even a very weak or slow gelling secondary network (here, PVP) can significantly alter the phase structure of a stiffer and faster-gelling primary network (here, PNIPAM) relative to a homopolymer hydrogel, as evidenced by the clear power-law contribution to the PVP contrast-matched IPN profile (i.e. showing only PNIPAM-related network features) that was not observed in the PNIPAM single network materials.

Considered together, these results significantly inform the design of injectable IPN hydrogels for applications. Specifically, as the gelation time of the secondary network is slowed, increased phase segregation and temperature-responsive network perturbations can be achieved, as evidenced by the appearance of the broadened mid-q peaks above the VPTT in IPNs with weak PVP secondary networks. This observation has significant relevance to the design of drug delivery vehicles based on IPN structures for example, in which the kinetics and capacity for thermal burst or entrapment of drug could both be rationally tuned based on this microstructural insight.

Table 4.6: Summary of key fitting parameters for IPNs using contrast matching.

(Note that the hybrid model gave significantly better fits when PVP was contrast-matched at 25:75 D_2O:H_2O, while the Porod model alone gave acceptable fits when the PNIPAM was contrast-matched at 50:50 D_2O:H_2O.)

	Network Matched Out	Model Used	T (°C)	Porod exponent	Squared Lorentzian Correlation Length (nm)	Fluid Term Correlation Length (nm)	Fluid Term exponent
$IPN_{30\text{-high}}$	PVP	Hybrid	25	3.3	29	1.3	2.3
			32	3.3	28	1.5	1.8
			45	3.3	27	0.8	3.2
$IPN_{30\text{-low}}$		Hybrid	25	3.4	7.5	3.5	2.0
			32	3.3	8.3	5.3	2.1
			45	3.5	11	5.3	2.9
$IPN_{15\text{-high}}$		Hybrid	25	3.2	19	1.4	2.4
			32	3.1	18	1.4	2.7
			45	3.0	18	0.9	2.5
$IPN_{15\text{-med}}$		Hybrid	25	3.4	16	1.2	3.1
			32	3.3	15	1.1	2.9
			45	3.2	13	0.6	4.0
$IPN_{30\text{-high}}$	PNIPAM	Porod	25	3.3	-	0.77	3.1
			32	3.3	-	0.83	3.0
			45	3.3	-	0.78	3.3
$IPN_{30\text{-low}}$		Porod	25	3.2	-	1.9	1.9
			32	3.2	-	1.9	1.8
			45	3.2	-	1.6	2.0
$IPN_{15\text{-high}}$		Porod	25	3.2	-	1.1	2.2
			32	3.2	-	1.0	2.2
			45	3.2	-	1.0	2.4
$IPN_{15\text{-med}}$		Porod	25	3.2	-	0.81	3.4
			32	3.2	-	0.75	1.8
			45	3.2	-	0.70	2.2

4.4 Conclusion

A comprehensive small angle neutron scattering analysis of PNIPAM-hydrazone/PVP-disulfide IPN hydrogels formed by the interpenetration of a thermoresponsive PNIPAM network cross-linked by rapid hydrazone chemistry and a non-thermoresponsive PVP network cross-linked by slow disulfide chemistry demonstrated that significantly different IPN morphologies can be generated depending on the chemistry and gelation time of the PVP phase. Slower gelling PVP phases result in insignificant mixing of PVP clusters within PNIPAM-rich domains and larger degrees of PNIPAM phase separation (and thus network perturbation) upon heating compared to IPNs formed in which both the PVP and PNIPAM phase gel at similar rates. Furthermore, by reducing the molecular weight and/or the degree of functionalization of PVP pre-polymers used to prepare the IPNs, contrast matching fit results suggest that the correlation length between PNIPAM-rich static domains decreases. The results of this work can significantly inform the design of *in situ* gelling chemistries (both in terms of gelation kinetics and base chemistry) to facilitate the generation of well-defined interphases within injectable IPNs, materials with significant possible applications in drug delivery, wound healing, and tissue engineering.

Acknowledgements

This work utilized facilities supported in part by the National Science Foundation under Agreement No. DMR-0944772. We acknowledge the support of the National Institute of Standards and Technology, US Department of Commerce, in providing the neutron facilities used in this work.

We would also like to personally thank Boualem Hammouda and Yimin Mao, NCNR instrument scientists for the NG30 SANS, for supervising our neutron scattering experiments, as well as all the other NCNR staff who helped facilitate the research visits over which this data was collected.

Appendix 4S: Fitting parameter and X^2 values and component plots for hydrazone / disulfide IPN SANS models

Table 4S.1: PVP-disulfide single networks in D_2O Porod model fitting parameters

	PVP-SH_{30}			PVP-SH_{20}		PVP-SH_{15}	
	High MW	Med MW	Low MW	High MW	Med MW	High MW	Med MW
Porod Scale	1.25E-05	5.25E-06	4.74E-07	6.70E-05	4.02E-06	2.85E-06	2.19E-06
Porod Exponent	2.79	2.90	3.33	2.21	2.78	2.95	2.82
Lorentzian Scale	0.686	0.688	0.146	0.939	1.277	0.824	0.790
Fluid Correlation Length (nm)	2.25	2.52	2.07	3.61	3.66	2.59	2.76
Lorentzian Exponent	1.93	2.00	2.01	1.67	1.78	2.06	1.70
Bgd [1/cm]	0.0839	0.0750	0.405	0.0980	0.0737	0.0932	0.0713
X^2	1090	1370	339	275	304	2070	351
Sqrt(X^2/N)	2.19	2.44	1.21	1.10	1.15	2.99	1.27

Table 4S.2: PVP-disulfide single networks in D_2O hybrid model fitting parameters

	PVP-SH_{30}			PVP-SH_{20}		PVP-SH_{15}	
	High MW	Med MW	Low MW	High MW	Med MW	High MW	Med MW
Porod Scale	2.10E-06	5.47E-07	1.45E-07	2.90E-06	2.19E-06	7.72E-07	1.00E-07
Porod exponent	2.98	3.07	3.46	2.69	2.85	3.16	3.30
Static Domains scale	226	934	504	6.08	39.4	6.31	5.24
Domains Length 1	28.6	45.7	49.0	12.7	35.7	14.2	14.3
Fluid scale	1.08	1.19	0.278	1.27	1.43	0.879	0.842
Fluid Correlation Length (nm)	3.07	3.71	3.60	4.08	3.98	2.68	2.87
Fluid exponent	1.81	1.84	1.66	1.70	1.75	2.05	1.69
Incoherent Bgd (cm-1)	0.0821	0.0729	0.403	0.0982	0.0732	0.0932	0.0714
X^2	364	261	259	221	293	2050	286
Sqrt(X^2/N)	1.27	1.06	1.06	0.99	1.13	2.98	1.11

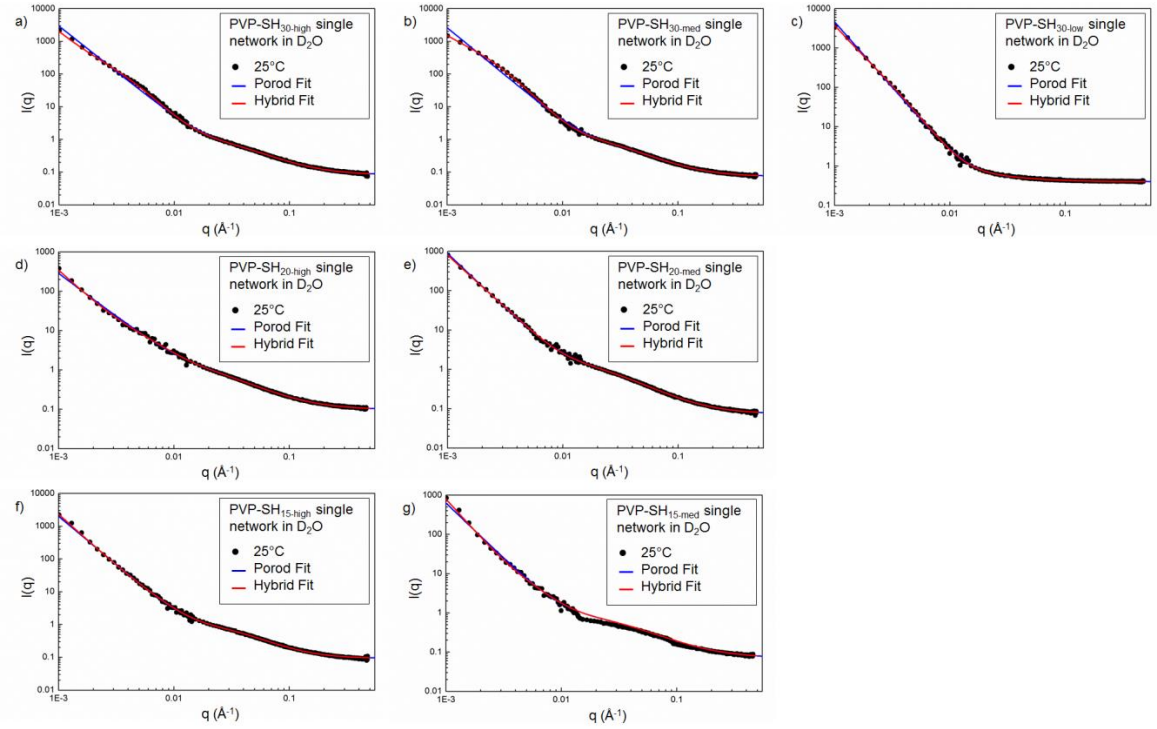

Figure 4S.1: SANS scattering profiles and comparison of Porod and hybrid model best-fits for all PVP-disulfide single networks measured in D_2O (3.5 wt% polymer): (a-c) 30% thiol functionalized high (PVP-$SH_{30\text{-high}}$, a), medium (PVP-$SH_{30\text{-med}}$, b) and low (PVP-$SH_{30\text{-low}}$, c) molecular weight PVP; (d,e) 20% thiol functionalized high (PVP-$SH_{20\text{-high}}$, d) and medium (PVP-$SH_{20\text{-med}}$, e) molecular weight PVP; (f,g) 15% thiol functionalized high (PVP-$SH_{15\text{-high}}$, f) and medium (PVP-$SH_{15\text{-med}}$, g) molecular weight PVP.

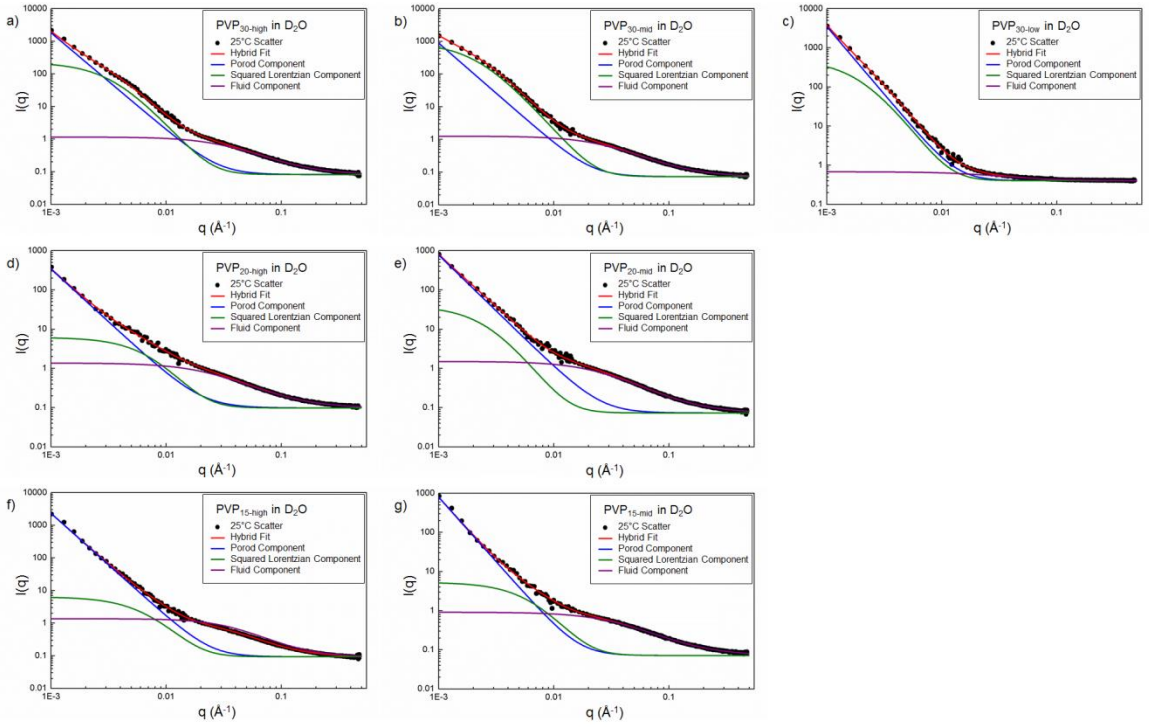

Figure 4S.2: Component breakdown of hybrid fits for a) PVP-$SH_{30\text{-}high}$; b) PVP-$SH_{30\text{-}med}$; c) PVP-$SH_{30\text{-}low}$; d) PVP-$SH_{20\text{-}high}$; e) PVP-$SH_{20\text{-}med}$; f) PVP-$SH_{15\text{-}high}$ and g) PVP-$SH_{15\text{-}med}$ single networks. The squared Lorentzian contributes significantly to the total fit in (a) and (b), but less so in the other compositions.

Table 4S.3: Hybrid model fitting parameters for IPNs prepared with PVP-SH_{30} pre-polymers in D_2O.

	$IPN_{30\text{-}high}$		
	25°C	32°C	45°C
Porod Scale	5.19E-06	1.1E-05	6.22E-05
Porod exponent	3.03	2.96	2.81
Static Domains scale	123	168	2345
Static Correlation Length (nm)	12.8	12.1	19.7
Fluid scale	5.01	3.68	1.41
Fluid Correlation Length (nm)	4.50	3.40	2.61
Fluid exponent	1.95	2.16	1.98
Incoherent Bgd (cm-1)	0.117	0.126	0.119
X^2	290	890	382
Sqrt(X^2/N)	1.12	1.96	1.28
	$IPN_{30\text{-}med}$		
	25°C	32°C	45°C
Porod Scale	7.74E-06	8.84E-06	2.41E-06
Porod exponent	2.99	2.97	3.18
Static Domains scale	41	67	276
Static Correlation Length (nm)	7.7	8.6	12.4
Fluid scale	3.18	4.44	29.2
Fluid Correlation Length (nm)	3.09	3.51	6.19
Fluid exponent	2.11	2.15	2.54
Incoherent Bgd (cm-1)	0.0979	0.0980	0.110
X^2	505	235	926
Sqrt(X^2/N)	1.48	1.01	2
	$IPN_{30\text{-}low}$		
	25°C	32°C	45°C
Porod Scale	9.29E-05	0.000185	0.000211
Porod exponent	2.72	2.62	2.66
Static Domains scale	89	131	651
Static Correlation Length (nm)	38.4	22.2	14.9
Fluid scale	2.56	2.06	0.318
Fluid Correlation Length (nm)	3.87	3.55	1.10
Fluid exponent	1.73	1.77	2.28
Incoherent Bgd (cm-1)	0.135	0.139	0.148
X^2	317	304	623
Sqrt(X^2/N)	1.17	1.14	1.64

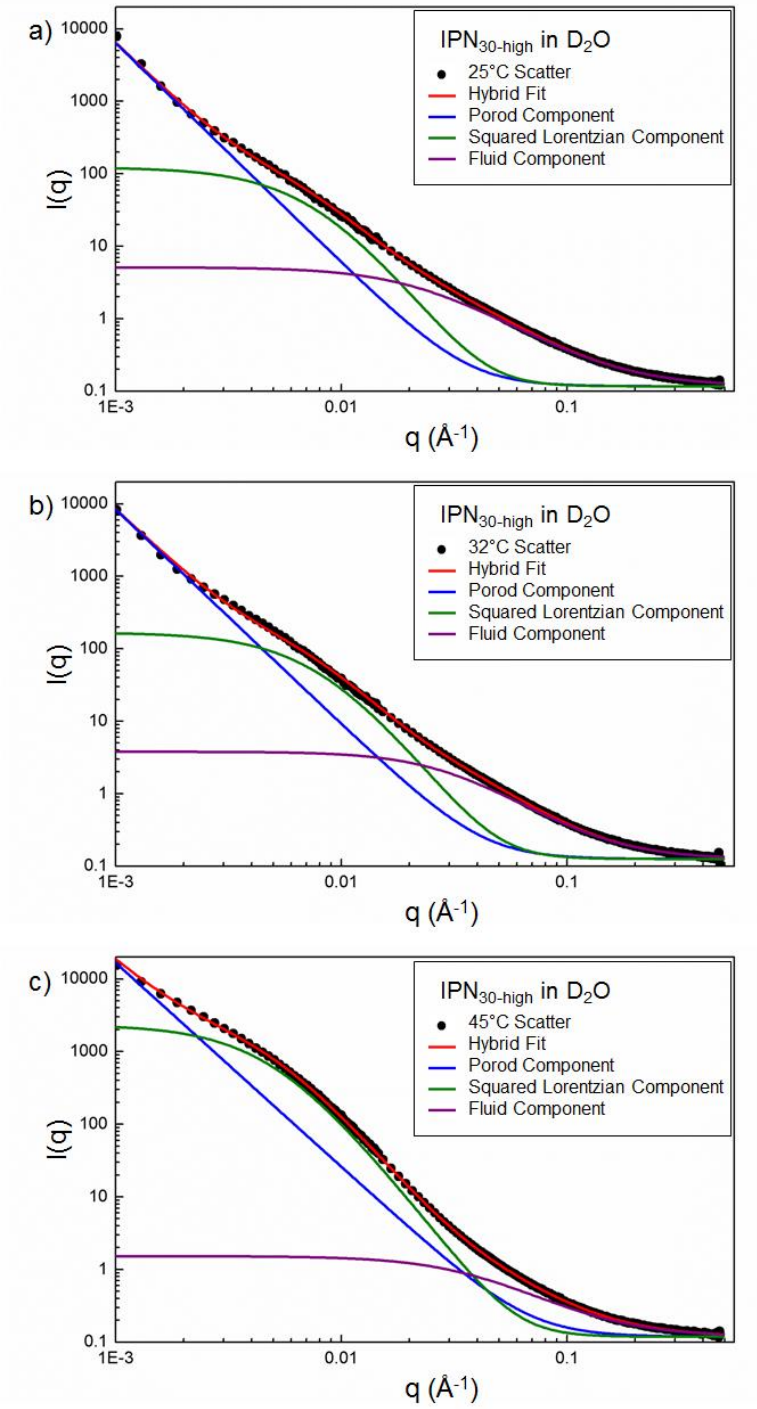

Figure 4S.3: Individual plots (with component breakdown) of hybrid fits for IPNs prepared using PVP-$SH_{30\text{-}high}$: a) 25°C (T<VPTT of PNIPAM); b) 32°C (T~VPTT of PNIPAM); c) 45°C (T>VPTT of PNIPAM). The squared Lorentzian component is a significant contributor to the total fit profile at mid-*q* ranges coinciding with the peak feature, while the Porod contribution dominates low-*q* scattering.

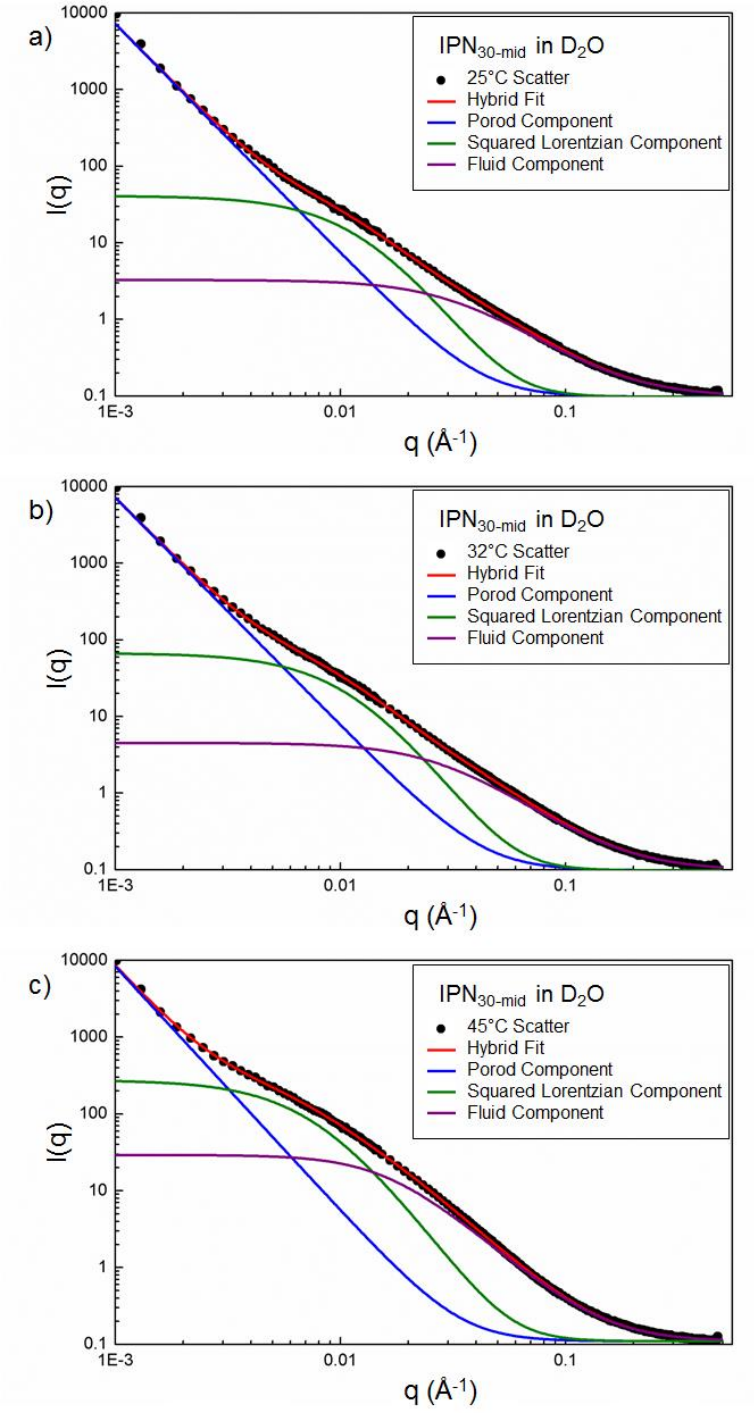

Figure 4S.4: Individual plots (with component breakdown) of hybrid fits for IPN using PVP-$SH_{30\text{-}med}$: a) 25°C (T<VPTT of PNIPAM); b) 32°C (T~VPTT of PNIPAM); c) 45°C (T>VPTT of PNIPAM). The squared Lorentzian component is a significant contributor to the total fit profile at mid-*q* ranges coinciding with the peak feature, while the Porod contribution dominates low-*q* scattering.

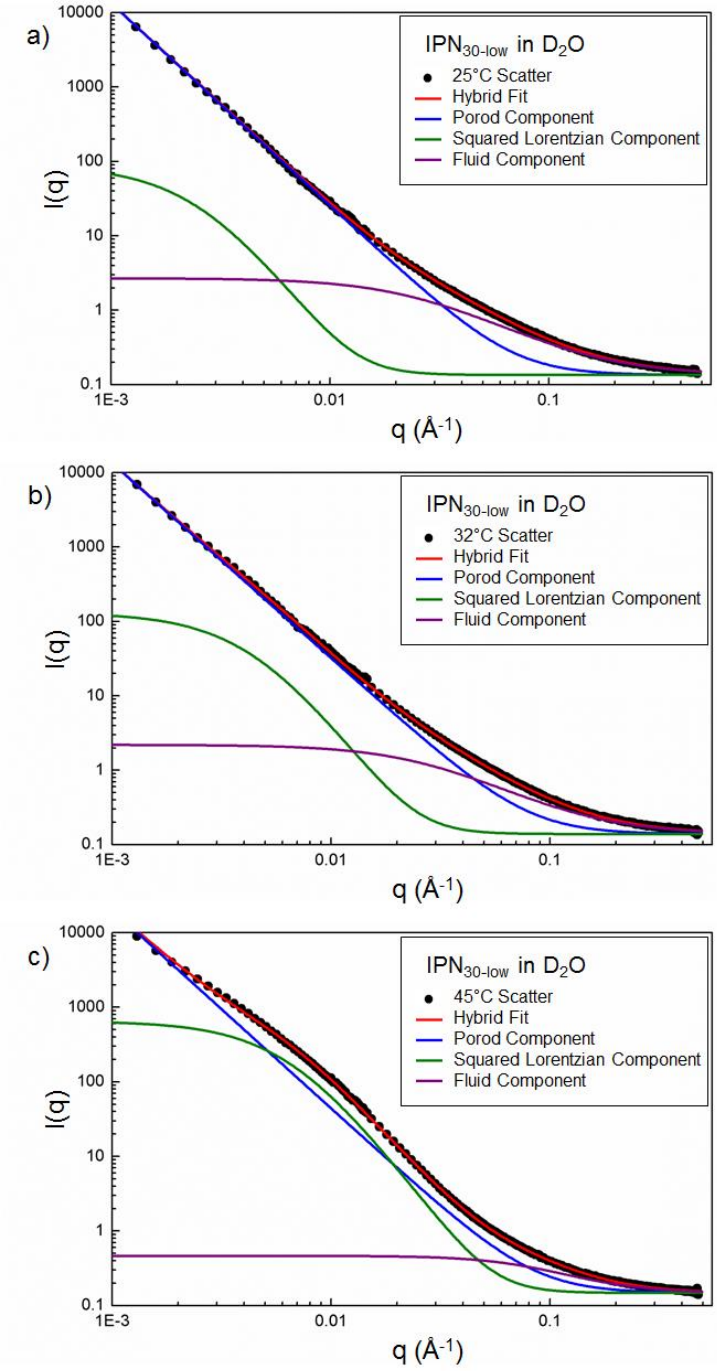

Figure 4S.5: Individual plots (with component breakdown) of hybrid fits for IPN using PVP-$SH_{30\text{-}low}$: a) 25°C (T<VPTT of PNIPAM); b) 32°C (T~VPTT of PNIPAM); c) 45°C (T>VPTT of PNIPAM). The hybrid fits for this IPN are considerably more Porod-dominated than those using higher molecular weight PVP-SH 70-30 (especially at 25°C and 32°C), corresponding to a smaller peak and therefore a lesser extent of domain formation.

Table 4S.4: Hybrid model fitting parameters for IPNs prepared with PVP-SH_{20} pre-polymers in D_2O.

	$IPN_{20\text{-high}}$		
	25°C	32°C	45°C
Porod Scale	1.32E-06	2.12E-06	7.97E-05
Porod exponent	3.15	3.10	2.68
Static Domains scale	68.7	180.6	571.9
Static Correlation Length (nm)	8.76	11.00	10.44
Fluid Correlation Length (nm)	5.13	7.14	6.50
Fluid exponent	3.91	4.03	8.27
Incoherent Bgd (cm-1)	2.10	2.31	1.78
X^2	0.123	0.131	0.121
Sqrt(X^2/N)	715	637	3140
Porod Scale	1.76	1.66	3.68
			(Poor fit)
	$IPN_{20\text{-med}}$		
	25°C	32°C	45°C
Porod Scale	3.21E-07	1.9E-06	1.68E-05
Porod exponent	3.38	3.11	2.83
Static Domains scale	40.8	89.0	282.1
Static Correlation Length (nm)	7.34	9.03	7.92
Fluid scale	4.88	8.30	11.96
Fluid Correlation Length (nm)	3.52	4.18	7.12
Fluid exponent	2.23	2.33	2.21
Incoherent Bgd (cm-1)	0.103	0.105	0.103
X^2	524	519	7180
Sqrt(X^2/N)	1.5	1.5	5.56
			(Poor fit)

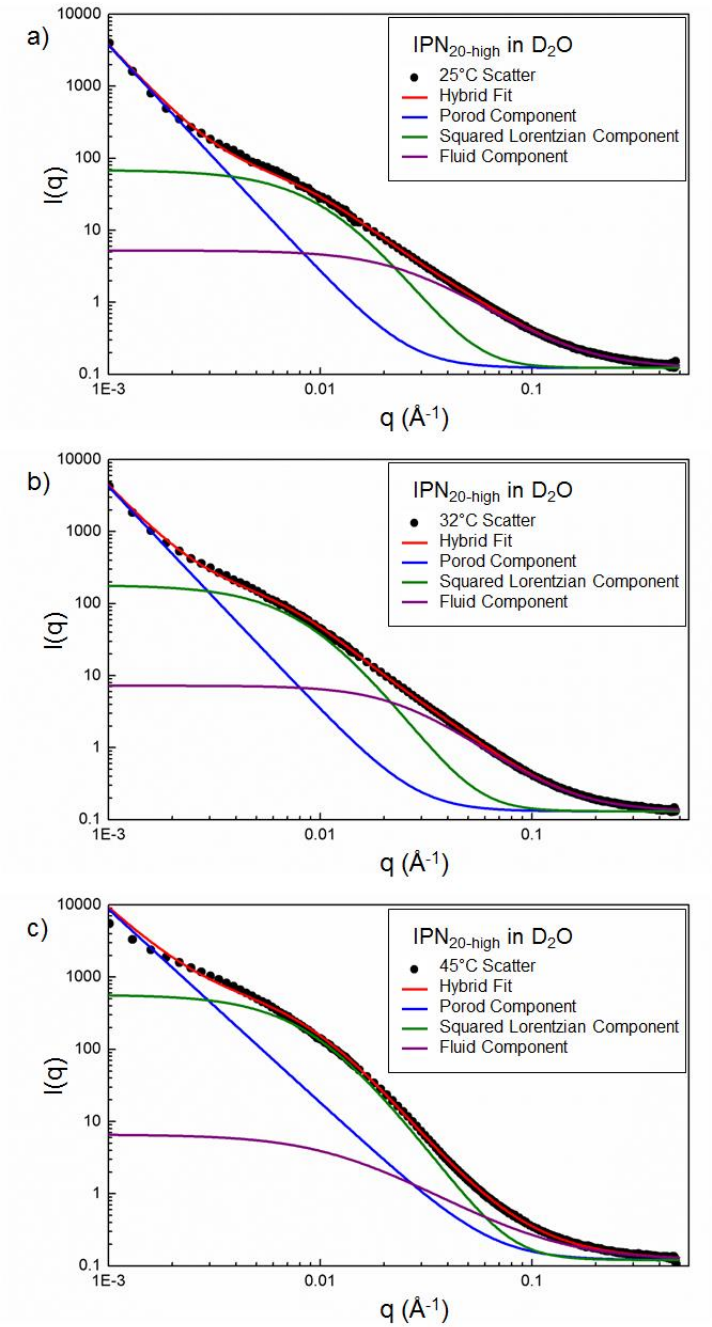

Figure 4S.6: Individual plots (with component breakdown) of hybrid fits for IPN using PVP-$SH_{20\text{-}high}$: a) 25°C (T<VPTT of PNIPAM); b) 32°C (T~VPTT of PNIPAM); c) 45°C (T>VPTT of PNIPAM). The squared Lorentzian component is a significant contributor to the total fit profile at mid-*q* ranges coinciding with the peak feature, while the Porod contribution dominates low-*q* scattering. The hybrid model achieves accurate fits at 25°C and 32°C, but cannot completely account for the width of the scattering feature arising from static inhomogeneities at 45°C, deviating from the data at low q.

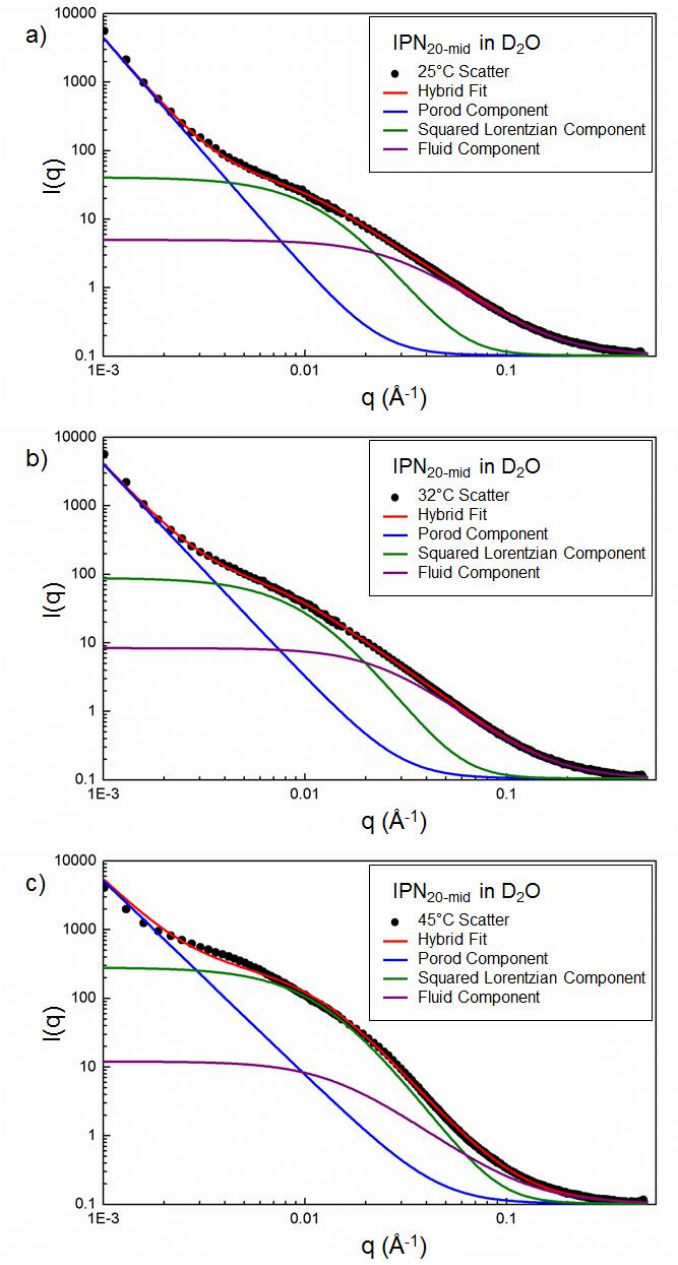

Figure 4S.7: Individual plots (with component breakdown) of hybrid fits for IPN using PVP-$SH_{20\text{-}med}$: a) 25°C (T<VPTT of PNIPAM); b) 32°C (T~VPTT of PNIPAM); c) 45°C (T>VPTT of PNIPAM). The squared Lorentzian component is a significant contributor to the total fit profile at mid-*q* ranges, but does not perfectly accurately capture the profile of the peak feature. The Porod contribution dominates low-*q* scattering. The hybrid model achieves accurate fits at 25°C and 32°C, but cannot completely account for the width of the scattering feature arising from static inhomogeneities at 45°C, deviating from the data at low q.

Table 4S.5: Hybrid model fitting parameters for IPNs prepared with PVP-SH_{15} pre-polymers in D_2O.

	$IPN_{15\text{-high}}$		
	25°C	32°C	45°C
Porod Scale	1.03E-07	5.69E-08	1.02E-07
Porod exponent	3.66	3.75	3.71
Static Domains scale	76.9	90.8	127
Static Correlation Length (nm)	13.5	11.3	7.08
Fluid scale	4.55	5.30	2.68
Fluid Correlation Length (nm)	5.27	4.80	4.61
Fluid exponent	1.56	1.76	1.48
Incoherent Bgd (cm-1)	0.127	0.137	0.124
X^2	232	514	1830
Sqrt(X^2/N)	1	1.49	2.81
			(Poor fit)
	$IPN_{15\text{-med}}$		
	25°C	32°C	45°C
Porod Scale	2.4E-05	0.000429	1.04E-05
Porod exponent	2.60	2.29	3.00
Static Domains scale	218	498	3110
Static Correlation Length (nm)	11.0	12.2	14.7
Fluid scale	15.9	16.4	0.234
Fluid Correlation Length (nm)	7.25	6.67	1.00
Fluid exponent	2.03	2.38	2.02
Incoherent Bgd (cm-1)	0.110	0.120	0.101
X^2	553	3210	24000
Sqrt(X^2/N)	1.54	3.72	10.2
		(Poor and very poor fits)	

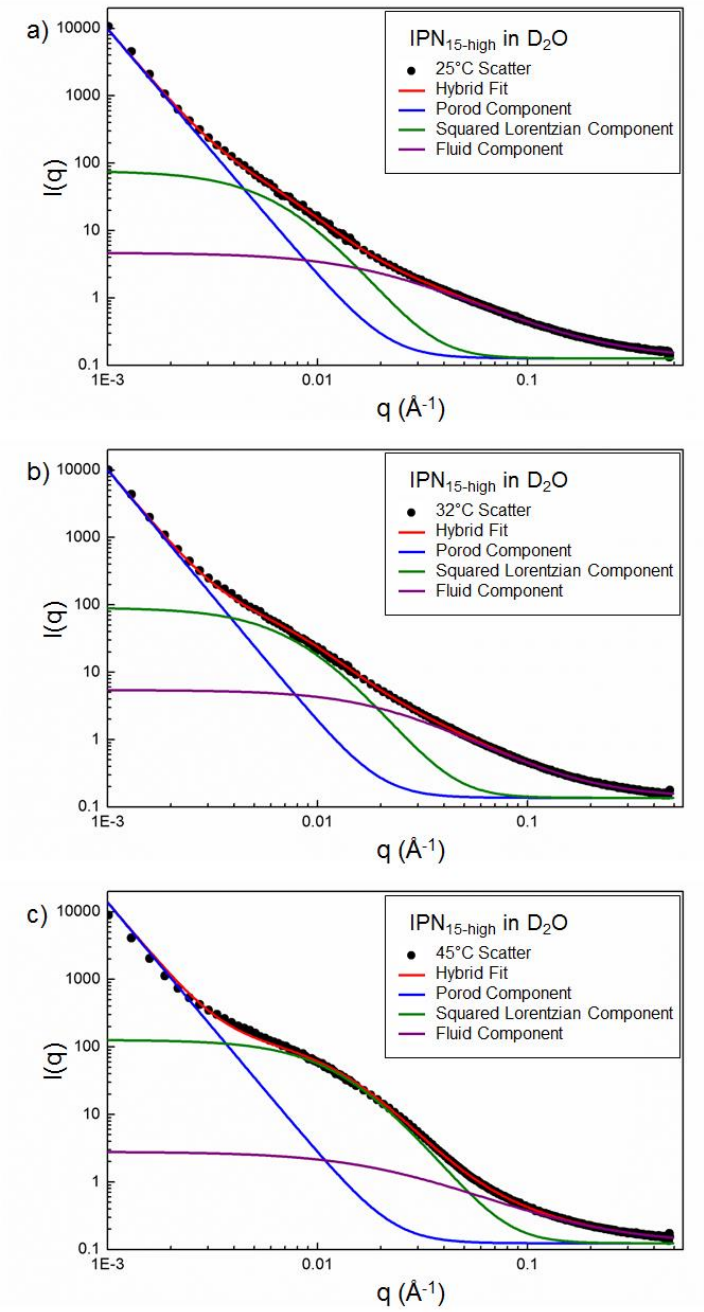

Figure 4S.8: Individual plots (with component breakdown) of hybrid fits for IPN using PVP-SH$_{15\text{-high}}$: a) 25°C (T<VPTT of PNIPAM); b) 32°C (T~VPTT of PNIPAM); c) 45°C (T>VPTT of PNIPAM). The squared Lorentzian component is a significant contributor to the total fit profile at mid-*q* ranges, but does not perfectly accurately capture the profile of the peak feature. The Porod contribution dominates low-*q* scattering. The hybrid model achieves accurate fits at 25°C and 32°C, but cannot completely account for the width of the scattering feature arising from static inhomogeneities at 45°C, deviating from the data at low q.

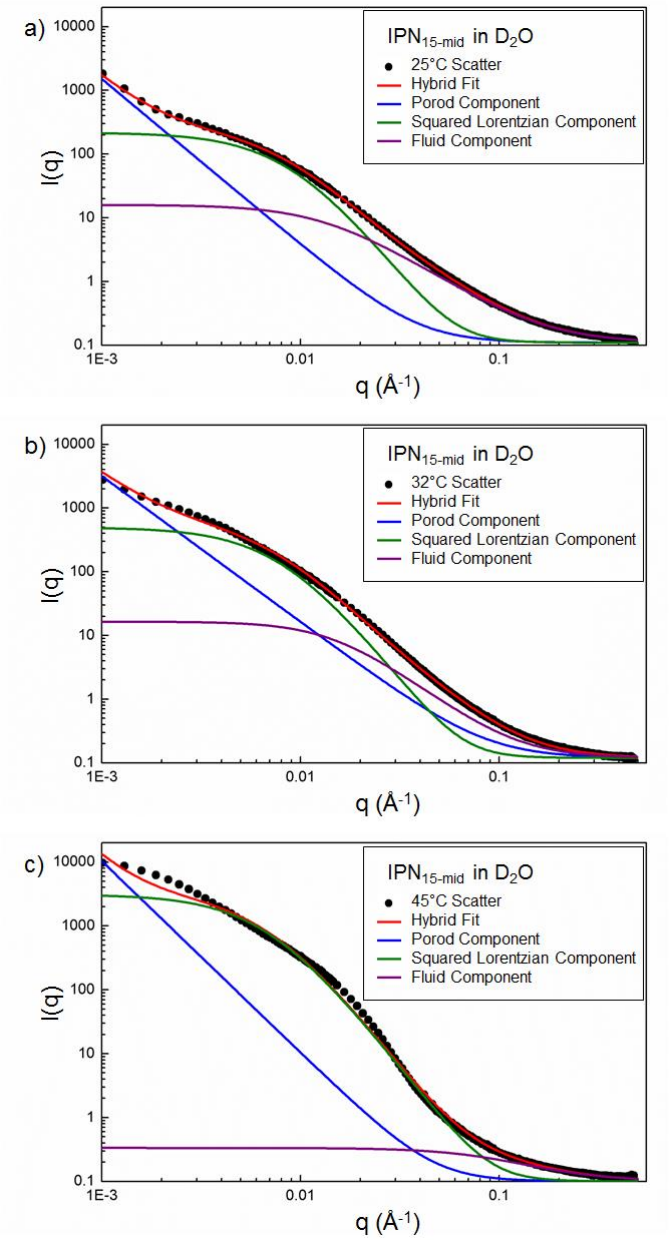

Figure 4S.9: Individual plots (with component breakdown) of hybrid fits for IPN using PVP-$SH_{15\text{-}med}$: a) 25°C (T<VPTT of PNIPAM); b) 32°C (T~VPTT of PNIPAM); c) 45°C (T>VPTT of PNIPAM). The squared Lorentzian component is a significant contributor to the total fit profile at mid-*q* ranges, but poorly captures the profile of the peak feature, while the Porod contribution dominates low-*q* scattering. The hybrid model achieves accurate fits at 25°C, but cannot completely account for the width of the scattering feature arising from static inhomogeneities at higher temperatures, deviating from the data at low *q* slightly at 32°C and more significantly at 45°C.

Table 4S.6: Porod model best-fit parameters for IPNs with deuterated PNIPAM network scattering contrast-suppressed

	IPN_{30} (deuterated PNIPAM network matched out)					
	High MW			Med MW		
	25°C	32°C	45°C	25°C	32°C	45°C
Porod Scale	1.93E-06	2.27E-06	2.27E-06	2.00E-06	1.66E-06	1.57E-06
Porod Exponent	3.29	3.25	3.27	3.16	3.21	3.22
Lorentzian Scale	0.0562	0.0580	0.0541	0.138	0.137	0.111
Fluid Correlation Length (nm)	0.769	0.831	0.781	1.87	1.88	1.56
Lorentzian Exponent	3.12	3.00	3.31	1.93	1.81	2.02
Bgd [1/cm]	0.575	0.580	0.582	0.500	0.501	0.502
Chi^2	286.7	320.5	357.6	376.3	291.8	369.6
Sqrt(X^2/N)	1.1	1.16	1.22	1.26	1.1	1.24
	IPN_{15} (deuterated PNIPAM network matched out)					
	High MW			Med MW		
	25°C	32°C	45°C	25°C	32°C	45°C
Porod Scale	1.24E-06	1.40E-06	1.44E-06	1.59E-06	1.60E-06	1.71E-06
Porod Exponent	3.21	3.19	3.19	3.18	3.18	3.22
Lorentzian Scale	0.0465	0.0433	0.0361	0.0242	0.0324	0.0345
Fluid Correlation Length (nm)	1.14	0.955	0.968	0.812	0.751	0.697
Lorentzian Exponent	2.16	2.15	2.37	3.38	1.83	2.25
Bgd [1/cm]	0.483	0.485	0.494	0.564	0.561	0.562
Chi^2	302.6	348.9	317.8	430.6	456.8	366.9
Sqrt(X^2/N)	1.13	1.21	1.15	1.35	1.38	1.24

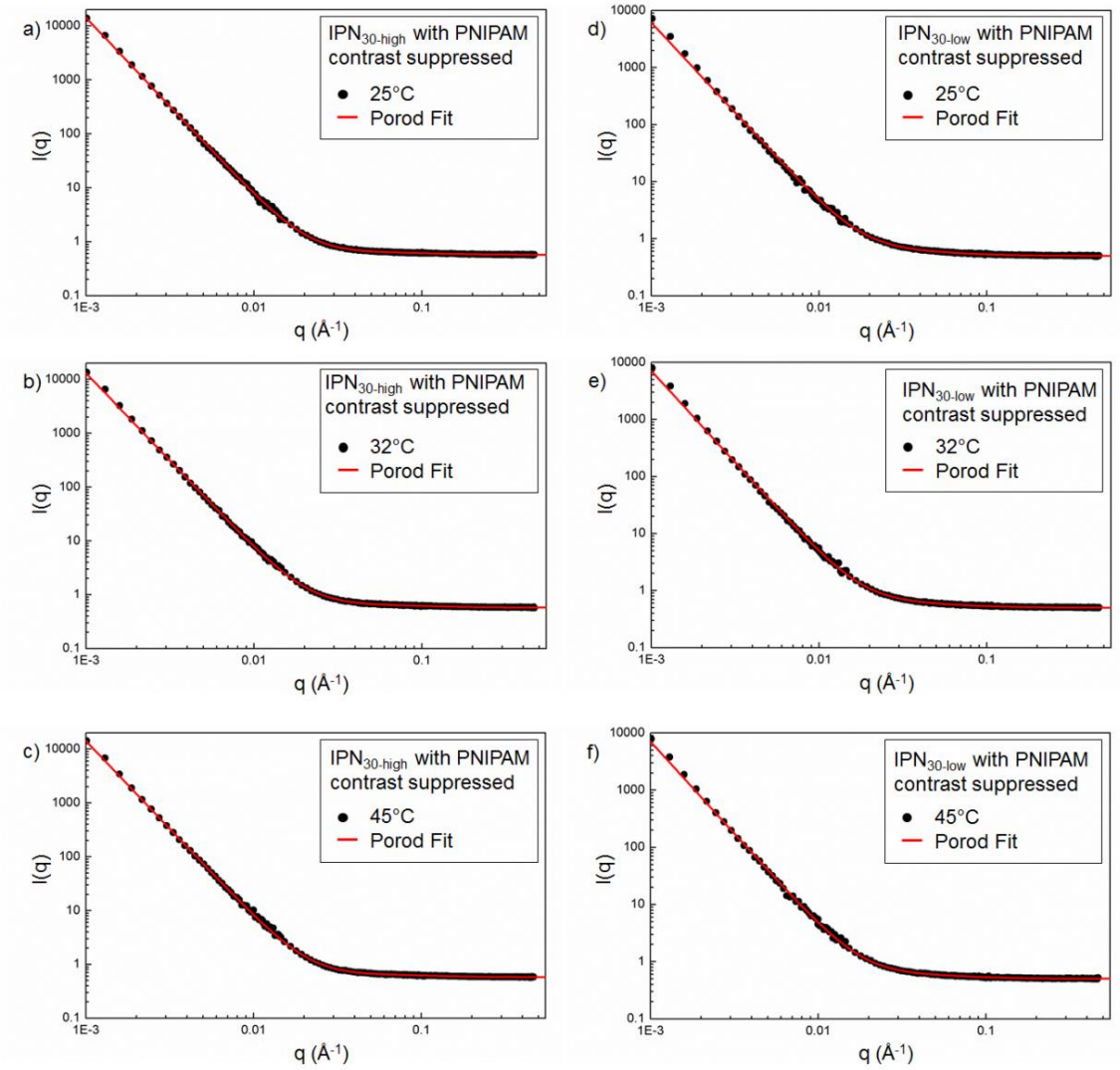

Figure 4S.10: Porod model fits for IPNs made with PVP-SH_{30} and PNIPAM contrast-suppressed for (a,c,e) PVP-$SH_{30\text{-high}}$ and (b,d,f) PVP-$SH_{30\text{-low}}$ at (a,b) 25°C, (c,d) 32°C and (e,f) 45°C

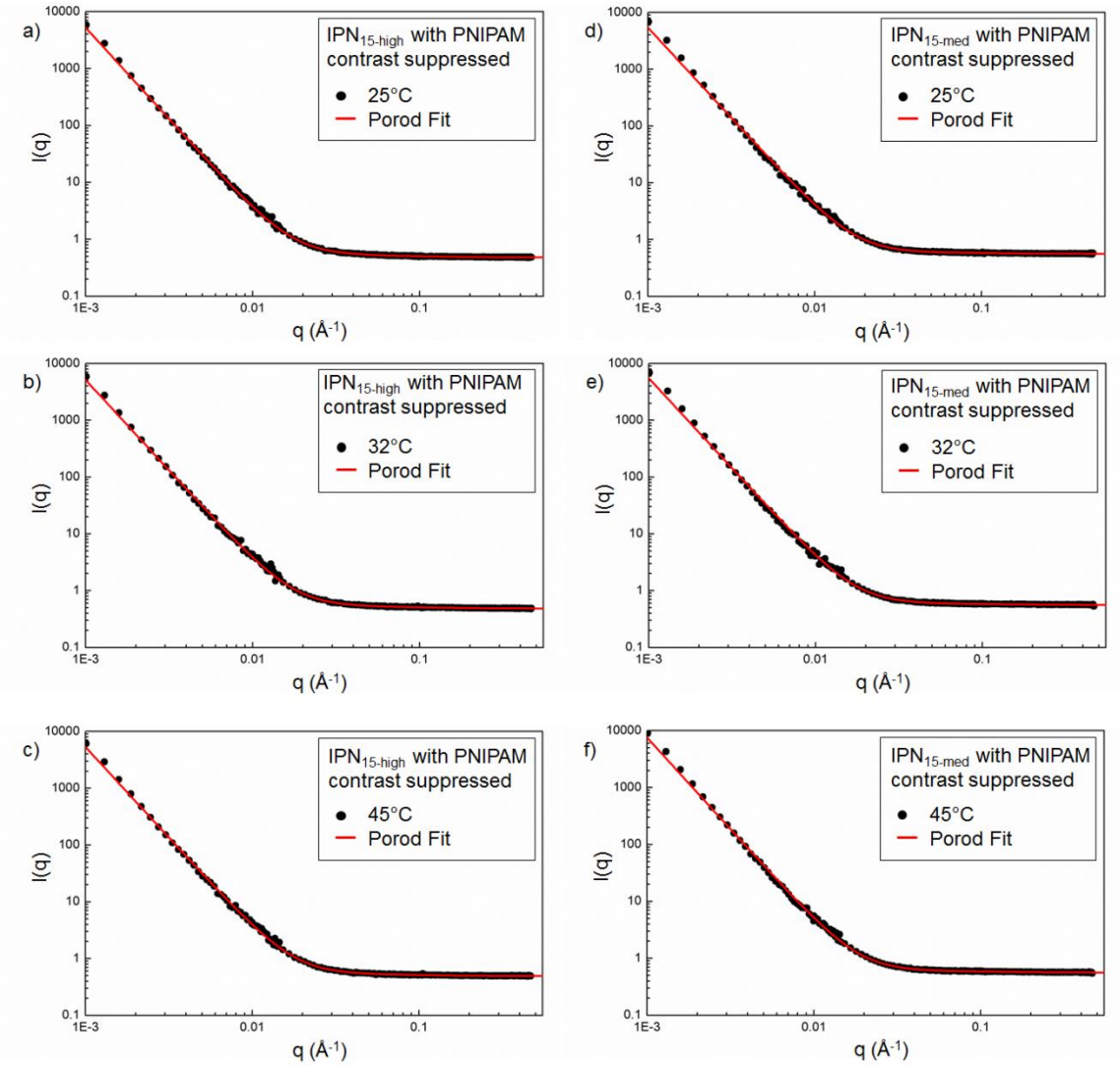

Figure 4S.11: Porod model fits for IPNs made with PVP-SH_{15} and PNIPAM contrast-suppressed for (a,c,e) PVP-$SH_{15\text{-high}}$ and (b,d,f) PVP-$SH_{15\text{-med}}$ at (a,b) 25°C, (c,d) 32°C and (e,f) 45°C

Table 4S.7: Hybrid model best-fit parameters for IPN_{30} networks with PVP scattering contrast-suppressed

	$IPN_{30\text{-high}}$ (PVP matched out)		
	25°C	32°C	45°C
Porod Scale	7.36E-07	1.00E-06	1.59E-06
Porod exponent	3.32	3.29	3.26
Static Domains scale	773	831	1060
Static Correlation Length (nm)	28.8	28.0	26.7
Fluid scale	0.0917	0.100	0.0352
Fluid Correlation Length (nm)	1.32	1.51	0.845
Fluid exponent	2.32	1.82	3.16
Incoherent Bgd (cm-1)	0.761	0.760	0.770
X^2	330	337	461
Sqrt(X^2/N)	1.18	1.19	1.39
	$IPN_{30\text{-low}}$ (PVP matched out)		
	25°C	32°C	45°C
Porod Scale	1.62E-07	1.90E-07	8.40E-08
Porod exponent	3.36	3.34	3.48
Static Domains scale	9.8	11.5	18.5
Static Correlation Length (nm)	7.5	8.3	11.1
Fluid scale	0.547	1.360	3.91
Fluid Correlation Length (nm)	3.46	5.28	5.30
Fluid exponent	1.99	2.06	2.86
Incoherent Bgd (cm-1)	0.736	0.736	0.744
X^2	268	221	248
Sqrt(X^2/N)	1.06	0.97	1.02

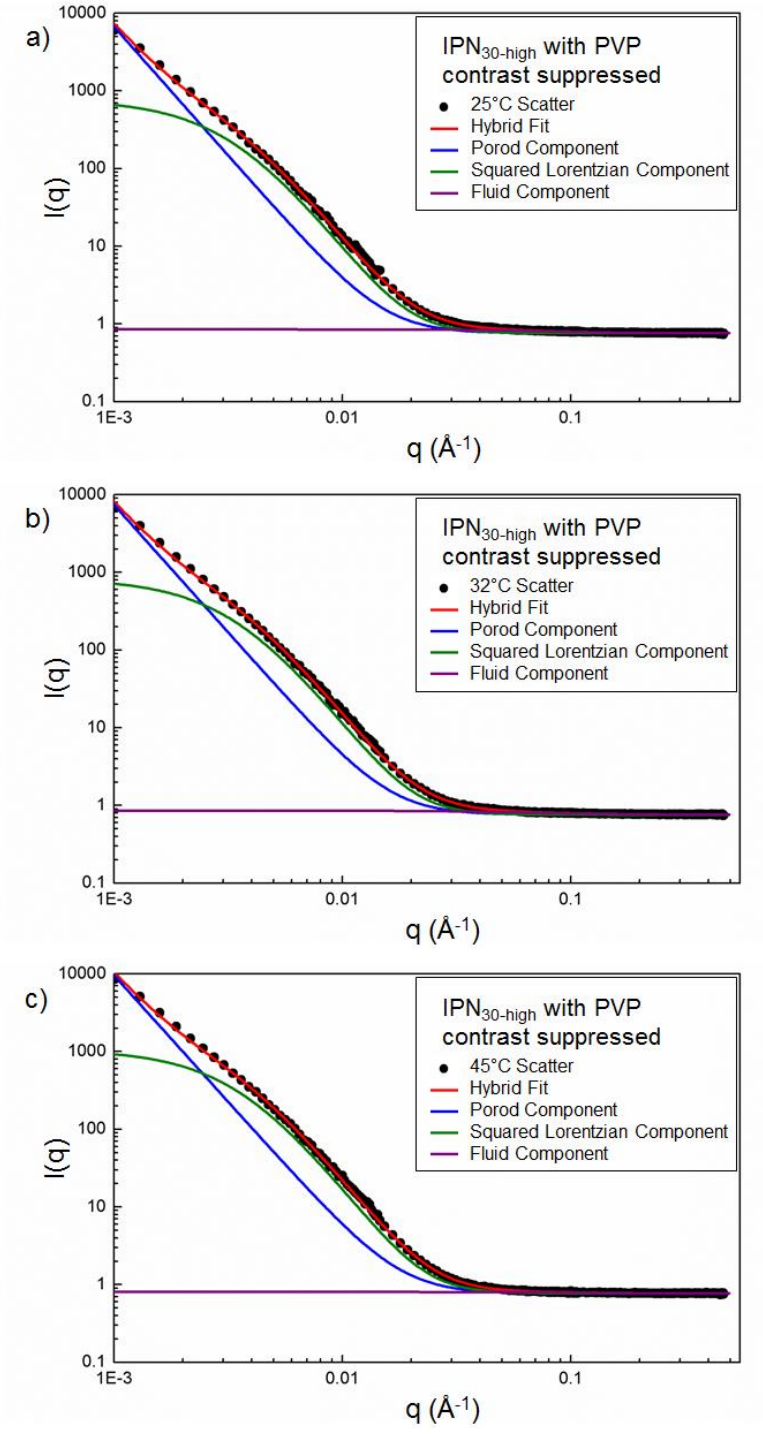

Figure 4S.12: Individual plots (with component breakdown) of hybrid fits for IPNs made with PVP-$SH_{30\text{-}high}$ and PVP scattering contrast-suppressed: a) 25°C; b) 32°C; c) 45°C. Hybrid fit profiles are Porod-dominated at low q, with the squared Lorentzian component more significant at mid-*q* ranges.

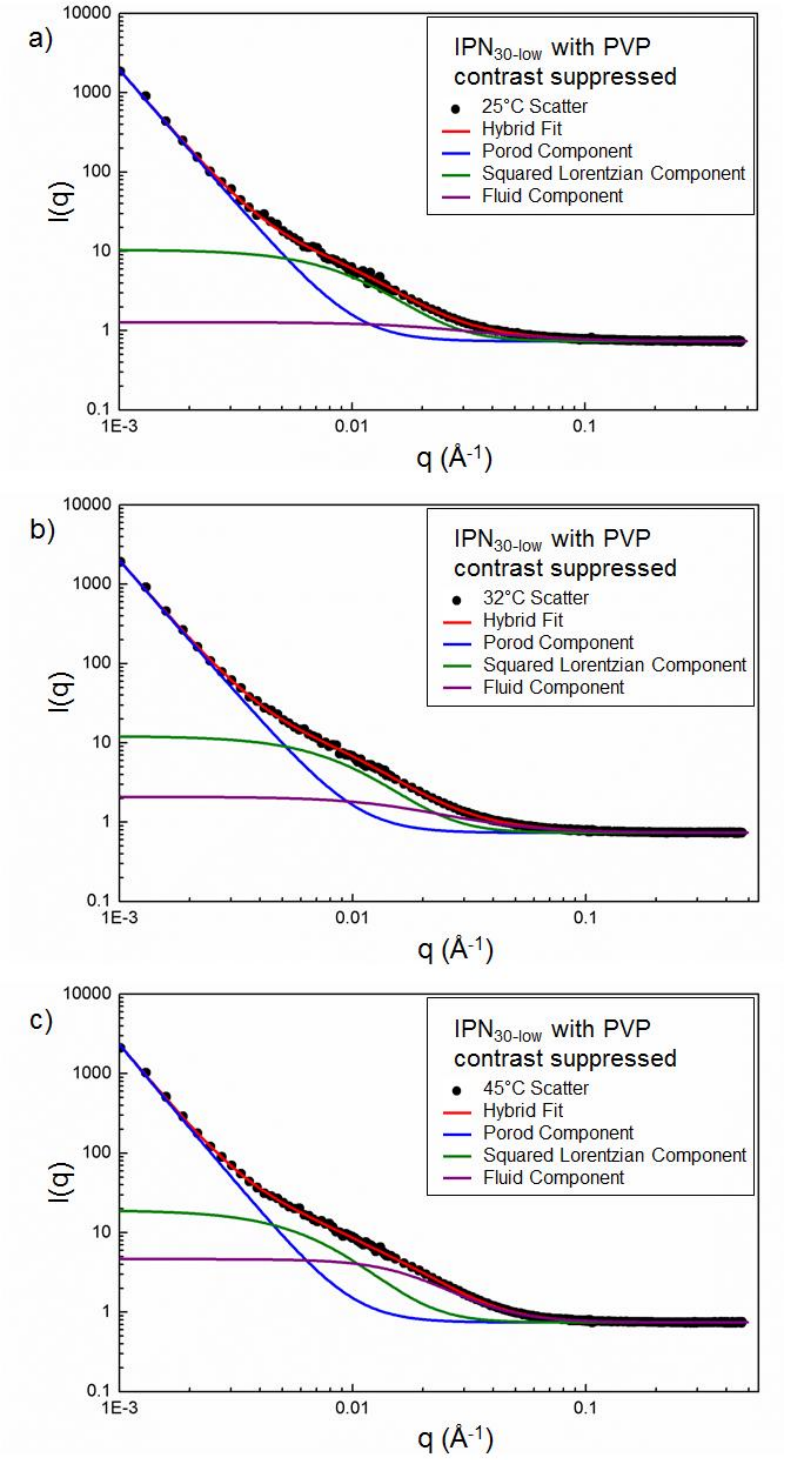

Figure 4S.13: Individual plots (with component breakdown) of hybrid fits for IPNs made using PVP-$SH_{30\text{-}low}$ and PVP scattering contrast-suppressed: a) 25°C; b) 32°C; c) 45°C. Fit profiles are more Porod-dominated than the corresponding high molecular weight formulations.

Table 4S.8: Hybrid model parameters for IPN_{15} networks with PVP scattering contrast-suppressed.

	$IPN_{15\text{-high}}$ (PVP matched out)		
	25°C	32°C	45°C
Porod Scale	1.01E-06	1.27E-06	3.84E-06
Porod exponent	3.16	3.14	3.02
Static Domains scale	137	133	169
Static Correlation Length (nm)	19.4	18.2	17.8
Fluid Correlation Length (nm)	0.0787	0.0788	0.0327
Fluid exponent	1.38	1.35	0.94
Incoherent Bgd (cm-1)	2.39	2.68	2.52
X^2	0.769	0.768	0.769
Sqrt(X^2/N)	303	342	329
Porod Scale	1.13	1.19	1.17
	$IPN_{15\text{-med}}$ (PVP matched out)		
	25°C	32°C	45°C
Porod Scale	1.25E-07	2.82E-07	5.69E-07
Porod exponent	3.41	3.30	3.23
Static Domains scale	133	126	138
Static Correlation Length (nm)	15.7	14.9	13.3
Fluid scale	0.0611	0.0528	0.0155
Fluid Correlation Length (nm)	1.20	1.15	0.61
Fluid exponent	3.11	2.95	4.00
Incoherent Bgd (cm-1)	0.685	0.687	0.691
X^2	425	442	544
Sqrt(X^2/N)	1.34	1.36	1.51

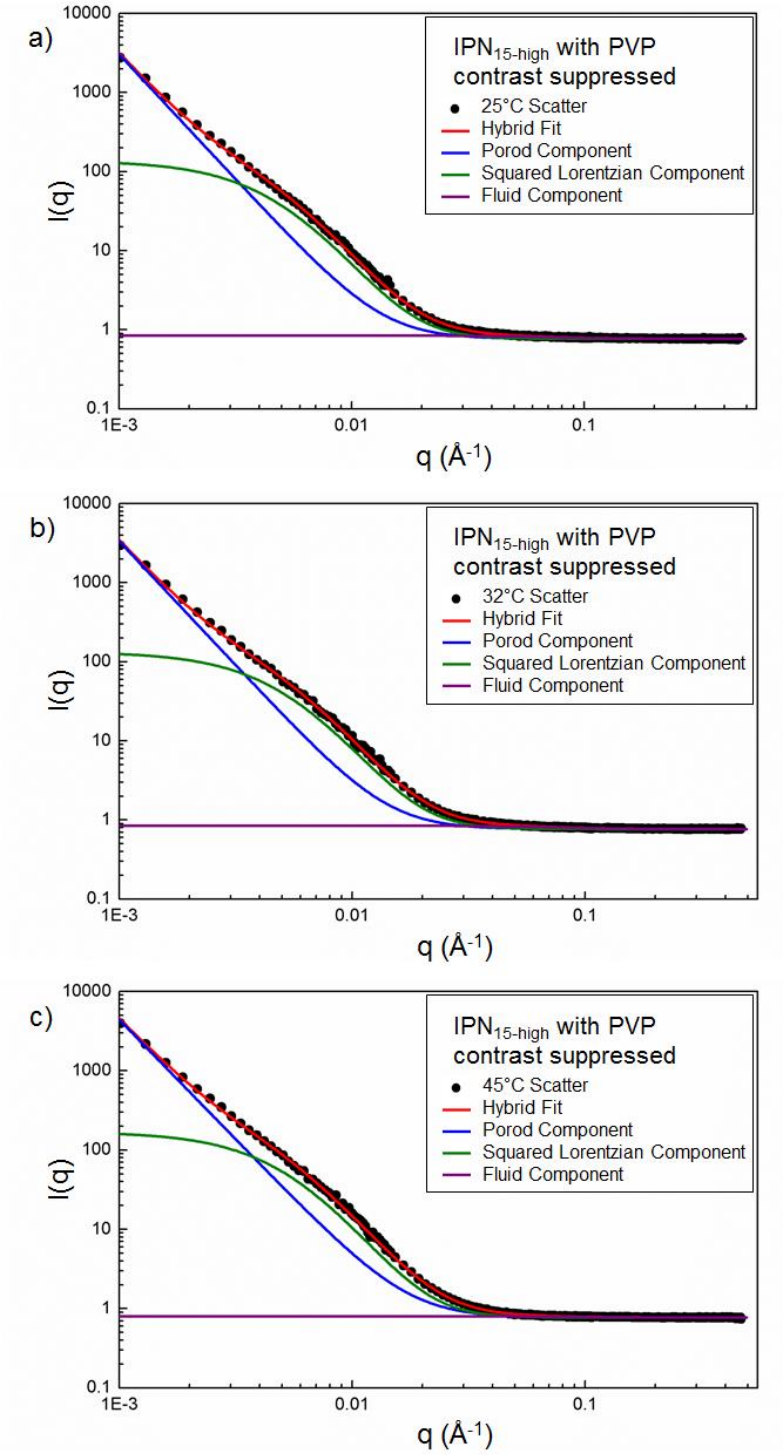

Figure 4S.14: Component breakdown of hybrid fits for $IPN_{15\text{-}high}$ with PVP scattering contrast-suppressed: a) 25°C; b) 32°C; c) 45°C. Fit profiles are Porod-dominated at low q, with the squared Lorentzian component more significant at mid-*q* ranges.

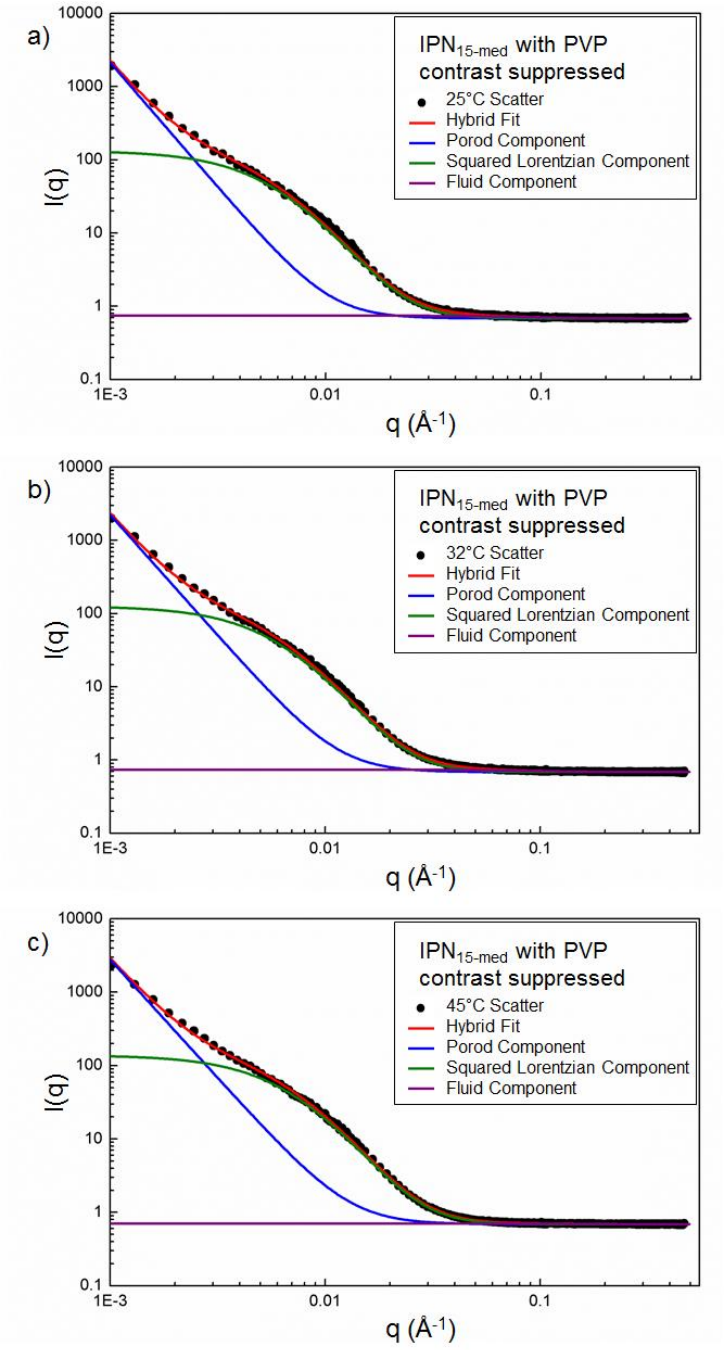

Figure 4S.15: Component breakdown of hybrid fits for $IPN_{15\text{-}med}$ with PVP scattering contrast-suppressed: a) 25°C; b) 32°C; c) 45°C. The Porod component contribution dominates the hybrid model at low q, but the squared Lorentzian component is more important at mid-q.

Chapter 5: A synthetic platform for measuring the mechanics of hydrogel adhesion to mucin layers bound to soft substrates – an *in vitro* alternative to soft tissue mucoadhesion studies

Preface

The thiol-based cross-linking reactions used in the PVP networks described in the previous chapters suggest that these formulations may also be capable of adhering to thiol-bearing surfaces, such as the cysteine-rich mucin layer found on biological mucin membranes. This chapter describes progress toward development of an artificial platform for assessing the mucoadhesive properties of disulfide-cross-linked hydrogels on functionalized soft material substrates used as models for mucous membranes. The system is designed to more closely recapitulate the biological context of mucin films coating underlying tissue than alternative *in vitro* measurement, while mitigating some of the disadvantages of using *ex vivo* tissue samples. Sample holders were designed in collaboration with Biomomentum Inc., with preliminary proof of concept testing carried out at their facilities using an appropriate load cell (a copy of which is on order to use with our installation to complete testing).

Trevor Gilbert[1], Eric Quenneville[2], and Todd Hoare*[1]

1 Department of Chemical Engineering, McMaster University, 1280 Main St. W, Hamilton, Ontario, Canada L8S 4L7

2 Biomomentum Inc., 970 Rue Michelin, Laval, Québec, Canada H7L 5C1

Abstract:

While mucoadhesion is widely applied in biomaterials for drug delivery and wound healing, the *a priori* measurement of mucoadhesive force is challenging given the practical difficulties associated with truly representative use of *ex vivo* tissues. Furthermore, molecular-scale measurements of mucoadhesion are inherently local and do not always predict adhesive performance of macroscopic materials. Herein, we describe a new lap shear testing configuration based on the immobilization of mucin on a functionalized soft silicone substrate that models the mechanics of soft biological tissues. Preliminary proof of concept testing using disulfide cross-linked gels adhered directly to the functionalized substrates demonstrated the system's capability to measure the work of adhesion and the critical stress / strain to failure for the adhesive interface. Small-amplitude, non-destructive testing was also able to demonstrate the shear modulus of the hydrogel sample itself, while shear tests after breaking the interface were able to detect stick-slip behaviour attributable to physical tack. We anticipate this approach can minimize the sample-to-sample variability and interfacial flatness challenges of *ex vivo* testing while still providing a bulk mechanical measurement on a tissue-mimetic substrate.

5.1 Introduction

The adhesion of hydrogels to mucosal membranes is of interest in the design of a range of biomedical devices, predominantly drug delivery[173] and wound healing[249]. From a drug delivery perspective, mucoadhesion facilitates potential targeting to, prolonged retention at and/or higher bioavailability to local sites coated with mucin layers, including

the gastrointestinal, oral, nasal, reproductive, ocular and respiratory systems (subject to natural turnover in that local mucosal layer)[180]. From a wound healing perspective, mucoadhesive gels have potential for immobilizing a wound dressing, minimizing the risk of infiltrative infections. Mucoadhesive formulations also have potential applications for physical treatment of dry eye syndrome[249], surgical adhesives[250], and other applications in which prolonged retention of a hydrogel (bulk or particulate) is desirable at a local site.

Current methods of testing mucoadhesion can generally be divided into three categories: *ex vivo* analysis, nanoscale analysis on model mucin surfaces, or bulk mechanical testing on mucin-coated substrates. *Ex vivo* methods in which mucosal tissues recovered from animal cadavers[181-182] are of obvious interest in terms of providing an optimally representative test sample to the targeted mucosal interface to be studied. However, cadaver tissue samples are subject to significant non-uniformity and have a relatively short usable window before degradation begins. This is problematic for longer-term adhesion studies (i.e. tracking adhesion as a function of hydrogel degradation), as well as requiring testing within a short time window following sample acquisition. Cadaver tissues are also geometrically non-uniform and thus can be challenging to mount repeatably and flatly for mechanical testing purposes, particularly in light of the importance of knowing the support geometry (e.g. thickness and width) for the calculation of a modulus from the raw force versus displacement data.

Nanoscale measurement techniques such as atomic force microscopy[188, 251] (AFM) or quartz crystal microbalance with dissipation[180, 183] (QCM-D) experiments offer an alternative in that they can sensitively and locally probe interfacial forces. In AFM experiments, a mucin-coated colloidal probe is typically lowered on a biomaterial, with

the force required for pull-off (in tapping mode) measured. In QCM-D experiments, one of the biomaterial or mucin is coated on the QCM chip while the other is flowed over the chip, with the measured change in both frequency and dissipation used to assess the amount of polymer adhered and the viscoelastic properties of the adherent layer. However, both these techniques can only probe small model surfaces, and neither (particularly QCM) can accurately assess the bulk mechanical interactions essential for the success of many mucoadhesive polymers.

More macroscopic adhesion information can be gained by specialized mechanical testing approaches, but these also have limitations for assessing the mucoadhesion of hydrogels. For mucoadhesive polymers or particles, rheological synergism in which the geometric sum of a rheological parameter (typically G') of the mucin and polymer solutions measured individually is compared to the value of that same parameter when the two solutions are mixed can give a reasonable estimate of the mucoadhesive potential of the material[187, 189]. However, this method is challenging to use for pre-formed bulk hydrogels, as it relies on intimate mixing between the mucin and polymer throughout the test volume. Direct mechanical tests are also possible for materials adhered to highly concentrated pellets of hydrated mucin[189], or for measuring the pull-out force of samples on a Wilhelmy plate submerged in a dilute mucin solution[178]. Such configurations have the advantage of comparative simplicity, and can generally rank compositions from most to least adhesive. However, due to the use of mucin concentrations far removed from physiological, they are limited in capability to predict actual adhesive properties of bulk hydrogels to physiological mucous membranes. In addition, fabricating hydrogels amenable to use in a Wilhelmy plate configuration can be

practically challenging, particularly when the gel thickness and degree of surface coverage are both essential to interpreting the force results acquired.

Based on these limitations of molecular-scale techniques, *ex vivo* tests, and existing bulk mechanical testing protocols, it is clear that translating the reproducibility and standardization of synthetic surfaces for measurements of mechanical properties such as work of adhesion and maximal failure stress is highly desirable for early-stage screening of putative adhesive chemistries. In order to mimic the physiological environment as accurately as possible, it would be advantageous to covalently assemble the synthetic glycoprotein layer on a soft substrate with mechanical properties that are tunable to match those of various targeted underlying biological tissues. Silicone rubber (PDMS) functionalized with thiol[252] or maleimide moieties would be an ideal such substrate given that its elasticity is easily tailorable by the amount of cross-linker added and functionalization of the substrate with groups that will covalently bond the mucin layer (via disulfide or thiosuccinimide bonding) is relatively straightforward.

In previous chapters of this thesis, the design of interpenetrating network hydrogels based on hydrazone cross-linked poly(N-isopropylacrylamide) (PNIPAM) and either disulfide or thiosuccininide cross-linked poly(N-vinylpyrrolidone) (PVP) has been disclosed. From a mucoadhesive perspective, these materials offer several potential advantages: (1) they are fully injectable and thus could be minimally invasively delivered to a target site; (2) they contain high (and tunable) densities of thiol (and in some cases, maleimide) groups that can form disulfide bridges with cysteine-rich mucin to enhance adhesion; and (3) their enhanced mechanical properties due to mechanical interlocking should improve the cohesion of the gel adhesive versus other alternative gel materials.

As such, assessment of the mucoadhesion potential of these hydrogels (either the IPN or the disulfide/thiosuccinimide cross-linked networks alone) offers potential to validate these hydrogels for a range of mucoadhesive applications.

Herein, we demonstrate the production of maleimide-functionalized PDMS specimens for assessing a simplified model of the mucoadhesive potential of disulfide cross-linked poly(N-vinylpyrrolidone) (PVP) hydrogels, capturing critical stress and strain, work of adhesion, and physical tack information.

5.2 Materials and Methods

5.2.1 Materials:

N-vinyl-pyrrolidone, thioglycolic acid, 3-mercaptopropionic acid, (3-mercaptopropyl)trimethoxysilane, (3-mercaptopropyl)trimethoxysilane, triethylamine and 1,1-(methylenedi-4,1-phenylene)bismaleimide were purchased form Sigma Aldrich (Oakville, Canada). N-vinylformamide was purchased from Toronto Research Chemicals (Toronto, Canada). The Sylgard 184 elastomer kit was purchased from Dow Corning. 2,2-azobisisobutyric acid (AIBME, 98%) was purchased from Waterstone and stored under nitrogen. 1-ethyl-3-(3-dimethylaminopropyl) carbodiimide hydrochloride (EDC, 98%) was purchased from Carbosynth (Berkshire, UK). All water used was of Milli-Q grade.

5.2.2 Preparation of functional silicone substrates:

Silicone substrates were produced using the Sylgard 184 elastomer kit (Dow Corning) and a 1:10 volume ratio of base to curing agent. Test substrates were molded to dimensions of 78 mm x 25 mm x 2mm and cured, first overnight at room temperature

followed by an additional 24 h at 50°C. The surface of the resulting silicone strip was subsequently thiolated based on previously reported methods[252]. Briefly, the substrates were sonicated for 6 hours in 20% w/v (3-mercaptopropyl)trimethoxysilane and 1% w/v KOH in isopropanol at 50°C, followed by washing (4 x 100 mL, sonicating 10 minutes at room temperature during each cycle) with dichloromethane. The resulting thiol groups were subsequently converted to maleimide groups by reacting the thiolated PDMS with a large excess of 1,1-(methylenedi-4,1-phenylene)bismaleimide with catalytic amounts of trimethylamine to facilitate deprotonation of the thiol groups, with an 80/20 volume ratio of isopropanol to water used as the solvent.

5.2.3 Synthesis of hydrogel precursor polymers:

Precursor polymers to the fully-injectable PNIPAM-PVP IPN hydrogel were produced as previously described in Chapter 4; proof of concept testing was carried out with the PVP-SH 70-30 high molecular weight disulfide network. Thiolated PVP was prepared by solution polymerization of 10 mL of a 70:30 molar ratio of N-vinylpyrrolidone and N-vinylformamide, using 10 mg 2,2-azobisisobutyric acid dimethyl ester as the radical initiator, 2 µL thiogylcolic acid as a chain transfer agent, and 10 mL isopropanol as the solvent. Polymerizations were carried out overnight at 60°C, after which the isopropanol was removed by rotary evaporation and the product was dissolved in water and dialyzed (6 x 6+ hour cycles) against Milli-Q water. N-vinylformamide residues were subsequently hydrolysed to primary amine groups by adding 1 M NaOH and reacting for 24 h at 70°C. Following another round of dialysis, the polymer was lyophilized and the amine content was determined by conductometric titration (base-into-acid, 1 mM NaOH titrant, 1 mg/mL polymer in 1 mM NaCl as sample, ManTech Associates). Amine groups were then converted to thiol groups by conjugation of a 1:1.2:3 molar ratio of polymer-

bound amine residues : 1-ethyl-3-(3-dimethylaminopropyl) carbodiimide hydrochloride (EDC; Carbosynth) : 3-mercaptopropionic acid (Sigma Aldrich), with manual pH control at 4.75 over the course of the conjugation. The thiolated product was then dialyzed against dilute HCl (pH<5) to avoid disulfide formation, after which the solution pH was adjusted to pH 7.4 and immediately lyophilized. The polymer was stored dry at -20°C until use.

5.2.4 Preparation of test samples:

A Mach 1 mechanical tester (BioMomentum, Laval, PQ) equipped with a 3.5 kg load cell was used for the initial proof of concept measurements. A new set of accessories was developed to cast hydrogels between a pair of functionalized PDMS substrates and mount the resulting 'sandwich' configuration for tests on the Mach-1. The parts kit developed for lap shear testing of PDMS substrates for mucoadhesive analysis is shown in Figures 5.1 and 5.2, with a sequential schematic of hydrogel preparation. PDMS wafers were attached with double-sided adhesive to a support equipped with mounting holes enabling attachment to the Mach-1 tester (Figures 5.1 b & c). Removable corner brackets were then tightly fitted to contain the precursor polymer between the lower and upper PDMS wafers (Figures 5.1 d & e). Following mounting of the second PDMS surface, an anchoring plate was then mounted with screws to hold the assembly together while the hydrogel cures (Figure 5.1f). Hydrogels were prepared by dissolving PVP-SH at 3.5 wt% in phosphate buffered saline and injecting the pre-gel solution into the assembly. Following hydrogel curing, the retaining walls were removed and threaded rods with pin and nut connections were used to attach the plastic support plates to the base and vertical motion stage of the Mach-1 tester (Figure 5.1g-j; also shown in Figure 5.2c).

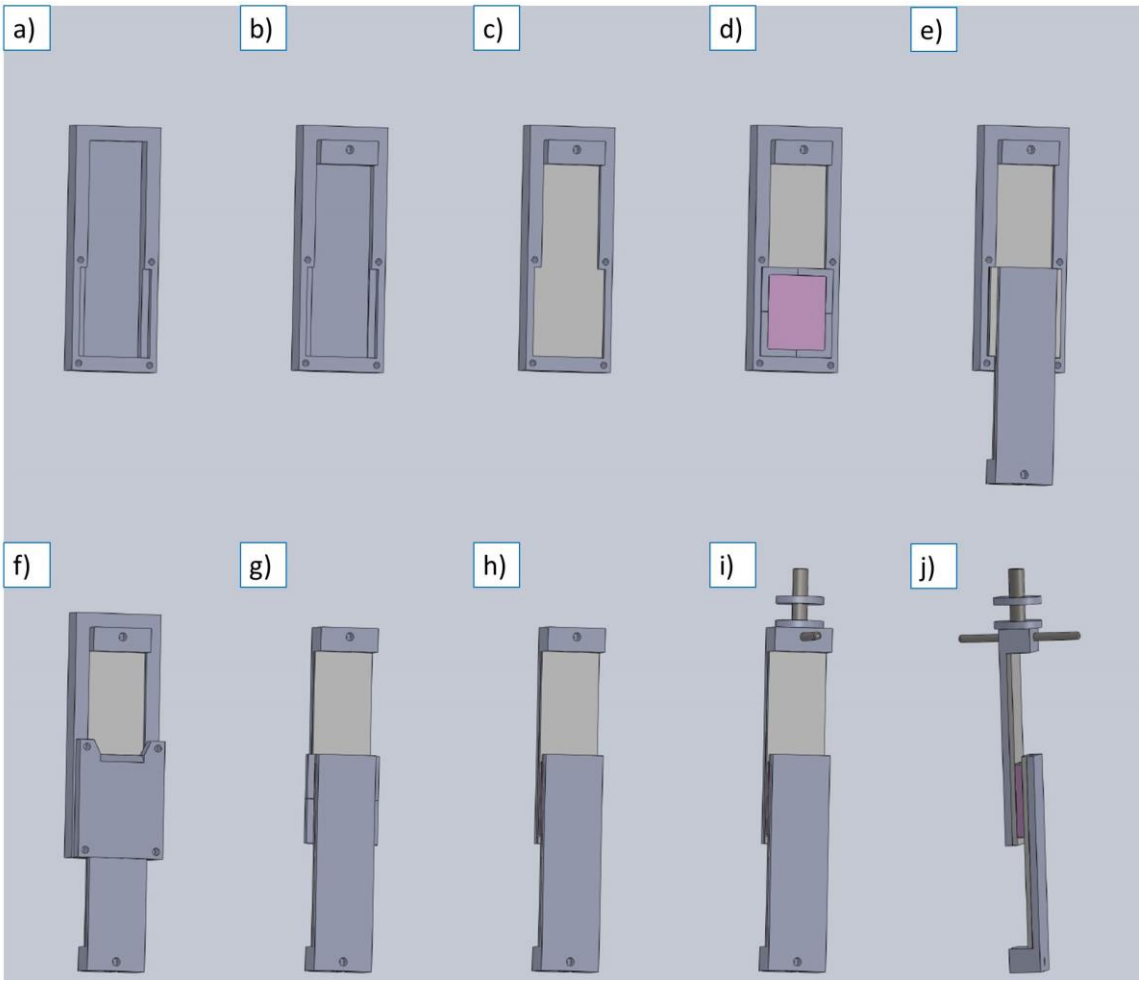

Figure 5.1: Sample holder kit design: a) mold backplate; b) backplate with support for mounting PDMS wafers to Mach-1 tester; c) assembly in (b) with PDMS wafer inserted (held to the plastic support via double-sided tape); d) insertion of mold walls and subsequent addition of polymer precursor solution (pink); e) second PDMS wafer (mounted on the support via double-sided tape) added; f) top plate added to secure second PDMS wafer/support (assembly screwed together until hydrogel cures); g) removal of back plate and top plate following gel curing; h) removal of mold walls following gel curing; i) insertion of mounting screw on top of assembly (bottom plate is attached to the base of the tester using the same method); j) mounting of test assembly to the instrument.

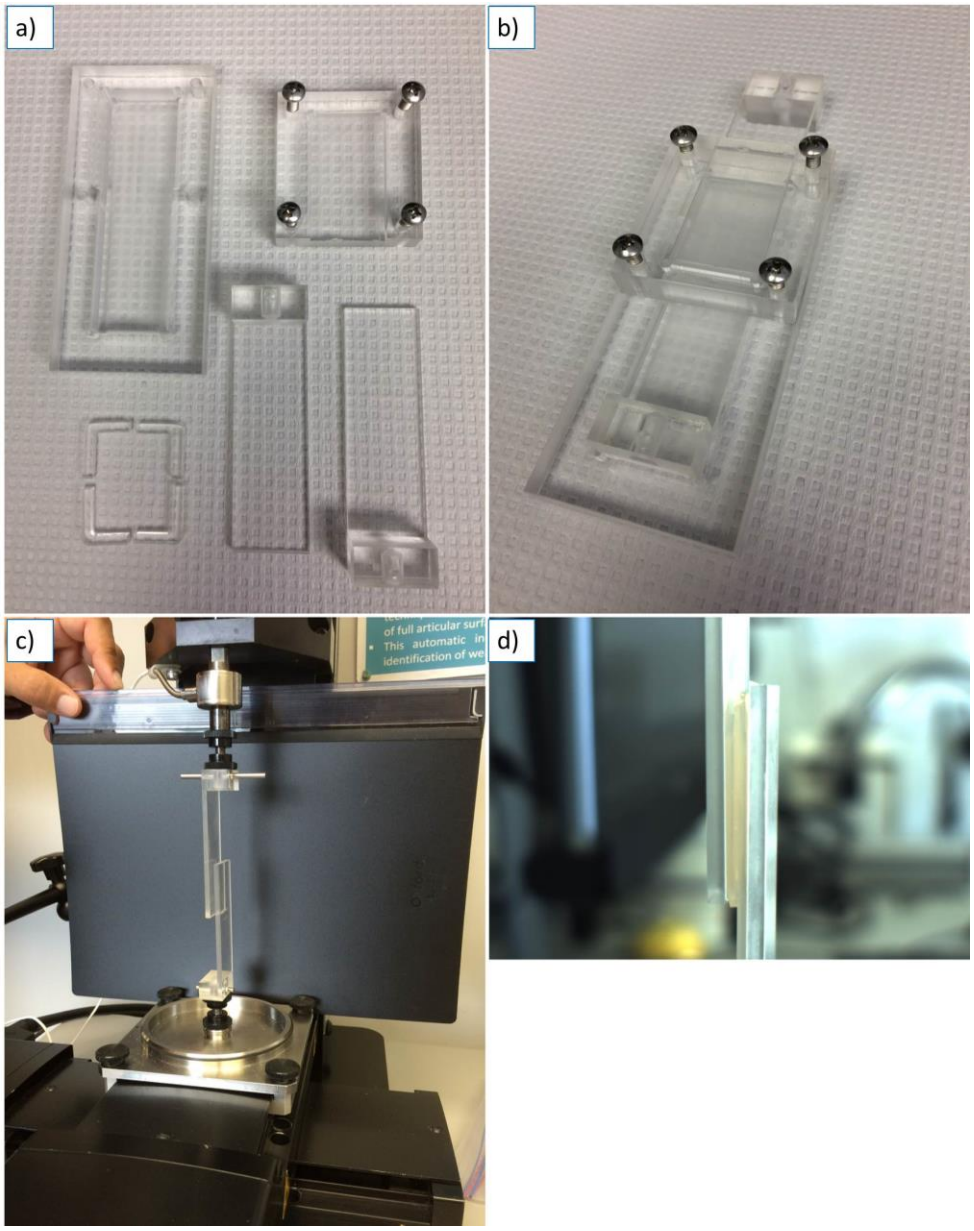

Figure 5.2: Sample holder kit fabricated from acrylic plastic that facilitates injection of a polymer precursor solution: a) individual components; b) assembled (without PDMS or hydrogel); c) mounting of support plates to load cell and motion stage (without sample); d) picture of a PVP-disulfide hydrogel attached to PDMS-maleimide test substrate.

5.2.5 Non-destructive analysis of adhered gel properties and destructive analysis of adhesive interface:

Several small-amplitude, non-destructive test sequences were used to assess the internal viscoelastic properties of the hydrogel as well as the versatility of the sample holder design before proceeding to destructive testing. Sinusoidal shear stretching was carried out using combinations of 0.05 mm, 0.1 mm and 0.15 mm amplitude / 0.1, 0.5 and 1 Hz frequency (for five cycles at each condition) to determine the complex shear modulus (i.e. storage and loss moduli). Small-amplitude stress relaxation cycles (0.1 mm stretching steps at 0.1 mm/s) were also used to determine the linear shear modulus, with 5 steps and a reset back to the starting position after each cycle. Thirty second relaxation breaks were included between each stretching step, during which the kinetics of shear force relaxation can be used to derive viscosity information about the hydrogel.

Destructive testing was carried out by expanding the amplitude of stress relaxation cycles to 0.3 mm and then to 1 mm (continuing to reset to the initial position after each sequence) until the hydrogel broke away from one of the PDMS substrates.

After failure of the adhesive interface, the gel was left to rest against the PDMS substrate for 30 s before resuming shearing. This measurement of physical tack (i.e. the shear needed to resume sliding behaviour) provides a lower bound on the adhesive forces expected in testing with the full mucin-coated PDMS configuration. This test also demonstrates how the system might potentially be used to test for self-healing of the adhesive interface in certain gel compositions.

5.3 Results and Discussion

The device assembly was designed to allow the hydrogel to be injected directly between the model substrates at a defined geometry and subsequently cure in the presence of maleimide-functionalized PDMS to mimic direct *in vivo* injection of such materials. Note that such direct contact between the coated substrate and the mucoadhesive hydrogel during the gelation process is typically not achievable with other test methods reported, particularly combined with the role of the test assembly to fix the dimensions of the gel sample and thus enhance the repeatability of the mechanical measurements. The clear (or at least translucent) optical properties of all the components of the test frame also enable qualitative assessment of the quality of the injected hydrogel sample, allowing the user to ensure complete filling of the reservoir and the absence of air bubbles often produced in injectable hydrogel systems and highly problematic in the interpretation of mechanical measurements.

Once samples are mounted, this configuration can be used for a range of tests modes. Specifically, non-destructive testing can be used to assess the mechanical properties of the hydrogel itself, while destructive testing can be used to assess the adhesive interactions between the gel and the functionalized PDMS substrate. Using small deformation amplitudes that stretch the hydrogel without damaging it or peeling it away from the PDMS surface, sinusoidal stretching in the vertical direction can be used to calculate the storage and loss modulus of the hydrogels (Figure 5.3a). Although a reasonably limited range of frequencies and amplitudes were employed during this proof-of-concept testing, the absence of apparent frequency dependence in the G' results suggests we were likely operating in the linear viscoelastic regime.

Using the stress relaxation function (stretching with pauses), the shear modulus of the hydrogel can be assessed from the slope of the force-displacement plot during stretching phases (Figure 5.3b). As expected given that the storage modulus is a complex analogue of the shear modulus (Equations 5.1 & 5.2), the values agreed reasonably closely between the different testing regimes (G of 1450 Pa by force-displacement slope, vs. G' 1240 Pa to 1380 Pa for the various parameters of sinusoids tested with negligible G").

Equation 5.1: Complex shear modulus G* (G' is the storage modulus, G" is the loss modulus)

$$G^* = G' + iG''$$

Equation 5.2: Shear modulus for linear deformation in the z direction (F is the applied force, t is the sample thickness, A is the cross-sectional area, Δz is the shear displacement)

$$G = \frac{Ft}{A\,\Delta z}$$

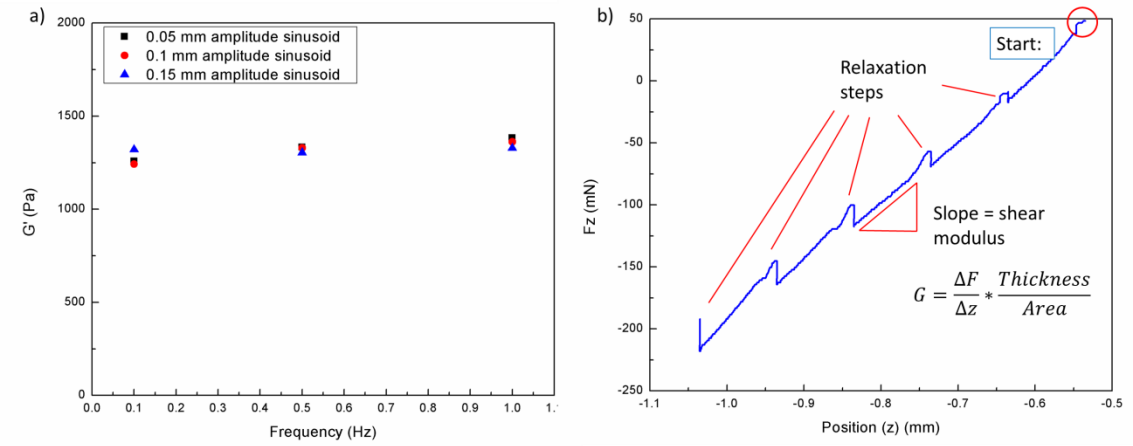

Figure 5.3: Non-destructive testing of hydrogel properties using lap shear geometry. a) shear modulus measured from small amplitude sinusoids in the z direction; b) stress relaxation results with 0.1 mm step size (small amplitude), with linear stress-strain response observed between relaxation steps.

Alternately, destructive testing can be used to elucidate the mechanical properties particular to the adhesive interface that are typically used to characterize commercial adhesives, including the ultimate shear stress and strain (Figure 5.4b, corresponding to the coordinates of the failure point) and the work of adhesion (Figure 5.4b and Equation 5.1, corresponding to the area under the force-displacement plot prior to failure). By performing stress-relaxation steps with increasing amplitude during the loading process, information about both the hydrogel mechanics as well as the mechanics of the interfacial adhesion can be achieved from a single experiment. However, it must be noted that if the work of adhesion was prioritized for measurement, a monotonic shear stretching sequence without relaxation steps would be more beneficial to improve accuracy. Thus, the test frame design can effectively enable measurement of both the fundamental (and relatively weak) properties of the hydrogel itself as well as the strength of the interfacial bonding between a hydrogel and an adhesive interface.

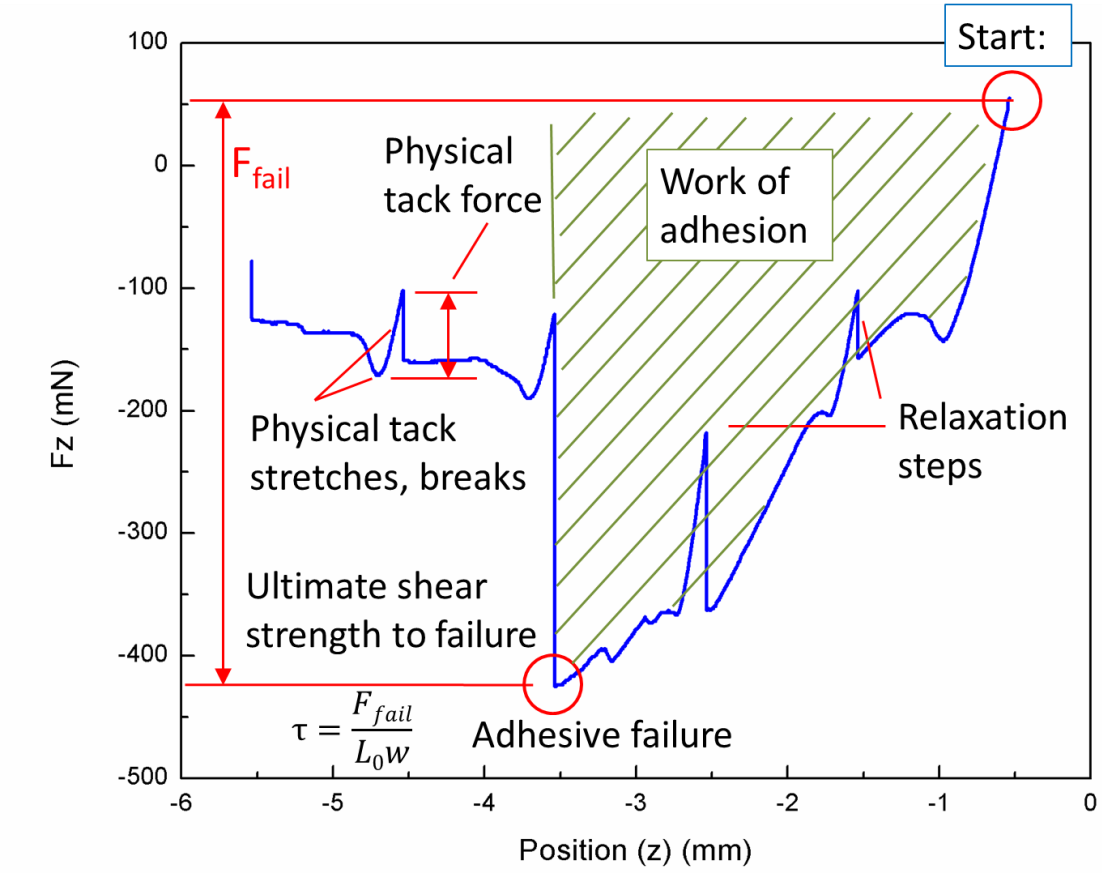

Figure 5.4: Destructive testing of the adhesive interface between hydrogels and maleimide-functionalized PDMS, using larger amplitudes of stress relaxation sequences. Destructive testing shows the ultimate stress and strain to failure of the adhesive interface, and can be used to find the work of adhesion.

Validation of the testing strategy was performed using a maleimide-functionalized PDMS surface that is known to form strong covalent bonds with thiol groups contained in the PVP-SH test gel. Given that the interface between the hydrogel and the mucin film in the final configuration will almost certainly be weaker than in this direct bonding of hydrogel thiol molecules to the maleimide-functionalized silicone substrate used for preliminary testing, we also aimed to assess the detection threshold of the test protocol

by testing the physical tack of a fractured sample. After rupturing the adhesive interface, the hydrogel was allowed to rest for 30 s against the exposed PDMS substrate (already used for the test), after which motion was resumed using the same 1 mm step stress relaxation protocol as used for work of adhesion measurements. This resulted in a much smaller linear strain region (also shown in Figure 5.4b) before motion resumes, a stick-slip behaviour attributable to the tack between the PDMS interface and the hydrogel. This experiment confirms that even small adhesion forces can be detected using this test protocol, facilitating the testing of weak mucoadhesives as well as negative control samples using non-adhesive hydrogels or unmodified PDMS.

The use of a flexible PDMS substrate for the measurements also raises the potential that the deformability of the PDMS itself may obfuscate the interpretation of the results (i.e. an applied stress is borne not only by the gel or the adhesive interface but by the PDMS support). While this was considered unlikely given that the PDMS supports are attached to the plastic back plates in the designed device, we tested the mechanics of the PDMS by slowly stretching a PDMS sheet using the Mach-1 tensile grip accessory (Figure 5.5). PDMS deformation was observed to be trivial at forces comparable to those required to rupture the adhesion between hydrogels and functionalized PDMS, with the deformation of PDMS samples of equal length to the hydrogels used in the designed test approximately three orders of magnitude smaller under equivalent applied force). This result clearly indicates that the testing protocol is successfully isolating the mechanical properties of the hydrogel and the adhesive bond instead of the PDMS supports. Thus, the test protocol designed is both sensitive enough to analyze weak hydrogels with minimal mucoadhesion and robust enough to collect relevant data over a range of hydrogel compositions.

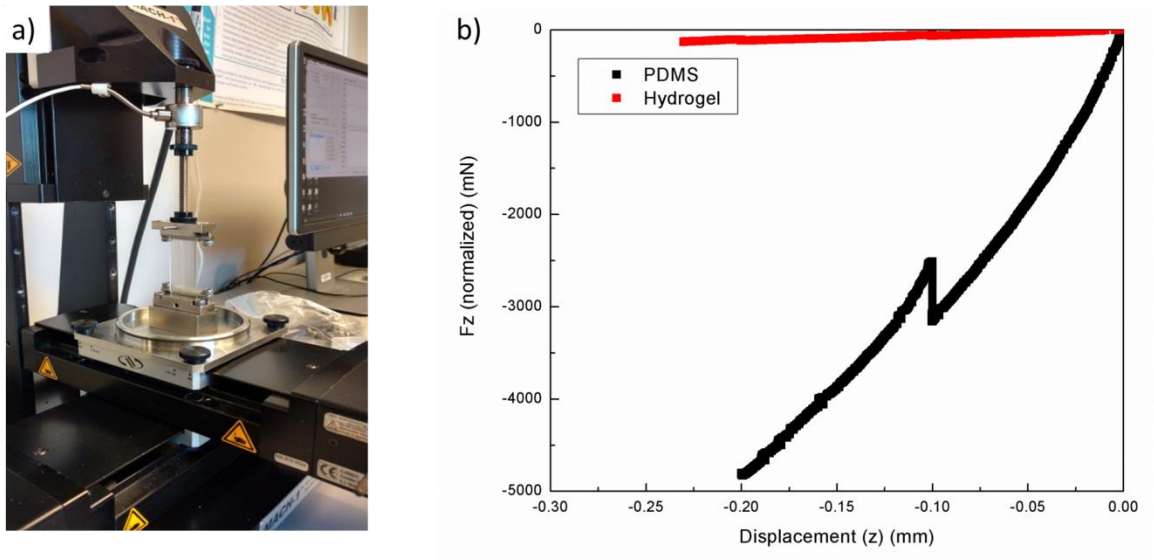

Figure 5.5: Elastic testing of a single PDMS substrate: (a) set-up of tensile test of PDMS; (b) comparison of force versus displacement curves for PDMS alone (tensile testing) and the mounted hydrogel (linear shear testing).

With proof of concept testing successful completed on the strongly adhered model system using the facilities at Biomomentum, we have ordered a load cell suitable for this testing configuration on our installation of the Mach-1 test frame at McMaster. This will enable measurement of the mucoadhesion forces of PVP-disulfide and PVP-thiosuccinimide single networks and their IPNs with hydrazone cross-linked PNIPAM (as described in Chapters 2-4 of this thesis) to maleimide-functionalized PDMS substrates dip-coated in mucin prior to testing. The macroscopic adhesion protocol used, coupled with the optical transparency of most of the components, should also allow identification of the failure mode(s) during destructive testing (i.e. hydrogel/mucin rupture vs. hydrogel cohesion vs. mucin/PDMS delamination failure); note that this latter failure mode, while possible in dip-coated mucin samples, is unlikely if sufficient bonds are formed between

the mucin coating and the functionalized PDMS substrate. Failure modes can be tested qualitatively by fluorescently labelling the mucin and examining whether it is predominantly stuck to the hydrogel or PDMS support after sample fracture. Combining the quantitative force measurements (both destructive and non-destructive) possible with this test frame design with the qualitative assessment of the nature of the failure is anticipated to give a clear picture of the effects of gel chemistry and gel mechanics on the mucoadhesive potential of the IPN hydrogels.

The testing protocol and set-up developed herein could also be used to assess other types of dynamic adhesive interactions of interest. Self-healing of adhesive interfaces (using a testing protocol similar to that used for the physical tack tests) could be analyzed using this technique provided that self-healing occurs on a time scale over which the hydrogel samples do not appreciably dry. Also, alternative materials that are designed to adhere on contact (rather than require casted in place) could be tested in the same configuration, although the inherent benefits of this device design are somewhat reduced in this case relative to more conventional testing strategies.

5.4 Conclusions

A new sample holder for lap shear mechanical testing that enables the *in situ* gelation of hydrogels in direct contact with functionalized soft interfaces (based on silicone rubber) was designed and validated. Non-destructive oscillatory or stress-relaxation testing enabled quantification of the hydrogel mechanical properties, while destructive testing was demonstrated to enable measurement of the ultimate shear stress and work of adhesion between the gel and the adhering surface. The method is highly sensitive

(capable of even quantifying tack between two soft samples), and the mechanics of the PDMS substrate can be tuned to mimic different tissues or adhesive interfaces. This device, to our knowledge, uniquely enables bulk adhesion testing of injectable, *in situ*-gelling hydrogels that can be formed directly in contact with the adhesive substrate with a defined geometry appropriate for repeatable mechanical testing. We anticipate this approach will be highly beneficial for quantifying the mucoadhesion of injectable hydrogels, critical information for the application of such gels in various drug delivery or wound healing applications.

Acknowledgments

We wish to thank Paul Gatt (Chemical Engineering staff machinist at McMaster University) for fabricating the parts used in this prototype.

Chapter 6: Conclusions, Significance and Future Perspectives

The research described in this thesis describes the development of a novel method for preparing injectable IPN hydrogels through hydrazone/disulfide and hydrazone/thiosuccinimide chemistry. The central design principle is the production of independent networks through kinetically orthogonal reactions that occur following the mixing of solutions of multiple functionalized polymeric precursors. Characterization studies (including small angle neutron scattering and, for the first time to our knowledge on IPN hydrogels, dSTORM super-resolution fluorescence microscopy) were focused on probing the micro- and nanostructure of these systems in order to guide compositional choices for rational design of future applications-focused research, particularly toward the manipulation of drug loading and release via the controlled formation of domains within the IPN network.

Chapter 2 established the orthogonality of pairing hydrazide-aldehyde and thiol-maleimide click-like cross-linking reactions, as demonstrated using both small molecule model and polymer-bound NMR studies, and verifying the viability of the delivery of such IPN hydrogels through a double-barreled mixing injector. The resulting IPNs demonstrate distinctive mechanical enhancement and modulation of swelling and degradation properties compared to either single network. Freeze-fracture SEM studies demonstrated that structural differences exist in the material, although drying artefacts made it impossible to elucidate further details of the hydrated network structure. This represents the first published description of a fully injectable interpenetrating network hydrogel that requires no additional post-mixing chemistry to form the IPN, a significant step towards improving the practicality of this class of hydrogels for use as biomaterials.

Subsequent studies on the same system (Chapter 3) focused on elucidating the details of the structural differences in the hydrated state at the micro- and nanoscale, with an emphasis on tracking the distribution of each polymer phase to determine mixing vs. segregation. Small-angle neutron scattering with contrast matching was used to study nanoscale structures. The PNIPAM and PVP displayed overall domain segregation on the nanoscale, although significant amounts of PNIPAM appear to be incorporated into the PVP-rich clusters. This work represents the first application of contrast variation in SANS to study thermosensitive transitions in an IPN hydrogel. Dual-channel dSTORM super-resolution microscopy with fluorescent labelling of each polymer network (to our knowledge, the first such study of the structure of any multi-component hydrogel system) was used to study the distribution of both polymer phases on larger length scales. These measurements confirmed that the PVP network does form segregated phases, tending toward larger and more irregular geometry than the PNIPAM domains. PNIPAM-rich domains sometimes occur overlapped into larger PVP phases, but smaller labelled PVP features within the PNIPAM domains are extremely rare; both observations are consistent with the general trends from the SANS studies on the nanoscale. It should be noted though that greater overlap between the length scales accessed by the two techniques would be very helpful to validate the conclusions made; for example, the use of ultra-small angle neutron scattering to access larger length scales on SANS may enable bridging of the gap between the techniques. Combined with the results from Chapter 2 demonstrating moderated de-swelling and degradation kinetics in the IPN composites, these results on domain segregation suggest that these systems are promising candidates for drug delivery applications, with dual-cargo partitioning and reduced burst release kinetics both possible. However, an assessment of macroporisty

in the hydrated state (such as, for example, by environmental SEM) would be helpful in predicting behaviour.

Chapter 4 describes a separate SANS contrast matching study on a complementary IPN system comprised of hydrazone cross-linked PNIPAM and disulfide cross-linked PVP. In particular, we sought to investigate whether a hydrazone / disulfide dual (fast/slow) cross-linking system substantially alters the network structure compared to the hydrazone / thiosuccinimide (fast/fast) pairing. In this configuration, PNIPAM still primarily drives domain formation, but the significantly slower gelation kinetics of PVP in these IPNs significantly reduces the amount of PVP present in the PNIPAM domains versus the faster gelling thiosuccinimide system. Incorporation of PNIPAM into the PVP-rich amorphous clusters appears to vary based on the molecular weight and functionalization density of the thiolated PVP used, with static scattering features – albeit irregularly defined – being more prominent in IPNs employing lower molecular weight and lower-functionalized PVP-SH. This appears to indicate disruption of domain formation by the PVP chains before they cross-link, with the IPN's using comparatively faster cross-linking PVP-disulfide formulations tending towards more defined and less prominent domain scattering features. This study shows, to our knowledge for the first time, how the rate of gelation of each phase in simultaneous IPN structures affects the resulting morphology of the IPNs, again highly relevant to the rational design for biomedical applications.

Although the structural differences observed relative to the dual fast gelling hydrazone / thiosuccinimide cross-linked IPN were relatively modest, they raise the possibility that more prominent variations could be obtained in an IPN system where both phases

cross-linked slowly (such as PNIPAM-hydrazide / PNIPAM-ketone hydrogels[79]). More extensive phase separation may be beneficial in drug delivery applications, creating enhanced potential for more hydrophilic pharmaceutical cargoes to partition into the PVP-rich phase and less hydrophilic ones to associate with the PNIPAM domains.

The hydrazone / disulfide cross-linking formulation also has advantages over the hydrazone / thiosuccinimide combination for injectable and cell delivery applications in that the disulfide cross-linking process is slow enough that clogging of the mixing baffles of the double barrel syringe is not observed. Unlike the thiosuccinimide cross-link, this combination is also fully degradable through reductive cleavage of the disulfide bond back to free thiol. However, it comes at the price of reduced mechanical strength in the resulting bulk hydrogels, suggesting that the hydrazone / thiosuccinimide combination is likely preferable in stress-bearing applications (e.g. tissue adhesive hydrogels).

Chapter 5 describes the development of a new lap shear method and associated hardware to enable measurement of the adhesive interactions between injectable hydrogels and a functionalized flexible silicone surface. In the context of the rest of the thesis, this work was motivated by the fact that functional groups used in these IPN systems to cross-link the PVP networks are also reactive with the thiol groups in mucin, suggesting possible utility of these hydrogels as mucoadhesives. To address challenges with the irreproducibility of *ex vivo*-based tests and the excessive localization of molecular-based methods of adhesion testing, an alternative measurement system was developed that can accommodate flat artificial mucin layers on soft substrates that can mimic the elasticity of biological tissues with large contact areas. Proof-of-concept testing with self-gelling thiolated PVP indicated the method was able to resolve adhesive

interactions between hydrogels and PDMS substrates ranging from weak physical tack up to strong covalent adhesion directly to functionalized substrates. The prototype accessory demonstrated the required sensitivity for mucoadhesion testing and is to our knowledge the first such mounting system that can facilitate the *in situ* gelation of injectable hydrogels in direct contact with the desired adhesive interface, better mimicking *in vivo* usage conditions. This method will be further applied to characterize the mucoadhesion of the IPN systems described in Chapters 2-4 once our local mechanical tester is upgraded with an appropriate load cell.

Beyond the scope of this work, several further experiments on these IPN systems would be of interest. First, to complete primary characterization of the morphologies of injectable IPN hydrogels as a function of the gelation time of each phase, analogous dSTORM imaging on the hydrazone / disulfide cross-linked IPNs, including tracking of thermally induced structural changes in the pNIPAM phase, would give significant insight into the temperature-responsive morphologies of these IPNs. Second, more application-focused research including dual-cargo model drug release studies (e.g. hydrophobic drug in the PNIPAM phase, hydrophilic drug in the PVP phase), cell viability testing, and exploration of the adhesive potential of the thiol and maleimide chemistries on mucin films would be of interest based on the types of morphologies that can generated with the current PNIPAM-PVP IPN system described.

The primary limitation of these IPN formulations for progress toward clinical applications is the short shelf life of the thiolated precursor polymer due to premature or unwanted formation of disulfide bonds. Instead of working with fresh material, this problem might be mitigated by freeze-drying the polymer at lower pH for long-term storage in the dry

state. Alternately, precursor solutions could be prepared below physiological pH and mixed either with a buffered, neutral precursor polymer or a slightly basic precursor polymer such that the net pH of the extruded gel is neutral. Thiolated polymer batches might also be prepared mixed with a small concentration of a biologically benign small-molecule reducing agent such as glutathione incorporated, which would diffuse away from the injection site once introduced to the body and allow cross-linking to proceed. Alternately, a wider variety of cross-linking chemistries might be tested for orthogonality, to determine a more storage-stable combination to translate these early findings toward clinical application.

The mechanical properties of the hydrogels also need to be further enhanced for many applications, in particular their use as strong interfacial tissue adhesives. We anticipate such enhancements will be possible by increasing the concentration of the precursor polymers, which we have previously shown in other systems to lead to substantial modulus enhancements (although at the cost of accelerated gelation kinetics that may make the application of some formulations challenging[31]). Alternately, reinforcing fillers may be added to the gel (for example, cellulose nanocrystals as demonstrated in previous work from our lab[253]) to further enhance the mechanics of one or both networks.

In the broader sense, the theme of producing IPN's from orthogonal click-like cross-linking reactions could be expanded to other polymer backbones, such as poly(acrylic acid) (for pH responsiveness), poly(oligo ethylene glycol methacrylate) or poly(N-isopropyl methacrylamide) (for dual temperature sensitivities at different transition points, possibly in conjunction with hyperthermic drug release applications), cationic polymers

like poly(N,N-dimethylaminoethyl methacrylate) (to facilitate cell adhesion and/or anti-bacterial properties), or any of the range of natural biopolymers commonly used in biomedical hydrogels (to facilitate differential degradation mechanisms/rates between the phases); all would be directly enabled by the knowledge and basic chemistries generated in this work. Other combinations of “click-like” cross-linking chemistries could also be tested for orthogonality, particularly in light of the relatively short storage stability of thiolated polymers (particularly at high molecular weight) in the context of eventual clinical applications. The use of other chemistries can also tune the degradation rate or even whether or not degradation ultimately occurs in each phase, of benefit in designing long-term drug release depots.

References

1. Okay, O., General Properties of Hydrogels. In *Hydrogel Sensors and Actuators: Engineering and Technology*, Gerlach, G.; Arndt, K.-F., Eds. Springer Berlin Heidelberg: Berlin, Heidelberg, 2010; pp 1-14.
2. Nagaoka, S.; Mori, Y.; Takiuchi, H.; Yokota, K.; Tanzawa, H.; Nishiumi, S., Interaction between Blood Components and Hydrogels with Poly(Oxyethylene) Chain. *Abstr Pap Am Chem S* **1983,** *185* (Mar), 142-Poly.
3. Hoare, T. R.; Kohane, D. S., Hydrogels in drug delivery: Progress and challenges. *Polymer* **2008,** *49* (8), 1993-2007.
4. Pelton, R., Poly(N-isopropylacrylamide) (PNIPAM) is never hydrophobic. *J Colloid Interf Sci* **2010,** *348* (2), 673-674.
5. Oh, S. H.; Kim, J. K.; Song, K. S.; Noh, S. M.; Ghil, S. H.; Yuk, S. H.; Lee, J. H., Prevention of postsurgical tissue adhesion by anti-inflammatory drug-loaded Pluronic mixtures with sol-gel transition behavior. *J Biomed Mater Res A* **2005,** *72a* (3), 306-316.
6. Smeets, N. M. B.; Bakaic, E.; Patenaude, M.; Hoare, T., Injectable poly(oligoethylene glycol methacrylate)-based hydrogels with tunable phase transition behaviours: Physicochemical and biological responses. *Acta Biomater* **2014,** *10* (10), 4143-4155.
7. Hu, Y.; Zhao, N. N.; Li, J. S.; Yang, W. T.; Xu, F. J., Temperature-responsive porous polycaprolactone-based films via surface-initiated ATRP for protein delivery. *J Mater Chem* **2012,** *22* (39), 21257-21264.
8. Kabra, B. G.; Gehrke, S. H.; Spontak, R. J., Microporous, responsive hydroxypropyl cellulose gels. 1. Synthesis and microstructure. *Macromolecules* **1998,** *31* (7), 2166-2173.
9. Gupta, A.; Mohanty, B.; Bohidar, H. B., Flory temperature and upper critical solution temperature of gelatin solutions. *Biomacromolecules* **2005,** *6* (3), 1623-1627.
10. Boustta, M.; Colombo, P. E.; Lenglet, S.; Poujol, S.; Vert, M., Versatile UCST-based thermoresponsive hydrogels for loco- regional sustained drug delivery. *J Control Release* **2014,** *174*, 1-6.
11. Shimada, N.; Kidoaki, S.; Maruyama, A., Smart hydrogels exhibiting UCST-type volume changes under physiologically relevant conditions. *Rsc Adv* **2014,** *4* (94), 52346-52348.
12. Phan, V. H. G.; Thambi, T.; Duong, H. T. T.; Lee, D. S., Poly(amino carbonate urethane)-based biodegradable, temperature and pH-sensitive injectable hydrogels for sustained human growth hormone delivery. *Scientific Reports* **2016,** *6*, 29978.
13. Zhang, L.; Jeong, Y.-I.; Zheng, S.; Jang, S. I.; Suh, H.; Kang, D. H.; Kim, I., Biocompatible and pH-sensitive PEG hydrogels with degradable phosphoester and phosphoamide linkers end-capped with amine for controlled drug delivery. *Polym Chem* **2013,** *4* (4), 1084-1094.
14. Ehrick, J. D.; Luckett, M. R.; Khatwani, S.; Wei, Y. N.; Deo, S. K.; Bachas, L. G.; Daunert, S., Glucose Responsive Hydrogel Networks Based on Protein Recognition. *Macromol Biosci* **2009,** *9* (9), 864-868.
15. Zhao, B.; Moore, J. S., Fast pH- and ionic strength-responsive hydrogels in microchannels. *Langmuir* **2001,** *17* (16), 4758-4763.
16. Patenaude, M.; Smeets, N. M. B.; Hoare, T., Designing Injectable, Covalently Cross-Linked Hydrogels for Biomedical Applications. *Macromol Rapid Comm* **2014,** *35* (6), 598-617.

17. Aguilar, M. E., C; Gallardo, A. V., B; Roman, J., Smart Polymers and their Applications as Biomaterials. In *Topics in Tissue Engineering, Expert Issues e-book*, Ashammakhi, N. R., R; Chielline, Eds. 2007; pp 1-27.
18. Drury, J. L.; Mooney, D. J., Hydrogels for tissue engineering: scaffold design variables and applications. *Biomaterials* **2003,** *24* (24), 4337-4351.
19. Hollister, S. J., Porous scaffold design for tissue engineering. *Nat Mater* **2005,** *4* (7), 518-524.
20. Vacanti, J. P.; Langer, R., Tissue engineering: the design and fabrication of living replacement devices for surgical reconstruction and transplantation. *Lancet* **1999,** *354*, Si32-Si34.
21. Rouwkema, J.; Rivron, N. C.; van Blitterswijk, C. A., Vascularization in tissue engineering. *Trends Biotechnol* **2008,** *26* (8), 434-441.
22. Annabi, N.; Nichol, J. W.; Zhong, X.; Ji, C. D.; Koshy, S.; Khademhosseini, A.; Dehghani, F., Controlling the Porosity and Microarchitecture of Hydrogels for Tissue Engineering. *Tissue Eng Part B-Re* **2010,** *16* (4), 371-383.
23. Tan, B.; Lee, J. Y.; Cooper, A. I., Synthesis of emulsion-templated poly(acrylamide) using CO2-in-water emulsions and poly(vinyl acetate)-based block copolymer surfactants. *Macromolecules* **2007,** *40* (6), 1945-1954.
24. Li, L.; Hsieh, Y. L., Ultra-fine polyelectrolyte hydrogel fibres from poly(acrylic acid)/poly(vinyl alcohol). *Nanotechnology* **2005,** *16* (12), 2852-2860.
25. Lee, J. Y.; Tan, B.; Cooper, A. I., CO2-in-water emulsion-templated poly(vinyl alcohol) hydrogels using poly(vinyl acetate)-based surfactants. *Macromolecules* **2007,** *40* (6), 1955-1961.
26. Park, J. S.; Woo, D. G.; Sun, B. K.; Chung, H. M.; Im, S. J.; Choi, Y. M.; Park, K.; Huh, K. M.; Park, K. H., In vitro and in vivo test of PEG/PCL-based hydrogel scaffold for cell delivery application. *J Control Release* **2007,** *124* (1-2), 51-59.
27. Sheridan, M. H.; Shea, L. D.; Peters, M. C.; Mooney, D. J., Bioabsorbable polymer scaffolds for tissue engineering capable of sustained growth factor delivery. *J Control Release* **2000,** *64* (1–3), 91-102.
28. Dadsetan, M.; Hefferan, T. E.; Szatkowski, J. P.; Mishra, P. K.; Macura, S. I.; Lu, L.; Yaszemski, M. J., Effect of hydrogel porosity on marrow stromal cell phenotypic expression. *Biomaterials* **2008,** *29* (14), 2193-2202.
29. Quirk, R. A.; France, R. M.; Shakesheff, K. M.; Howdle, S. M., Supercritical fluid technologies and tissue engineering scaffolds. *Curr Opin Solid St M* **2004,** *8* (3-4), 313-321.
30. Anderson, J. M.; Shive, M. S., Biodegradation and biocompatibility of PLA and PLGA microspheres. *Adv Drug Deliver Rev* **2012,** *64*, 72-82.
31. Smeets, N. M. B.; Bakaic, E.; Patenaude, M.; Hoare, T., Injectable and tunable poly(ethylene glycol) analogue hydrogels based on poly(oligoethylene glycol methacrylate). *Chem Commun* **2014,** *50* (25), 3306-3309.
32. Patenaude, M.; Hoare, T., Injectable, Mixed Natural-Synthetic Polymer Hydrogels with Modular Properties. *Biomacromolecules* **2012,** *13* (2), 369-378.
33. Kim, S.; Healy, K. E., Synthesis and characterization of injectable poly(N-isopropylacrylamide-co-acrylic acid) hydrogels with proteolytically degradable cross-links. *Biomacromolecules* **2003,** *4* (5), 1214-1223.
34. Levesque, S. G.; Shoichet, M. S., Synthesis of enzyme-degradable, peptide-cross-linked dextran hydrogels. *Bioconjugate Chem* **2007,** *18* (3), 874-885.

35. Tsarevsky, N. V.; Matyjaszewski, K., Combining atom transfer radical polymerization and disulfide/thiol redox chemistry: A route to well-defined (bio)degradable polymeric materials. *Macromolecules* **2005,** *38* (8), 3087-3092.
36. Choh, S. Y.; Cross, D.; Wang, C., Facile Synthesis and Characterization of Disulfide-Cross-Linked Hyaluronic Acid Hydrogels for Protein Delivery and Cell Encapsulation. *Biomacromolecules* **2011,** *12* (4), 1126-1136.
37. Singh, S.; Topuz, F.; Hahn, K.; Albrecht, K.; Groll, J., Embedding of Active Proteins and Living Cells in Redox-Sensitive Hydrogels and Nanogels through Enzymatic Cross-Linking. *Angewandte Chemie-International Edition* **2013,** *52* (10), 3000-3003.
38. Discher, D. E.; Janmey, P.; Wang, Y. L., Tissue cells feel and respond to the stiffness of their substrate. *Science* **2005,** *310* (5751), 1139-1143.
39. Kim, B. S.; Nikolovski, J.; Bonadio, J.; Mooney, D. J., Cyclic mechanical strain regulates the development of engineered smooth muscle tissue. *Nat Biotechnol* **1999,** *17* (10), 979-983.
40. Butler, D. L.; Goldstein, S. A.; Guilak, F., Functional tissue engineering: The role of biomechanics. *J Biomech Eng-T Asme* **2000,** *122* (6), 570-575.
41. Cowin, S. C., How is a tissue built? *J Biomech Eng-T Asme* **2000,** *122* (6), 553-569.
42. Sikavitsas, V. I.; Temenoff, J. S.; Mikos, A. G., Biomaterials and bone mechanotransduction. *Biomaterials* **2001,** *22* (19), 2581-2593.
43. Schmedlen, K. H.; Masters, K. S.; West, J. L., Photocrosslinkable polyvinyl alcohol hydrogels that can be modified with cell adhesion peptides for use in tissue engineering. *Biomaterials* **2002,** *23* (22), 4325-4332.
44. Bella, J.; Humphries, M. J., C alpha-H center dot center dot center dot O=C hydrogen bonds contribute to the specificity of RGD cell-adhesion interactions. *Bmc Struct Biol* **2005,** *5*.
45. Sun, J.; Wei, D.; Zhu, Y. D.; Zhong, M. L.; Zuo, Y. C.; Fan, H. S.; Zhang, X. D., A spatial patternable macroporous hydrogel with cell-affinity domains to enhance cell spreading and differentiation. *Biomaterials* **2014,** *35* (17), 4759-4768.
46. Hern, D. L.; Hubbell, J. A., Incorporation of adhesion peptides into nonadhesive hydrogels useful for tissue resurfacing. *J Biomed Mater Res* **1998,** *39* (2), 266-276.
47. Shu, X. Z.; Ghosh, K.; Liu, Y. C.; Palumbo, F. S.; Luo, Y.; Clark, R. A.; Prestwich, G. D., Attachment and spreading of fibroblasts on an RGD peptide-modified injectable hyaluronan hydrogel. *J Biomed Mater Res A* **2004,** *68a* (2), 365-375.
48. Amende, M. T.; Hariharan, D.; Peppas, N. A., Factors Influencing Drug and Protein-Transport and Release from Ionic Hydrogels. *React Polym* **1995,** *25* (2-3), 127-137.
49. Nakamae, K.; Nishino, T.; Kato, K.; Miyata, T.; Hoffman, A. S., Synthesis and characterization of stimuli-sensitive hydrogels having a different length of ethylene glycol chains carrying phosphate groups: loading and release of lysozyme. *J Biomat Sci-Polym E* **2004,** *15* (11), 1435-1446.
50. Sato, T.; Uchida, R.; Tanigawa, H.; Uno, K.; Murakami, A., Application of polymer gels containing side-chain phosphate groups to drug-delivery contact lenses. *J Appl Polym Sci* **2005,** *98* (2), 731-735.
51. Nuttelman, C. R.; Tripodi, M. C.; Anseth, K. S., Dexamethasone-functionalized gels induce osteogenic differentiation of encapsulated hMSCs. *J Biomed Mater Res A* **2006,** *76a* (1), 183-195.
52. Schoenmakers, R. G.; van de Wetering, P.; Elbert, D. L.; Hubbell, J. A., The effect of the linker on the hydrolysis rate of drug-linked ester bonds. *J Control Release* **2004,** *95* (2), 291-300.

53. Chen, W. L.; Shah, L. A.; Yuan, L.; Siddiq, M.; Hu, J. H.; Yang, D., Polymer-paclitaxel conjugates based on disulfide linkers for controlled drug release. *Rsc Adv* **2015,** *5* (10), 7559-7566.
54. Zhang, Y.; Gao, M.; Chen, C.; Wang, Z.; Zhao, Y. J., Residue cytotoxicity of a hydrazone-linked polymer-drug conjugate: implication for acid-responsive micellar drug delivery. *Rsc Adv* **2015,** *5* (44), 34800-34802.
55. Larson, N.; Ghandehari, H., Polymeric Conjugates for Drug Delivery. *Chem Mater* **2012,** *24* (5), 840-853.
56. Weissleder, R.; Poss, K.; Wilkinson, R.; Zhou, C.; Bogdanov, A., Quantitation of Slow Drug-Release from an Implantable and Degradable Gentamicin Conjugate by in-Vivo Magnetic-Resonance-Imaging. *Antimicrob Agents Ch* **1995,** *39* (4), 839-845.
57. Sawhney, A. S.; Lyman, M. D.; Jarrett, P. K.; Rudowsky, R. S., Compliant tissue sealants. Google Patents: 2001.
58. Thein-Han, W. W.; Stevens, W. F., Transdermal delivery controlled by a chitosan membrane. *Drug Dev Ind Pharm* **2004,** *30* (4), 397-404.
59. Coneac, G.; Vlaia, V.; Olariu, I.; Mut, A. M.; Anghel, D. F.; Ilie, C.; Popoiu, C.; Lupuleasa, D.; Vlaia, L., Development and Evaluation of New Microemulsion-Based Hydrogel Formulations for Topical Delivery of Fluconazole. *Aaps Pharmscitech* **2015,** *16* (4), 889-904.
60. Gulsen, D.; Chauhan, A., Dispersion of microemulsion drops in HEMA hydrogel: a potential ophthalmic drug delivery vehicle. *Int J Pharm* **2005,** *292* (1-2), 95-117.
61. Gao, W. W.; Vecchio, D.; Li, J. M.; Zhu, J. Y.; Zhang, Q. Z.; Fu, V.; Li, J. Y.; Thamphiwatana, S.; Lu, D. N.; Zhang, L. F., Hydrogel Containing Nanoparticle-Stabilized Liposomes for Topical Antimicrobial Delivery. *ACS Nano* **2014,** *8* (3), 2900-2907.
62. Anirudhan, T. S.; Parvathy, J.; Nair, A. S., A novel composite matrix based on polymeric micelle and hydrogel as a drug carrier for the controlled release of dual drugs. *Carbohyd Polym* **2016,** *136*, 1118-1127.
63. Sivakumaran, D.; Maitland, D.; Hoare, T., Injectable Microgel-Hydrogel Composites for Prolonged Small-Molecule Drug Delivery. *Biomacromolecules* **2011,** *12* (11), 4112-4120.
64. Kawano, T.; Niidome, Y.; Mori, T.; Katayama, Y.; Niidome, T., PNIPAM Gel-Coated Gold Nanorods, for Targeted Delivery Responding to a Near-Infrared Laser. *Bioconjugate Chem* **2009,** *20* (2), 209-212.
65. Maitland, D.; Campbell, S. B.; Chen, J.; Hoare, T., Controlling the resolution and duration of pulsatile release from injectable magnetic 'plum-pudding' nanocomposite hydrogels. *Rsc Adv* **2016,** *6* (19), 15770-15781.
66. Quinn, C. A. P.; Connor, R. E.; Heller, A., Biocompatible, glucose-permeable hydrogel for in situ coating of implantable biosensors. *Biomaterials* **1997,** *18* (24), 1665-1670.
67. Peroglio, M.; Grad, S.; Mortisen, D.; Sprecher, C. M.; Illien-Jünger, S.; Alini, M.; Eglin, D., Injectable thermoreversible hyaluronan-based hydrogels for nucleus pulposus cell encapsulation. *European Spine Journal* **2012,** *21* (6), 839-849.
68. Ding, C. X.; Zhao, L. L.; Liu, F. Y.; Cheng, J.; Gu, J. X.; Shan-Dan; Liu, C. Y.; Qu, X. Z.; Yang, Z. Z., Dually Responsive Injectable Hydrogel Prepared by In Situ Cross-Linking of Glycol Chitosan and Benzaldehyde-Capped PEO-PPO-PEO. *Biomacromolecules* **2010,** *11* (4), 1043-1051.
69. Smetana, K.; Vacik, J.; Souckova, D.; Krcova, Z.; Sulc, J., The Influence of Hydrogel Functional-Groups on Cell Behavior. *J Biomed Mater Res* **1990,** *24* (4), 463-470.

70. Van Tomme, S. R.; Storm, G.; Hennink, W. E., In situ gelling hydrogels for pharmaceutical and biomedical applications. *Int J Pharm* **2008,** *355* (1-2), 1-18.
71. Brubaker, C. E.; Kissler, H.; Wang, L. J.; Kaufman, D. B.; Messersmith, P. B., Biological performance of mussel-inspired adhesive in extrahepatic islet transplantation. *Biomaterials* **2010,** *31* (3), 420-427.
72. Kim, K.; Ryu, J. H.; Lee, D. Y.; Lee, H., Bio-inspired catechol conjugation converts water-insoluble chitosan into a highly water-soluble, adhesive chitosan derivative for hydrogels and LbL assembly. *Biomater Sci-Uk* **2013,** *1* (7), 783-790.
73. Lee, Y.; Chung, H. J.; Yeo, S.; Ahn, C. H.; Lee, H.; Messersmith, P. B.; Park, T. G., Thermo-sensitive, injectable, and tissue adhesive sol-gel transition hyaluronic acid/pluronic composite hydrogels prepared from bio-inspired catechol-thiol reaction. *Soft Matter* **2010,** *6* (5), 977-983.
74. Ryu, J. H.; Lee, Y.; Kong, W. H.; Kim, T. G.; Park, T. G.; Lee, H., Catechol-Functionalized Chitosan/Pluronic Hydrogels for Tissue Adhesives and Hemostatic Materials. *Biomacromolecules* **2011,** *12* (7), 2653-2659.
75. Anumolu, S. S.; Menjoge, A. R.; Deshmukh, M.; Gerecke, D.; Stein, S.; Laskin, J.; Sinko, P. J., Doxycycline hydrogels with reversible disulfide crosslinks for dermal wound healing of mustard injuries. *Biomaterials* **2011,** *32* (4), 1204-1217.
76. Bernkop-Schnurch, A.; Kast, C. E.; Richter, M. F., Improvement in the mucoadhesive properties of alginate by the covalent attachment of cysteine. *J Control Release* **2001,** *71* (3), 277-285.
77. Anderson, J. M., Biological responses to materials. *Ann Rev Mater Res* **2001,** *31*, 81-110.
78. Christie, R. J.; Anderson, D. J.; Grainger, D. W., Comparison of Hydrazone Heterobifunctional Cross-Linking Agents for Reversible Conjugation of Thiol-Containing Chemistry. *Bioconjugate Chem* **2010,** *21* (10), 1779-1787.
79. Patenaude, M.; Campbell, S.; Kinio, D.; Hoare, T., Tuning Gelation Time and Morphology of Injectable Hydrogels Using Ketone-Hydrazide Cross-Linking. *Biomacromolecules* **2014,** *15* (3), 781-790.
80. Lee, K. Y.; Alsberg, E.; Mooney, D. J., Degradable and injectable poly(aldehyde guluronate) hydrogels for bone tissue engineering. *J Biomed Mater Res* **2001,** *56* (2), 228-233.
81. Campbell, S. B.; Patenaude, M.; Hoare, T., Injectable Superparamagnets: Highly Elastic and Degradable Poly(N-isopropylacrylamide)-Superparamagnetic Iron Oxide Nanoparticle (SPION) Composite Hydrogels. *Biomacromolecules* **2013,** *14* (3), 644-653.
82. Patenaude, M.; Hoare, T., Injectable, Degradable Thermoresponsive Poly(N-isopropylacrylamide) Hydrogels. *ACS Macro Lett* **2012,** *1* (3), 409-413.
83. Dittmer, D. C.; Davis, F. A., Evidence for a Thiete (Thiacyclobutene)1,2. *J Am Chem Soc* **1965,** *87* (9), 2064-2065.
84. Friedman, M., Chemistry, Biochemistry, and Safety of Acrylamide. A Review. *Journal of Agricultural and Food Chemistry* **2003,** *51* (16), 4504-4526.
85. Kim, J.; Park, Y.; Tae, G.; Lee, K. B.; Hwang, C. M.; Hwang, S. J.; Kim, I. S.; Noh, I.; Sun, K., Characterization of low-molecular-weight hyaluronic acid-based hydrogel and differential stem cell responses in the hydrogel microenvironments. *J Biomed Mater Res A* **2009,** *88A* (4), 967-975.
86. Chen, C.; Wang, L.; Deng, L.; Hu, R.; Dong, A., Performance optimization of injectable chitosan hydrogel by combining physical and chemical triple crosslinking structure. *J Biomed Mater Res A* **2013,** *101A* (3), 684-693.

87. DuBose, J. W.; Cutshall, C.; Metters, A. T., Controlled release of tethered molecules via engineered hydrogel degradation: Model development and validation. *J Biomed Mater Res A* **2005,** *74A* (1), 104-116.
88. Cai, S.; Liu, Y.; Zheng Shu, X.; Prestwich, G. D., Injectable glycosaminoglycan hydrogels for controlled release of human basic fibroblast growth factor. *Biomaterials* **2005,** *26* (30), 6054-6067.
89. Sekine, Y.; Moritani, Y.; Ikeda-Fukazawa, T.; Sasaki, Y.; Akiyoshi, K., A Hybrid Hydrogel Biomaterial by Nanogel Engineering: Bottom-Up Design with Nanogel and Liposome Building Blocks to Develop a Multidrug Delivery System. *Advanced Healthcare Materials* **2012,** *1* (6), 722-728.
90. Tsurkan, M. V.; Chwalek, K.; Prokoph, S.; Zieris, A.; Levental, K. R.; Freudenberg, U.; Werner, C., Defined Polymer–Peptide Conjugates to Form Cell-Instructive starPEG–Heparin Matrices In Situ. *Adv Mater* **2013,** *25* (18), 2606-2610.
91. Koehler, K. C.; Anseth, K. S.; Bowman, C. N., Diels–Alder Mediated Controlled Release from a Poly(ethylene glycol) Based Hydrogel. *Biomacromolecules* **2013,** *14* (2), 538-547.
92. Fu, Y.; Kao, W. Y. J., In situ forming poly(ethylene glycol)-based hydrogels via thiol-maleimide Michael-type addition. *J Biomed Mater Res A* **2011,** *98A* (2), 201-211.
93. Allazetta, S.; Hausherr, T. C.; Lutolf, M. P., Microfluidic Synthesis of Cell-Type-Specific Artificial Extracellular Matrix Hydrogels. *Biomacromolecules* **2013,** *14* (4), 1122-1131.
94. McGann, C. L.; Levenson, E. A.; Kiick, K. L., Resilin-Based Hybrid Hydrogels for Cardiovascular Tissue Engineering. *Macromolecular Chemistry and Physics* **2013,** *214* (2), 203-213.
95. Jin, R.; Dijkstra, P. J.; Feijen, J., Rapid gelation of injectable hydrogels based on hyaluronic acid and poly(ethylene glycol) via Michael-type addition. *J Control Release* **2010,** *148* (1), e41-e43.
96. Peng, G.; Wang, J.; Yang, F.; Zhang, S.; Hou, J.; Xing, W.; Lu, X.; Liu, C., In situ formation of biodegradable dextran-based hydrogel via Michael addition. *J Appl Polym Sci* **2013,** *127* (1), 577-584.
97. Lyon, R. P.; Setter, J. R.; Bovee, T. D.; Doronina, S. O.; Hunter, J. H.; Anderson, M. E.; Balasubramanian, C. L.; Duniho, S. M.; Leiske, C. I.; Li, F.; Senter, P. D., Self-hydrolyzing maleimides improve the stability and pharmacological properties of antibody-drug conjugates. *Nat Biotechnol* **2014,** *32* (10), 1059-1062.
98. Vercruysse, K. P.; Marecak, D. M.; Marecek, J. F.; Prestwich, G. D., Synthesis and in vitro degradation of new polyvalent hydrazide cross-linked hydrogels of hyaluronic acid. *Bioconjugate Chem* **1997,** *8* (5), 686-694.
99. Zhang, H. W.; Qadeer, A.; Chen, W., In Situ Gelable Interpenetrating Double Network Hydrogel Formulated from Binary Components: Thiolated Chitosan and Oxidized Dextran. *Biomacromolecules* **2011,** *12* (5), 1428-1437.
100. Aliyar, H. A.; Hamilton, P. D.; Ravi, N., Refilling of ocular lens capsule with copolymeric hydrogel containing reversible disulfide. *Biomacromolecules* **2005,** *6* (1), 204-211.
101. Swindle-Reilly, K. E.; Shah, M.; Hamilton, P. D.; Eskin, T. A.; Kaushal, S.; Ravi, N., Rabbit Study of an In Situ Forming Hydrogel Vitreous Substitute. *Invest Ophth Vis Sci* **2009,** *50* (10), 4840-4846.
102. Klaikherd, A.; Nagamani, C.; Thayumanavan, S., Multi-Stimuli Sensitive Amphiphilic Block Copolymer Assemblies. *J Am Chem Soc* **2009,** *131* (13), 4830-4838.

103. Oh, J. K.; Siegwart, D. J.; Lee, H. I.; Sherwood, G.; Peteanu, L.; Hollinger, J. O.; Kataoka, K.; Matyjaszewski, K., Biodegradable nanogels prepared by atom transfer radical polymerization as potential drug delivery carriers: Synthesis, biodegradation, in vitro release, and bioconjugation. *J Am Chem Soc* **2007,** *129* (18), 5939-5945.
104. Ryu, J. H.; Chacko, R. T.; Jiwpanich, S.; Bickerton, S.; Babu, R. P.; Thayumanavan, S., Self-Cross-Linked Polymer Nanogels: A Versatile Nanoscopic Drug Delivery Platform. *J Am Chem Soc* **2010,** *132* (48), 17227-17235.
105. Sourkohi, B. K.; Cunningham, A.; Zhang, Q.; Oh, J. K., Biodegradable Block Copolymer Micelles with Thiol-Responsive Sheddable Coronas. *Biomacromolecules* **2011,** *12* (10), 3819-3825.
106. Shu, X. Z.; Liu, Y. C.; Luo, Y.; Roberts, M. C.; Prestwich, G. D., Disulfide cross-linked hyaluronan hydrogels. *Biomacromolecules* **2002,** *3* (6), 1304-1311.
107. Yang, J.; Stuart, M. A. C.; Kamperman, M., Jack of all trades: versatile catechol crosslinking mechanisms. *Chem Soc Rev* **2014,** *43* (24), 8271-8298.
108. Burzio, L. A.; Waite, J. H., Cross-linking in adhesive quinoproteins: Studies with model decapeptides. *Biochemistry-Us* **2000,** *39* (36), 11147-11153.
109. Holten-Andersen, N.; Harrington, M. J.; Birkedal, H.; Lee, B. P.; Messersmith, P. B.; Lee, K. Y. C.; Waite, J. H., pH-induced metal-ligand cross-links inspired by mussel yield self-healing polymer networks with near-covalent elastic moduli. *P Natl Acad Sci USA* **2011,** *108* (7), 2651-2655.
110. Sever, M. J.; Weisser, J. T.; Monahan, J.; Srinivasan, S.; Wilker, J. J., Metal-mediated cross-linking in the generation of a marine-mussel adhesive. *Angewandte Chemie-International Edition* **2004,** *43* (4), 448-450.
111. Lee, H.; Scherer, N. F.; Messersmith, P. B., Single-molecule mechanics of mussel adhesion. *P Natl Acad Sci USA* **2006,** *103* (35), 12999-13003.
112. Ossipov, D. A.; Hilborn, J., Poly(vinyl alcohol)-Based Hydrogels Formed by "Click Chemistry". *Macromolecules* **2006,** *39* (5), 1709-1718.
113. Wang, Q.; Chan, T. R.; Hilgraf, R.; Fokin, V. V.; Sharpless, K. B.; Finn, M. G., Bioconjugation by Copper(I)-Catalyzed Azide-Alkyne [3 + 2] Cycloaddition. *J Am Chem Soc* **2003,** *125* (11), 3192-3193.
114. Hodgson, S. M.; Bakaic, E.; Stewart, S. A.; Hoare, T.; Adronov, A., Properties of Poly(ethylene glycol) Hydrogels Cross-Linked via Strain-Promoted Alkyne-Azide Cycloaddition (SPAAC). *Biomacromolecules* **2016,** *17* (3), 1093-1100.
115. Sikorski, P.; Mo, F.; Skjak-Braek, G.; Stokke, B. T., Evidence for egg-box-compatible interactions in calcium-alginate gels from fiber X-ray diffraction. *Biomacromolecules* **2007,** *8* (7), 2098-2103.
116. Pasparakis, G.; Bouropoulos, N., Swelling studies and in vitro release of verapamil from calcium alginate and calcium alginate-chitosan beads. *Int J Pharm* **2006,** *323* (1-2), 34-42.
117. Lee, K. W.; Yoon, J. J.; Lee, J. H.; Kim, S. Y.; Jung, H. J.; Kim, S. J.; Joh, J. W.; Lee, H. H.; Lee, D. S.; Lee, S. K., Sustained release of vascular endothelial growth factor from calcium-induced alginate hydrogels reinforced by heparin and chitosan. *Transplant P* **2004,** *36* (8), 2464-2465.
118. Cuadros, T. R.; Skurtys, O.; Aguilera, J. M., Mechanical properties of calcium alginate fibers produced with a microfluidic device. *Carbohyd Polym* **2012,** *89* (4), 1198-1206.

119. Takei, T.; Sakai, S.; Ijima, H.; Kawakami, K., Development of mammalian cell-enclosing calcium-alginate hydrogel fibers in a co-flowing stream. *Biotechnology Journal* **2006,** *1* (9), 1014-1017.
120. Rowley, J. A.; Madlambayan, G.; Mooney, D. J., Alginate hydrogels as synthetic extracellular matrix materials. *Biomaterials* **1999,** *20* (1), 45-53.
121. Bajpai, S. K.; Sharma, S., Investigation of swelling/degradation behaviour of alginate beads crosslinked with Ca2+ and Ba2+ ions. *React Funct Polym* **2004,** *59* (2), 129-140.
122. Kong, X.; Narine, S. S., Physical properties of sequential interpenetrating polymer networks produced from canola oil-based polyurethane and poly(methyl methacrylate). *Biomacromolecules* **2008,** *9* (5), 1424-1433.
123. Myung, D.; Waters, D.; Wiseman, M.; Duhamel, P. E.; Noolandi, J.; Ta, C. N.; Frank, C. W., Progress in the development of interpenetrating polymer network hydrogels. *Polymers for Advanced Technologies* **2008,** *19* (6), 647-657.
124. Sperling, L. H., Interpenetrating Polymer Networks - an Overview. *Adv Chem Ser* **1994,** *239*, 3-38.
125. Li, S. F.; Yang, Y. J.; Yang, X. L.; Xu, H. B., In vitro degradation and protein release of Semi-IPN hydrogels consisted of poly(acrylic acid-acrylamide-methacrylate) and amylose. *J Appl Polym Sci* **2007,** *105* (6), 3432-3438.
126. Lim, Y. H.; Kim, D.; Lee, D. S., Drug releasing characteristics of thermo- and PH-sensitive interpenetrating polymer networks based on poly(N-isopropylacrylamide). *J Appl Polym Sci* **1997,** *64* (13), 2647-2655.
127. Matricardi, P.; Di Meo, C.; Coviello, T.; Hennink, W. E.; Alhaique, F., Interpenetrating Polymer Networks polysaccharide hydrogels for drug delivery and tissue engineering. *Adv Drug Deliver Rev* **2013,** *65* (9), 1172-1187.
128. Taira, Y.; Yanagida, H.; Matsumura, H.; Yoshida, K.; Atsuta, M.; Suzuki, S., Adhesive bonding of titanium with a thione-phosphate dual functional primer and self-curing luting agents. *Eur J Oral Sci* **2000,** *108* (5), 456-460.
129. Jia, D. M.; Pang, Y. X.; Liang, X., Mechanism of Adhesion of Polyurethane Polymethacrylate Simultaneous Interpenetrating Networks Adhesives to Polymer Substrates. *J Polym Sci Pol Phys* **1994,** *32* (5), 817-823.
130. Li, M.; Zheng, Z.; Liu, S.; Su, Y.; Wei, W.; Wang, X., Polyurethane (urea)/polyacrylates interpenetrating polymer network (IPN) adhesives for low surface energy materials. *Polymers for Advanced Technologies* **2011**, n/a-n/a.
131. Perlin, L.; MacNeil, S.; Rimmer, S., Cell adhesive hydrogels synthesised by copolymerisation of arg-protected Gly-Arg-Gly-Asp-Ser methacrylate monomers and enzymatic deprotection. *Chem Commun* **2008,** (45), 5951-5953.
132. Frisch, K. C.; Klempner, D.; Migdal, S.; Frisch, H. L.; Dunlop, A. P., Polyurethane–polyacrylate interpenetrating polymer networks. II. *J Appl Polym Sci* **1975,** *19* (7), 1893-1904.
133. Han, Y. A.; Lee, E. M.; Ji, B. C., Mechanical properties of semi-interpenetrating polymer network hydrogels based on poly(2-hydroxyethyl methacrylate) copolymer and chitosan. *Fiber Polym* **2008,** *9* (4), 393-399.
134. Yamashita, K.; Nishimura, T.; Nango, M., Preparation of IPN-type stimuli responsive heavy-metal-ion adsorbent gel. *Polymers for Advanced Technologies* **2003,** *14* (3-5), 189-194.
135. Fried, J., *Polymer Science & Technology*. 2 ed.; New Jersey, 2003.

136. Zdrahala, R. J.; Zdrahala, I. J., Biomedical applications of polyurethanes: A review of past promises, present realities, and a vibrant future. *J Biomater Appl* **1999,** *14* (1), 67-90.
137. Guelcher, S. A.; Patel, V.; Gallagher, K. M.; Connolly, S.; Didier, J. E.; Doctor, J. S.; Hollinger, J. O., Synthesis and in vitro biocompatibility of injectable polyurethane foam scaffolds. *Tissue Eng* **2006,** *12* (5), 1247-1259.
138. Annunziato, M. E.; Patel, U. S.; Ranade, M.; Palumbo, P. S., P-Maleimidophenyl Isocyanate - a Novel Heterobifunctional Linker for Hydroxyl to Thiol Coupling. *Bioconjugate Chem* **1993,** *4* (3), 212-218.
139. Hermanson, G., *Bioconjugation Techniques*. 2 ed.; Elsevier: London, 2008.
140. Lee, C. H.; Brauer, G. M., Oligomers with Pendant Isocyanate Groups as Adhesives for Dentin and Other Tissues. *Journal of Dental Research* **1989,** *68* (3), 484-488.
141. Sternberg, K.; Rohm, H. W.; Lurtz, C.; Wegmann, J.; Odermatt, E. K.; Behrend, D.; Michalik, D.; Schmitz, K. P., Development of a biodegradable tissue adhesive based on Functionalized 1,2-ethylene glycol bis(dilactic acid). I. *J Biomed Mater Res B* **2010,** *94B* (2), 318-326.
142. Gong, J. P., Why are double network hydrogels so tough? *Soft Matter* **2010,** *6* (12), 2583-2590.
143. Ker, R. F., The design of soft collagenous load-bearing tissues. *J Exp Biol* **1999,** *202* (23), 3315-3324.
144. Vanderhooft, J. L.; Alcoutlabi, M.; Magda, J. J.; Prestwich, G. D., Rheological Properties of Cross-Linked Hyaluronan-Gelatin Hydrogels for Tissue Engineering. *Macromol Biosci* **2009,** *9* (1), 20-28.
145. Tang, Q. W.; Sun, X. M.; Li, Q. H.; Wu, J. H.; Lin, J. M., A simple route to interpenetrating network hydrogel with high mechanical strength. *J Colloid Interf Sci* **2009,** *339* (1), 45-52.
146. Xing, Z. M.; Wang, C. L.; Yan, J.; Zhang, L.; Li, L.; Zha, L. S., Dual stimuli responsive hollow nanogels with IPN structure for temperature controlling drug loading and pH triggering drug release. *Soft Matter* **2011,** *7* (18), 7992-7997.
147. Zhang, J.; Peppas, N. A., Synthesis and characterization of pH- and temperature-sensitive poly(methacrylic acid)/poly(N-isopropylacrylamide) interpenetrating polymeric networks. *Macromolecules* **2000,** *33* (1), 102-107.
148. Wang, L.; Liu, M. Z.; Gao, C. M.; Ma, L. W.; Cui, D. P., A pH-, thermo-, and glucose-, triple-responsive hydrogels: Synthesis and controlled drug delivery. *React Funct Polym* **2010,** *70* (3), 159-167.
149. Ju, H. K.; Kim, S. Y.; Lee, Y. M., pH/temperature-responsive behaviors of semi-IPN and comb-type graft hydrogels composed of alginate and poly (N-isopropylacrylamide). *Polymer* **2001,** *42* (16), 6851-6857.
150. Shi, J.; Alves, N. M.; Mano, J. F., Chitosan coated alginate beads containing poly(N-isopropylacrylamide) for dual-stimuli-responsive drug release. *J Biomed Mater Res B* **2008,** *84b* (2), 595-603.
151. Kurisawa, M.; Yui, N., Dual-stimuli-responsive drug release from interpenetrating polymer network-structured hydrogels of gelatin and dextran. *J Control Release* **1998,** *54* (2), 191-200.
152. Alvarado, A. G.; Cortés, J.; Pérez-Carrillo, L. A.; Rabelero, M.; Arellano, J.; Sánchez-Díaz, J. C.; Puig, J. E.; Arellano, M., Temperature and pH-Responsive Polyacrylamide/Poly(Acrylic Acid)

Interpenetrating Polymer Network Nanoparticles. *Journal of Macromolecular Science, Part B* **2016,** *55* (11), 1086-1098.
153. Lee, W. F.; Chen, Y. J., Studies on preparation and swelling properties of the N-isopropylacrylamide/chitosan semi-IPN and IPN hydrogels. *J Appl Polym Sci* **2001,** *82* (10), 2487-2496.
154. Marsano, E.; Bianchi, E.; Viscardi, A., Stimuli responsive gels based on interpenetrating network of hydroxy propylcellulose and poly (N-isopropylacrylamide). *Polymer* **2004,** *45* (1), 157-163.
155. Zhao, S. P.; Li, L. Y.; Cao, M. J.; Xu, W. L., pH- and thermo-sensitive semi-IPN hydrogels composed of chitosan, N-isopropylacrylamide, and poly(ethylene glycol)-co-poly(epsilon-caprolactone) macromer for drug delivery. *Polym Bull* **2011,** *66* (8), 1075-1087.
156. Liu, Y. X.; Chan-Park, M. B., Hydrogel based on interpenetrating polymer networks of dextran and gelatin for vascular tissue engineering. *Biomaterials* **2009,** *30* (2), 196-207.
157. Saha, K.; Pollock, J. F.; Schaffer, D. V.; Healy, K. E., Designing synthetic materials to control stem cell phenotype. *Curr Opin Chem Biol* **2007,** *11* (4), 381-387.
158. Mohan, N.; Nair, P. D., Polyvinyl alcohol-poly(caprolactone) semi IPN scaffold with implication for cartilage tissue engineering. *J Biomed Mater Res B* **2008,** *84b* (2), 584-594.
159. Guo, Y.; Yuan, T.; Xiao, Z. W.; Tang, P. P.; Xiao, Y. M.; Fan, Y. J.; Zhang, X. D., Hydrogels of collagen/chondroitin sulfate/hyaluronan interpenetrating polymer network for cartilage tissue engineering. *J Mater Sci-Mater M* **2012,** *23* (9), 2267-2279.
160. DeKosky, B. J.; Dormer, N. H.; Ingavle, G. C.; Roatch, C. H.; Lomakin, J.; Detamore, M. S.; Gehrke, S. H., Hierarchically Designed Agarose and Poly(Ethylene Glycol) Interpenetrating Network Hydrogels for Cartilage Tissue Engineering. *Tissue Eng Part C-Me* **2010,** *16* (6), 1533-1542.
161. Chen, S. C.; Wu, Y. C.; Mi, F. L.; Lin, Y. H.; Yu, L. C.; Sung, H. W., A novel pH-sensitive hydrogel composed of N,O-carboxymethyl chitosan and alginate cross-linked by genipin for protein drug delivery. *J Control Release* **2004,** *96* (2), 285-300.
162. Mohamadnia, Z.; Zohuriaan-Mehr, A. J.; Kabiri, K.; Jamshidi, A.; Mobedi, H., pH-Sensitive IPN hydrogel beads of carrageenan-alginate for controlled drug delivery. *J Bioact Compat Pol* **2007,** *22* (3), 342-356.
163. Zhang, X. Z.; Wu, D. Q.; Chu, C. C., Synthesis, characterization and controlled drug release of thermosensitive IPN-PNIPAAm hydrogels. *Biomaterials* **2004,** *25* (17), 3793-3805.
164. Holland, T. A.; Tabata, Y.; Mikos, A. G., Dual growth factor delivery from degradable oligo(poly(ethylene glycol) fumarate) hydrogel scaffolds for cartilage tissue engineering. *J Control Release* **2005,** *101* (1-3), 111-125.
165. Konishi, M.; Tabata, Y.; Kariya, M.; Hosseinkhani, H.; Suzuki, A.; Fukuhara, K.; Mandai, M.; Takakura, A.; Fujii, S., In vivo anti-tumor effect of dual release of cisplatin and adriamycin from biodegradable gelatin hydrogel. *J Control Release* **2005,** *103* (1), 7-19.
166. Ma, D.; Tu, K.; Zhang, L. M., Bioactive Supramolecular Hydrogel with Controlled Dual Drug Release Characteristics. *Biomacromolecules* **2010,** *11* (9), 2204-2212.
167. Numata, K.; Yamazaki, S.; Naga, N., Biocompatible and Biodegradable Dual-Drug Release System Based on Silk Hydrogel Containing Silk Nanoparticles. *Biomacromolecules* **2012,** *13* (5), 1383-1389.

168. Song, B. T.; Wu, C. T.; Chang, J., Dual drug release from electrospun poly(lactic-co-glycolic acid)/mesoporous silica nanoparticles composite mats with distinct release profiles. *Acta Biomater* **2012,** *8* (5), 1901-1907.
169. Wei, L.; Cai, C. H.; Lin, J. P.; Chen, T., Dual-drug delivery system based on hydrogel/micelle composites. *Biomaterials* **2009,** *30* (13), 2606-2613.
170. Perale, G.; Rossi, F.; Santoro, M.; Peviani, M.; Papa, S.; Llupi, D.; Torriani, P.; Micotti, E.; Previdi, S.; Cervo, L.; Sundstrom, E.; Boccaccini, A. R.; Masi, M.; Forloni, G.; Veglianese, P., Multiple drug delivery hydrogel system for spinal cord injury repair strategies. *J Control Release* **2012,** *159* (2), 271-280.
171. Shi, J.; Alves, N. M.; Mano, J. F., Drug release of pH/temperature-responsive calcium alginate/poly(N-isopropylacrylamide) semi-IPN beads. *Macromol Biosci* **2006,** *6* (5), 358-363.
172. Guo, B. L.; Gao, Q. Y., Preparation and properties of a pH/temperature-responsive carboxymethyl chitosan/poly(N-isopropylacrylamide)semi-IPN hydrogel for oral delivery of drugs. *Carbohyd Res* **2007,** *342* (16), 2416-2422.
173. Shaikh, R.; Raj Singh, T. R.; Garland, M. J.; Woolfson, A. D.; Donnelly, R. F., Mucoadhesive drug delivery systems. *Journal of Pharmacy and Bioallied Sciences* **2011,** *3* (1), 89-100.
174. Strous, G. J.; Dekker, J., Mucin-Type Glycoproteins. *Crit Rev Biochem Mol* **1992,** *27* (1-2), 57-92.
175. Peppas, N. A.; Sahlin, J. J., Hydrogels as mucoadhesive and bioadhesive materials: A review. *Biomaterials* **1996,** *17* (16), 1553-1561.
176. Yu, T.; Andrews, G. P.; Jones, D. S., Mucoadhesion and Characterization of Mucoadhesive Properties. In *Mucosal Delivery of Biopharmaceuticals: Biology, Challenges and Strategies*, das Neves, J.; Sarmento, B., Eds. Springer US: Boston, MA, 2014; pp 35-58.
177. Lee, J. W.; Park, J. H.; Robinson, J. R., Bioadhesive-based dosage forms: The next generation. *J Pharm Sci* **2000,** *89* (7), 850-866.
178. Carvalho, F. C.; Bruschi, M. L.; Evangelista, R. C.; Gremião, M. P. D., Mucoadhesive drug delivery systems. *Braz J Pharm Sci* **2010,** *46*, 1-17.
179. Ding, J.; He, R.; Zhou, G.; Tang, C.; Yin, C., Multilayered mucoadhesive hydrogel films based on thiolated hyaluronic acid and polyvinylalcohol for insulin delivery. *Acta Biomater* **2012,** *8* (10), 3643-3651.
180. Mazzarino, L.; Coche-Guerente, L.; Labbe, P.; Lemos-Senna, E.; Borsali, R., On the Mucoadhesive Properties of Chitosan-Coated Polycaprolactone Nanoparticles Loaded with Curcumin Using Quartz Crystal Microbalance with Dissipation Monitoring. *J Biomed Nanotechnol* **2014,** *10* (5), 787-794.
181. Chivers, R. A.; Wolowacz, R. G., The strength of adhesive-bonded tissue joints. *Int J Adhes Adhes* **1997,** *17* (2), 127-132.
182. Standard Test Method for Strength Properties of Tissue Adhesives in Lap-Shear by Tension Loading. ASTM International: 2015.
183. Oh, S.; Borrós, S., Mucoadhesion vs mucus permeability of thiolated chitosan polymers and their resulting nanoparticles using a quartz crystal microbalance with dissipation (QCM-D). *Colloids and Surfaces B: Biointerfaces* **2016,** *147*, 434-441.
184. Chen, Q.; Tang, W.; Wang, D. Z.; Wu, X. J.; Li, N.; Liu, F., Amplified QCM-D biosensor for protein based on aptamer-functionalized gold nanoparticles. *Biosens Bioelectron* **2010,** *26* (2), 575-579.

185. Rodahl, M.; Hook, F.; Fredriksson, C.; Keller, C. A.; Krozer, A.; Brzezinski, P.; Voinova, M.; Kasemo, B., Simultaneous frequency and dissipation factor QCM measurements of biomolecular adsorption and cell adhesion. *Faraday Discuss* **1997,** *107*, 229-246.
186. Xu, K. R.; Ouberai, M. M.; Welland, M. E., A comprehensive study of lysozyme adsorption using dual polarization interferometry and quartz crystal microbalance with dissipation. *Biomaterials* **2013,** *34* (5), 1461-1470.
187. Ivarsson, D.; Wahlgren, M., Comparison of in vitro methods of measuring mucoadhesion: Ellipsometry, tensile strength and rheological measurements. *Colloids and Surfaces B: Biointerfaces* **2012,** *92*, 353-359.
188. Sriamornsak, P.; Wattanakorn, N.; Takeuchi, H., Study on the mucoadhesion mechanism of pectin by atomic force microscopy and mucin-particle method. *Carbohyd Polym* **2010,** *79* (1), 54-59.
189. Tamburic, S.; Craig, D. Q. M., A comparison of different in vitro methods for measuring mucoadhesive performance. *Eur J Pharm Biopharm* **1997,** *44* (2), 159-167.
190. Singh, I.; Rana, V., Techniques for the Assessment of Mucoadhesion in Drug Delivery Systems: An Overview. *Journal of Adhesion Science and Technology* **2012,** *26* (18-19), 2251-2267.
191. Lee, K. Y.; Bouhadir, K. H.; Mooney, D. J., Degradation behavior of covalently cross-linked poly(aldehyde guluronate) hydrogels. *Macromolecules* **2000,** *33* (1), 97-101.
192. Maia, J.; Ferreira, L.; Carvalho, R.; Ramos, M. A.; Gil, M. H., Synthesis and characterization of new injectable and degradable dextran-based hydrogels. *Polymer* **2005,** *46* (23), 9604-9614.
193. Dahlmann, J.; Krause, A.; Moller, L.; Kensah, G.; Mowes, M.; Diekmann, A.; Martin, U.; Kirschning, A.; Gruh, I.; Drager, G., Fully defined in situ cross-linkable alginate and hyaluronic acid hydrogels for myocardial tissue engineering. *Biomaterials* **2013,** *34* (4), 940-951.
194. Martinez-Sanz, E.; Ossipov, D. A.; Hilborn, J.; Larsson, S.; Jonsson, K. B.; Varghese, O. P., Bone reservoir: Injectable hyaluronic acid hydrogel for minimal invasive bone augmentation. *J Control Release* **2011,** *152* (2), 232-240.
195. Varghese, O. P.; Sun, W. L.; Hilborn, J.; Ossipov, D. A., In Situ Cross-Linkable High Molecular Weight Hyaluronan-Bisphosphonate Conjugate for Localized Delivery and Cell-Specific Targeting: A Hydrogel Linked Prodrug Approach. *J Am Chem Soc* **2009,** *131* (25), 8781-8783.
196. Nie, T.; Baldwin, A.; Yamaguchi, N.; Kiick, K. L., Production of heparin-functionalized hydrogels for the development of responsive and controlled growth factor delivery systems. *J Control Release* **2007,** *122* (3), 287-296.
197. Hiemstra, C.; van der Aa, L. J.; Zhong, Z. Y.; Dijkstra, P. J.; Feijen, J., Rapidly in situ-forming degradable hydrogels from dextran thiols through michael addition. *Biomacromolecules* **2007,** *8* (5), 1548-1556.
198. Metters, A.; Hubbell, J., Network formation and degradation behavior of hydrogels formed by Michael-type addition reactions. *Biomacromolecules* **2005,** *6* (1), 290-301.
199. Salinas, C. N.; Anseth, K. S., Mixed mode thiol-acrylate photopolymerizations for the synthesis of PEG-peptide hydrogels. *Macromolecules* **2008,** *41* (16), 6019-6026.
200. Hiemstra, C.; van der Aa, L. J.; Zhong, Z. Y.; Dijkstra, P. J.; Feijen, J., Novel in situ forming, degradable dextran hydrogels by Michael addition chemistry: Synthesis, rheology, and degradation. *Macromolecules* **2007,** *40* (4), 1165-1173.

201. Lutolf, M. P.; Hubbell, J. A., Synthesis and physicochemical characterization of end-linked poly(ethylene glycol)-co-peptide hydrogels formed by Michael-type addition. *Biomacromolecules* **2003,** *4* (3), 713-722.
202. Qiu, B.; Stefanos, S.; Ma, J. L.; Lalloo, A.; Perry, B. A.; Leibowitz, M. J.; Sinko, P. J.; Stein, S., A hydrogel prepared by in situ cross-linking of a thiol-containing poly(ethylene glycol)-based copolymer: a new biomaterial for protein drug delivery. *Biomaterials* **2003,** *24* (1), 11-18.
203. Yu, Y. X.; Deng, C.; Meng, F. H.; Shi, Q.; Feijen, J.; Zhong, Z. Y., Novel injectable biodegradable glycol chitosan-based hydrogels crosslinked by Michael-type addition reaction with oligo(acryloyl carbonate)-b-poly(ethylene glycol)-b-oligo(acryloyl carbonate) copolymers. *J Biomed Mater Res A* **2011,** *99a* (2), 316-326.
204. Naficy, S.; Kawakami, S.; Sadegholvaad, S.; Wakisaka, M.; Spinks, G. M., Mechanical properties of interpenetrating polymer network hydrogels based on hybrid ionically and covalently crosslinked networks. *J Appl Polym Sci* **2013,** *130* (4), 2504-2513.
205. Lopes, C. M. A.; Felisberti, M. I., Mechanical behaviour and biocompatibility of poly(1-vinyl-2-pyrrolidinone)-gelatin IPN hydrogels. *Biomaterials* **2003,** *24* (7), 1279-1284.
206. Mandal, B. B.; Kapoor, S.; Kundu, S. C., Silk fibroin/polyacrylamide Semi-interpenetrating network hydrogels for controlled drug release. *Biomaterials* **2009,** *30* (14), 2826-2836.
207. Liu, Y. Y.; Fan, X. D.; Wei, B. R.; Si, Q. F.; Chen, W. X.; Sun, L., pH-responsive amphiphilic hydrogel networks with IPN structure: A strategy for controlled drug. *Int J Pharm* **2006,** *308* (1-2), 205-209.
208. Zhao, J.; Zhao, X.; Guo, B. L.; Ma, P. X., Multifunctional Interpenetrating Polymer Network Hydrogels Based on Methacrylated Alginate for the Delivery of Small Molecule Drugs and Sustained Release of Protein. *Biomacromolecules* **2014,** *15* (9), 3246-3252.
209. Xiao, W. Q.; He, J. K.; Nichol, J. W.; Wang, L. Y.; Hutson, C. B.; Wang, B.; Du, Y. A.; Fan, H. S.; Khademhosseini, A., Synthesis and characterization of photocrosslinkable gelatin and silk fibroin interpenetrating polymer network hydrogels. *Acta Biomater* **2011,** *7* (6), 2384-2393.
210. Berger, J.; Reist, M.; Mayer, J. M.; Felt, O.; Peppas, N. A.; Gurny, R., Structure and interactions in covalently and ionically crosslinked chitosan hydrogels for biomedical applications. *Eur J Pharm Biopharm* **2004,** *57* (1), 19-34.
211. Kim, S.; Chung, E. H.; Gilbert, M.; Healy, K. E., Synthetic MMP-13 degradable ECMs based on poly(N-isopropylacrylamide-co-acrylic acid) semi-interpenetrating polymer networks. I. Degradation and cell migration. *J Biomed Mater Res A* **2005,** *75A* (1), 73-88.
212. Zhou, Y. S.; Yang, D. Z.; Gao, X. Y.; Chen, X. M.; Xu, Q.; Lu, F. M.; Nie, J., Semi-interpenetrating polymer network hydrogels based on water-soluble N-carboxylethyl chitosan and photo polymerized poly (2-hydroxyethyl methacrylate). *Carbohyd Polym* **2009,** *75* (2), 293-298.
213. Ganji, F.; Vasheghani-Farahani, S.; Vasheghani-Farahani, E., Theoretical Description of Hydrogel Swelling: A Review. *Iran Polym J* **2010,** *19* (5), 375-398.
214. Matsui, S.; Aida, H., Hydrolysis of Some N-Alkylmaleimides. *J Chem Soc Perk T 2* **1978,** (12), 1277-1280.
215. Liao, I. C.; Moutos, F. T.; Estes, B. T.; Zhao, X. H.; Guilak, F., Composite Three-Dimensional Woven Scaffolds with Interpenetrating Network Hydrogels to Create Functional Synthetic Articular Cartilage. *Adv Funct Mater* **2013,** *23* (47), 5833-5839.

216. Cetin, D.; Kahraman, A. S.; Gumusderelioglu, M., Novel Scaffolds Based on Poly(2-hydroxyethyl methacrylate) Superporous Hydrogels for Bone Tissue Engineering. *J Biomat Sci-Polym E* **2011,** *22* (9), 1157-1178.
217. Zeng, M. F.; Fang, Z. P., Preparation of sub-micrometer porous membrane from chitosan/polyethylene glycol semi-IPN. *J Membrane Sci* **2004,** *245* (1-2), 95-102.
218. Zhang, Y. S.; Liu, J.; Huang, L.; Wang, Z.; Wang, L., Design and performance of a sericin-alginate interpenetrating network hydrogel for cell and drug delivery. *Scientific Reports* **2015,** *5*.
219. Suthar, B.; Xiao, H. X.; Klempner, D.; Frisch, K. C., A review of kinetic studies on the formation of interpenetrating polymer networks. *Polymers for Advanced Technologies* **1996,** *7* (4), 221-233.
220. Yamamoto, N.; Kurisawa, M.; Yui, N., Double-stimuli-responsive degradable hydrogels: Interpenetrating polymer networks consisting of gelatin and dextran with different phase separation. *Macromol Rapid Comm* **1996,** *17* (5), 313-318.
221. Lohani, A.; Singh, G.; Bhattacharya, S. S.; Verma, A., Interpenetrating Polymer Networks as Innovative Drug Delivery Systems. *Journal of Drug Delivery* **2014,** *2014*, 11.
222. Huelck, V.; Thomas, D. A.; Sperling, L. H., Interpenetrating Polymer Networks of Poly(ethyl acrylate) and Poly(styrene-co-methly methacrylate). I. Morphology via Electron Microscopy. *Macromolecules* **1972,** *5* (4), 340-347.
223. Turner, J. S.; Cheng, Y. L., Morphology of PDMS-PMAA IPN membranes. *Macromolecules* **2003,** *36* (6), 1962-1966.
224. Burford, R. P.; Markotsis, M. G.; Knott, R. B., Real-time SANS study of interpenetrating polymer network (IPN) formation. *Physica B* **2006,** *385*, 766-769.
225. Tominaga, T.; Tirumala, V. R.; Lee, S.; Lin, E. K.; Gong, J. P.; Wu, W. L., Thermodynamic interactions in double-network hydrogels. *J Phys Chem B* **2008,** *112* (13), 3903-3909.
226. Tominaga, T.; Tirumala, V. R.; Lin, E. K.; Gong, J. P.; Furukawa, H.; Osada, Y.; Wu, W. L., The molecular origin of enhanced toughness in double-network hydrogels: A neutron scattering study. *Polymer* **2007,** *48* (26), 7449-7454.
227. Endo, H.; Miyazaki, S.; Haraguchi, K.; Shibayama, M., Structure of nanocomposite hydrogel investigated by means of contrast variation small-angle neutron scattering. *Macromolecules* **2008,** *41* (14), 5406-5411.
228. Helminger, M.; Wu, B. H.; Kollmann, T.; Benke, D.; Schwahn, D.; Pipich, V.; Faivre, D.; Zahn, D.; Colfen, H., Synthesis and Characterization of Gelatin-Based Magnetic Hydrogels. *Adv Funct Mater* **2014,** *24* (21), 3187-3196.
229. Waters, D. J.; Engberg, K.; Parke-Houben, R.; Ta, C. N.; Jackson, A. J.; Toney, M. F.; Frank, C. W., Structure and Mechanism of Strength Enhancement in Interpenetrating Polymer Network Hydrogels. *Macromolecules* **2011,** *44* (14), 5776-5787.
230. Leung, B. O.; Chou, K. C., Review of Super-Resolution Fluorescence Microscopy for Biology. *Appl Spectrosc* **2011,** *65* (9), 967-980.
231. van de Linde, S.; Heilemann, M.; Sauer, M., Live-Cell Super-Resolution Imaging with Synthetic Fluorophores. *Annu Rev Phys Chem* **2012,** *63*, 519-540.
232. Moerner, W. E., Microscopy beyond the diffraction limit using actively controlled single molecules. *J Microsc-Oxford* **2012,** *246* (3), 213-220.
233. Klein, T.; Loschberger, A.; Proppert, S.; Wolter, S.; van de Linde, S. V.; Sauer, M., Live-cell dSTORM with SNAP-tag fusion proteins. *Nat Methods* **2011,** *8* (1), 7-9.

234. Wilmes, S.; Staufenbiel, M.; Lisse, D.; Richter, C. P.; Beutel, O.; Busch, K. B.; Hess, S. T.; Piehler, J., Triple-Color Super-Resolution Imaging of Live Cells: Resolving Submicroscopic Receptor Organization in the Plasma Membrane. *Angewandte Chemie-International Edition* **2012,** *51* (20), 4868-4871.
235. Muranyi, W.; Malkusch, S.; Muller, B.; Heilemann, M.; Krausslich, H. G., Super-Resolution Microscopy Reveals Specific Recruitment of HIV-1 Envelope Proteins to Viral Assembly Sites Dependent on the Envelope C-Terminal Tail. *Plos Pathog* **2013,** *9* (2).
236. Endesfelder, U.; van de Linde, S.; Wolter, S.; Sauer, M.; Heilemann, M., Subdiffraction-Resolution Fluorescence Microscopy of Myosin-Actin Motility. *Chemphyschem* **2010,** *11* (4), 836-840.
237. Gilbert, T.; Smeets, N. M. B.; Hoare, T., Injectable Interpenetrating Network Hydrogels via Kinetically Orthogonal Reactive Mixing of Functionalized Polymeric Precursors. *ACS Macro Lett* **2015,** *4* (10), 1104-1109.
238. Park, J. W.; Kim, Y.; Lee, K. J.; Kim, D. J., Novel Cyanine Dyes with Vinylsulfone Group for Labeling Biomolecules. *Bioconjugate Chem* **2012,** *23* (3), 350-362.
239. Sheikholeslami, P. Highly Shear-Thinning Mucoadhesive Hydrogels for Ophthalmic Applications. McMaster University, 2013.
240. Azuah, R. T.; Kneller, L. R.; Qiu, Y. M.; Tregenna-Piggott, P. L. W.; Brown, C. M.; Copley, J. R. D.; Dimeo, R. M., DAVE: A Comprehensive Software Suite for the Reduction, Visualization, and Analysis of Low Energy Neutron Spectroscopic Data. *J Res Natl Inst Stan* **2009,** *114* (6), 341-358.
241. Kline, S. R., Reduction and analysis of SANS and USANS data using IGOR Pro. *J Appl Crystallogr* **2006,** *39*, 895-900.
242. Hammouda, B.; Ho, D. L.; Kline, S., Insight into clustering in poly(ethylene oxide) solutions. *Macromolecules* **2004,** *37* (18), 6932-6937.
243. Hammouda, B., Scattering from Fractal Systems. In *Probing Nanoscale Structures - The SANS Toolbox*, National Institute of Standards and Technology: Gaithersburg, Marlyand.
244. Hammouda, B.; Ho, D. L., Insight into chain dimensions in PEO/water solutions. *J Polym Sci Pol Phys* **2007,** *45* (16), 2196-2200.
245. Shibayama, M.; Isono, K.; Okabe, S.; Karino, T.; Nagao, M., SANS Study on Pressure-Induced Phase Separation of Poly(N-isopropylacrylamide) Aqueous Solutions and Gels. *Macromolecules* **2004,** *37* (8), 2909-2918.
246. Ovesný, M.; Křížek, P.; Borkovec, J.; Švindrych, Z.; Hagen, G. M., ThunderSTORM: a comprehensive ImageJ plugin for PALM and STORM data analysis and super-resolution imaging. *Bioinformatics* **2014**.
247. Smeets, N. M. B.; Patenaude, M.; Kinio, D.; Yavitt, F. M.; Bakaic, E.; Yang, F. C.; Rheinstadter, M.; Hoare, T., Injectable hydrogels with in situ-forming hydrophobic domains: oligo(D,L-lactide) modified poly(oligoethylene glycol methacrylate) hydrogels. *Polym Chem* **2014,** *5* (23), 6811-6823.
248. Okada, Y.; Tanaka, F., Cooperative hydration, chain collapse, and flat LCST behavior in aqueous poly(N-isopropylacrylamide) solutions. *Macromolecules* **2005,** *38* (10), 4465-4471.
249. Mongia, N. K.; Anseth, K. S.; Peppas, N. A., Mucoadhesive poly(vinyl alcohol) hydrogels produced by freezing/thawing processes: Applications in the development of wound healing systems. *J Biomat Sci-Polym E* **1996,** *7* (12), 1055-1064.
250. Schnurrer, J.; Lehr, C. M., Mucoadhesive properties of the mussel adhesive protein. *Int J Pharm* **1996,** *141* (1-2), 251-256.

251. Joergensen, L.; Klosgen, B.; Simonsen, A. C.; Borch, J.; Hagesaether, E., New insights into the mucoadhesion of pectins by AFM roughness parameters in combination with SPR. *Int J Pharm* **2011,** *411* (1-2), 162-168.
252. Zhang, J. F.; Chen, Y.; Brook, M. A., Facile Functionalization of PDMS Elastomer Surfaces Using Thiol Ene Click Chemistry. *Langmuir* **2013,** *29* (40), 12432-12442.
253. De France, K. J.; Chan, K. J. W.; Cranston, E. D.; Hoare, T., Enhanced Mechanical Properties in Cellulose Nanocrystal-Poly(oligoethylene glycol methacrylate) Injectable Nanocomposite Hydrogels through Control of Physical and Chemical Cross-Linking. *Biomacromolecules* **2016,** *17* (2), 649-660.